

**The Reactivity of Ni Complexes in Conjugated Polymer Synthesis**

by

Matthew D. Hannigan

A dissertation submitted in partial fulfillment  
of the requirements for the degree of  
Doctor of Philosophy  
(Chemistry)  
in the University of Michigan  
2022

Doctoral Committee:

Professor Anne J. McNeil, Co-Chair  
Associate Professor Paul M. Zimmerman, Co-Chair  
Assistant Professor Bryan R. Goldsmith  
Professor Melanie S. Sanford

Matthew D. Hannigan

mdhannig@umich.edu

ORCID iD: 0000-0002-2267-1388

© Matthew D. Hannigan 2022

## **Dedication**

For Donald Hannigan, whom I miss dearly, and Maryann Hannigan, whom I treasure.

Thank you for being my champions throughout my life.

## Acknowledgements

When I embarked on my PhD, I did not know the people who would help me make it to the end. Thankfully, it is impossible to do anything for nearly six years without making strong connections to the people that you're surrounded with. As such, I would like to truly thank everyone who has helped me along the way, because this thesis would not be possible without their support.

First and foremost, I would like to thank my advisors Anne McNeil and Paul Zimmerman. I am grateful to both of you for the many ways that you have helped me to expand my mind. Of course, the chemistry I learned from you is invaluable, but I am most thankful for the mentoring, patience, and opportunities you've given me which have made me a better scientist. Additionally, I would like to thank the other members of my committee, Melanie Sanford and Bryan Goldsmith, who have been helpful during committee meetings and in conversations about science and academia.

Next, thank you to the many members of the McNeil and Zimmerman labs who I've overlapped with during my time here (by my count, 112 people between the two labs). I've always had someone to turn to because of the willingness of my colleagues to help me when I needed it. There are particular people who I would like to thank. First, thank you to the people who mentored me at the start: Amanda Leone, Allison Roessler, and Andy Vitek. Thank you for teaching me the fundamentals and being pillars of support and encouragement throughout. Additionally, I would like to thank a few friends in the lab who have been supporters during my PhD. Emily Mueller,



thank you for always being there to discuss CTP and PhD woes. Gloria De La Garza, thank you for your friendship and encouragement especially during difficult times with thienothiophene. Jessica Tami, thank you for being a friend, for encouraging Anne to get a lab espresso machine, and for all of your help in the *J*-coupling project. Justin Harris, Takunda Chazovachii, Nikki Perkins, Khoi Dang, and Vai Shastri, thank you for being such great lab mates and for providing much needed distractions from some of the more difficult moments. Han Kim, thank you for your kindness, conversations, and for help with thesis stuff in these past few months. Kevin Skinner and Alan Rask, thank you for being there to get tea, joke around, and sort out computational chemistry problems. Chen Kong, thank you for helping me to interpret my first <sup>31</sup>P NMR spectra, to say it was important to my thesis would be an understatement. Patrick Lutz, thank you for always being willing to discuss catalysis and chem twitter. Mina Jafari, thank you for your encouragement in orienting me and my projects in the middle of my PhD. Woojung Ji and Tan Nguyen, thank you for helping me during my job searches. And last but not least, Danielle Fagnani: thank you for being such a great educator, mentor, and friend. I genuinely think that the last few years would have been *impossible* without your support in all aspects; I am so grateful for you and all the ways you have helped me grow along this journey.

Of course, I would like to thank the technical staff of the chemistry department: Eugenio Alvarado, Chris Kojiro, James Windak, Jeff Kampf, and Russ Bornschein. My PhD would have been literally impossible without your efforts to keep instruments running. Roy Wentz, thank you for your masterful glasswork, my PhD would have been much more difficult without all of your carefully crafted air-free glassware. Thank you, Sanford, Schindler, Matzger, Montgomery, Bartlett, Lehnert, Pecoraro, and Szymczak labs for helping me by letting me borrow chemicals, supplies, or expertise. Thank you, chemistry student services and main-office staff, particularly

Katie Foster, Heather Hanosh, and Emma Houle, for helping me with the academic requirements of the PhD, and for your support during my time as president of the chemistry graduate student council.

As you will see, a theme of my thesis is catalyst-transfer polymerization; it's a difficult reaction to study, so I would also like to thank all graduate students and post-docs who have *ever* studied catalyst-transfer polymerization. You know the frustrations that I have faced, and the studies that you all have published have been a source of encouragement for me.

I would not be doing a PhD were it not for my previous mentors. Thank you, Nancy Goroff, for giving me my first research experiences as an undergraduate and for being so encouraging. Thank you, Stony Brook professors, including Melanie Chiu, Andreas Mayr, and Joseph Lauher for engaging with me in my curiosity toward physical organic chemistry and organometallic chemistry. Ms. Naoual Eljastimi, thank you for being such an incredible high school chemistry teacher, your engaging and clear way of teaching inspired me to pursue the subject further, and I am forever grateful to you for first exposing me to the subject.

Thank you to the Rackham Graduate School for support and for a Rackham Merit Fellowship that funded four semesters of my PhD. Thank you to the U.S. Department of Defense for a National Defense Science and Engineering Graduate Fellowship that funded four years of my PhD.

Most importantly, thank you to my family. Robert, thank you for keeping me grounded and being my memory. Lea, thank you for being my light and giving me so much joy. Aunt Pat and Uncle Lou, thank you for your encouragement and love. And Mom and Dad, thank you for being my biggest supporters throughout all of this – my PhD would have truly been impossible without the intense love I feel from both of you every day. Because of you, I felt confident and empowered

to tackle the struggles I encountered on the journey toward this degree. Thank you for providing for me, giving me opportunities, encouraging my love of science, and supporting my decision to pursue an education. You mean the world to me, and I truly feel that this degree belongs to all of us.

## Table of Contents

Dedication.....	ii
Acknowledgements .....	iii
List of Tables .....	x
List of Figures.....	xi
List of Equations.....	xvii
List of Schemes .....	xviii
List of Appendices.....	xx
Abstract.....	xxiii
Chapter 1 Catalyst-Transfer Polymerization .....	1
1.1 Monomer Scope of CTP .....	7
1.2 Reactivity of $M^0$ $\pi$ -Complexes in CTP .....	11
1.2.1 Thermodynamic and Kinetic Stability of $LM-Ar$ $\pi$ -Complexes .....	12
1.2.2 Dissociation Reactions of $\pi$ -Complexes .....	14
1.2.3 Ring-walking Reactions of $\pi$ -Complexes .....	16
1.2.4 C-X Oxidative Addition From $\pi$ -Complexes .....	19
1.3 Reactivity of $M^{II}$ species in CTP .....	20
1.3.1 Transmetalation Reactions of $LM(Ar)X$ complexes.....	21
1.3.2 Reductive Elimination Reactions from $LMAr_2$ Complexes.....	24
1.4 Scope of This Thesis.....	25
1.5 References.....	27
Chapter 2 Using $J_{PP}$ to Identify Ni Bidentate Phosphine Complexes <i>in Situ</i> .....	35

2.1 Introduction.....	35
2.2 Literature Survey of Measured $ J_{PP} $ Values.....	39
2.3 Signs of $J_{PP}$ for Ni Bidentate Phosphine Complexes.....	42
2.4 Effects of Ligand Donation on $J_{PP}$ .....	44
2.5 Effect of Linker Length on $J_{PP}$ .....	49
2.6 Implication for the Analysis of $^{31}\text{P}$ NMR Spectra.....	50
2.7 Conclusion and Outlook.....	51
2.7.1 Broadly Relating to Coordination Complexes.....	51
2.7.2 Specifically Relating to Complexes in Catalyst-Transfer Polymerization.....	52
2.8 References.....	54
Chapter 3 Rethinking Catalyst Trapping in Ni-Catalyzed Thieno[3,2- <i>b</i> ]thiophene Polymerization.....	60
3.1 Introduction.....	60
3.2 Reanalyzing the Polymerization of Thieno[3,2- <i>b</i> ]thiophene.....	63
3.3 Reaction Paths for Thienothiophene Catalyst-Transfer Polymerization.....	65
3.4 Off-Cycle Reaction Paths and Catalyst Traps.....	68
3.5 Identifying Catalysts That Avoid C–S Insertion.....	74
3.6 Conclusions and Outlook.....	75
3.7 References.....	77
Chapter 4 Elucidating Ring-Walking in Catalyst-Transfer Polymerization.....	81
4.1 Introduction.....	81
4.2 Dataset Construction.....	84
4.3 Trends Between Structure and $\pi$ -Binding Energy.....	87
4.4 Ring-Walking in $\pi$ -Complexes.....	93
4.5 Conclusions and Outlook.....	100
4.6 References.....	101

Chapter 5 Conclusions and Outlook.....	104
Appendices .....	110

## List of Tables

<b>Table 2.1</b> Distribution of $ J_{PP} $ values reported in the 2C and 3C datasets. ....	41
<b>Table A1.1</b> Density functional screen for $J_{PP}$ calculations, sorted in order of most accurate to least accurate. O3LYP, the functional used for all other $J_{PP}$ calculations, is highlighted in green. ....	123
<b>Table A1.2</b> Benchmarks of basis sets for $J_{PP}$ calculations (O3LYP functional). ....	124
<b>Table A1.3</b> Ramsey contributors to $J_{PP}$ for a subset of complexes in this study. ....	126
<b>Table A2.1</b> Peak assignments for mass spectra in Figure A2.2.....	150
<b>Table A2.2</b> Monomer activation data from GC analysis of the quenched monomer solution ...	160
<b>Table A2.3</b> Monomer consumption from GC analysis of the quenched polymerizations .....	160
<b>Table A2.4</b> Monomer activation data from GC analysis of the quenched monomer solution ...	166
<b>Table A2.5</b> Monomer consumption from GC analysis of the quenched polymerizations .....	166
<b>Table A2.6</b> Computed $J_{PP}$ values for complexes in Chapter 3. ....	184
<b>Table A2.7</b> Crystal data and structure refinement for Ni(1,2-bis(dicyclohexylphosphino)ethane)[(C,S- $\kappa^2$ )-thieno[3,2- <i>b</i> ]thiophene]. ....	191
<b>Table A2.8</b> Atomic coordinates ( $\text{\AA} \times 10^4$ ) and equivalent isotropic displacement parameters ( $\text{\AA}^2 \times 10^3$ ) for Ni(1,2-bis(dicyclohexylphosphino)ethane)[(C,S- $\kappa^2$ )-thieno[3,2- <i>b</i> ]thiophene]. $U(\text{eq})$ is defined as one third of the trace of the orthogonalized $U_{ij}$ tensor .....	192
<b>Table A2.9</b> Bond lengths [A] and angles [deg] for Ni(1,2-bis(dicyclohexylphosphino)ethane)[(C,S- $\kappa^2$ )-thieno[3,2- <i>b</i> ]thiophene]. ....	193

## List of Figures

- Figure 2.1** Ni bidentate phosphine complexes and their  $J_{PP}$  values.....36
- Figure 2.2** a) Violin plots showing the distributions of experimentally observed  $|J_{PP}|$  for different Ni oxidation states ( $Ni^0$ ,  $Ni^{II}$ ) and phosphine linker lengths (2-carbon, 3-carbon). Bold lines represent medians, fine lines represent 25<sup>th</sup> and 75<sup>th</sup> percentiles. b) Probability that an observed  $|J_{PP}|$  represents a  $Ni^0$  or  $Ni^{II}$  complex for 2C and c) 3C datasets. The gap at the 60–70 Hz range is due to the lack of 3C complexes with  $|J_{PP}|$  in that range. ....41
- Figure 2.3** Violin plots showing distributions of computed  $J_{PP}$  for different Ni oxidation states ( $Ni^0$ ,  $Ni^{II}$ ) and phosphine linker lengths (2-carbon, 3-carbon). Bold lines represent medians, fine lines represent 25<sup>th</sup> and 75<sup>th</sup> percentiles.....43
- Figure 2.4** Plot of  $J_{PP}$  versus P-to-Ni charge transfer with regression lines shown in black. 2C line of best fit:  $J_{PP} = -1.648 \text{ Hz/me}^- \text{ CT}_{P\text{-to-Ni}} + 108.6 \text{ Hz}$ . 3C line of best fit:  $J_{PP} = -1.542 \text{ Hz/me}^- \text{ CT}_{P\text{-to-Ni}} + 50.22 \text{ Hz}$ . Grey areas indicate the 95% confidence interval for lines of best fit. A single outlier, complex 2-2329, is shown as a grey circle and was excluded from the analysis. ....45
- Figure 2.5** Three series of complexes that differ by identity of *trans* ligands.....47
- Figure 2.6** A series of structurally similar complexes with varied phosphine and *trans* ligands. 48
- Figure 2.7** Parity plot comparing values of  $J_{PP}$  computed from DFT calculations to the  $J_{PP}$  predicted by equation 2. Slope = 1.00, Y-intercept = 0.00 Hz. ....50
- Figure 3.1** Reaction of **M1** with  $Ni(dppp)Cl_2$ , yielding a catalyst trap that appears in  $^{31}P$  NMR spectra as two doublets with  $\delta = 12.08 \text{ ppm}$  ( $|J_{PP}| = 60.4 \text{ Hz}$ ) and  $\delta = 5.14 \text{ ppm}$  ( $|J_{PP}| = 60.4 \text{ Hz}$ ). ....63
- Figure 3.2** Computed  $|J_{PP}|$  for all on-cycle species expected in the CTP of **M1**<sub>Me</sub>. RMS error for  $|J_{PP}|$  calculations is ~11 Hz. red =  $Ni^0$ , blue =  $Ni^{II}$ .....65
- Figure 3.3** Reaction paths for initiation in  $Ni(dppp)$  CTP of **M1** (red =  $Ni^0$ , blue =  $Ni^{II}$ ). ....66
- Figure 3.4** Reaction paths for ring-walking and chain-end oxidative addition during  $Ni(dppp)$  catalyzed CTP of **M1** (red =  $Ni^0$ , blue =  $Ni^{II}$ ). ....67
- Figure 3.5** a) Reaction of 2,5-dibromo-3,6-dithiooctylthienothiophene with  $Ni(COD)_2$  and *dppp*, yielding  $Ni(dppp)_2$  at  $\delta = 11.6 \text{ ppm}$ , and a set of doublets assigned to **I** at  $\delta = 18.8 \text{ ppm}$  ( $|J_{PP}| = 72.8$



Hz) and  $\delta = -2.8$  ppm ( $|J_{PP}| = 73.1$  Hz) and b) attempted polymerization of **M2** with Ni(dppp)Cl<sub>2</sub>.  
.....68

**Figure 3.6** C–S oxidative addition into thienothiophene (C, grey; P, orange; Ni, green; S, yellow). Hydrogens excluded from the crystal structure for clarity. ....69

**Figure 3.7** Reaction paths from **III**<sub>Me</sub>, showing ring-walking and C–S insertion. ....70

**Figure 3.8** <sup>31</sup>P NMR spectra of the reaction between Ni(dcpe)(COD) and 2-bromothiopheno[3,2-*b*]thiophene at 0.5 h and 48 h. Red = Ni<sup>0</sup>, blue = Ni<sup>II</sup>. ....72

**Figure 3.9** Reaction of Ni bis(cycloocta-1,5-diene) with 3,6-dithiooctylthienothiophene and dcpp, yielding a set of doublets assigned to **CS4** at  $\delta = 12.0$  ppm ( $|J_{PP}| = 55.2$  Hz) and  $\delta = 7.02$  ppm ( $|J_{PP}| = 55.5$  Hz), and another set of doublets assigned to **CS5** at  $\delta = 19.6$  ppm ( $|J_{PP}| = 56.1$  Hz) and  $\delta = 5.27$  ppm ( $|J_{PP}| = 55.9$  Hz) Red = Ni<sup>0</sup>, blue = Ni<sup>II</sup>. ....73

**Figure 3.10** a) Computational ligand screening for enabling TTh polymerization and b) results of the ligand screen, showing the dependence of  $\Delta\Delta G^\ddagger$  on the  $\pi$ -backbonding ability of the ligand. ....74

**Figure 4.1** a) Orbitals involved in bonding between arenes and late transition metals, b) Energy of  $\pi^*$  orbital of the arenes and c) energy of the d orbital of the catalyst. ....88

**Figure 4.2**  $\Delta G_{\text{bind}}$  for metal/arene  $\pi$ -complexes, sorted by arene  $\pi^*$  energy (increasing to the right).  
.....89

**Figure 4.3**  $\Delta G_{\text{bind}}$  as a function of the energy gap between metal d-orbitals and  $\pi^*$  orbitals. ....89

**Figure 4.4**  $\Delta G_{\text{bind}}$  for metal/arene  $\pi$ -complexes, sorted by metal catalyst. ....91

**Figure 4.5**  $\Delta G_{\text{bind}}$  of  $\pi$ -complexes as a function of  $CT_{\text{M-to-Ar}}$ , the charge transfer from the metal to the arene in the  $\pi$ -complex. ....92

**Figure 4.6**  $\Delta G_{\text{bind}}$  of  $\pi$ -complexes as a function of  $CT_{\text{M-to-L}}$ , the charge transfer from the metal to the ancillary ligand in the  $\pi$ -complex. ....93

**Figure 4.7** Mechanism of ring-walking for a) Ni  $\pi$ -complexes and b) Pd  $\pi$ -complexes showing differences in the c) Ni–centroid and d) Pd–centroid distances along the reaction path.....94

**Figure 4.8** Transition states and backbonding orbitals present in ring-walking of a) Ni(IPr) and b) Pd(IPr) over thiophene. Orbitals are rendered at an isovalue = 0.03. ....95

**Figure 4.9** Barriers for ring-walking in Ni and Pd  $\pi$ -complexes. ....96

**Figure 4.10**  $\Delta G_{\text{RW}}^\ddagger$  for metal/arene  $\pi$ -complexes, sorted by arene  $\pi^*$  energy (increasing to the right). ....97

**Figure 4.11**  $\Delta G_{\text{RW}}^\ddagger$  vs.  $\Delta G_{\text{bind}}$  for the  $\pi$ -complexes in the dataset. ....97

<b>Figure 4.12</b> $\Delta G_{\text{RW}}^\ddagger$ of $\pi$ -complexes as a function of $CT_{\text{M-to-Ar}}$ , the backbonding charge transfer from the metal to the arene in the $\pi$ -complex. ....	98
<b>Figure 4.13</b> a) classes of arenes based on the number of substituents b) ring-walking barriers within each class. ....	99
<b>Figure A1.1</b> The query used for identifying complexes with 2-carbon backbones. The dotted bonds between P and Ni correspond to "any" bond. The [C,N,O] group attached to the P atoms enables search for structures with P-C, P-N, and P-O bonds. ....	111
<b>Figure A1.2</b> Narrowing the query results by using available data; specifically, only those substances that contain single-crystal X-ray structures by selecting only "Interatomic Distances and Angles". ....	112
<b>Figure A1.3</b> Narrowing down the query results by using available data; specifically, only those substances that contain reported NMR Spectroscopy by selecting only "NMR Spectroscopy".	112
<b>Figure A1.4</b> Substructures used as filters to exclude tridentate P ligands. ....	113
<b>Figure A1.5</b> The query used for the substructure search for Ni complexes with 3-carbon linkers. Dotted lines correspond to "any" bond between P and Ni, and the [C,N,O] enables a search for any substructures that have P-C, P-N, or P-O bonds. ....	113
<b>Figure A1.6</b> Narrowing down the query results by using available data; specifically, only those substances that contain reported NMR Spectroscopy. ....	114
<b>Figure A1.7</b> Tridentate substructures used as filter structures to exclude phosphine complexes with trans $J_{\text{PP}}$ values. ....	115
<b>Figure A1.8</b> Violin plot of chemical shifts of 2C and 3C complexes. All complexes in these datasets showed two separate $^{31}\text{P}$ chemical shifts - both shifts are included in the data above. .	119
<b>Figure A1.9</b> $^{31}\text{P}$ chemical shift versus $ J_{\text{PP}} $ for all complexes in the 2C and 3C datasets. ....	119
<b>Figure A1.10</b> Difference in the two $^{31}\text{P}$ chemical shifts of each complex versus $ J_{\text{PP}} $ in the 2C and 3C datasets. ....	120
<b>Figure A1.11</b> average of the two $^{31}\text{P}$ chemical shifts versus $ J_{\text{PP}} $ for each complex in the 2C and 3C datasets. ....	120
<b>Figure A1.12</b> Fragmentation scheme for charge transfer analysis of most complexes. ....	127
<b>Figure A1.13</b> Ni-to-P charge transfer versus $ J_{\text{PP}} $ with regression lines shown in black. ....	128
<b>Figure A1.14</b> P-Ni-P Bite angle for 2C and 3C complexes. ....	129
<b>Figure A1.15</b> Violin plots for comparison of bite angles between complexes with olefinic and aliphatic 2C or 3C linkers. ....	130

<b>Figure A1.16</b> Plot of bite angle vs. chemical shift for 2C and 3C complexes .....	131
<b>Figure A1.17</b> Calculated $J_{PP}$ versus P–Ni–P bite angle. Lines of best fit for the 2C and 3C datasets in black, line of best fit for the 2C+3C combined dataset in grey.....	132
<b>Figure A1.18</b> P-Ni-P Bite angle versus $J_{PP} + L$ . Lines of best fit for the 2C and 3C datasets in black, line of best fit for the 2C+3C combined dataset in grey.....	133
<b>Figure A1.19</b> P-Ni-P Bite angle versus P-to-Ni charge transfer. ....	134
<b>Figure A2.1</b> species that result from a) quenching of a $\pi$ -complex and b) quenching of the C–S insertion adduct. ....	148
<b>Figure A2.2</b> a) full and b) zoomed-in ESI+ mass spectra from the quenched polymerization mixture, with peaks arising from ring-opened and debrominated species as well as <b>D1</b> .....	149
<b>Figure A2.3</b> binding energies of the on-cycle $\pi$ -complexes relative to free <b>D1</b> + Ni(dppp). Note, $SC_8H_{17}$ have been truncated to $SMe$ groups to reduce computational complexity. ....	151
<b>Figure A2.4</b> A mechanism for catalyst trapping in CTP, showing the pathways that enable dimer formation and C–S insertion. Note, initiation is not shown. ....	152
<b>Figure A2.5</b> Degradation products observed by Vicic and Jones for a) benzothiophene and b) dibenzothiophene C–S insertion adducts. c) analogous degradation products that may be present in the current system.....	153
<b>Figure A2.6</b> $^{31}P$ NMR (202 MHz, THF) spectra taken at different time points for the reaction of Ni(COD)(dcpe) with 2-bromothiophene. ....	154
<b>Figure A2.7</b> $^{31}P$ NMR (243 MHz, THF) spectra taken at different time points for the reaction of Ni(COD) $_2$ with dcpp and 3,6-dioctylthiophene.....	156
<b>Figure A2.8</b> $^1H$ NMR spectra at 1 h (top) and 18 h (bottom) reaction times. ....	157
<b>Figure A2.9</b> $^{31}P$ NMR spectra at 1 h (top) and 18 h (bottom) reaction times, showing peaks at $\delta$ 18.74 (d, $J = 72.8$ Hz), 11.60, 8.97, -2.82 (d, $J = 73.1$ Hz). Peaks at 11.6 and 8.97 are assigned to Ni(dppp) $_2$ and Ni(dppp)(COD) respectively. ....	158
<b>Figure A2.10</b> GPC of the monomer solution A, $M_n = 1099$ , $M_w = 1138$ , $\mathcal{D} = 1.03$ .....	161
<b>Figure A2.11</b> GPC of the monomer solution B, $M_n = 1069$ , $M_w = 1112$ , $\mathcal{D} = 1.04$ .....	162
<b>Figure A2.12</b> GPC of the polymerization 1, $M_n = 1107$ , $M_w = 1208$ , $\mathcal{D} = 1.09$ .....	162
<b>Figure A2.13</b> GPC of the polymerization 2, $M_n = 1157$ , $M_w = 1281$ , $\mathcal{D} = 1.11$ .....	163
<b>Figure A2.14</b> GPC of the polymerization 3, $M_n = 1108$ , $M_w = 1204$ , $\mathcal{D} = 1.09$ .....	163
<b>Figure A2.15</b> GPC of the polymerization 4, $M_n = 1154$ , $M_w = 1304$ , $\mathcal{D} = 1.13$ .....	164

- Figure A2.16**  $^{31}\text{P}$  NMR spectra of polymerization 1 with  $\text{Ni}(\text{dppp})\text{Cl}_2$  at 0.5 h (top) with two peaks at 19.72 (d,  $J = 72.9$  Hz), -1.85 (d,  $J = 73.0$  Hz) and 6 h (bottom), with peaks at  $\delta$  19.72 (d,  $J = 73.0$  Hz), 12.06 (d,  $J = 60.1$  Hz), 5.12 (d,  $J = 60.3$  Hz), -1.84 (d,  $J = 72.9$  Hz)..... 168
- Figure A2.17**  $^{31}\text{P}$  NMR spectra of polymerization 2, with  $\text{Ni}(\text{dppp})\text{Cl}_2$  and  $\text{LiCl}$ , at 0.5 h (top) and 6 h (bottom) showing peaks at 12.06 (d,  $J = 60.4$  Hz), 5.12 (d,  $J = 60.4$  Hz)..... 168
- Figure A2.18**  $^{31}\text{P}$  NMR spectra of polymerization 3, with  $\text{Ni}(\text{dppe})\text{Cl}_2$  at 0.5 h (top) and 6 h (bottom) showing the same peaks at  $\delta$  62.44 (d,  $J = 41.7$  Hz), 45.36 (d,  $J = 41.2$  Hz)..... 169
- Figure A2.19**  $^{31}\text{P}$  NMR spectra of polymerization 4, at 0.5 h (top) with peaks at  $\delta$  51.44 (d,  $J = 30.9$  Hz), 49.28 (d,  $J = 10.9$  Hz), 46.42 (d,  $J = 10.9$  Hz), 44.02 (d,  $J = 31.3$  Hz). And at 6 h (bottom) with  $\delta$  51.44 (d,  $J = 30.9$  Hz) and 44.02 (d,  $J = 31.3$  Hz)..... 171
- Figure A2.20**  $^1\text{H}$  and  $^{13}\text{C}$  NMR spectra of 3,6-dimethoxythieno[3,2-*b*]thiophene.  $^1\text{H}$  NMR (500 MHz,  $\text{CDCl}_3$ )  $\delta$  6.26 (s, 1H), 3.92 (s, 3H).  $^{13}\text{C}$  NMR (126 MHz,  $\text{CDCl}_3$ )  $\delta$  151.02, 128.61, 97.52, 57.71. .... 172
- Figure A2.21**  $^1\text{H}$  and  $^{13}\text{C}$  NMR spectra of 3,6-dioctylthiothieno[3,2-*b*]thiophene.  $^1\text{H}$  NMR (700 MHz,  $\text{CD}_2\text{Cl}_2$ )  $\delta$  7.28 (s, 2H), 2.90 (t,  $J = 7.2$  Hz, 4H), 1.65 – 1.57 (m, 4H), 1.40 (m, 4H), 1.31 – 1.20 (m, 16H), 0.87 (t,  $J = 7.1$  Hz, 6H).  $^{13}\text{C}$  NMR (176 MHz,  $\text{CD}_2\text{Cl}_2$ )  $\delta$  141.31, 127.11, 125.11, 34.76, 31.93, 29.80, 29.31, 29.24, 28.71, 22.79, 14.24. .... 173
- Figure A2.22**  $^1\text{H}$  and  $^{13}\text{C}$  NMR spectra of 2,5-dibromo-3,6-dioctylthiothieno[3,2-*b*]thiophene.  $^1\text{H}$  NMR (500 MHz,  $\text{CDCl}_3$ )  $\delta$  2.87 (t,  $J = 7.3$  Hz, 4H), 1.54 (q,  $J = 7.6$  Hz, 4H), 1.44 – 1.36 (m, 4H), 1.32 – 1.17 (m, 16H), 0.87 (t,  $J = 6.9$  Hz, 6H).  $^{13}\text{C}$  NMR (126 MHz,  $\text{CDCl}_3$ )  $\delta$  139.69, 125.95, 119.50, 35.09, 32.17, 30.38, 29.54, 29.44, 28.82, 23.04, 14.50. .... 174
- Figure A2.23**  $^1\text{H}$  and  $^{13}\text{C}$  NMR spectra of 2,5-dichloro-3,6-dioctylthiothieno[3,2-*b*]thiophene.  $^1\text{H}$  NMR (500 MHz,  $\text{CD}_2\text{Cl}_2$ )  $\delta$  2.88 (t,  $J = 7.5$  Hz, 4H), 1.54 (t,  $J = 7.5$  Hz, 4H), 1.43 – 1.35 (m, 4H), 1.24 (s, 16H), 0.87 (t,  $J = 7.3$ , 6H).  $^{13}\text{C}$  NMR (126 MHz,  $\text{CD}_2\text{Cl}_2$ )  $\delta$  136.63, 133.77, 123.51, 35.10, 32.34, 30.60, 29.69, 29.59, 28.91, 23.21, 14.42. .... 175
- Figure A2.24**  $^1\text{H}$  and  $^{13}\text{C}$  NMR spectra of 2,5-di(2-thienyl)-3,6-dioctylthiothieno[3,2-*b*]thiophene.  $^1\text{H}$  NMR (500 MHz,  $\text{CD}_2\text{Cl}_2$ )  $\delta$  7.48 (dd,  $J = 3.7, 1.2$  Hz, 2H), 7.41 (dd,  $J = 5.1, 1.2$  Hz, 2H), 7.09 (dd,  $J = 5.1, 3.7$  Hz, 2H), 2.91 (t,  $J = 7.3$  Hz, 4H), 1.57 (p,  $J = 7.3$  Hz, 4H), 1.36 (p,  $J = 7.2$  Hz, 4H), 1.31 – 1.18 (m, 16 H), 0.85 (t,  $J = 7.0$  Hz, 6H).  $^{13}\text{C}$  NMR (126 MHz,  $\text{CD}_2\text{Cl}_2$ )  $\delta$  141.13, 140.69, 136.30, 127.52, 127.48, 127.19, 120.24, 35.92, 32.35, 30.55, 29.70, 29.61, 29.14, 23.20, 14.42. .... 176
- Figure A2.25**  $^1\text{H}$  and  $^{13}\text{C}$  NMR spectra of 2-(5'-bromothien-2'-yl)-5-(2''-thienyl)-3,6-dioctylthiothieno[3,2-*b*]thiophene.  $^1\text{H}$  NMR (500 MHz,  $\text{CD}_2\text{Cl}_2$ )  $\delta$  7.47 (dd,  $J = 3.7, 1.2$  Hz, 1H), 7.40 (dd,  $J = 5.1, 1.2$  Hz, 1H), 7.19 (d,  $J = 4.0$  Hz, 1H), 7.08 (dd,  $J = 5.1, 3.7$  Hz, 1H), 7.04 (d,  $J = 4.0$  Hz, 1H), 2.95 – 2.83 (m, 4H), 1.56 (dp,  $J = 10.4, 7.4$  Hz, 4H), 1.36 (d,  $J = 7.2$  Hz, 4H), 1.29 – 1.15 (m, 16H), 0.84 (td,  $J = 7.0, 1.9$  Hz, 6H).  $^{13}\text{C}$  NMR (126 MHz,  $\text{CD}_2\text{Cl}_2$ )  $\delta$  141.27, 140.93, 140.13, 137.94, 136.19, 130.14, 127.63, 127.55, 127.29, 126.79, 120.56, 120.24, 114.78, 36.13, 35.95, 32.35, 30.56, 29.72, 29.69, 29.62, 29.16, 29.13, 23.22, 14.42. .... 177

<b>Figure A2.26</b> $^1\text{H}$ , solvent-suppressed $^1\text{H}$ , and $^{31}\text{P}$ NMR spectra of nickel(1,2-bis(dicyclohexylphosphino)ethane)[(C,S- $\kappa^2$ )-thieno[3,2- <i>b</i> ]thiophene]. $^1\text{H}$ NMR (500 MHz, THF) $\delta$ 7.16 (ddd, $J = 22.5, 10.2, 6.2$ Hz, 2H), 6.97 (d, $J = 5.1$ Hz, 1H), 6.79 (d, $J = 5.0$ Hz, 1H), 2.22 (s, 8H), 1.39 – 0.79 (m, 26H). $^{31}\text{P}$ NMR (202 MHz, THF) $\delta$ 74.88 (d, $J = 23.4$ Hz), 64.06 (d, $J = 23.5$ Hz), 59.70 (impurity, Ni(dcpe)(COD)).	178
<b>Figure A2.27</b> $^1\text{H}$ and $^{13}\text{C}$ NMR of 2-bromothieno[3,2- <i>b</i> ]thiophene. $^1\text{H}$ NMR (500 MHz, $\text{CD}_2\text{Cl}_2$ ) $\delta$ 7.44 (d, $J = 5.3$ Hz, 1H), 7.31 (s, 1H), 7.20 (d, $J = 5.3$ Hz, 1H). $^{13}\text{C}$ NMR (126 MHz, $\text{CD}_2\text{Cl}_2$ ) $\delta$ 140.02, 138.60, 127.32, 122.76, 122.47, 119.60, 113.90, 110.58.	179
<b>Figure A2.28</b> $^1\text{H}$ and $^{13}\text{C}$ NMR spectra of tetrakis(2,2,2-trifluoroethyl) ethane-1,2-diylbis(phosphonite). $^1\text{H}$ NMR (500 MHz, THF) $\delta$ 4.03 (ddq, $J = 16.2, 7.9, 3.5$ Hz, 8H), 1.61 (t, $J = 7.2$ Hz, 4H). $^{13}\text{C}$ NMR (126 MHz, THF) $\delta$ 123.13 (q, $J = 278.8, 278.3$ Hz), 76.85 (t, $J = 32.1$ Hz), 66.10 – 63.79 (m).	180
<b>Figure A2.29</b> $^{19}\text{F}$ and $^{31}\text{P}$ NMR spectra of tetrakis(2,2,2-trifluoroethyl) ethane-1,2-diylbis(phosphonite). $^{19}\text{F}$ NMR (471 MHz, THF) $\delta$ -75.77 (t, $J = 8.2$ Hz). $^{31}\text{P}$ NMR (202 MHz, THF) $\delta$ 198.83 (s).	181
<b>Figure A2.30</b> $^1\text{H}$ , $^{19}\text{F}$ and $^{31}\text{P}$ NMR spectra of nickel tetrakis(2,2,2-trifluoroethyl)ethane-1,2-diylbis(phosphonite) dichloride. $^1\text{H}$ NMR (500 MHz, Chloroform- <i>d</i> ) $\delta$ 5.23 (s, 4H), 4.75 (s, 4H), 2.03 (d, $J = 21.6$ Hz, 4H). $^{19}\text{F}$ NMR (471 MHz, Chloroform- <i>d</i> ) $\delta$ -74.91 (d, $J = 8.3$ Hz). $^{31}\text{P}$ NMR (202 MHz, Chloroform- <i>d</i> ) $\delta$ 175.46.	182
<b>Figure A2.31</b> Reactions and catalysts examined for catalyst screening.	187
<b>Figure A2.32</b> Plot of barriers vs. $\pi$ -backbonding charge transfer	188
<b>Figure A2.33</b> ORTEP of Ni(1,2-bis(dicyclohexylphosphino)ethane)[(C,S- $\kappa^2$ )-thieno[3,2- <i>b</i> ]thiophene].	190
<b>Figure A3.1.</b> Plot of $\Delta G^\ddagger_{\text{RW}}$ vs % buried volume.	205

## List of Equations

<b>Equation 2.1</b> .....	44
<b>Equation 2.2</b> .....	50

## List of Schemes

<b>Scheme 1.1</b> Mechanism of a) cross-coupling polymerization and b) small-molecule cross-coupling. ....	4
<b>Scheme 1.2</b> The mechanism of catalyst-transfer polymerization. ....	5
<b>Scheme 1.3</b> Monomer scope of Ni-catalyzed CTP. Reprinted with permission from Leone, A. K.; McNeil, A. J. Matchmaking in Catalyst-Transfer Polycondensation: Optimizing Catalysts based on Mechanistic Insight <i>Acc. Chem. Res.</i> <b>2016</b> , <i>49</i> , 2822–2831. Copyright 2016 American Chemical Society. ....	8
<b>Scheme 1.4</b> Monomer Scope of Pd-catalyzed CTP. Reprinted with permission from Leone, A. K.; McNeil, A. J. Matchmaking in Catalyst-Transfer Polycondensation: Optimizing Catalysts based on Mechanistic Insight <i>Acc. Chem. Res.</i> <b>2016</b> , <i>49</i> , 2822–2831. Copyright 2016 American Chemical Society. ....	9
<b>Scheme 1.5</b> Two subsets of problematic monomers in CTP. ....	10
<b>Scheme 1.6</b> Ring-walking and oxidative addition in CTP. Arene color indicates polymer (grey) and chain-end monomer residue (blue). ....	12
<b>Scheme 1.7</b> The backbonding (d-to- $\pi^*$ ) interactions present in $\pi$ -complexes to heteroarenes. M = any transition metal, E = NR, O, S, Se, Te. ....	13
<b>Scheme 1.8</b> Mechanisms of a) unimolecular dissociation and b) bimolecular dissociation. ....	15
<b>Scheme 1.9</b> Energy diagram showing the hypothesized relationship between ring-walking and binding energies in successful CTP. ....	17
<b>Scheme 1.10</b> Mechanistic views for how $\pi$ -complex structure affects ring-walking barriers. ....	18
<b>Scheme 1.11</b> Oxidative addition of a $\pi$ -complex into the polymer chain-end. ....	20
<b>Scheme 1.12</b> Reactions of $M^{II}$ complexes in CTP. ....	21
<b>Scheme 1.13</b> The $LM(Ar)X$ species is observed as the resting state in Ni(dppp)-catalyzed CTP of thiophene. ....	22
<b>Scheme 1.14</b> Transmetalation effects on the regioregularity of polymers synthesized via KCTP. ....	23
<b>Scheme 1.15</b> Disproportionation in CTP, resulting in off-cycle species that broaden the molar mass distribution. ....	24
<b>Scheme 1.16</b> The $LMAr_2$ species is observed as the resting state in Ni(dppe) catalyzed polymerization of thiophene. ....	24

<b>Scheme 3.1</b> A mechanism for CTP of thienothiophene. For clarity, Ni <sup>0</sup> complexes are colored red, while Ni <sup>II</sup> complexes are colored blue.....	61
<b>Scheme 3.2</b> Proposed mechanism for reaction of 2-bromothiophene with Ni(1,2-bis(dicyclohexylphosphino)ethane)(cycloocta-1,5-diene) (red = Ni <sup>0</sup> , blue = Ni <sup>II</sup> ). .....	71
<b>Scheme 4.1</b> The mechanism of Kumada catalyst-transfer polymerization.....	82
<b>Scheme 4.2</b> a) Structures of the Ni complexes, b) Pd complexes, and c) arenes that make up the $\pi$ -complexes in this study. Polymer chains were truncated to methyl groups (bolded). Side chains were truncated to methyl groups (un-bolded). .....	86
<b>Scheme 5.1</b> Areas of investigation for future studies into $J_{PP}$ of metal complexes. ....	105
<b>Scheme 5.2</b> Areas of investigation for future studies into CTP of fused arenes.....	107
<b>Scheme 5.3</b> Areas of investigation for future studies into ring-walking and reactions of M <sup>0</sup> complexes in CTP.....	108



## List of Appendices

Appendix 1 Supporting Information for Using $J_{PP}$ to Identify Ni Bidentate Phosphine Complexes in Situ.....	111
A1.1 Dataset Construction and Processing.....	111
A1.1.1 Two-carbon linker dataset.....	111
A1.1.2 Three-carbon linker dataset.....	113
A1.1.3 Manual dataset processing .....	115
A1.2 Correlations with experimental $^{31}\text{P}$ chemical shift .....	118
A1.3 Computational details .....	121
A1.3.1 Geometry optimization.....	121
A1.3.2 Internuclear spin-spin coupling (J-coupling) calculations .....	121
A1.3.3 Charge transfer calculations .....	127
A1.4 Backbonding $\text{CT}_{\text{Ni-to-P}}$ vs $J_{PP}$ .....	128
A1.5 Correlations with bite angle and linker identity.....	128
A1.5.1 Bite angle measurements.....	128
A1.5.2 Linker identity and correlations with bite angle.....	128
A1.5.3 Chemical shift correlations with bite angle.....	130
A1.5.4 $J_{PP}$ correlations with Bite Angle.....	131
A1.6 XYZ coordinates .....	134
A1.7 References.....	135
Appendix 2 Supporting Information for Rethinking Catalyst Trapping in Ni-Catalyzed Polymerization of Thieno[3,2- <i>b</i> ]thiophenes.....	139
A2.1 Materials.....	139
A2.2 General Experimental Details .....	140

A2.3 Synthetic Procedures.....	142
A2.4 Explaining Dimers in the Quenched Reaction Mixture .....	148
A2.5 Small Molecule NMR Studies .....	154
A2.5.1 NMR study of reaction of 2-bromothiophene with Ni(dcpe)(COD).....	154
A2.5.2 NMR study of reaction of 3,6-dioctylthiophene with Ni(COD) <sub>2</sub> and dcpp .....	155
A2.5.3 Reaction of Ni(COD) <sub>2</sub> with 2,5-dibromo-3,6-dithiooctylthiophene .....	156
A2.6 Polymerization Reactions .....	159
A2.6.1 Polymerization of 2-magnesiocloro-5-dibromo-3,6-dithiooctylthieno[3,2-b]thiophene, M1 with Ni(dppe) and Ni(dppp). .....	159
A2.6.2 Polymerization of 2-magnesiocloro-5-dibromo-3,6-dithiooctylthieno[3,2-b]thiophene, M1 with Ni(dppp) and Ni(dppe) for NMR studies .....	165
A2.6.3 Polymerization of 2-(5'-bromothiophen-2'-yl)-5-(5''-chloromagnesiothiophen-2''-yl)-3,6-dithiooctylthieno[3,2-b]thiophene, M2. ....	171
A2.7 Small Molecule NMR Spectra .....	172
A2.8 Computational Details.....	183
A2.8.1 Simulations for On-Cycle and Off-Cycle reactions with Ni(dppp)Cl <sub>2</sub> .....	183
A2.8.2 Signed J <sub>PP</sub> values for Ni complexes .....	183
A2.8.3 Discovery of C–S insertion in a TTh containing molecule.....	185
A2.8.4 Simulations for Catalyst Screening.....	186
A2.9 X-Ray Crystallography Data.....	188
A2.9.1 Structure Determination .....	188
A2.9.2 Coordinates and Angles .....	192
A2.10 XYZ coordinates .....	202
A2.11 References.....	203
Appendix 3 Supporting Information for Elucidating Ring-Walking in Catalyst-Transfer Polymerization.....	204

A3.1 Computational Details.....	204
A3.2 Trends with Buried Volume.....	205
A3.3 XYZ Coordinates .....	205
A3.4 References .....	206

## Abstract

Catalyst-transfer polymerization (CTP) is a living, chain-growth polymerization method used to synthesize conjugated polymers with control over molar mass, sequence, and end-group identity. CTP is one of the few chain-growth polymerizations that can be used for accessing conjugated polymers, but its utility is limited by its monomer scope, which primarily includes small electron-rich arenes. This limit to the monomer scope arises in part from an inability to rationally identify catalysts for new monomers, which in turn arises from our inability to observe or study key intermediates of CTP. Discovering ways to observe intermediates during CTP would enable establishing structure–reactivity relationships and could enable us to new identify catalysts for CTP. My work in this dissertation is therefore focused on identifying intermediates in CTP and understanding the structure/property relationships that govern the reactivity of these intermediates.

In Chapter 1, I describe previous work aimed at understanding the mechanism of CTP and identifying structure–reactivity relationships. I highlight the knowledge gaps with respect to the reactions of  $\pi$ -complexes and explain why these  $\pi$ -complexes cannot be observed easily via experimental studies, precluding our understanding of their reactivity.

In Chapter 2, I discuss how Ni bidentate phosphines, a major class of complexes used in CTP, can be identified using the  $J_{PP}$  value derived from  $^{31}\text{P}$  NMR spectroscopy. Specifically, I show that  $J_{PP}$  depends on the oxidation state of Ni, the linker length of the phosphine, and the donating or withdrawing character of the ligands bound to Ni. Given these correlations between structure and  $J_{PP}$ , I propose that  $J_{PP}$  analysis can be used to identify complexes during reactions in which isolation and purification of intermediates is difficult or impractical, such as in CTP.

In Chapter 3, I use  $J_{PP}$  values along with computational and synthetic investigations to elucidate the structure of the catalyst trap in Ni-catalyzed CTP of thienothiophene. The catalyst trap we identify is a  $Ni^{II}$  species which arises from off-cycle C–S insertion of Ni into the thienothiophene ring. We propose that this C–S insertion trap may occur in CTP of other sulfur-containing arenes and that this reactivity mode may explain some of the limitations on large monomers in the scope of CTP.

In Chapter 4, I describe our efforts at understanding the structure–reactivity relationships inherent to Ni and Pd  $\pi$ -complexes in CTP. Using density functional theory-based simulations, we find that the Dewar-Chatt-Duncanson model adequately describes binding in  $\pi$ -complexes. Additionally, we find that the barrier to ring-walking does not correlate strongly with the  $\pi$ -binding energy, indicating that ring-walking barrier and  $\pi$ -binding energy can be modulated independently based on the catalyst choice.

Lastly, in Chapter 5, I describe the current limitations on CTP and open questions for future consideration. I anticipate that the work described herein will aid future investigators in uncovering relationships that are important for synthesizing conjugated polymers.

## Chapter 1 Catalyst-Transfer Polymerization

Polymers are ubiquitous materials, found in an array of applications in the modern world.<sup>1</sup> Commodity plastics such as polyethylene and polystyrene are found in many consumer goods and packaging and are among the highest volume materials produced in the chemical industry.<sup>2</sup> Other common polymers such as poly(methyl methacrylate) and poly(amides), are found in high performance applications such as in construction<sup>3</sup> or in bullet-proof materials.<sup>4</sup> Some polymers have specialty applications, including conjugated polymers which are found in organic electronic devices such as organic light emitting diodes<sup>5</sup> or organic solar cells.<sup>6,7</sup> Regardless of their applications, the properties and performance of polymers are strongly influenced by their structure.

In small molecules, structure may refer to the atoms, the specific types of chemical bonds, and the conformation of the molecule. In polymers, the structure also refers to the average molar mass of the polymer chains in a sample,<sup>8</sup> because average molar mass can have a large impact on the resulting properties. Molar mass of a polymer determines its processability, its density, and its rigidity,<sup>8</sup> hence why some types of polyethylene are very flexible, such as the low density polyethylene (LDPE) used in plastic bags,<sup>9</sup> while some types of polyethylene are very rigid, such as the ultra-high molecular weight polyethylene used in bone replacement implants,<sup>10</sup> despite both being branched polyethylene based materials. Additionally, the dispersity of the polymer (i.e., the breadth of the molar mass distribution) can also have a dramatic impact on the properties of the material. For example, linear low-density polyethylene (LLDPE) is a lower dispersity material than LDPE and tends to be more flexible and more prone to elongation than LDPE,<sup>11</sup> although the differences in the branching architectures between these also likely affect properties. Given the

dependence of polymer properties on molar mass and dispersity, control over these attributes is vital to producing functional materials.

Generally, molar mass control in a polymer is achieved during its synthesis rather than via post-polymerization purification methods.<sup>8</sup> Anionic polymerizations,<sup>12,13</sup> organometallic olefin polymerizations<sup>14,15</sup> and ring-opening metathesis polymerizations<sup>16</sup> provide access to aliphatic polymers like polyethylene,<sup>17</sup> polypropylene,<sup>18</sup> and polystyrene<sup>13</sup> with control over average molar mass,<sup>16,18,19</sup> as well as other features that affect polymer properties such as branching,<sup>20,21</sup> tacticity,<sup>18</sup> and end-group functionality.<sup>15,22</sup> It is possible to control these properties because these polymerization methods are chain-growth polymerizations, in which molar mass control arises from the reactivity differences between monomers, oligomers, and polymers. For chain-growth to occur, the oligomers must be more reactive toward polymerization than the monomers.<sup>8</sup> If this condition is satisfied, then once catalysts or initiators enable oligomers to form in the early stages of a polymerization, the reactive oligomers (or polymer chains) will continue to grow until all monomers are consumed. If the number of reactive chains can be controlled by controlling the amount of catalyst or initiator, and there are no termination reactions that shut-down reactivity, then the resulting average molar mass at the endpoint of the polymerization will be determined by the equivalents of monomers relative to the reactive chains.

By contrast, the oligomers and monomers in step-growth polymerizations have nearly equal reactivity toward polymerization reactions. As such, the early stages of a step-growth polymerization involve the generation of dimers and low-molar mass oligomers through the coupling of monomers with monomers, or monomers with dimers (or trimers, tetramers, etc.).<sup>8</sup> Polymers can only form in step-growth polymerization when there is a sufficient quantity of high molar mass oligomers, enough that oligomers can react with other oligomers, which tends to only

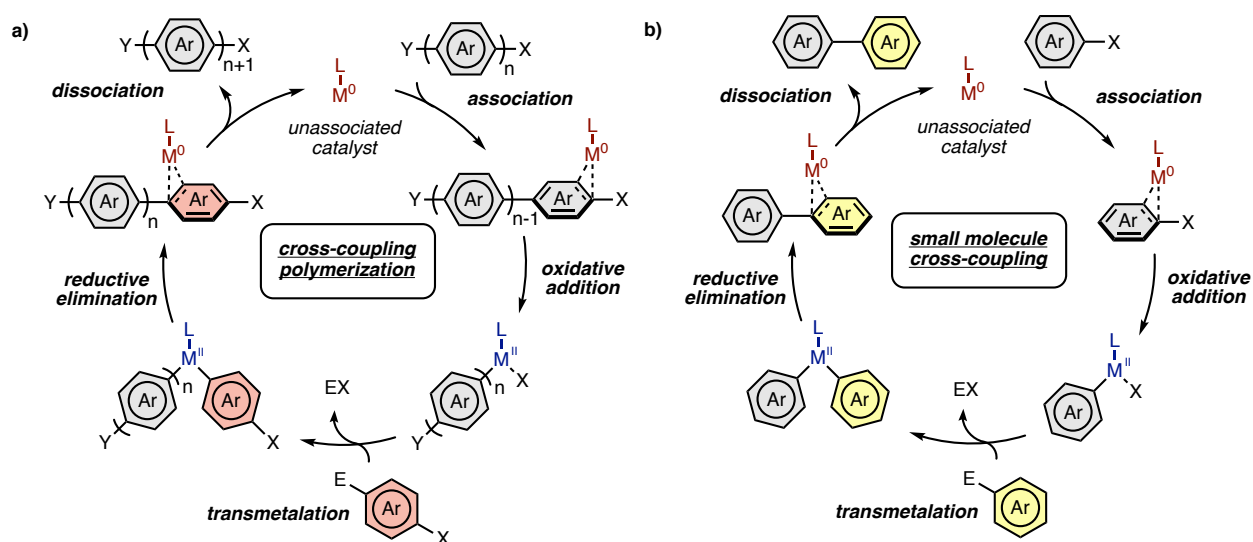
occur at the end of the polymerization reaction when the concentration of monomers is diminished.<sup>8</sup> Given that the number of reactive chains varies during the polymerization, step-growth polymerizations only give limited control over average molar mass, and the average molar mass can be highly dependent on the initial purity of the monomer, the temperature of the polymerization, and the rate of stirring in the reaction flask<sup>8</sup> – features which may be difficult to reproduce. Given the ease of molar mass control enabled by chain-growth polymerizations compared to step-growth polymerizations, there has been a focus to develop chain-growth polymerizations such that they encompass larger monomer scopes or enable access to more polymer architectures.<sup>23</sup>

Most chain-growth polymerizations only enable access to polymers with saturated backbones,<sup>24–27</sup> precluding the synthesis of conjugated polymers.<sup>23,28,29</sup> The inability to use chain-growth methods to synthesize conjugated polymers is potentially limiting conjugated polymer applications.<sup>27,30</sup> Like most polymers, average molar mass determines the material properties, however molar mass also determines optoelectronic properties in conjugated polymers by affecting conjugation length, conductivity, or aggregation behavior.<sup>30,31</sup> Therefore, chain-growth polymerizations are especially needed for conjugated polymers to impart higher control over polymer optoelectronic properties.<sup>30</sup>

Cross-coupling polymerizations are often used to access conjugated polymers (Scheme 1.1a).<sup>32,33</sup> These strategies enables forming aryl–aryl or aryl–olefin bonds and mimic those used in small-molecule cross-coupling reactions (Scheme 1.1b).<sup>34–36</sup> The variety of substrates amenable to small-molecule cross-coupling enables access to a wide scope of conjugated polymers including donor polymers (i.e., polymers that are easily oxidized due to incorporating electron-rich substructures), acceptor polymers (i.e., polymers that are easily reduced due to incorporating

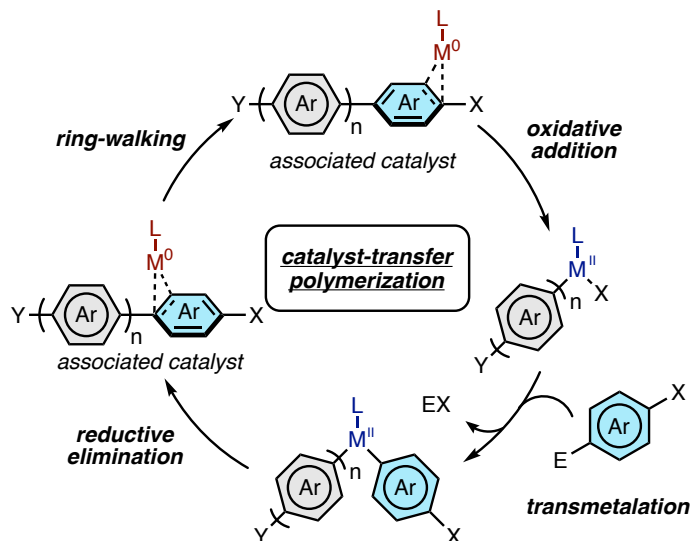


electron-deficient substructures), and mixed donor-acceptor polymers<sup>37</sup> (i.e., polymers with a mix of electron-rich and electron-deficient substructures) with highly tunable bandgaps.<sup>38,39</sup> However, most cross-coupling polymerizations are step-growth polymerizations, offering little control over average molar mass or other properties.<sup>28</sup>



**Scheme 1.1** Mechanism of a) cross-coupling polymerization and b) small-molecule cross-coupling.

Catalyst-transfer polymerization (CTP), is an exception; as a cross-coupling based *chain-growth* polymerization, CTP is commonly used to synthesize conjugated polymers with control over average molar mass, sequence, and end-group functionality (Scheme 1.2).<sup>40,41</sup> These features of CTP provide chemists access to polymer architectures inaccessible via other polymerization methods,<sup>30</sup> such as polymers used in chemical sensing,<sup>42,43</sup> energy generation,<sup>44</sup> bioimaging,<sup>45</sup> and other applications which require precision polymer synthesis.<sup>30</sup>



**Scheme 1.2** The mechanism of catalyst-transfer polymerization.

The difference between standard cross-coupling polymerization and CTP lies in their mechanisms (Scheme 1.1a and Scheme 1.2).<sup>40</sup> Both mechanisms mimic small-molecule cross-coupling (Scheme 1.1b) in that a M<sup>0</sup> catalyst (M = Ni or Pd) performs oxidative addition into an aryl halide, followed by transmetalation of a monomer and reductive elimination to form an aryl-aryl bond. The fate of the M<sup>0</sup> catalyst after reductive elimination determines whether the mechanism is a catalyst-transfer polymerization or a standard cross-coupling polymerization. In CTP, the M<sup>0</sup> complex remains bound to the polymer as a  $\pi$ -complex after reductive elimination, isomerizing to other  $\pi$ -complexes via a process known as ring-walking,<sup>40,46</sup> and eventually inserts into the C-X bond (X = Cl, Br, or I) at the polymer chain end. The association between catalyst and polymer enables selective insertion of the M<sup>0</sup> catalyst into the polymer chain end and is therefore what enables chain-growth. If the catalyst can dissociate, then the unbound M<sup>0</sup> species that is generated may not be selective for the chain-end and can insert into any C-X bonds in solution (i.e., the mechanism of standard cross-coupling polymerization). The unbound M<sup>0</sup> catalyst

can then initiate new chains, ultimately resulting in a polymerization with step-growth character rather than chain-growth.

Despite the unrivaled level of structural control that can be imparted by CTP,<sup>30</sup> the utility of CTP is limited by its monomer scope.<sup>40,41,46</sup> CTP is known for only a handful of monomers,<sup>47</sup> consisting primarily of electron-rich small arenes.<sup>47</sup> CTP of other monomer types, such as electron-deficient arenes or arenes with large  $\pi$ -systems, is challenging<sup>48–50</sup> often giving rise to step-growth polymerizations rather than CTP. If the monomer scope of CTP could be expanded to include these classes of monomers, then polymers such as acceptor or donor-acceptor polymers<sup>27,51</sup> could be accessible via chain-growth polymerization. This expanded monomer scope would likely enable precision synthesis of advanced optoelectronic materials<sup>27</sup> and would potentially enable enhanced performance of conjugated polymers in applications such as in solar cells, transistors, or light emitting diodes.<sup>27</sup>

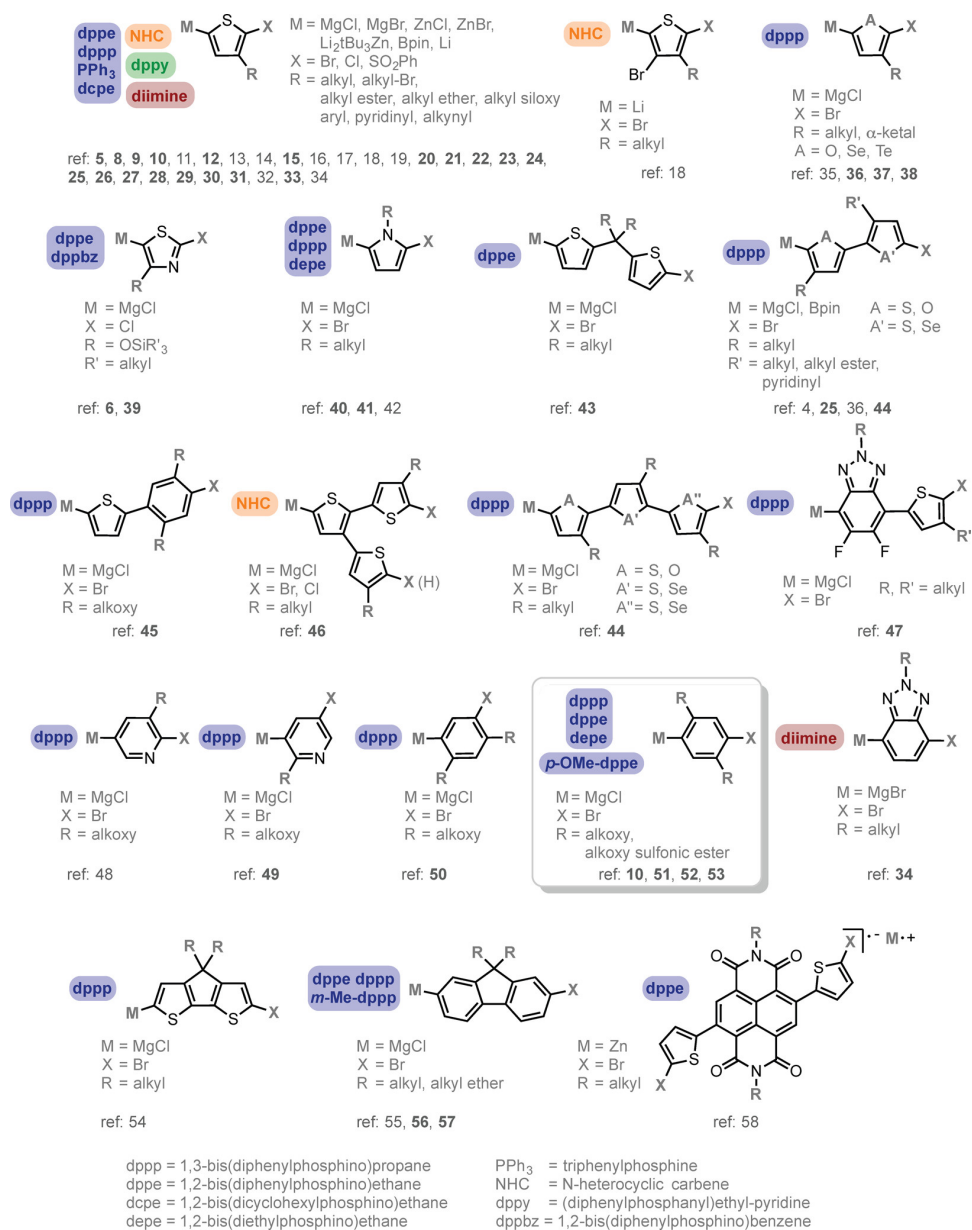
Expanding the monomer scope of CTP is challenging because it is difficult to determine which catalysts will enable CTP for a given monomer.<sup>40,47,52</sup> Part of this difficulty arises from holes in our understanding of the structure–property relationships important for enabling CTP. For example, it can be difficult to identify whether a catalyst will enable CTP by giving rise to strong  $\pi$ -binding or low ring-walking barrier because few structure-property relationships exist for describing ring-walking. Additionally, our limited ability to identify off-cycle species during CTP makes expanding the monomer scope difficult. As such, if side reactions occur (e.g., dissociation, catalyst oxidation, unexpected insertion reactions of catalysts) and shut down catalysis in CTP, we may be unable to identify the side reaction and therefore are unable to identify catalysts that would prevent it. Therefore, investigators undergo extensive screening of monomer/catalyst pairs,<sup>53</sup> or use small molecule model reactions<sup>40,47,54</sup> and other mechanistic investigations<sup>55,56,57</sup> to understand

why specific catalyst/monomer pairs are do not give rise to CTP. The success of these methods is often limited; catalyst screening is ineffective without insight into the reactivity of intermediates of the reaction, and small molecules have inherently different reactivity to conjugated polymers, complicating the interpretation of model reactions.<sup>40,47,54</sup>

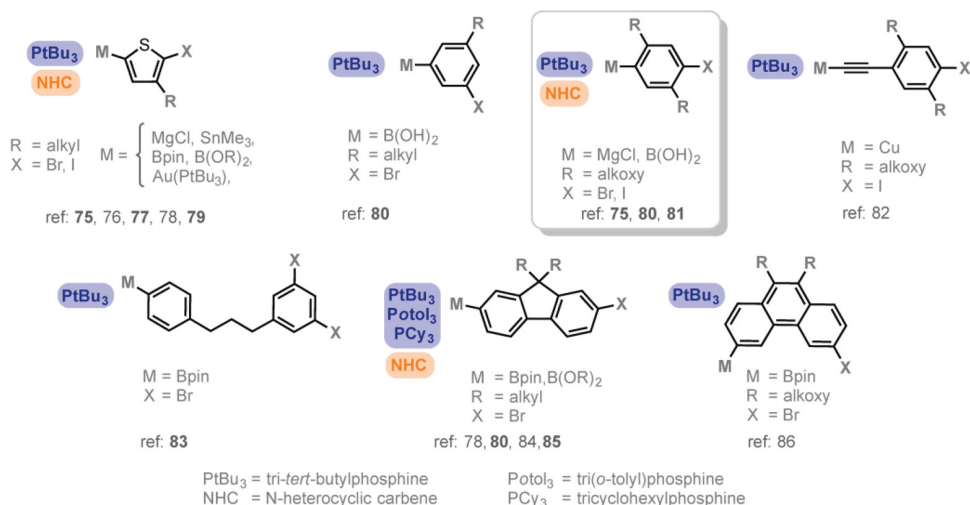
Increasing our insight into the on-cycle and off-cycle reactivity of intermediates in CTP would enable rational catalyst design. As such, the investigations I have undertaken during my thesis research have been focused on understanding how to identify the complexes that form during CTP (Chapter 2), as well as identifying off-cycle reactions during CTP (Chapter 3) and understanding the structure-property relationships that enable on-cycle reactions (Chapter 4). To appreciate the structure-property relationships relevant to the rest of this thesis, the following sections detail the monomer scope of CTP, the on-cycle reactions, and the knowledge gaps with regard to optimizing catalyst reactivity in these on-cycle reactions.

## **1.1 Monomer Scope of CTP**

The monomer scope of CTP was reviewed by Leone and McNeil in 2016 (Scheme 1.3 and Scheme 1.4).<sup>47</sup> Since then, the functional group tolerance and air-tolerance have been improved.<sup>58,59</sup> Monomers that are most highly represented are electron-rich arenes (such as thiophene, benzene, and furan) with alkyl or alkoxy side chains.<sup>47</sup> Electron-deficient arenes are more difficult to polymerize, as evidenced by their limited representation in the monomer scope. Additionally, large arenes are not highly represented.



**Scheme 1.3** Monomer scope of Ni-catalyzed CTP. Reprinted with permission from Leone, A. K.; McNeil, A. J. Matchmaking in Catalyst-Transfer Polycondensation: Optimizing Catalysts based on Mechanistic Insight *Acc. Chem. Res.* **2016**, *49*, 2822–2831. Copyright 2016 American Chemical Society.

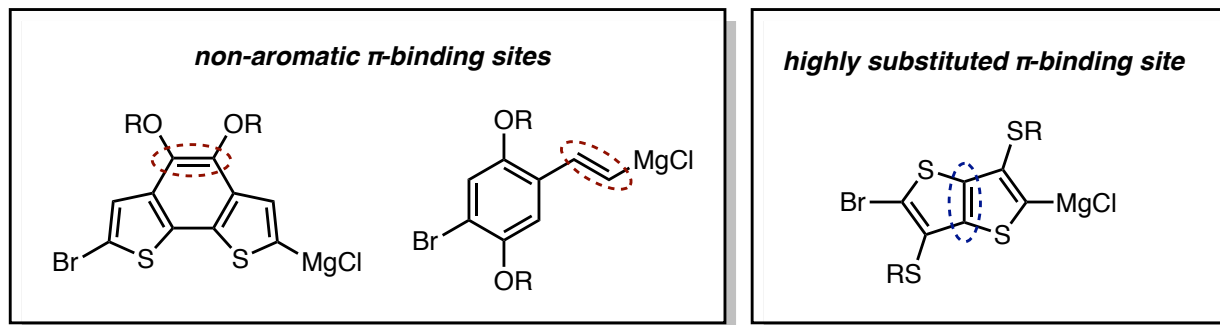


**Scheme 1.4** Monomer Scope of Pd-catalyzed CTP. Reprinted with permission from Leone, A. K.; McNeil, A. J. Matchmaking in Catalyst-Transfer Polycondensation: Optimizing Catalysts based on Mechanistic Insight *Acc. Chem. Res.* **2016**, *49*, 2822–2831. Copyright 2016 American Chemical Society.

Only being able to polymerize small, electron-rich arenes via CTP is limiting from an applications standpoint. Polymers derived from electron-rich arenes tend to be electron-donor materials and polymers derived from electron-deficient arenes tend to be electron-acceptor materials. In an electronic device, both donors and acceptors are needed to enable charge-transfer, so only being able to polymerize donor materials with high structural control limits the resulting properties of conjugated polymer-based devices. Additionally, copolymers containing both donor and acceptor units can have distinct properties compared to homopolymers of donors and acceptors. Therefore, only being able to polymerize donor materials precludes synthesizing donor-acceptor copolymers via CTP, and therefore limits investigators who may wish to understand how average molar mass or sequence affect donor-acceptor polymer properties.

The limit to the scope of arenes that can be polymerized via CTP is thought to arise from the stability and reactions of  $\pi$ -complexes to these arenes (*vide infra*, Chapter 1.2). The electronic effect of  $\pi$ -complex stability on monomer scope is evidenced by the difference between electron-

rich and electron-deficient arenes in the monomer scope, but also by the other substructures that are underrepresented. For example, monomers with non-aromatic double bonds cannot be polymerized, likely due to the strong catalyst  $\pi$ -binding which prevents turnover.<sup>60,94</sup> This limitation means that CTP cannot be used to synthesize alkene-containing polymers, like poly(phenylene vinylenes) a highly studied class of polymers used in solar cells and light emitting diodes. Additionally, monomers that contain fused arenes are represented, but monomers whose structure requires ring-walking over fused double-bonds are underrepresented or are known to be problematic (Scheme 1.5), as in the case of thienothiophene (*vide infra*, Chapter 3).<sup>92</sup> Given that fused arenes are highly represented in polymers investigated for solar cells<sup>61</sup> and light emitting diodes,<sup>62</sup> this limitation to the monomer scope of CTP means that large classes of conjugated polymers containing fused arenes cannot be synthesized via chain-growth polymerization methods.



**Scheme 1.5** Two subsets of problematic monomers in CTP.

The limitations to the scope of arenes that can be polymerized via CTP hinders our understanding of the relationships between polymer structure and performance. To expand the monomer scope, we must understand why some monomers cannot be polymerized by understanding the reactivity of intermediates in CTP. Given that the arene structure determines

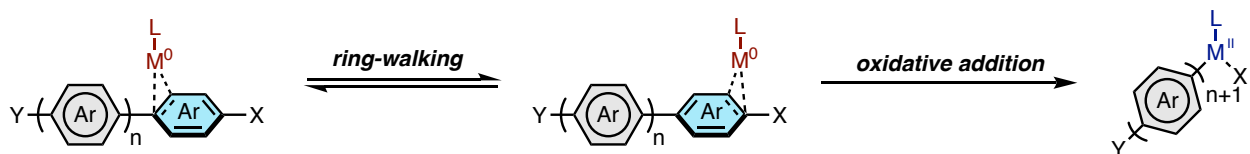
whether the catalyst can ring-walk and  $\pi$ -bind, understanding how arene structure affects reactivity of CTP can help us to understand how to expand the monomer scope.

## 1.2 Reactivity of $M^0$ $\pi$ -Complexes in CTP

Requirements of catalysts in CTP are distinct from requirements of catalysts in small molecule cross-coupling because of the difference in the key steps. In small-molecule cross-coupling, the step which enables forming C–C or C–N bond (reductive elimination) is vital to enabling cross-coupling, therefore, small molecule catalysts are optimized to enable reductive elimination (and particularly optimized for Pd).<sup>63</sup> For example, many ligands used for Buchwald-Hartwig amination are designed to be sterically encumbered to provide bulk which enables C–N reductive elimination.<sup>64,65</sup> This encumbrance of Buchwald ligands has led to uses for these ligands in a variety of reactions, beyond amination, where the reductive elimination may be challenging.<sup>66–68</sup> Although transmetalation and oxidative addition are also vital to ensuring turnover, the key feature of a cross-coupling is *coupling* two different groups, which occurs during reductive elimination, hence the importance of steric bulk in choosing catalysts.

In CTP, the key step that determines the outcome is the ring-walking step (Scheme 1.6) because this step enables the selective chain-growth of the catalyst. If ring-walking cannot occur, either because the barrier to ring-walking is too high<sup>92</sup> or because the  $\pi$ -complex preceding ring-walking is too unstable and dissociates,<sup>47</sup> then chain-growth polymerization will not occur. As such, understanding the factors that affect  $\pi$ -complex stability, the barrier to ring-walking, and the available off-cycle reactions from  $\pi$ -complexes is vital for understanding and enabling CTP.





**Scheme 1.6** Ring-walking and oxidative addition in CTP. Arene color indicates polymer (grey) and chain-end monomer residue (blue).

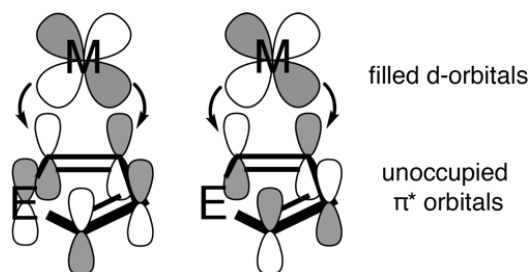
### 1.2.1 Thermodynamic and Kinetic Stability of $LM$ -Ar $\pi$ -Complexes

Evaluating  $\pi$ -complex stability in CTP is difficult - generally, their stability can be thought of in terms of how stable the  $M$ -Ar bonds are in the  $\pi$ -complex (i.e., its thermodynamic stability) and how likely a  $\pi$ -complex is to react (i.e., its kinetic stability). The thermodynamic stability of a  $\pi$ -complex affects CTP because a more stable  $\pi$ -complex is less likely to dissociate. The kinetic stability, however, affects our ability to observe the  $\pi$ -complexes during CTP, because if the barrier to the ring-walking or oxidative addition is low, then the  $\pi$  complex will quickly convert to another species before reaching a high enough concentration. Indeed, the kinetic stability of  $\pi$ -complexes in CTP is low, because the  $C$ - $X$  bond at the polymer chain end promotes oxidative addition (Scheme 1.6).<sup>91</sup> The low kinetic stability of  $\pi$ -complexes means that  $\pi$ -complexes are rarely observed during CTP,<sup>69</sup> obscuring our understanding of  $\pi$ -complexes via experimental measurements.

Despite the low kinetic stability of  $\pi$ -complexes, the thermodynamic stability can still affect the outcome of CTP. If the thermodynamic stability is sufficiently low, then unbinding may be more favorable than ring-walking or oxidative addition, causing dissociation and resulting step-growth polymerization. The thermodynamic stability of  $\pi$ -complexes in CTP depends on the structure and electronic properties of the metal ( $M$ ), arene ( $Ar$ ), and ancillary ligands ( $L$ ). Computational modeling supports that some  $\pi$ -complexes in CTP have binding energies of greater

than 40 kcal/mol,<sup>70</sup> while some  $\pi$ -complexes in CTP have very weak binding energies, less than 10 kcal/mol,<sup>71</sup> supporting that the specific structure of the polymer and catalyst play an important role in the binding energy and thermodynamic stability.

The strength of metal–arene bonds that dictate the thermodynamic stability of  $\pi$ -complexes can be explained via Dewar-Chatt-Duncanson (DCD) model, which was developed to explain the binding of metal complexes to olefins.<sup>72,73</sup> In early transition metal complexes the major M/Ar bonding interactions are  $\pi$ -to-d orbital interactions due to the presence of unfilled d-orbitals in early transition metals. Late transition metal complexes have filled d-orbitals which instead enable d-to- $\pi^*$  backbonding interactions to dominate in M/Ar  $\pi$ -complexes. In  $d^{10}$  metals, like in the  $Ni^0$  and  $Pd^0$   $\pi$ -complexes in CTP, the d-orbitals are entirely filled, meaning that  $\pi$ -backbonding interactions make up the majority of interactions between metal and arene (Scheme 1.7). Additionally, these d-to- $\pi^*$  interactions can occur to any of the  $\pi^*$  orbitals, given the appropriate symmetry (but for 5-membered rings, Huckel molecular orbital theory predicts only two  $\pi^*$  orbitals, shown in Scheme 1.7).<sup>74</sup> The dative, backbonding interactions that arise from d-to- $\pi^*$  charge transfer are weaker than covalent bonds to Ni and Pd,<sup>75</sup> but can be strong enough to form stable M–Ar  $\pi$ -bonds if  $\pi$ -backbonding is maximized.



**Scheme 1.7** The backbonding (d-to- $\pi^*$ ) interactions present in  $\pi$ -complexes to heteroarenes. M = any transition metal, E = NR, O, S, Se, Te.

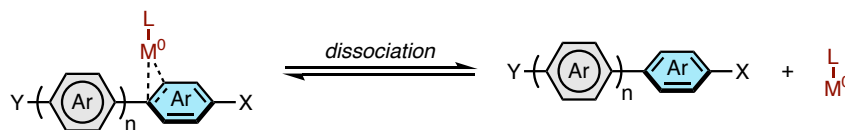
Given the DCD model, Ni  $\pi$ -complexes should generally be more strongly bound than Pd  $\pi$ -complexes due to the higher energy of the d-orbitals of Ni.<sup>76,77</sup> Additionally ancillary ligands that increase the energy of the d-orbitals (i.e., electron-rich,  $\sigma$ -donor ligands)<sup>78</sup> and arenes that have lower energy LUMO orbitals should also enable stronger M–Ar  $\pi$ -backbonding interactions by decreasing the energy gap between occupied d-orbitals and unoccupied  $\pi^*$ -orbitals.<sup>79</sup> Generally, the structures of catalysts used in CTP agree with these rules. Particularly, we can understand why Ni catalysts are so common in CTP<sup>47</sup> (while Pd catalysts dominate in other cross-coupling reactions)<sup>80,81,82</sup> because the increased  $\pi$ -binding affinity of Ni.<sup>83</sup> Additionally, the ancillary ligands on catalysts in CTP are almost exclusively phosphines, carbenes, or diimines<sup>47,80,84</sup> which are all strong  $\sigma$ -donors. However, the monomer scope in CTP, primarily electron-rich arenes, is peculiar through the lens of the DCD model. Electron-rich arenes typically have *higher* energy unoccupied orbitals,<sup>85</sup> which means that d-orbitals are less able to donate into the  $\pi^*$  of the arene, decreasing the stability compared to  $\pi$ -complexes to electron deficient arenes. Understanding why electron-rich arenes dominate in the monomer scope of CTP is a major question of this work (see Chapter 4), but potentially the observation that electron-rich arenes form less-stable  $\pi$ -complexes than electron-deficient arenes indicates that we must also consider the reactions of  $\pi$ -complexes to understand the monomer scope.

### ***1.2.2 Dissociation Reactions of $\pi$ -Complexes***

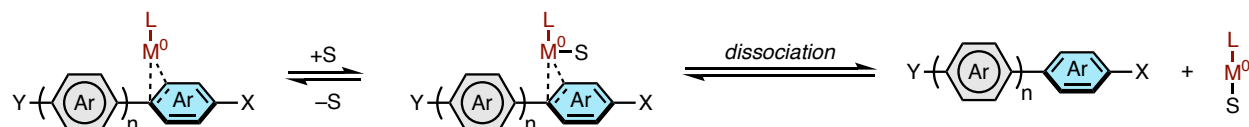
Dissociation of a  $\pi$ -complex into a free LM<sup>0</sup> fragment and a polymer chain can happen via multiple processes but generally, unimolecular dissociation and bimolecular dissociation have been reported. In unimolecular dissociation, the  $\pi$ -complex fragments spontaneously into an LM<sup>0</sup> complex and a free polymer (Scheme 1.8a).<sup>47</sup> Given that generally the only driving force is the entropy gain in the reaction, this mode of dissociation is only available for weakly bound  $\pi$ -

complexes (e.g.,  $\pi$ -complexes with Pd, or  $\pi$ -complexes with weak donor ancillary ligands). In contrast, bimolecular dissociation involves coordination of an additional ligand (e.g., monomer, solvent, ion, or excess ancillary ligand) to the metal (Scheme 1.8b). Once bound, the higher-coordination metal center can then undergo ligand dissociation to relieve steric crowding, resulting in the loss of the polymer ligand. Because the association of an additional ligand changes the binding energy of all other ligands on the metal, bimolecular dissociation is available to both weakly bound and strongly bound  $\pi$ -complexes. Given the need for an association, coordinatively unsaturated complexes (i.e., those with less than  $16e^-$ ) may undergo bimolecular dissociation more readily. Additionally, Ni complexes, being both more  $\pi$ -accepting<sup>83</sup> and more oxophilic<sup>86</sup> than Pd complexes, are potentially more susceptible to bimolecular dissociation as these features of Ni enable ligands to associate more easily.

**a) unimolecular dissociation**



**b) bimolecular dissociation**



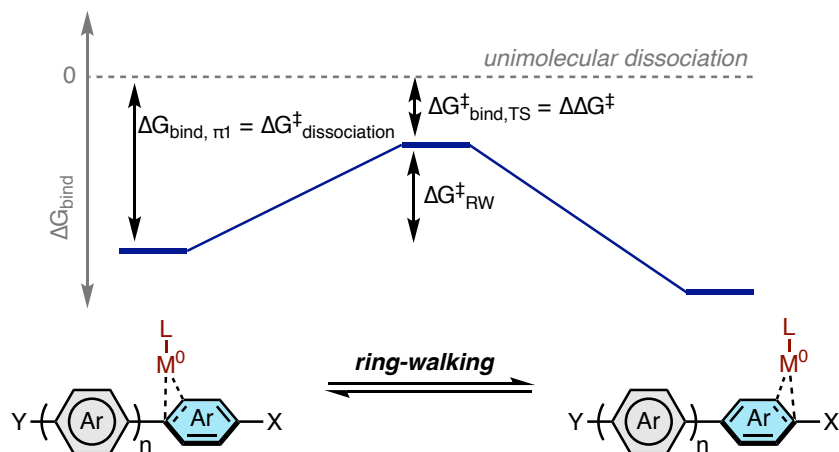
**Scheme 1.8** Mechanisms of a) unimolecular dissociation and b) bimolecular dissociation.

In the polymerization of thiophene with Ni(diimine) catalysts, dissociation of the catalyst is known to occur based on end-group analysis of the resulting polymers.<sup>87</sup> Computational work on the mechanism of CTP for this system indicates that the binding energy of the  $\pi$ -complex is approximately 5 kcal/mol,<sup>88</sup> similar to the ring-walking barrier, causing unimolecular dissociation to be competitive with ring-walking. Additionally, McNeil and Zimmerman have found that

bimolecular dissociation is operative in Ni(dppe)-catalyzed polymerization of thiazole.<sup>55</sup> They were able to suppress the initial ligand association that caused polymer dissociation by using an ancillary ligand with a more rigid backbone, which attenuated dissociation and enabled molar mass control and narrow dispersity. However, these are rare cases where the dissociation mechanism was elucidated, and in other cases, when dissociation occurs the mechanism of dissociation is not determined, limiting insight into unimolecular, bimolecular, or other dissociation reactions in CTP.

### ***1.2.3 Ring-walking Reactions of $\pi$ -Complexes***

The success of catalyst-transfer polymerization depends on the catalyst's ability to ring-walk without dissociating. Phrased differently, success in CTP depends on the competition between ring-walking and dissociation (Scheme 1.9). To understand the preference for ring-walking or dissociation, consider the binding energies *during* ring-walking. In the conventional view of ring-walking, the binding energy decreases as the catalyst approaches the transition state, meaning that the effective barrier to dissociation also decreases in the transition state of ring-walking. Whether dissociation can occur therefore depends on the magnitude of the  $\Delta\Delta G^\ddagger$  between dissociation and ring-walking because, at sufficiently low  $\Delta\Delta G^\ddagger$ , unbinding from the  $\pi$ -complex or transition state can occur. Given this competition, maximizing the binding energy ( $\Delta G_{\text{bind}}$ ) and minimizing the ring-walking barrier ( $\Delta G_{\text{RW}}^\ddagger$ ) should enable increased preference for ring-walking in CTP as these would result in larger  $\Delta\Delta G^\ddagger$ .



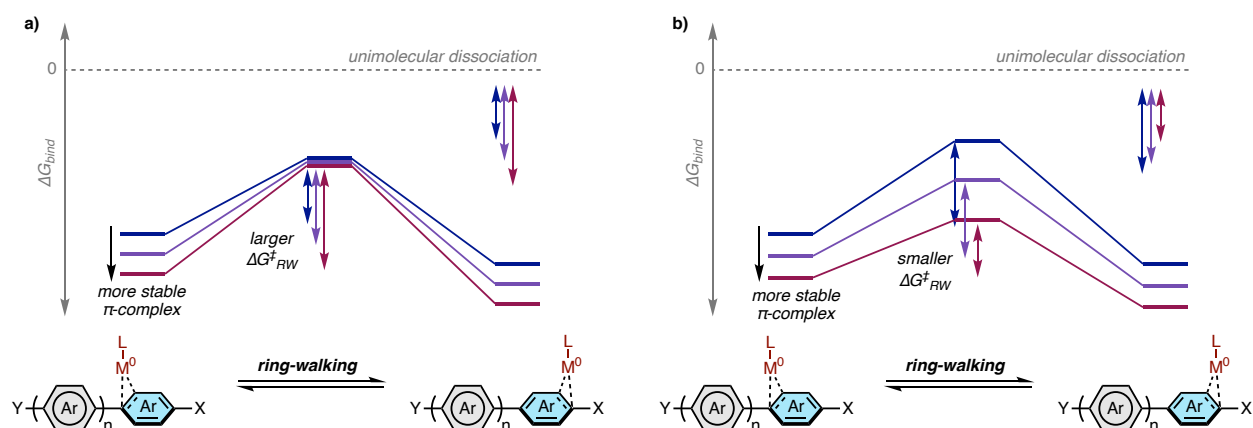
**Scheme 1.9** Energy diagram showing the hypothesized relationship between ring-walking and binding energies in successful CTP.

Understanding how to maximize the binding energy and minimize the ring-walking barrier is not trivial. Ring-walking is not commonly studied outside of CTP, meaning that there are few investigations into its mechanism. Studies that attempt to interrogate ring-walking show that it is generally a low-barrier reaction.<sup>46,89</sup> However, besides calculating ring-walking barriers in specific systems, studies on ring-walking fall short at producing structure-property relationships that enable identifying catalysts with low ring-walking barriers. Computational studies indicate that ring-walking is faster for  $\pi$ -complexes that have less-donating ancillary ligands or bulkier ligands,<sup>46,90</sup> but these studies were performed only for  $\pi$ -complexes to thiophene. Therefore, whether these studies are applicable to other monomers, such as electron-deficient arenes, is unclear.

In studies where the arene identity is varied, arene identity affects the barrier to ring-walking more so than ancillary ligands. Computational studies of ring-walking of Ni catalysts shows that ring-walking over electron-rich monomers, such as thiophene<sup>46,88,89,91</sup> and benzene,<sup>46</sup> proceeds with lower barriers ( $\Delta G_{RW}^\ddagger < 10$  kcal/mol) than ring-walking over electron-deficient monomers, such as thiazole<sup>55</sup> and pyridine<sup>46</sup> ( $\Delta G_{RW}^\ddagger > 12$  kcal/mol). However, experimental

studies find the opposite trend, where highly electron-rich arenes are resistive to ring-walking,<sup>92,93,94</sup> indicating that the effect of is more nuanced.

The disagreement in the effects of ancillary ligand donation and arene on the barrier to ring-walking speak to two different mechanistic hypotheses on how binding energy affects the barrier to ring-walking. In one hypothesis, more bound  $\pi$ -complexes have higher ring-walking barriers due to the need to dissociate from the  $\pi$ -bonds in the reactant complex (Scheme 1.10a), consistent with studies that claim that more electron-deficient arenes have higher ring-walking barrier<sup>52,55,94,9548</sup> and studies which show that ring-walking is easier with less-donating ancillary ligands.<sup>90</sup>



**Scheme 1.10** Mechanistic views for how  $\pi$ -complex structure affects ring-walking barriers.

In another view, more strongly bound  $\pi$ -complexes may cause lower barriers to ring-walking, due to the stronger, more stabilizing M-to- $\pi^*$  interactions in the transition state of ring-walking, (Scheme 1.10b). This view would be consistent with experimental studies which show that more-donating ancillary ligands give rise to chain-growth polymerization more easily (by increasing the backbonding ability of the metal),<sup>50,79,91,96</sup> as well as studies which show that

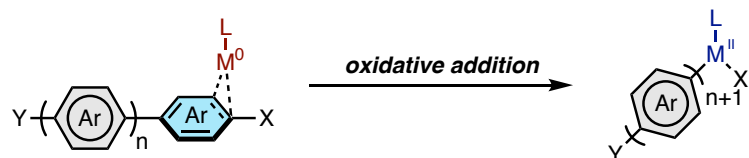
increasing the steric encumbrance of ancillary ligands increases the barrier to ring-walking (by preventing M-to-L interactions).<sup>90,92</sup>

Despite these different mechanistic hypotheses regarding effect of  $\pi$ -binding affinity on ring-walking barriers, many authors who study CTP seem to have accepted that higher ring-walking barriers result from more strongly bound  $\pi$ -complexes,<sup>47,52,55,90,92,95</sup> consistent with the first hypothesis. As such, the veracity of whether binding energy and barrier are related, and which mechanistic view of ring-walking is appropriate for identifying catalysts that enable CTP will be discussed throughout this thesis, and in particular, in investigations as part of Chapter 4.

#### ***1.2.4 C–X Oxidative Addition From $\pi$ -Complexes***

After ring-walking,  $\pi$ -complexes in CTP undergo oxidative addition at the chain-end (Scheme 1.11). The mechanism of this oxidative addition is rarely debated, due to the similarities with small molecule reactions and the existing studies on oxidative addition of group 10 metals into aryl halides.<sup>97</sup> However, in some circumstances, the oxidative addition step can be problematic for turnover in CTP. For example, in the polymerization of chlorothiophene monomers with Ni(dppe)-based catalysts, Seferos reported observing both (dppe)NiAr<sub>2</sub> and free Ni(dppe), the latter arising from dissociation of the  $\pi$ -complex.<sup>98</sup> In the same study, Seferos observed that bromothiophene and iodothiophene monomers do not result in catalyst dissociation, likely because oxidative addition into aryl bromides and iodides is less challenging than aryl chlorides. The difficulty of oxidative addition into C–Cl bonds likely causes the  $\pi$ -complex to be more long-lived, making it more prone to dissociation.





**Scheme 1.11** Oxidative addition of a  $\pi$ -complex into the polymer chain-end.

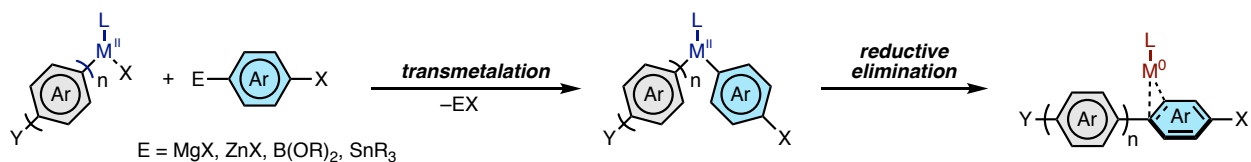
Electrophiles that are not halides are rare in CTP, but an example by Mori reported successful CTP when utilizing phenylsulfoxythiophenes as electrophiles,<sup>99</sup> indicating that other electrophiles may be used. In principle, more  $\sigma$ -donating ligands should enable activation of more mild electrophiles like aryl ethers,<sup>100</sup> but this approach for activating such electrophiles has yet to be explored in CTP. However, given the recent developments in air-tolerant CTP,<sup>58,59</sup> the use of alternative, non-halogen electrophiles may enable more mild CTP reactions in the future.

For off-cycle reactions, there are few reports of significant off-cycle activity arising from oxidative addition reactions of  $\pi$ -complexes.<sup>101</sup> However, small-molecule studies investigating reactivity of  $\text{Ni}^0$  have reported C–S insertion<sup>91,102,103</sup> and C–CN insertion<sup>104,105,106</sup> - the relevance of these reaction paths to CTP, and catalyst trapping in particular, will be discussed in Chapter 3.

### 1.3 Reactivity of $\text{M}^{\text{II}}$ species in CTP

After the  $\pi$ -complex reacts with the polymer chain-end via oxidative addition, an  $\text{LM}^{\text{II}}(\text{Ar})\text{X}$  species forms (Scheme 1.12). Due to the electrophilic M–X bond, these species are reactive toward transmetalation with nucleophilic monomers, enabling  $\text{LM}^{\text{II}}\text{Ar}_2$  species to form which can then react in reductive elimination, forming a new bond between the polymer and monomer. Transmetalation and reductive elimination are extensively studied<sup>125</sup> and are expected to proceed via similar mechanism in both polymerizations and small-molecule cross-coupling. Given the existence of investigations into structure/property relationships that govern these

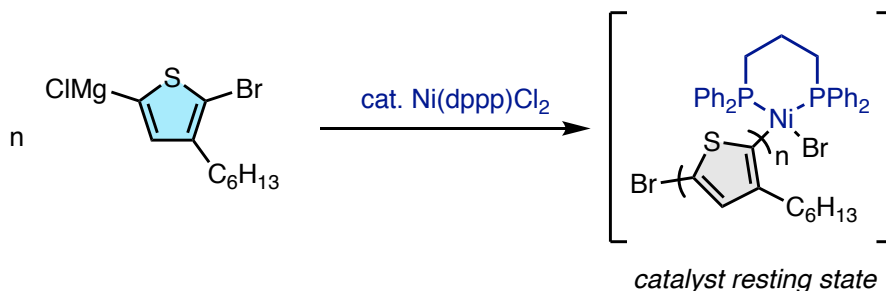
reactions, and that both transmetalation and reductive elimination have been observed as turnover limiting steps in CTP,<sup>40,107,108</sup> we will only cover the mechanistic details of these reactions that affect turnover rates in CTP specifically.



**Scheme 1.12** Reactions of M<sup>II</sup> complexes in CTP.

### 1.3.1 Transmetalation Reactions of LM(Ar)X complexes

Similar to small-molecule cross-coupling, multiple types of nucleophilic monomers can be used in CTP.<sup>109,110</sup> Monomers with organomagnesium functionality give rise to Kumada CTP (KCTP), organozinc gives Negishi CTP, organoboron gives Suzuki CTP, and organotin gives Stille CTP. Potentially due to the historical precedent that many of the first examples of CTP were Ni-catalyzed KCTP,<sup>111,112</sup> and the fact that Ni complexes enable highly stable  $\pi$ -complexes, Ni-catalyzed the KCTP is most commonly used.<sup>47,113,114</sup> Regardless of the metal complex or transmetalating agent, the LM(Ar)X species in CTP is often observed as the resting state, including in Ni(dppp)-catalyzed polymerization of thiophene (Scheme 1.13), indicating that transmetalation is turnover-limiting.<sup>108</sup> Therefore, the rate of transmetalation directly affects the rate of the polymerization,<sup>115</sup> and catalyst identity and reaction conditions can be adjusted to enable faster transmetalation and rates of polymerization.

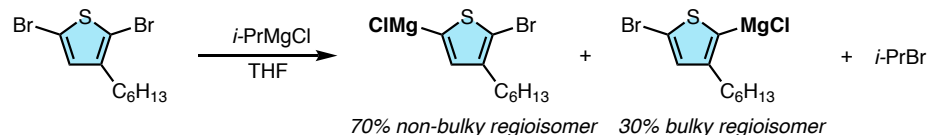


**Scheme 1.13** The LM(Ar)X species is observed as the resting state in Ni(dppp)-catalyzed CTP of thiophene.

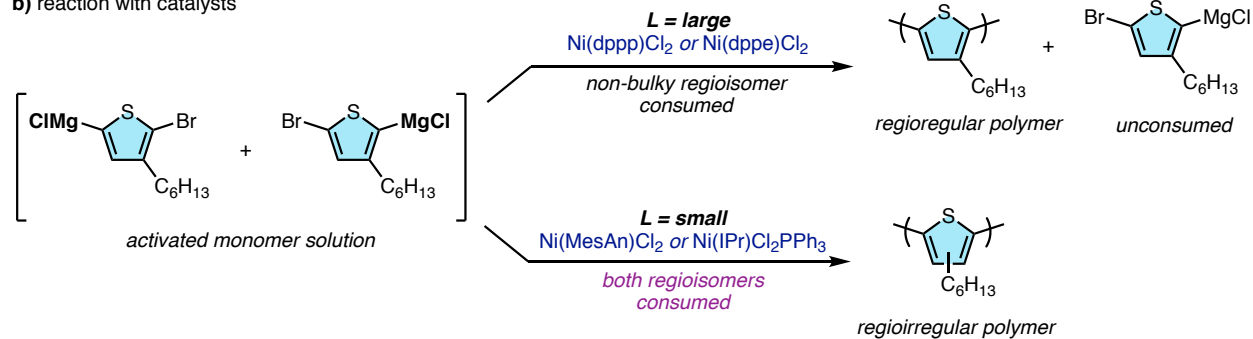
For ancillary ligands, electron-rich  $\sigma$ -donating ligands enable facile transmetalation both in CTP<sup>90</sup> and small-molecule cross-coupling,<sup>116</sup> due to the trans-effect.<sup>117</sup> This electronic dependence demonstrates why phosphine, carbene, and imine ligands dominate in CTP, as their highly  $\sigma$ -donating ligand character<sup>118</sup> enables both  $\pi$ -complexation (via the DCD model) and transmetalation in CTP. However, given the redox-neutral character of the transmetalation reaction (i.e., both reactant and product are M<sup>II</sup> species), electronic effects from the ancillary ligands are not as large as they may be in other steps of the catalytic cycle. For polymerization of non-symmetric monomers, often multiple regioisomers of the monomer will be present in the reaction mixture, depending on the activation method.<sup>98,111,112</sup> For sterically bulky catalysts, like Ni(dppe) and Ni(dppp),<sup>119</sup> only one regioisomer of thiophene monomer can be polymerized, leading to regioregular polymers (Scheme 1.14).<sup>89,111,112</sup> For less-bulky catalysts, like Ni(IPr) and Ni(MesAn),<sup>120</sup> both regioisomers of the monomer can be consumed,<sup>87,89</sup> leading to lower regioregularity. Based on these observations, Kiriy has investigated the polymerization of sterically encumbered thiophenes and found that transmetalation was entirely prevented in the Ni-catalyzed KCTP of 3,4-dialkylthiophenes.<sup>56</sup> Therefore, steric bulk in CTP can be favorable for some applications (i.e., regioregular polymer synthesis) but deleterious in others (polymerization of sterically encumbered monomers). Investigation into the steric effects of transmetalation of

sterically encumbered monomers, and their effect on turnover in thienothiophene CTP, will be investigated in Chapter 3.

a) Grignard metathesis activation



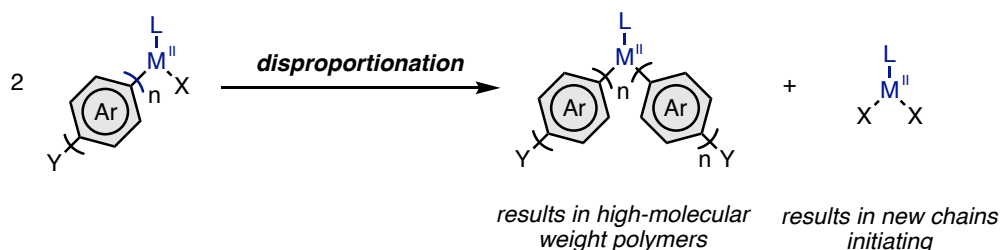
b) reaction with catalysts



**Scheme 1.14** Transmetalation effects on the regioregularity of polymers synthesized via KCTP.

Additives and concentrations can also affect transmetalation. Added lithium chloride in the reaction medium can increase the rate of transmetalation significantly by stabilizing the buildup of charge in the transmetalation transition state and/or by breaking up Grignard aggregates, increasing the reactivity of monomers. As such, it is common to add LiCl to the monomer solution in CTP<sup>108,121</sup> or use turbo-Grignard solutions<sup>92,122</sup> in monomer activation to speed up transmetalation. Additionally, CTP reactions are often run at low concentrations, approximately 0.05 M or less in catalyst.<sup>84,87,89,92,107,108,121</sup> While, in principle, a lower concentration of catalyst slows down the rate of transmetalation,<sup>123</sup> lower concentration of LM(Ar)X also prevents disproportionation (Scheme 1.15) the major side reaction that competes with transmetalation. Catalysts can also be modulated to reduce the likelihood of disproportionation, as discussed in work by Locklin<sup>124</sup> but generally choosing a catalyst to prevent disproportionation is secondary to

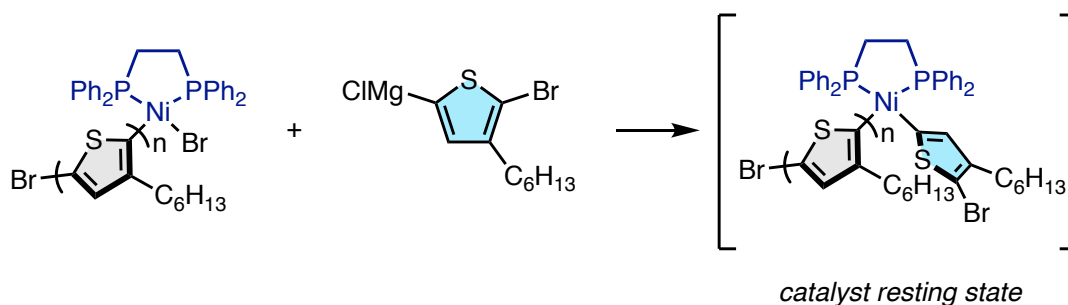
choosing catalyst for enabling faster on-cycle reactions because polymerizations can usually be run more dilute to prevent disproportionation.



**Scheme 1.15** Disproportionation in CTP, resulting in off-cycle species that broaden the molar mass distribution.

### 1.3.2 Reductive Elimination Reactions from $LMAr_2$ Complexes

After transmetalation, the resulting species is the  $LMAr_2$  complex which is reactive toward reductive elimination. In CTP of thiophene or benzene catalyzed by Ni(dppe), the  $LMAr_2$  complex is observed as the resting state, indicating that reductive elimination is turnover-limiting (Scheme 1.16). The shift in turnover limiting step between the Ni(dppe) and Ni(dppp)-catalyzed thiophene polymerization reactions is likely due to the smaller P–Ni–P bite angle in complexes with smaller backbones. This smaller P–Ni–P bite angle enables larger Ar–Ni–Ar bite angle, reducing the orbital overlap between the Ar fragments and slowing down reductive elimination.<sup>125</sup>



**Scheme 1.16** The  $LMAr_2$  species is observed as the resting state in Ni(dppe) catalyzed polymerization of thiophene.

Using Ni(dppe) based complexes has enabled chemists to gather insight on the structure–property relationships that affect the barrier to reductive elimination in CTP. For example, McNeil and coworkers saw increased rates of reductive elimination when electron-withdrawing groups were added to the ligands,<sup>96</sup> consistent with small molecule studies.<sup>63</sup> Additionally, the more sterically encumbered catalysts seem to give rise to lower reductive elimination barriers according to computational results from Seferos and coworkers.<sup>90</sup> Zimmerman and coworkers finds similar results in a study on reductive elimination in thiophene polymerization,<sup>126</sup> but these results show a smaller effect of steric bulk, potentially due to differences in the regioisomers of the monomer considered.<sup>127</sup> Similar results are likely in other systems, given that these effects are well-known in small molecule cross-coupling as well.<sup>128</sup>

Side reactions from  $\text{LMAR}_2$  complexes are not commonly observed, so optimizing the reactivity of  $\text{LMAR}_2$  complexes is only necessary to enhance turnover in CTP reactions when reductive elimination is rate-limiting. However, most other CTP reactions do not appear to have turnover-limiting reductive elimination, meaning catalysts that enable more facile reductive elimination are not commonly investigated beyond the studies described above.

## 1.4 Scope of This Thesis

The rest of this thesis concerns work I have performed on the on-cycle and off-cycle reactions of intermediates in CTP. Given that CTP is a polymerization reaction in which characterization of organometallic intermediates is challenging, Chapter 2 investigates *in-situ* characterization of the Ni complexes in the reaction mixture. The results from Chapter 2 enable reanalyzing the catalyst trap observed during Ni-catalyzed polymerization of thieno[3,2-*b*]thiophenes, explored in Chapter 3. Particularly, we identify that the catalyst trap is a  $\text{Ni}^{\text{II}}$  complex that arises from off-cycle C–S insertion, and the impacts of this mode of off-cycle reactivity on

the monomer scope of CTP is discussed. Lastly, the mechanism of ring-walking in Ni and Pd-catalyzed CTP will be investigated and discussed in Chapter 4, with particular emphasis on elucidating the relationships between  $\pi$ -binding energy and ring-walking barrier that are currently unclear in literature.

## 1.5 References

- <sup>1</sup> Andrady, A. L.; Neal, M. A. Applications and Societal Benefits of Plastics. *Philos. Trans. R. Soc. B Biol. Sci.* **2009**, *364* (1526), 1977–1984. <https://doi.org/10.1098/RSTB.2008.0304>.
- <sup>2</sup> Association of Plastic Manufacturers (Organization). Plastics – the Facts 2020. *PlasticEurope 2020*, <https://www.plasticseurope.org/en/resources/publications/4312-plastics-facts-2020> (accessed 20 Feb 2022).
- <sup>3</sup> Key Applications of Polymethyl Methacrylate (PMMA). *Omnexus*. **2022** <https://omnexus.specialchem.com/selection-guide/polymethyl-methacrylate-pmma-acrylic-plastic/key-applications> (accessed 28 Feb 2022).
- <sup>4</sup> All About Kevlar. *Fiber Brokers* <https://www.fiberbrokers.com/body-armor-disposal/all-about-kevlar/> (accessed 28 Feb 2022)
- <sup>5</sup> Will, P.-A.; Reineke, S. Organic Light-Emitting Diodes in *Handbook of Organic Materials for Electronic and Photonic Devices*, 2<sup>nd</sup> ed.; Elsevier, 2019.
- <sup>6</sup> Mdluli, S. B.; Ramoroka, M. E.; Yussuf, S. T.; Modibane, K. D.; John-Denk, V. S.; Iwuoha, E. I.  $\pi$ -Conjugated Polymers and Their Application in Organic and Hybrid Organic-Silicon Solar Cells. *Polymers* **2022**, *14*, 716–753.
- <sup>7</sup> Ma, L.; Zhang, S.; Wang, J.; Xu, Y.; Hou, J. Recent Advances in Non-fullerene Organic Solar Cells: From Lab to Fab. *Chem. Commun.* **2020**, *56*, 14337–14352.
- <sup>8</sup> Cowie, J. M. G.; Arrighi, V. *Polymers: Chemistry and Physics of Modern Materials*, 3<sup>rd</sup> ed.; CRC Press, 2008.
- <sup>9</sup> Simpson, D.M. and Vaughan, G.A. Ethylene Polymers, LLDPE. In *Encyclopedia of Polymer Science and Technology*, 1<sup>st</sup> ed. Wiley, 2001.
- <sup>10</sup> Kurtz, S. M. The UHMWPE Handbook: Ultra-High Molecular Weight Polyethylene in Total Joint Replacement, 1st ed.; Elsevier, 2004.
- <sup>11</sup> Utracki, L.A.; Schlund, B. Linear Low Density Polyethylenes and Their Blends: Part 4 Shear Flow of LLDPE Blends With LLDPE and LDPE. *Polym. Eng. Sci.* **1987**, *27*, 1512-1522.
- <sup>12</sup> Szwarc, M. ‘Living’ Polymers. *Nature* **1956**, *1168–1169*.
- <sup>13</sup> Szwarc, M.; Levy, M.; Milkovich, R. Polymerization Initiated by Electron Transfer to Monomer. A New Method of Formation of Block Polymers. *J. Am. Chem. Soc.* **1956**, *78*, 2656–2657.
- <sup>14</sup> Klosin, J.; Fontaine, P. P.; Figueroa, R. Development of Group IV Molecular Catalysts for High Temperature Ethylene- $\alpha$ -Olefin Copolymerization Reactions. *Acc. Chem. Res.* **2015**, *48*, 2004–2016.
- <sup>15</sup> Domski, G. J.; Rose, J. M.; Coates, G. W.; Boli, A. D.; Brookhart, M. Living Alkene Polymerization: New Methods for the Precision Synthesis of Polyolefins. *Prog. Polym. Sci.* **2007**, *32*, 30–92.
- <sup>16</sup> Bielawski, C. W.; Grubbs, R. H. Living Ring-Opening Metathesis Polymerization. *Prog. Polym. Sci.* **2007**, *32*, 1–29.
- <sup>17</sup> Gromada, J.; Carpentier, J.-F.; Mortreux, A. Group 3 Metal Catalysts for Ethylene and  $\alpha$ -Olefin Polymerization. *Coord. Chem. Rev.* **2004**, *248*, 397–410.
- <sup>18</sup> Brintzinger, H. H.; Fischer, D.; Mülhaupt, R.; Rieger, B.; Waymouth, R. M. Stereospecific Olefin Polymerization with Chiral Metallocene Catalysts. *Angew. Chem. Int. Ed.* **1995**, *34*, 1143–1170.
- <sup>19</sup> Grubbs, R. H. *Handbook of Metathesis*; Wiley-VCH: Weinheim, Germany, 2003; Vol. 3.



- 
- <sup>20</sup> Camacho, D. H.; Salo, E. V.; Ziller, J. W.; Guan, Z. Cyclophane-Based Highly Active Late-Transition-Metal Catalysts for Ethylene Polymerization. *Angew. Chem., Int. Ed.* **2004**, *43*, 1821–1825.
- <sup>21</sup> Gates, D. P.; Svejda, S. A.; Onate, E.; Killian, C. M.; Johnson, L. K.; White, P. S.; Brookhart, M. Synthesis of Branched Polyethylene Using ( $\alpha$ -Diimine)nickel(II) Catalysts: Influence of Temperature, Ethylene Pressure, and Ligand Structure on Polymer Properties. *Macromolecules* **2000**, *33*, 2320–2334.
- <sup>22</sup> Franssen, N. M. G.; Reek, J. N. H.; de Bruin, B. Synthesis of Functional ‘Polyolefins’: State of the Art and Remaining Challenges. *Chem. Soc. Rev.* **2013**, *42*, 5809–5832.
- <sup>23</sup> Grubbs, R. B.; Grubbs, R. H. 50th Anniversary Perspective: Living Polymerization — Emphasizing the Molecule in Macromolecules. *Macromolecules* **2017**, *50*, 6979–6997.
- <sup>24</sup> Matyjaszewski, K. Atom Transfer Radical Polymerization (ATRP): Current Status and Future Perspectives. *Macromolecules* **2012**, *45*, 4015–4039.
- <sup>25</sup> Semsarilar, M.; Abetz, V. Polymerizations by RAFT: Developments of the Technique and Its Application in the Synthesis of Tailored (Co)polymers. *Macromol. Chem. Phys.* **2021**, *222*, 2000311.
- <sup>26</sup> Truong, N. P.; Jones, G. R.; Bradford, K. G. E.; Konokolewicz, D.; Anastasaki, A. A Comparison of RAFT and ATRP Methods for Controlled Radical Polymerization. *Nat. Rev. Chem.* **2021**, *5*, 859–869.
- <sup>27</sup> Swager, T. M. 50th Anniversary Perspective: Conducting/Semiconducting Conjugated Polymers. A Personal Perspective on the Past and the Future. *Macromolecules* **2017**, *50*, 4867–4886.
- <sup>28</sup> Qiu, Z.; Hammer, B. A. G.; Müllen, K. Conjugated Polymers – Problems and Promises. *Prog. Polym. Sci.* **2020**, *100*, 101179.
- <sup>29</sup> Aplan, M. P.; Gomez, E. D. Recent Developments in Chain-Growth Polymerizations of Conjugated Polymers. *Ind. Eng. Chem. Res.* **2017**, *56*, 7888–7901.
- <sup>30</sup> Lutz, J. P.; Hannigan, M. D.; McNeil, A. J. Polymers synthesized via catalyst-transfer polymerization and their applications *Coord. Chem. Rev.* **2018**, *376*, 225–247.
- <sup>31</sup> Kline, R. J.; McGehee, M. D.; Kadnikova, E. N.; Liu, J.; Fréchet, J. M. J.; Toney, M. F. Dependence of regioregular poly(3-hexylthiophene) film morphology and field-effect mobility on molecular weight. *Macromolecules* **2005**, *38*, 3312–3319.
- <sup>32</sup> Despite the widespread use of cross-coupling, electropolymerization is commonly explored (for more, see: Zhao, M.; Zhang, H.; Gu, C.; Ma, Y. Electrochemical polymerization: an emerging approach for fabricating high-quality luminescent films and super-resolution OLEDs. *J. Mat. Chem. C* **2020**, *8*, 5310–5320.) as well as photopolymerizations (for more, see: reference 25)
- <sup>33</sup> Woods, E. F; Berl, A. J.; Kalow, J. A. Advances in the Synthesis of  $\pi$ -Conjugated Polymers by Photopolymerization. *Chem. Photo. Chem.* **2020**, *5*, 4–11.
- <sup>34</sup> Despite the widespread use of cross-coupling, electropolymerization is commonly explored (for more, see: Zhao, M.; Zhang, H.; Gu, C.; Ma, Y. Electrochemical polymerization: an emerging approach for fabricating high-quality luminescent films and super-resolution OLEDs. *J. Mat. Chem. C* **2020**, *8*, 5310–5320.) as well as photopolymerizations (for more, see: reference 25)
- <sup>35</sup> Woods, E. F; Berl, A. J.; Kalow, J. A. Advances in the Synthesis of  $\pi$ -Conjugated Polymers by Photopolymerization. *Chem. Photo. Chem.* **2020**, *5*, 4–11.
- <sup>36</sup> Han, F. S. Transition-Metal-Catalyzed Suzuki-Miyaura Cross Coupling Reactions: A Remarkable Advance From Palladium to Nickel Catalysts. *Chem. Soc. Rev.* **2013**, *42*, 5270–5298.

- 
- <sup>37</sup> Xu, S.; Kim, E. H.; Wei, A.; Negishi, E. I. Pd- and Ni-catalyzed cross-coupling reactions in the synthesis of organic electronic materials *Sci. Technol. Adv. Mater.* **2014**, *15*, 044201.
- <sup>38</sup> Müllen, K.; Pisula, W. Donor–Acceptor Polymers. *J. Am. Chem. Soc.* **2015**, *137*, 9503–9505.
- <sup>39</sup> Hahesh, K.; Karpagam, S.; Pandian, K. How to Design Donor–Acceptor Based Heterocyclic Conjugated Polymers for Applications from Organic Electronics to Sensors. *Top. Curr. Chem.* **2019**, *377*, 12.
- <sup>40</sup> Bryan, Z. J.; McNeil, A. J. Conjugated Polymer Synthesis via Catalyst-Transfer Polycondensation (CTP): Mechanism, Scope, and Applications. *Macromolecules* **2013**, *46*, 8395–8405.
- <sup>41</sup> Yokozawa, T.; Ohta, Y. Transformation of Step-Growth Polymerization into Living Chain-Growth Polymerization. *Chem. Rev.* **2016**, *116*, 1950–1968.
- <sup>42</sup> Zhu, Y.-Y.; Yin, T.-T.; Yin, J.; Liu, N.; Yu, Z.-P.; Zhu, Y.-W.; Ding, Y.-S.; Yin, J.; Wu, Z.-Q. Poly(3-hexylthiophene)-block-poly(5,8-di-p-tolylquinoxaline-2,3-diyl) Conjugated Rod–Rod Copolymers: One Pot Synthesis, Self-Assembly and Highly Selective Sensing of Cobalt. *RSC Adv.* **2014**, *4*, 40241–40250.
- <sup>43</sup> Monnaie, F.; Verheyen, L.; De Winter, J.; Gerbaux, P.; Brullot, W.; Verbiest, T.; Koeckelberghs, G. Influence of Structure of End-Group-Functionalized Poly(3-hexylthiophene) and Poly(3-octylselenophene) Anchored on Au Nanoparticles. *Macromolecules* **2015**, *48*, 8752–8759.
- <sup>44</sup> Zhu, M.; Kim, H.; Jang, Y. J.; Park, S.; Ryu, D. Y.; Kim, K.; Tang, P.; Qiu, F.; Kim, D. H.; Peng, J. Toward High Efficiency Organic Photovoltaic Devices with Enhanced Thermal Stability Utilizing P3HT-b-P3PHT Block Copolymer Additives. *J. Mater. Chem. A* **2016**, *4*, 18432–18443.
- <sup>45</sup> Fischer, C. S.; Jenewin, C.; Mecking, S. Conjugated Star Polymers from Multidirectional Suzuki–Miyaura Polymerization for Live Cell Imaging. *Macromolecules* **2015**, *48*, 483–491
- <sup>46</sup> Bilbrey, J. A.; Bootsma, A. N.; Bartlett, M. A.; Locklin, J.; Wheeler, S. E.; Allen, W. D. Ring-Walking of zerovalent Nickel on Aryl Halides. *J. Chem. Theory Comput.* **2017**, *13*, 1706–1711.
- <sup>47</sup> Leone, A. K.; McNeil, A. J. Matchmaking in Catalyst-Transfer Polycondensation: Optimizing Catalysts based on Mechanistic Insight *Acc. Chem. Res.* **2016**, *49*, 2822–2831.
- <sup>48</sup> Yamamoto, T. Cross-Coupling Reactions for Preparation of  $\pi$ -Conjugated Polymers. *J. Organomet. Chem.* **2002**, *653*, 195–199.
- <sup>49</sup> Senkovskyy, V.; Tkachov, R.; Komber, H.; John, A.; Sommer, J.-U.; Kiriya, A. Mechanistic Insight into Catalyst-Transfer Polymerization of Unusual Anion-Radical Naphthalene Diimide Monomers: An Observation of Ni(0) Intermediates. *Macromolecules* **2012**, *45*, 7770–7777.
- <sup>50</sup> Bridges, C. R.; McCormick, T. M.; Gibson, G. L.; Hollinger, J.; Seferos, D. S. Designing And Refining Ni(II)Diimine Catalysts Toward The Controlled Synthesis Of Electron-Deficient Conjugated Polymers. *J. Am. Chem. Soc.* **2013**, *135*, 13212–13219.
- <sup>51</sup> Cui, Y.; Yao, H.; Hong, L.; Zhang, T.; Xu, Y.; Xizn, K.; Gao, B.; Qin, J. Zhang, J.; Wei, Z. Hou, J. High Efficiency (15.8%) All-Polymer Solar Cells Enabled by a Regioregular Narrow Bandgap Polymer Acceptor. *Adv. Mater.* **2019**, *31*, 1808356.
- <sup>52</sup> Jarrett-Wilkins, C. N.; Pollit, A. A.; Seferos, D. S. Polymerization Catalysts Take a Walk on the Wild Side. *Trends. Chem.* **2020**, *2*, 493–505.
- <sup>53</sup> Van Den Eede, M.-P.; De Winter, J.; Gerbaux, P.; Koeckelberghs, G. Controlled Polymerization of a Cyclopentadithiophene–Phenylene Alternating Copolymer. *Macromolecules* **2018**, *51*, 9043–9051
- <sup>54</sup> Bryan, Z. J.; Hall, A. O.; Zhao, C. T.; Chen, J.; McNeil, A. J. Limitations of Using Small Molecules to Identify Catalyst-Transfer Polycondensation Reactions. *ACS Macro Lett.* **2016**, *5*, 1, 69–72.

- 
- <sup>55</sup> Smith, M. L.; Leone, A. K.; Zimmerman, P. M.; McNeil, A. J. Impact of Preferential  $\pi$ -Binding in Catalyst-Transfer Polycondensation of Thiazole Derivatives *ACS Macro Lett.* **2016**, *5*, 1411–1415.
- <sup>56</sup> Tkachov, R.; Senkovskyy, V.; Komber, H.; Kiriya, A. Influence of Alkyl Substitution Pattern on Reactivity of Thiophene-Based Monomers in Kumada Catalyst-Transfer Polycondensation. *Macromolecules* **2011**, *44*, 7, 2006–2015
- <sup>57</sup> Nojima, M.; Ohta, Y.; Yokozawa, T. Investigation of Catalyst-Transfer Condensation Polymerization for Synthesis of Poly(p-phenylenevinylene) *J. Polym. Sci. A. Polym. Chem.* **2014**, *52*, 2643–2653.
- <sup>58</sup> Magnin, G.; Clifton, J.; Schoenebeck, F. A General and Air-tolerant Strategy to Conjugated Polymers within Seconds under Palladium(I) Dimer Catalysis. *Angew. Chem. Int. Ed.* **2019**, *58*, 10179–10183.
- <sup>59</sup> Kubo, T.; Young, M. S.; Souther, K. D.; Hannigan, M. D.; McNeil, A. J. Air-tolerant Poly(3-hexylthiophene) Synthesis via Catalyst-Transfer Polymerization. *J. Polym. Sci. A - Polym. Chem.* **2021**, *59*, 268–273.
- <sup>60</sup> Bedi, A.; De Winter, J.; Gerbaux, P.; Koeckelberghs, G. Detrimental Ni(0) Transfer in Kumada Catalyst Transfer Polycondensation of Benzo[2,1-b:3,4-b']dithiophene. *J. Polym. Sci. A - Polym. Chem.* **2016**, *54*, 1706–1712.
- <sup>61</sup> Lee, C.; Lee, S.; Kim, G.-U.; Lee, W.; Kim, B. J. Recent Advances, Design Guidelines, and Prospects of All-Polymer Solar Cells. *Chem. Rev.* **2019**, *13*, 8028–8086.
- <sup>62</sup> Cheng, Y.-J.; Yang, S.-H.; Hsu, C.-S. Synthesis of Conjugated Polymers for Organic Solar Cell Applications. *Chem. Rev.* **2009**, *109*, 5868–5923.
- <sup>63</sup> Balcells, D.; Nova, A. Designing Pd and Ni Catalysts for Cross-Coupling Reactions by Minimizing Off-Cycle Species. *ACS Catal.* **2018**, *8*, 3499–3515.
- <sup>64</sup> Surry, D. S.; Buchwald, S. L. Biaryl Phosphane Ligands in Palladium-Catalyzed Amination. *Angew. Chem. Int. Ed.* **2008**, *47*, 6338–6361.
- <sup>65</sup> Ruiz-Castillo, R.; Buchwald, S. L. Applications of Palladium-Catalyzed C–N Cross-Coupling Reactions. *Chem. Rev.* **2016**, *116*, 12564–12649.
- <sup>66</sup> Bruno, N. C.; Tudge, M. T.; Buchwald, S. L. Design and Preparation of New Palladium Precatalysts for C–C and C–N Cross-coupling Reactions. *Chem. Sci.* **2013**, *4*, 916–920.
- <sup>67</sup> Collier, G. S.; Reynolds, J. R. Exploring the Utility of Buchwald Ligands for C–H Oxidative Direct Arylation Polymerizations. *ACS Macro Lett.* **2019**, *8*, 931–936.
- <sup>68</sup> Schlummer, B.; Scholz, U. Palladium-Catalyzed C–N and C–O Coupling –A Practical Guide from an Industrial Vantage Point. *Adv. Synth. Catal.* **2004**, *346*, 1599–1626.
- <sup>69</sup> Koeckelberghs and coworkers claimed to observe a  $\pi$ -complex as a catalyst trap in polymerization of thienothiophene (in Willot, P.; Koeckelberghs, G. Evidence for Catalyst Association in the Catalyst Transfer Polymerization of Thieno[3,2-*b*]thiophene. *Macromolecules* **2014**, *47*, 8548–8555.) but, the discussion in chapters 2 and 3 of this thesis give reasons why the species they observed is likely not a  $\pi$ -complex. Similarly, Kiriya claims to have observed a  $\pi$ -complex during the polymerization of naphthalene diimide monomers (in Senkovskyy, V.; Tkachov, R.; Komber, H.; John, A.; Sommer, J.-U.; Kiriya, A. Mechanistic Insight into Catalyst-Transfer Polymerization of Unusual Anion-Radical Naphthalene Diimide Monomers: An Observation of Ni(0) Intermediates. *Macromolecules* **2012**, *45*, 7770–7777.) but based on their <sup>31</sup>P NMR spectra and the structure of the ligand used, it is unlikely they observed the  $\pi$ -complex.
- <sup>70</sup> The  $\pi$ -complexes in references 11 (*J. Chem. Theory Comput.* **2017**, *13*, 1706–1711.) have binding energies between 20 and 45 kcal/mol.

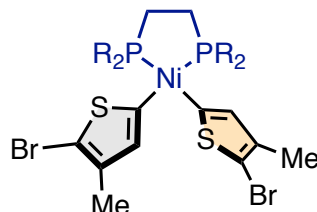
- 
- <sup>71</sup> The triplet  $\pi$ -complexes in reference 42 (Pollit, A. A.; Lough, A. J.; Seferos, D. S. Examining the Spin State and Redox Chemistry of Ni(Diimine) Catalysts during the Synthesis of  $\pi$ -Conjugated Polymers. *Macromol. Chem. Phys.* **2020**, *221*, 2000321.) have  $\pi$ -binding energies less than 5 kcal/mol.
- <sup>72</sup> Dewar, M. A Review of  $\pi$ -Complex Theory. *Bull. Soc. Chim. Fr.* **1951**, *1*, C79.
- <sup>73</sup> Chatt, J.; Duncanson, L. A. Olefin Co-ordination Compounds. Part III. Infra-red Spectra and Structure: Attempted Preparation of Acetylene Complexes. *J. Chem. Soc.* **1953**, *0*, 2939–2947.
- <sup>74</sup> Coulson, C. A.; O’Leary, B. T.; Mallion, R. B. *Hückel Theory for Organic Chemists*, 1<sup>st</sup> ed.; Academic Press: 1978.
- <sup>75</sup> Setiawan, D.; Kalescky, R.; Kraka, E.; Cremer, D. Direct Measure of Metal–Ligand Bonding Replacing the Tolman Electronic Parameter. *Inorg. Chem.* **2016**, *55*, 2332–2344.
- <sup>76</sup> Based on reduction potentials of Ni and Pd: Lide, D. R. CRC Handbook of Chemistry and Physics, 87th ed.; CRC Press: 2008.
- <sup>77</sup> Ziegler, T.; Tschinke, V.; Ursemnach, C. Thermal Stability and Kinetic Lability of the Metal-Carbonyl Bond. A Theoretical Study on M(CO)<sub>6</sub> (M = Cr, Mo, W), M(CO)<sub>5</sub> (M = Fe, Ru, Os), and M(CO)<sub>4</sub> (M = Ni, Pd, Pt). *J. Am. Chem. Soc.* **1987**, *109*, 4825–4837.
- <sup>78</sup> Griffith, J. S.; Orgel, L. E. Ligand-Field Theory. *Q. Rev. Chem. Soc.* **1957**, *11*, 381–393.
- <sup>79</sup> Desnoyer, A. N.; He, W.; Behyan, D.; Chiu, W.; Love, J. A.; Kennepohl, P. The Importance of Ligand-Induced Backdonation in the Stabilization of Square Planar d<sup>10</sup> Nickel  $\pi$ -Complexes. *Chem. Eur. J.* **2019**, *25*, 5259–5268.
- <sup>80</sup> Biffis, A.; Centomo, P.; Del Zotto, A.; Zecca, M. Pd Metal Catalysts for Cross-Couplings and Related Reactions in the 21st Century: A Critical Review. *Chem. Rev.* **2018**, *118*, 2249–2295.
- <sup>81</sup> Campeau, L.-C.; Hazari, N. Cross-Coupling and Related Reactions: Connecting Past Success to the Development of New Reactions for the Future. *Organometallics* **2019**, *38*, 3–35.
- <sup>82</sup> Leone, A. K.; Muller, E. A.; McNeil, A. J. The History of Palladium-Catalyzed Cross-Couplings Should Inspire the Future of Catalyst-Transfer Polymerization. *J. Am. Chem. Soc.* **2018**, *140*, 15126–15139.
- <sup>83</sup> Dicciani, J.; Lin, Q.; Diao, T. Mechanisms of Nickel-Catalyzed Coupling Reactions and Applications in Alkene Functionalization. *Acc. Chem. Res.* **2020**, *53*, 906–919.
- <sup>84</sup> Bryan, Z. J.; McNeil, A. K. Evidence For a Preferential Intramolecular Oxidative Addition in Ni-Catalyzed Cross-Coupling Reactions and Their Impact on Chain-Growth Polymerizations. *Chem. Sci.* **2013**, *4*, 1620–1624.
- <sup>85</sup> For more discussion on this, see chapter 4.
- <sup>86</sup> Kepp, K. A Quantitative Scale of Oxophilicity and Thiophilicity. *Inorg. Chem.* **2016**, *55*, 9461–9470.
- <sup>87</sup> Leone, A. K.; Souther, K. D.; Vitek, A. K.; LaPointe, A. M.; Coates, G. W.; Zimmerman, P. M.; McNeil, A. J. Mechanistic Insight into Thiophene Catalyst-Transfer Polymerization Mediated by Nickel Diimine Catalysts. *Macromolecules* **2017**, *50*, 9121–9127.
- <sup>88</sup> Pollit, A. A.; Lough, A. J.; Seferos, D. S. Examining the Spin State and Redox Chemistry of Ni(Diimine) Catalysts during the Synthesis of  $\pi$ -Conjugated Polymers. *Macromol. Chem. Phys.* **2020**, *221*, 2000321.
- <sup>89</sup> Leone, A. K.; Goldberg, P. K.; McNeil, A. J. Ring-Walking in Catalyst-Transfer Polymerization. *J. Am. Chem. Soc.* **2018**, *140*, 7846–7850.
- <sup>90</sup> Pollit, A. A. Ye, S.; Seferos, D. S. Elucidating the Role of Catalyst Steric and Electronic Effects in Controlling the Synthesis of  $\pi$ -Conjugated Polymers. *Macromolecules* **2020**, *53*, 138–148.

- 
- <sup>91</sup> He, W.; Patrick, B. O.; Kennepohl, P. Identifying the Missing Link in Catalyst Transfer Polymerization *Nat. Commun.* **2018**, *9*, 3866–3866.
- <sup>92</sup> Willot, P.; Koeckelberghs, G. Evidence for Catalyst Association in the Catalyst Transfer Polymerization of Thieno[3,2-*b*]thiophene. *Macromolecules* **2014**, *47*, 8548–8555.
- <sup>93</sup> For more information, please read chapter 3.
- <sup>94</sup> Nojima, M.; Ohta, Y.; Yokozawa, T. Investigation of Catalyst-Transfer Condensation Polymerization for Synthesis of Poly(p-phenylenevinylene). *J. Polym. Sci. A - Polym. Chem.* **2014**, *52*, 2643–2653.
- <sup>95</sup> Yokozawa, T.; Nanashima, Y.; Ohta, Y. Precision Synthesis of n-Type  $\pi$ -Conjugated Polymers in Catalyst Transfer Condensation Polymerization. *ACS Macro Lett.* **2012**, *1*, 862–866.
- <sup>96</sup> Lee, S. R.; Bryan, Z. J.; Wagner, A. M.; McNeil, A. J. Effect of Ligand Electronic Properties on Precatalyst Initiation and Propagation in Ni-Catalyzed Cross-Coupling Polymerizations. *Chem. Sci.* **2012**, *3*, 1562–1566.
- <sup>97</sup> Labinger, J. A. Tutorial on Oxidative Addition. *Organometallics* **2015**, *34*, 4784–4795.
- <sup>98</sup> Ye, S.; Foster, S. M.; Pollit, A. A.; Cheng, S.; Seferos, D. S. The Role of Halogens in the Catalyst Transfer Polymerization for  $\pi$ -Conjugated Polymers. *Chem. Sci.* **2019**, *10*, 2075–2080.
- <sup>99</sup> Tamba, S. I.; Fuji, K. I.; Nakamura, K.; Mori, A. Nickel(II)-Catalyzed Cross-Coupling Polycondensation of Thiophenes via C–S Bond Cleavage. *Organometallics* **2014**, *33*, 12–15.
- <sup>100</sup> Boit, A. T.; Bulger, A. S.; Dander, J. E.; Garg, N. K. Activation of C–O and C–N Bonds Using Non-Precious-Metal Catalysis. *ACS Catal.* **2020**, *10*, 12109–12126.
- <sup>101</sup> The only reports that indicate that off-cycle reaction paths arising from oxidative addition are in references 91 and 56, but neither of these found that the oxidative addition adducts could act as catalyst-traps.
- <sup>102</sup> Vacic, D. A.; Jones, W. D. Room-Temperature Desulfurization of Dibenzothiophene Mediated by [(*i*-Pr<sub>2</sub>PCH<sub>2</sub>)<sub>2</sub>NiH]<sub>2</sub>. *J. Am. Chem. Soc.* **1997**, *119*, 10855–10856.
- <sup>103</sup> Vacic, D. A.; Jones, W. D. Modeling the Hydrodesulfurization Reaction at Nickel. Unusual Reactivity of Dibenzothiophenes Relative to Thiophene and Benzothiophene. *J. Am. Chem. Soc.* **1999**, *121*, 7606–7617.
- <sup>104</sup> Li, T.; García, J. J.; Brennessel, W. W.; Jones, W. D. C–CN Bond Activation of Aromatic Nitriles and Fluxionality of the  $\eta$ -2-Arene Intermediates: Experimental and Theoretical Investigations. *Organometallics* **2010**, *29*, 2430–2445.
- <sup>105</sup> García, J. J.; Brunkan, N. M.; Jones, W. D. Cleavage of Carbon–Carbon Bonds in Aromatic Nitriles Using Nickel(0). *J. Am. Chem. Soc.* **2002**, *124*, 9547–9555.
- <sup>106</sup> García, J. J.; Jones, W. D. Reversible Cleavage of Carbon–Carbon Bonds in Benzonitrile Using Nickel(0). *Organometallics* **2000**, *19*, 5544–5545.
- <sup>107</sup> Lanni, E. L.; McNeil, A. J. Mechanistic Studies on Ni(dppe)Cl<sub>2</sub>-Catalyzed Chain-Growth Polymerizations: Evidence for Rate Determining Reductive Elimination. *J. Am. Chem. Soc.* **2009**, *131*, 16573–16579.
- <sup>108</sup> Lanni, E. L.; McNeil, A. J. Evidence for Ligand-Dependent Mechanistic Changes in Nickel-Catalyzed Chain-Growth Polymerizations. *Macromolecules* **2010**, *43*, 8039–8044.
- <sup>109</sup> T. Yokozawa and Y. Ohta, Chapter 1: Controlled Synthesis of Conjugated Polymers in Catalyst-transfer Condensation Polymerization: Monomers and Catalysts, in *Semiconducting Polymers: Controlled Synthesis and Microstructure*, 2016, pp. 1-37  
DOI: 10.1039/9781782624004-00001

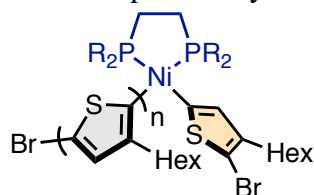
- 
- <sup>110</sup> Baker, M. A.; Tsai, C-H.; Noonan, K. J. T. Diversifying Cross-coupling Strategies, Catalysts, and Monomers for the Controlled Synthesis of Conjugated Polymers. *Chem. Eur. J.* **2018**, *24*, 13078–13088.
- <sup>111</sup> Yokoyama, A.; Miyakoshi, R.; Yokozawa, T. Chain-Growth Polymerization for Poly(3-hexylthiophene) with a Defined Molecular Weight and a Low Polydispersity. *Macromolecules* **2004**, *37*, 1169–1171.
- <sup>112</sup> Sheina, E. E.; Liu, J.; Iovu, M. C.; Laird, D. W.; McCullough, R. D. Chain Growth Mechanism for Regioregular Nickel-Initiated Cross-Coupling Polymerizations. *Macromolecules* **2004**, *37*, 3526–3528.
- <sup>113</sup> Baker, M. A.; Tsai, C-H.; Noonan, K. J. T. Diversifying Cross-coupling Strategies, Catalysts, and Monomers for the Controlled Synthesis of Conjugated Polymers. *Chem. Eur. J.* **2018**, *24*, 13078–13088.
- <sup>114</sup> T. Yokozawa and Y. Ohta, Chapter 1: Controlled Synthesis of Conjugated Polymers in Catalyst-transfer Condensation Polymerization: Monomers and Catalysts, in *Semiconducting Polymers: Controlled Synthesis and Microstructure*, 2016, pp. 1-37 DOI: 10.1039/9781782624004-00001
- <sup>115</sup> Kozuch, S.; Shaik, S. How to Conceptualize Catalytic Cycles? The Energetic Span Model. *Acc. Chem. Rev.* **2011**, *44*, 101–110.
- <sup>116</sup> Fairlamb, I. J. S. “Metal-Catalyzed Cross-Coupling Reactions and More” (Eds.: A. de Meijere, S. Bräse, M. Oestreich), Wiley-VCH, Weinheim, **2014**
- <sup>117</sup> Wovkulich, M. J.; Atwood, J. D. A Trans Effect on the Rate of Ligand Dissociation From Octahedral Organometallic Complexes. Dissociation Of L' From Cr(CO)<sub>4</sub>LL' (L, L' = PBu<sub>3</sub>, PPh<sub>3</sub>, P(OPh)<sub>3</sub>, P(OMe)<sub>3</sub>, AsPh<sub>3</sub>). *Organometallics* **1982**, *1*, 1316–1321.
- <sup>118</sup> Setiawan, D.; Kalescky, R.; Kraka, E.; Cremer, D. Direct Measure of Metal–Ligand Bonding Replacing the Tolman Electronic Parameter. *Inorg. Chem.* **2016**, *55*, 2332–2344.
- <sup>119</sup> The 3.5 Å-sphere % buried volume for Ni(dppe) and Ni(dppp) is 50.3% and 52.0% respectively. For more on buried volume: Falivene, L.; Cao, Z. Petra, A.; Serra, L.; Poater, A.; Oliva, R.; Scarano, V.; Cavallo, L. Toward the Online Computer-Aided Design of Catalytic Pockets. *Nature Chem.* **2019**, *11*, 872–879.
- <sup>120</sup> The 3.5 Å-sphere % buried volume for Ni(Mes) and Ni(IPr) is 45.2% and 45.5% respectively. For more on buried volume, see the paper in the previous reference.
- <sup>121</sup> Miyakoshi, R.; Shimono, K.; Yokoyama, A.; Yokozawa, T. Catalyst-Transfer Polycondensation for the Synthesis of Poly(p-phenylene) with Controlled Molecular Weight and Low Polydispersity. *J. Am. Chem. Soc.* **2006**, *128*, 16012–16013.
- <sup>122</sup> Stefan, M. C.; Javier, A. E.; Osaka, I.; McCullough, R. D. Grignard Metathesis Method (GRIM): Toward a Universal Method for the Synthesis of Conjugated Polymers. *Macromolecules* **2009**, *42*, 30–32.
- <sup>123</sup> Assuming a rate-law equation of  $v_{\text{transmetalation}} = k_{\text{transmetalation}} [\text{LM}(\text{Ar})\text{X}][\text{monomer}]$
- <sup>124</sup> Bilbrey, J. A.; Songag, K. S.; Huddleston, N. E.; Allen, W. D.; Locklin, J. On the Role of Disproportionation Energy in Kumada Catalyst-Transfer Polycondensation. *ACS Macro Lett.* **2012**, *1*, 995–1000.
- <sup>125</sup> Hartwig, J. F. *Organotransition Metal Chemistry: From Bonding to Catalysis*; University Science Books: 2010
- <sup>126</sup> Vitek, A. K.; Jugovic, T. M. E.; Zimmerman, P. M. Revealing the Strong Relationships between Ligand Conformers and Activation Barriers: A Case Study of Bisphosphine Reductive Elimination. *ACS Catal.* **2020**, *10*, 7136–7145.

---

<sup>127</sup> The study by Zimmerman in reference 126 interrogated reductive elimination from a complex with two (equivalently substituted) 4-methylthiophene ligands:



The computed structure for reductive elimination was therefore less bulky than the structures modeled by Seferos, and also less bulky than the structures expected during propagation in the real polymerization, where the two ligands are inequivalently substituted, similar to:



Where one of the thiophenes is substituted at the 3-position, and the other is substituted at the 4-position. This difference in the structure would make Zimmerman's study less sensitive to steric bulk of the ancillary ligand than Seferos' study, due to the larger encumbrance of monomers in the latter (propagation-like) system. However, Seferos' study ignored the effects of conformers, while Zimmerman's study performed extensive conformer sampling and statistical analyses so the conclusions from these studies are difficult to compare.

<sup>128</sup> Zuiderma, E.; van Leeuwen, P. W. N. M.; Bo, C. Reductive Elimination of Organic Molecules from Palladium–Diphosphine Complexes. *Organometallics* **2005**, *24*, 3703–3710.

## Chapter 2 Using $J_{PP}$ to Identify Ni Bidentate Phosphine Complexes *in Situ*

Portions of this chapter have been previously published and have been adapted with permission from Hannigan, M. D.; McNeil, A. J.; Zimmerman, P. M. Using  $J_{PP}$  to Identify Ni Bidentate Phosphine Complexes *In Situ*. *Inorg. Chem.* **2021**, *60*, 13400–13408.

Copyright 2021 American Chemical Society.

### 2.1 Introduction

Nickel complexes bearing bidentate phosphine ligands (Figure 2.1a) are ubiquitous to many synthetically relevant transformations.<sup>1</sup> The oxidation state of Ni typically determines the reactions available to the complex, with electron-rich Ni<sup>0</sup> complexes reacting via addition and insertion, while Ni<sup>II</sup> complexes commonly undergo elimination.<sup>2</sup> Kumada,<sup>3–11</sup> Suzuki,<sup>12–20</sup> Negishi,<sup>21–30</sup> and Stille<sup>31</sup> couplings as well as the Buchwald-Hartwig amination<sup>32–41</sup> utilize these reactivity differences to activate C–X bonds (where X = Cl, Br, or I) by addition to Ni<sup>0</sup>, and form C–C and C–N bonds by elimination from Ni<sup>II</sup>. Given the relevance of Ni complexes to these synthetically important bond-forming reactions, many investigations involving Ni complexes have utilized ligand design to impart control over reactivity. Bidentate phosphine complexes are useful in this regard, because the linker and other groups bound to P atoms are easily varied. Short linkers between the P atoms enforce a *cis* geometry at the metal center, enabling facile reductive elimination compared to complexes with *trans* geometry.<sup>2,42</sup> The other groups bound to the P atoms enable control over the coordination environment, imparting stereoselectivity or modified reactivity.<sup>1</sup> Additionally, due to the high abundance of the spin-active <sup>31</sup>P isotope,<sup>43</sup> obtaining



spectra via nuclear magnetic resonance (NMR) spectroscopy is easier compared to complexes of C-, N-, O-, and S-based ligands.

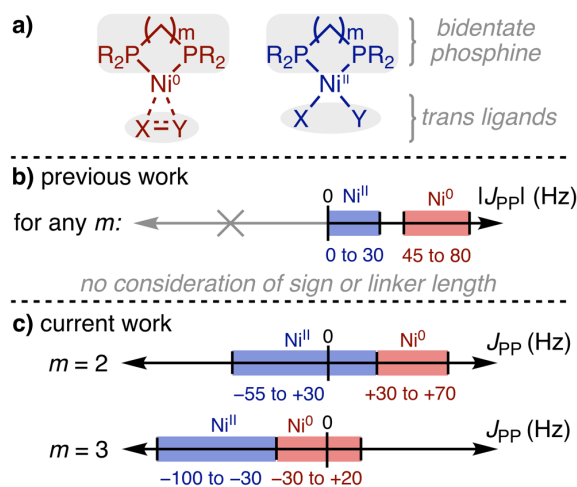


**Figure 2.1** Ni bidentate phosphine complexes and their  $J_{\text{PP}}$  values

Ni bidentate phosphine complexes can be characterized by NMR spectroscopy because many are diamagnetic<sup>44</sup> giving well-resolved spectra that are free of paramagnetic shifts and associated line broadening.<sup>45</sup> Ciofini and coworkers noted in a recent study, however, that predicting and rationalizing  $^{31}\text{P}$  chemical shifts of metal complexes is complicated by the contrasting effects of ligand donation and backbonding.<sup>46</sup> This challenge in rationalizing  $^{31}\text{P}$  chemical shifts makes analyzing organometallic reaction mixtures less straightforward than using  $^1\text{H}$  and  $^{13}\text{C}$  chemical shifts for organic molecules.<sup>47,48</sup> Additionally, this influence of donation and backbonding prevents identifying the oxidation state of the metal by chemical shift because  $\sigma$ -donation and  $\pi$ -backbonding in P–M bonds can change dramatically with oxidation state.<sup>47</sup> The utility of NMR spectroscopy—which otherwise is a convenient means for in-situ analysis of reactions—is therefore limited by its inability to assign oxidation state. Instead, oxidation state must be identified via other methods which often require isolation or purification of the desired complex. This ex-situ characterization can be especially challenging for reactive intermediates,

which may be short-lived or difficult to isolate. Given the ease of obtaining NMR spectra from reactions of Ni bidentate phosphines, and the ability to easily keep NMR samples moisture- and air-free,<sup>49,50</sup> a protocol for understanding structure of Ni bidentate phosphine complexes via <sup>31</sup>P NMR spectroscopy would be useful.

In place of chemical shift, *J*-coupling constants have been investigated to understand structure and properties of bidentate phosphine complexes.<sup>51</sup> *J*-coupling arises when spin-active nuclei in different electronic environments interact through bonds via magnetic interactions with electrons.<sup>52</sup> The strength of this interaction is described using a *J*-coupling constant denoted as <sup>*n*</sup>*J*<sub>XY</sub> where X and Y are the nuclei that are coupled, and *n* is the number of bonds separating the nuclei. *J*-coupling constants involving protons, such as *J*<sub>HH</sub>, have been useful for obtaining chemically meaningful information. For example, the sign of *J*-coupling (positive or negative) identifies whether *J*<sub>HH</sub> arises from 2-bond coupling (<sup>2</sup>*J*<sub>HH</sub>) or 3-bond coupling (<sup>3</sup>*J*<sub>HH</sub>) because the former tends to be negative and the latter is positive.<sup>53–58</sup> The <sup>2</sup>*J*<sub>HH</sub> values of CH<sub>2</sub> groups can give electronic information about the substituents on the carbon atom, with more σ-withdrawing substituents or π-donating substituents making the <sup>2</sup>*J*<sub>HH</sub> less negative.<sup>59</sup> The <sup>3</sup>*J*<sub>HH</sub> coupling gives structural information on the dihedral angle between the two H atoms via the Karplus equation, enabling chemists to understand geometry of pairs of H atoms from the *J*-coupling alone.<sup>60</sup> For this reason, analyses based on 3-bond *J*-couplings have proven useful for structural characterization of small molecules<sup>61,62</sup> as well as polymers,<sup>63</sup> peptides,<sup>64,65</sup> and proteins.<sup>66,67</sup>

Similar to *J*<sub>HH</sub>, *J*<sub>PP</sub> can convey important electronic and structural information about pairs of P atoms and the metals they are bound to.<sup>68</sup> For metal complexes with multiple monodentate phosphines, the magnitude of the <sup>2</sup>*J*<sub>PP</sub> can indicate *cis* or *trans* geometry, with <sup>2</sup>*J*<sub>PP</sub> being larger for complexes with *trans* phosphine ligands.<sup>51</sup> The <sup>2</sup>*J*<sub>PP</sub> can also provide electronic information about

the P atoms because  ${}^2J_{PP}$  depends on the electronegativity of the groups bound to P.<sup>48,69</sup> Additionally, complexes with *cis*-monodentate phosphine ligands tend to have different  $J_{PP}$  than complexes with bidentate phosphine ligands. For example, in Mo and W phosphine complexes,  $J$ -coupling between P atoms through the metal (the only  $J_{PP}$  coupling pathway for monodentate phosphine complexes) results in negative  ${}^2J_{PP}$  values while coupling through the metal and the carbon linker (only available in bidentate phosphine complexes) results in positive  $J_{PP}$  values.<sup>70</sup>

For Ni complexes, systematic studies into the structural effects on  $J_{PP}$  are lacking, but many authors have noted that the  $J_{PP}$  of Ni bidentate phosphine complexes correlates with the oxidation state of Ni.<sup>71–79</sup> Desnoyer et al. state that bidentate phosphine Ni<sup>II</sup> complexes often have low  $J_{PP}$  (less than 30 Hz), and Ni<sup>0</sup> complexes have higher  $J_{PP}$  (45–80 Hz; Figure 2.1b)<sup>80</sup> and propose that the dependence of  $J_{PP}$  on oxidation state is influenced by the electronegativity of ligands *trans* to the phosphines (*trans* ligands). Similar insights have aided identifying Ni complexes from reaction mixtures<sup>81–83</sup> but structural parameters that are commonly varied, such as linker length and R-groups, have not been explored with respect to their effect on  $J$ -coupling. Additionally, most 1-D NMR spectroscopies only give the magnitude of the  $J_{PP}$  (denoted herein as  $|J_{PP}|$ );<sup>89</sup> the sign of  $J_{PP}$ , which can be obtained experimentally by 2-D NMR experiments,<sup>70</sup> has not yet been explored but may contain useful chemical information. A deeper understanding of  $J$ -coupling in Ni bidentate phosphine complexes is needed to fill these knowledge gaps and improve our ability to identify Ni complexes in situ.

Herein a systematic survey of Ni bidentate phosphine complexes with 2-carbon linkers (2C) and 3-carbon linkers (3C) is used to understand how  $J_{PP}$  varies with chemical structure. Notably, we show that  $J_{PP}$  trends with oxidation state and linker length, where 2C linker complexes have distinct  $J_{PP}$  from 3C linker complexes. Additionally, calculations show the sign of  $J_{PP}$  is

related to chemical structure, with Ni<sup>0</sup> complexes having more positive  $J_{PP}$  than Ni<sup>II</sup> complexes, and 2C complexes having more positive  $J_{PP}$  than 3C complexes (Figure 2.1c). Lastly, using charge transfer analysis,  $J_{PP}$  is shown to vary with P-to-Ni donation, with more-donating phosphines or more-withdrawing *trans* ligands causing more negative  $J_{PP}$ . This study gives a more complete framework for identifying Ni complexes via <sup>31</sup>P NMR spectra and for interpreting  $J_{PP}$  in Ni bidentate phosphine complexes.

## 2.2 Literature Survey of Measured $|J_{PP}|$ Values

To understand the relationship between complex structure and  $J_{PP}$ , a Reaxys<sup>84</sup> search was performed to find Ni bidentate phosphine complexes with reported NMR spectra (see Appendix 2). For the 2C dataset, the results were limited to species that also had single-crystal X-ray structures, to verify the oxidation state of Ni. This search yielded a sizeable dataset of 449 complexes. A similar search for 3-carbon linker complexes yielded a dataset of only 67 complexes, the majority of which did not contain resolvable  $|J_{PP}|$  due to paramagnetism or symmetry. Therefore, 3C complexes without reported X-ray crystal structures were added to the dataset, giving 243 complexes (see Appendix 2). Afterwards, the 2C and 3C datasets were screened to remove species that did not have an observable  $J_{PP}$ , such as fluxional complexes or C<sub>2</sub>-symmetric complexes. Complexes of other linkers (e.g., 1-carbon, 4-carbon, etc.) were not included because few examples were available. Both the 2C and 3C datasets had more Ni<sup>II</sup> complexes compared to Ni<sup>0</sup> complexes. This difference in representation may be due to survivorship bias because Ni<sup>0</sup> complexes have high sensitivity toward air and moisture,<sup>85,86</sup> making isolation or characterization more difficult. Additionally, Ni<sup>0</sup>  $\pi$ -complexes often form fluxional structures in solution, in equilibrium with other  $\pi$ -complexes, causing peak broadening in NMR spectra and preventing clear assignment of  $|J_{PP}|$ .<sup>87,88</sup> Therefore, information provided by these datasets is limited to

complexes that are stable enough and rigid enough to show a  $|J_{PP}|$  and may not represent all possible  $|J_{PP}|$  values from all possible  $Ni^0$  and  $Ni^{II}$  bidentate phosphine complexes.

The datasets enabled examining the relationships between oxidation state and  $J$ -coupling (Figure 2.2a). The distributions of  $|J_{PP}|$  were compared statistically by analyzing the variance in  $|J_{PP}|$  for each oxidation state/linker length pair. The distribution of  $|J_{PP}|$  between oxidation states for each linker are significantly different, as indicated by the small  $p$ -values for the 2C  $Ni^0/Ni^{II}$  pair ( $p < 0.0001$ ) and the 3C  $Ni^0/Ni^{II}$  pair ( $p = 0.0034$ ). This statistical difference between oxidation states, along with the small overlap of the data ranges (Table 2.1), indicate it is possible to accurately assign oxidation states via experimentally observed  $|J_{PP}|$  values when the linker length is known. For the 2C dataset, the  $Ni^0$  complexes have higher  $|J_{PP}|$  than the  $Ni^{II}$  complexes, matching the relationship proposed by previous authors.<sup>71–80</sup> For the 3C linker dataset, however, we observed the opposite relationship, with  $Ni^0$  complexes giving lower  $|J_{PP}|$  than the  $Ni^{II}$  complexes, albeit with considerable overlap. Information about  $^{31}P$  chemical shift was also obtained from these datasets and analyzed, but we did not observe a relationship with oxidation state (Figure A1.8) or  $J_{PP}$  (Figure A1.9–A1.11).

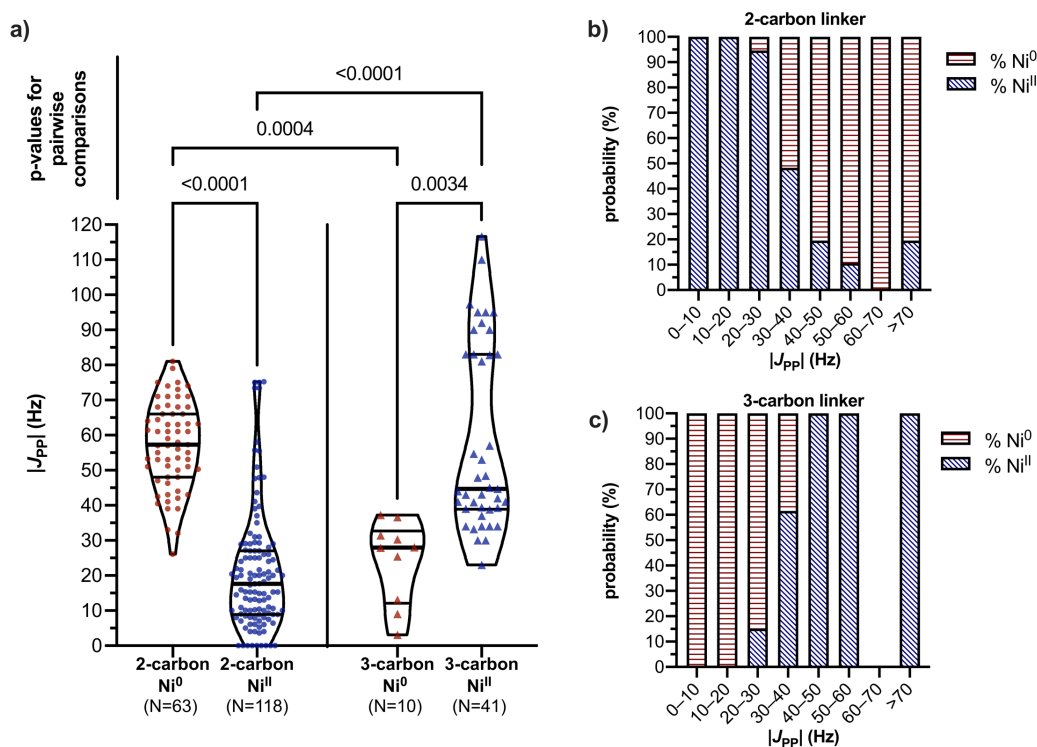


**Figure 2.2** a) Violin plots showing the distributions of experimentally observed  $|J_{PP}|$  for different Ni oxidation states ( $Ni^0$ ,  $Ni^{II}$ ) and phosphine linker lengths (2-carbon, 3-carbon). Bold lines represent medians, fine lines represent 25<sup>th</sup> and 75<sup>th</sup> percentiles. b) Probability that an observed  $|J_{PP}|$  represents a  $Ni^0$  or  $Ni^{II}$  complex for 2C and c) 3C datasets. The gap at the 60–70 Hz range is due to the lack of 3C complexes with  $|J_{PP}|$  in that range.

**Table 2.1** Distribution of  $|J_{PP}|$  values reported in the 2C and 3C datasets.

	2C $Ni^0$	2C $Ni^{II}$	3C $Ni^0$	3C $Ni^{II}$
90 <sup>th</sup> percentile	73.6 Hz	47.6 Hz	37.1 Hz	95.0 Hz
75 <sup>th</sup> percentile	66.0 Hz	27.1 Hz	32.7 Hz	83.0 Hz
Median	57.3 Hz	17.7 Hz	28.0 Hz	44.7 Hz
25 <sup>th</sup> percentile	48.0 Hz	8.9 Hz	12.1 Hz	38.9 Hz
10 <sup>th</sup> percentile	40.7 Hz	4.0 Hz	3.7 Hz	33.4 Hz

Based on the datasets, we also determined the probability of an experimentally observed  $|J_{PP}|$  arising from a  $Ni^0$  or  $Ni^{II}$  complex of a given linker length. When experimental  $|J_{PP}| < 30$  Hz or  $|J_{PP}| > 40$  Hz, the oxidation state can be assigned based on  $J_{PP}$  and the number of atoms in the

linker. For example, if a Ni bidentate phosphine complex with a 2-carbon linker is present in a reaction mixture, and  $^{31}\text{P}$  NMR spectra reveals a set of doublets with  $|J_{\text{PP}}| = 57$  Hz, there is a high likelihood (89%) that it is a  $\text{Ni}^0$  complex (Figure 2.2b). If the  $|J_{\text{PP}}|$  is instead 23 Hz, then there is a higher likelihood (93%) of it being a  $\text{Ni}^{\text{II}}$  complex. For 2C complexes with  $|J_{\text{PP}}|$  within the range of 30–40 Hz, there is nearly equal likelihood of the complex being  $\text{Ni}^0$  (52%) or  $\text{Ni}^{\text{II}}$  (48%). Similar results are observed for the 3C complexes (Figure 2.2c) where a  $|J_{\text{PP}}|$  in the range of 30–40 Hz has a 60% chance of arising from a  $\text{Ni}^{\text{II}}$  complex, and a 40% chance of arising from a  $\text{Ni}^0$  complex. Therefore,  $|J_{\text{PP}}|$  in the range of 30–40 Hz cannot reliably identify oxidation state of Ni in a bidentate phosphine complex, while  $|J_{\text{PP}}|$  outside of this 30–40 Hz range can provide an oxidation state assignment. The reason why  $|J_{\text{PP}}|$  increases with increasing oxidation state for 2C complexes and decreases with increasing oxidation state for 3C complexes was not immediately obvious, so quantum chemical calculations were used to elucidate the physical origin.

### 2.3 Signs of $J_{\text{PP}}$ for Ni Bidentate Phosphine Complexes

$J_{\text{PP}}$ , like all  $J$ -couplings, can have a positive or negative sign. A negative  $J$  corresponds to a more stable antiparallel nuclear spin alignment, while a positive  $J$  corresponds to a more stable parallel nuclear spin alignment.<sup>89</sup> Although most  $^{31}\text{P}$  NMR experiments can give the magnitude of  $J_{\text{PP}}$  (i.e.,  $|J_{\text{PP}}|$ ), few can give the sign. We sought to understand the signs of the experimentally observed  $|J_{\text{PP}}|$  in our datasets because sign of  $J_{\text{PP}}$  was shown relate to structure in other studies of  $J_{\text{PP}}$  in metal complexes.<sup>70</sup> To obtain signs for our dataset, quantum chemical simulations were used (see SI for computational details). The absolute values of the computed  $J_{\text{PP}}$  trend linearly with the experimental values ( $J_{\text{PP}}^{\text{experimental}} = 0.913 |J_{\text{PP}}^{\text{computed}}| + 2.24$  Hz ;  $R^2 = 0.852$ ), indicating that the coupling can be computed with reasonably good accuracy.

2-bond couplings, such as the  $J_{PP}$  arising from the through-Ni coupling pathway, are expected to have a negative sign.<sup>47,70,89,90</sup> Simulations show that this is not always true for Ni bidentate phosphine complexes, with many complexes having positive  $J_{PP}$  (Figure 2.3). Generally, the 3C complexes have more negative  $J_{PP}$  than 2C complexes by  $\sim 40$  Hz, and Ni<sup>II</sup> complexes have more negative  $J_{PP}$  than Ni<sup>0</sup> by  $\sim 60$  Hz regardless of linker length. The observation that Ni<sup>II</sup> complexes have more negative  $J_{PP}$  than Ni<sup>0</sup> regardless of linker length appears to contrast with the relationships observed with  $|J_{PP}|$ , where 2C complexes had the *smallest*  $|J_{PP}|$  for Ni<sup>II</sup>, and 3C complexes had the *largest*  $|J_{PP}|$  for Ni<sup>II</sup> (Figure 2.2). These differences between  $J_{PP}$  and  $|J_{PP}|$  become consistent when recognizing that a more negative  $J_{PP}$  results in smaller  $|J_{PP}|$  when  $J_{PP}$  is positive, and larger  $|J_{PP}|$  when  $J_{PP}$  is negative. Therefore  $|J_{PP}|$  is largest when both linker length and oxidation state are associated with the same shift in  $J_{PP}$ , such as in 2C Ni<sup>0</sup> complexes (both shift  $J_{PP}$  more positive) and 3C Ni<sup>II</sup> complexes (both shift  $J_{PP}$  more negative), explaining the odd relationship between  $J_{PP}$ , linker, and oxidation state derived from Figure 1. To relate the effects of structure and oxidation state on  $J_{PP}$ , the sign of a measured  $|J_{PP}|$  therefore needs to be considered (vide infra).

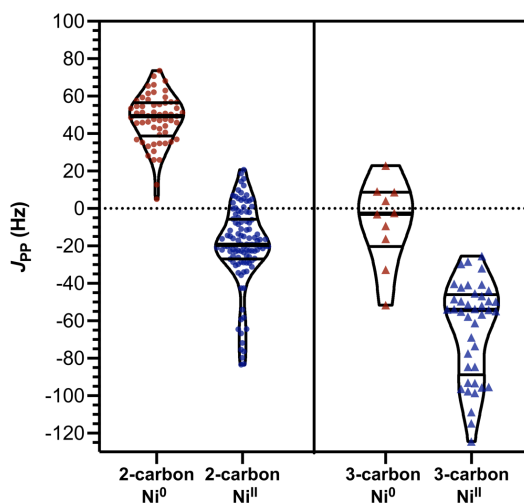


**Figure 2.3** Violin plots showing distributions of computed  $J_{PP}$  for different Ni oxidation states (Ni<sup>0</sup>, Ni<sup>II</sup>) and phosphine linker lengths (2-carbon, 3-carbon). Bold lines represent medians, fine lines represent 25<sup>th</sup> and 75<sup>th</sup> percentiles.



After identifying that  $J_{PP}$  correlates with ligand structure and oxidation state, an explanation is still needed to answer why  $J_{PP}$  becomes more negative upon oxidation from Ni<sup>0</sup> to Ni<sup>II</sup> or upon increasing the linker length from 2C to 3C. Given the observed dependence of  $|J_{PP}|$  on linker length and oxidation state,  $J_{PP}$  may be described as

### Equation 2.1

$$J_{PP} = {}^2J_{PP} + {}^{m+1}J_{PP}$$

Where the  ${}^2J_{PP}$  term arises from coupling through-Ni, and the  ${}^{m+1}J_{PP}$  term arises from through-linker coupling ( $m$  = number of carbons in the linker). The effect of changes in oxidation state and linker length on the values of through-Ni and through-linker coupling was therefore explored further with this model in mind.

## 2.4 Effects of Ligand Donation on $J_{PP}$

$J$ -coupling links pairs of nuclei through bonding electrons,<sup>52</sup> so it is expected that changes to the electron density in bonds along the coupling pathway can affect  $J$ . This dependence is evidenced by the electronic effects observed for many  ${}^2J_{HH}$  and  ${}^2J_{CH}$  couplings.<sup>59,91</sup> For Ni bidentate phosphine complexes, the  ${}^2J_{PP}$  (i.e., through-Ni) coupling term in equation 1 would likely depend on the electron density in the P–Ni bonds. Therefore, charge transfer analysis using absolutely localized molecular orbitals<sup>92–95</sup> was used to understand P–Ni bonds, including the effects of P-donation and backbonding (see Appendix 2 for computational details).

Charge transfer analysis showed a strong correlation of  $J_{PP}$  with the  $\sigma$ -bonding P-to-Ni charge transfer ( $CT_{P\text{-to-Ni}}$ ) (Figure 2.4), whereas the backbonding Ni-to-P charge transfer showed worse correlation with  $J_{PP}$  (Figure A1.13). The relationship of  $J_{PP}$  with the  $CT_{P\text{-to-Ni}}$  indicates that

$J_{PP}$  should become more negative with increased charge donated to Ni. Notably, the slopes of the 2C and 3C lines of best fit do not differ significantly (p-value = 0.3066), indicating that  $CT_{P-to-Ni}$  is independent of the linker length. This independence of  $CT_{P-to-Ni}$  on linker length signifies that P-to-Ni charge transfer solely affects the through-Ni  ${}^2J_{PP}$  term in equation 1. In principle, increased P-to-Ni donation can arise from increasing Lewis basicity of P, increasing Lewis acidity of Ni, or increasing overlap of Ni and P orbitals. The relationship between  $J_{PP}$  and P-to-Ni charge transfer also provides rationale for why  $J_{PP}$  varies with oxidation state, because  $Ni^{II}$  is generally more Lewis acidic than  $Ni^0$ , inducing more charge donation from P atoms.

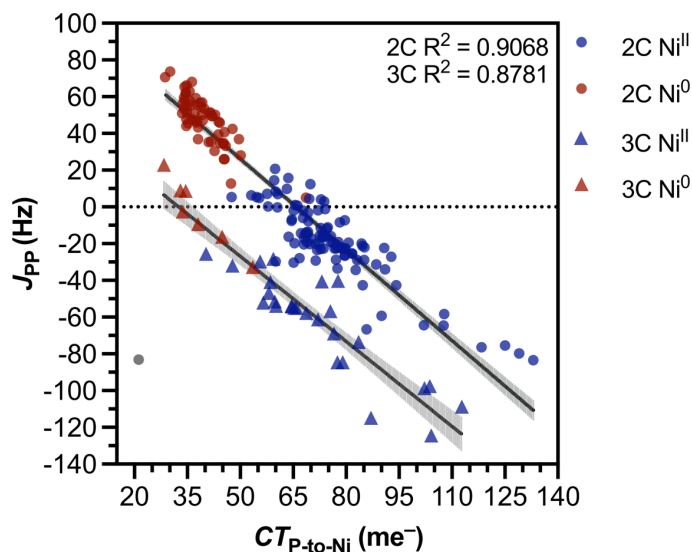


**Figure 2.4** Plot of  $J_{PP}$  versus P-to-Ni charge transfer with regression lines shown in black. 2C line of best fit:  $J_{PP} = -1.648 \text{ Hz/me}^- CT_{P-to-Ni} + 108.6 \text{ Hz}$ . 3C line of best fit:  $J_{PP} = -1.542 \text{ Hz/me}^- CT_{P-to-Ni} + 50.22 \text{ Hz}$ . Grey areas indicate the 95% confidence interval for lines of best fit. A single outlier, complex 2-2329, is shown as a grey circle and was excluded from the analysis.

While  $J_{PP}$  trends with P-to-Ni charge transfer, the physical origin of this dependence needed further elucidation. According to Ramsey,  $J$ -coupling occurs via four different mechanisms.<sup>52</sup> The Fermi contact mechanism is the dominant  $J$ -coupling mechanism for  $J_{PP}$  in other compounds<sup>96,97</sup> and was therefore expected to be dominant for complexes in our dataset.

Indeed, calculations of the four different Ramsey contributors to  $J_{PP}$  indicated that the Fermi contact contribution dominated the total  $J_{PP}$  (see SI). In the Fermi contact mechanism,  $J$ -coupling arises via spin-pairing of  $s$  electrons with a nucleus due to their non-zero electron density at the nuclei of atoms.<sup>89,52</sup> Given this, and the high  $3s$  character of the lone pairs of trivalent P atoms, it follows that the value of  $J_{PP}$  should be strongly affected by the donation of P lone pairs into Ni.

This relationship between  $J_{PP}$  and  $CT_{P-to-Ni}$  tracks with the presence of electron withdrawing groups on ligands *trans* to P atoms, likely by affecting the Lewis acidity of Ni. Structurally related Ni<sup>II</sup> complexes that differ by the number (e.g., **2-2025**, **2-2057**, **2-2087**) or strength (e.g., **2-2046e**, **2-2056**, **2-2035**)<sup>98</sup> of withdrawing groups on the *trans* ligands demonstrate this relationship between  $CT_{P-to-Ni}$  and  $J_{PP}$  (Figure 2.5), with complexes containing more withdrawing groups having more negative  $J_{PP}$  and larger  $|J_{PP}|$ . Complexes of Ni<sup>0</sup> (e.g., **2-2046d**, **2-2046f**, **2-2291**) also exhibit the trend of more negative  $J_{PP}$  with increased withdrawing groups on the *trans* ligand, but because Ni<sup>0</sup> complexes generally have positive  $J_{PP}$ , this manifests as a less positive  $J_{PP}$  and smaller  $|J_{PP}|$ .

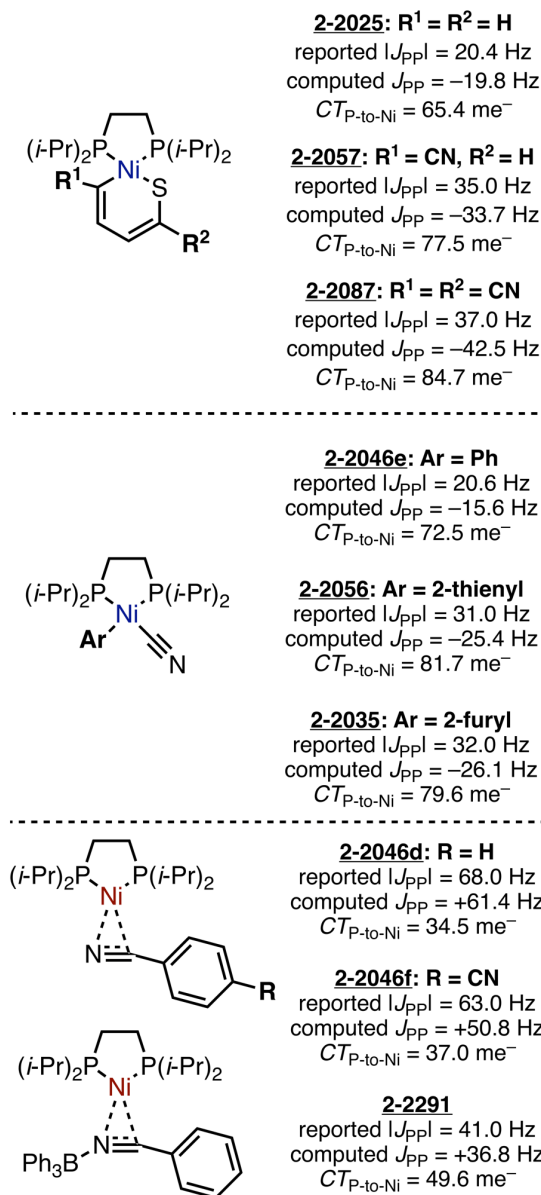


**Figure 2.5** Three series of complexes that differ by identity of *trans* ligands.

The relationship between  $J_{PP}$  and  $CT_{P-to-Ni}$  also tracks with the donating ability of the phosphine ligand (e.g., **2-2110** and **2-2296** of Figure 2.6), with more-donating phosphines<sup>99</sup> causing more negative  $J_{PP}$ . However, for complexes with large phosphines,  $J_{PP}$  were less negative and  $CT_{P-to-Ni}$  values were smaller than that of similar complexes with smaller phosphines. This trend is opposite of what is expected, given that large alkyl substituents (like *tert*-butyl) are more electron-rich than smaller alkyl substituents and should therefore impart larger P-to-Ni charge

transfer. This deviation might arise from the increased steric bulk of large ligands, causing P–Ni bonds to elongate, as observed in comparing complexes **2-2020** and **2-2143c** (Figure 2.6). The increased P–Ni bond length in complexes containing sterically bulky ligands may cause a decrease in the effective overlap of P and Ni orbitals, causing lower  $CT_{P-to-Ni}$  and less negative  $J_{PP}$  than expected based on the Lewis structure.

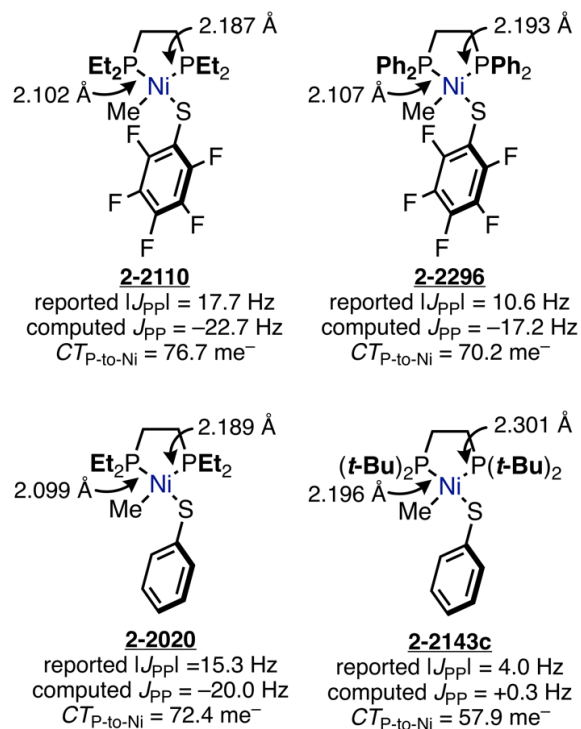


**Figure 2.6** A series of structurally similar complexes with varied phosphine and trans ligands.

While the effect of P-to-Ni charge transfer on  $J_{PP}$  is useful for understanding NMR spectra of Ni bidentate phosphine complexes, the trends observed with P-to-Ni charge transfer do not explain the differences in  $J_{PP}$  for 2C compared to 3C complexes. This limitation is evidenced by the ranges of  $CT_{P-to-Ni}$ , which span similar values for 2C complexes (28.2–133.0 me<sup>-</sup>) as 3C complexes (28.4–112.8 me<sup>-</sup>), but have trendlines with significantly different y-intercepts (p-value < 0.0001). Based on equation 1, the negative shift of  $J_{PP}$  of 3C complexes compared to 2C complexes may arise from differences in the through-linker  $^{m+1}J_{PP}$  coupling due to the difference

in linker identity. Alternatively, the negative shift of  $J_{PP}$  of 3C complexes may be due to the through-Ni  ${}^2J_{PP}$  term, most likely due to differences in P–Ni–P bite angle caused by the linker.

## 2.5 Effect of Linker Length on $J_{PP}$

Many  ${}^2J$ -coupling constants are dependent on the bond angle at the central atom,<sup>100,101</sup> therefore the relationship of  $J_{PP}$  with P–Ni–P bite angle was evaluated. If the linker affects the  $J_{PP}$  via the through-Ni ( ${}^2J_{PP}$ ) coupling term in equation 1, there would be a clear dependence of  $J_{PP}$  on bite angle. However, low correlation was observed between  $J_{PP}$  and bite angle for the combined datasets (Figure A1.17). The poor correlations of  $J_{PP}$  with bite angle indicates that the linker does not affect the through-Ni  ${}^2J_{PP}$  coupling term. This finding suggests that differences in  $J_{PP}$  between 2C and 3C complexes instead arise from differences in the through linker  ${}^{m+1}J_{PP}$  coupling terms in equation 1.

The through-linker  ${}^{m+1}J_{PP}$  coupling describes  ${}^3J_{PP}$  and  ${}^4J_{PP}$  for the 2C and 3C complexes respectively, which should obey Karplus-type relationships that depend on the linker geometry.<sup>100,102</sup> The range of  ${}^3J_{PP}$  values for complexes in the 2C dataset is expected to be small because there is little conformational flexibility available to bidentate ligands with such short linkers when bound to metals.<sup>103</sup> Similarly, the range of  ${}^4J_{PP}$  values is expected to be small, and therefore the average values of  ${}^{m+1}J_{PP}$  are sufficient for equation 2.1 to be useful.

With these considerations in mind, a 3-parameter model was found to be sufficient to describe  $J_{PP}$  for 2C and 3C complexes. The best-fit for the three parameters (one slope, one intercept, and one correction for 3C linkers) together enable equation 2.1 to become

### Equation 2.2

$$J_{PP} = -1.594 \text{ Hz/me}^{-} (CT_{P\text{-to-Ni}}) + 105.2 \text{ Hz} + L$$

$$L = \begin{cases} 0 \text{ Hz} & \text{for 2C complexes} \\ -48.47 \text{ Hz} & \text{for 3C complexes} \end{cases}$$

Where  $CT_{P\text{-to-Ni}}$  is the numerical value of charge transfer from P to Ni from a charge transfer analysis, and  $L$  is a parameter that describes the difference in average through-linker  $^{m+1}J_{PP}$ . Equation 2.2 shows a good  $R^2 = 0.9267$ , and RMS error = 11.8 Hz for the combined dataset of 203 complexes for which  $J_{PP}$  and  $CT_{P\text{-to-Ni}}$  values could be calculated (Figure 2.7).

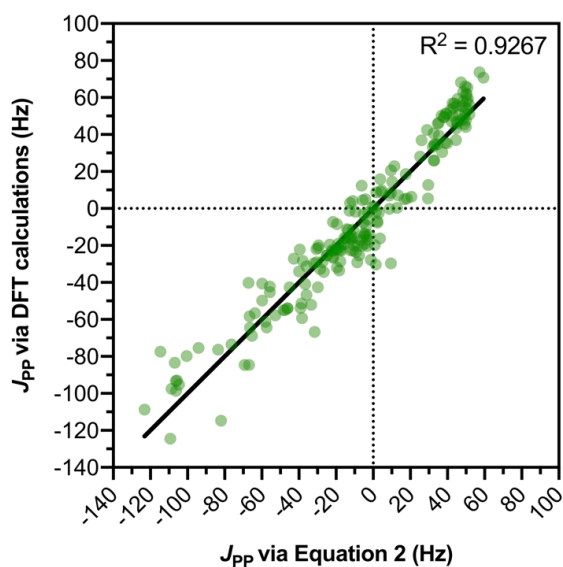


**Figure 2.7** Parity plot comparing values of  $J_{PP}$  computed from DFT calculations to the  $J_{PP}$  predicted by equation 2. Slope = 1.00, Y-intercept = 0.00 Hz.

## 2.6 Implication for the Analysis of $^{31}\text{P}$ NMR Spectra

Equation 2.2 can be used to interpret  $^{31}\text{P}$  NMR spectra of Ni bidentate phosphine complexes, even when the sign of  $J_{PP}$  is not directly available through measurements. For example, in the case where quantum chemical simulations are available, a computed value of  $CT_{P\text{-to-Ni}}$  can be used within equation 2.2 to find  $J_{PP}$ , for comparison to  $|J_{PP}|$  observed in spectra. Except for  $|J_{PP}|$

$\lesssim 10$  Hz, where the sign would be ambiguous, the sign will be apparent if the absolute value of the computed  $J_{PP}$  for the simulated Ni complex is near the experimentally observed  $|J_{PP}|$ .

Further utility of equation 2.2 comes from its description of the behavior of  $J_{PP}$ . The negative dependence of  $J_{PP}$  on P-to-Ni charge transfer enables one to deduce the sign of  $J_{PP}$  in a series of Ni bidentate phosphine complexes with varying ligand electronics. For example, for a sequence of Ni bidentate phosphine complexes with varying P-donating ability, 1-D  $^{31}\text{P}$  NMR spectroscopy will give a series of  $J_{PP}$  values. If  $|J_{PP}|$  increases as phosphine ligands become more donating, the observed  $J_{PP}$  values are likely negative. If  $|J_{PP}|$  decreases with more-donating phosphines, the  $J_{PP}$  values are likely positive. A similar screen can be performed by keeping the phosphine ligand the same and incorporating withdrawing groups on the *trans* ligands, because more negative  $J_{PP}$  is expected for increased withdrawing ability of *trans* ligands. Once the sign is deduced, the trends in Figure 2.3 suggest that the sign of  $J_{PP}$  can be used to make an oxidation state assignment. Given the complexities involved in determining the sign of  $J_{PP}$  via NMR spectroscopy, this approach—while indirect—may prove to be the simplest option in many cases. Additionally, the incorporation of a term (i.e.,  $L$ ) accounting for differences in through linker coupling may enable description of other complexes with varied linker lengths or linker identities, such as BINAP<sup>104</sup> and SPIRAP,<sup>105</sup> provided a value of  $L$  can be determined for the linker.

## 2.7 Conclusion and Outlook

### 2.7.1 Broadly Relating to Coordination Complexes

$J_{PP}$  is a convenient NMR parameter for elucidating the structure of Ni bidentate phosphine complexes. For 2C complexes,  $|J_{PP}| < 30$  Hz and  $|J_{PP}| > 40$  Hz are indicative of Ni<sup>II</sup> and Ni<sup>0</sup> respectively, while the reverse is true for 3C complexes. This seemingly odd relationship between  $|J_{PP}|$ , oxidation state, and linker length becomes more easily understood after examining *signed*



$J_{PP}$ , where a more negative  $J_{PP}$  is observed with the higher oxidation state for both linker lengths. The relationships between  $CT_{P-to-Ni}$  and  $J_{PP}$  will enable assignment of the sign of  $J_{PP}$  by examining how the  $|J_{PP}|$  changes with structures that induce P-to-Ni donation. Alternatively, at least for complexes that are structurally similar to any of the 232 complexes of the present dataset, the sign may be elucidated by comparison to the  $J_{PP}$  values listed in tables S4 and S5 of the SI.

Given the ease of obtaining  $^{31}P$  NMR spectra of reaction mixtures, the correlations between  $J_{PP}$  and ligand electronics are expected to be useful for identifying reaction intermediates *in situ*. Similar relationships of  $J_{PP}$  with charge transfer are likely present in other phosphine complexes, but more analysis will be needed to understand the effects of metal identity or metal geometry. Put together, these insights should enable a deeper understanding into the structure and properties of key intermediates in reactions of Ni bidentate phosphine complexes.

### ***2.7.2 Specifically Relating to Complexes in Catalyst-Transfer Polymerization***

Although *in situ* analysis involving  $J_{PP}$  values is likely to be useful for a variety of fields, *in-situ* methods for oxidation state assignment for are particularly useful for catalyst-transfer polymerization (CTP). Ni bidentate phosphine complexes are highly used in CTP, and due to the difficulties in characterizing, isolating, or even observing polymeric organometallic species, it can be difficult to understand the mechanism of a CTP reaction.  $J_{PP}$  analyses described in this work may therefore be useful for CTP because  $J_{PP}$  can be measured *in situ* and because its dependence on oxidation state and ligand properties enables some capacity for structural assignment based on  $J_{PP}$ . Given that other types of polymerization catalysts are also used in CTP (such as Ni complexes with diimine or carbene ligands, and Pd complexes with phosphine and carbene ligands)  $J_{PP}$  analysis is not suitable for all CTP reactions. Future investigations into *in-situ* analysis of cross-coupling catalysts could therefore focus on identifying other  $J$ -coupling constants that can aide in

structure determination. For example,  $^1J_{\text{Pd-C}}$  coupling constants likely have a dependence on the oxidation state of Pd, and  $J_{\text{NN}}$  for Ni diimine complexes may have similar dependence on oxidation state and ligand properties given the coupling pathway through the Ni. No matter what the method, we expect the development of a greater variety of in-situ analytical models for understanding structure and properties of organometallic Ni and Pd complexes will be highly useful for analysis of CTP reactions. We encourage others to investigate such methods for more facile analysis of the intermediates of polymerization reactions.

## 2.8 References

- <sup>1</sup> Clevenger, A. L.; Stolley, R. M.; Aderibigbe, J.; Louie, J. Trends in the Usage of Bidentate Phosphines as Ligands in Nickel Catalysis *Chem. Rev.* **2020**, *120*, 6124–6196.
- <sup>2</sup> Hartwig, J. F. *Organotransition Metal Chemistry: From Bonding to Catalysis*; University Science Books: California, 2010; pp 324.
- <sup>3</sup> Tamao, K.; Sumitani, K.; Kumada, M. Selective Carbon-Carbon Bond Formation by Cross-Coupling of Grignard Reagents with Organic Halides. Catalysis by Nickel-Phosphine Complexes *J. Am. Chem. Soc.* **1972**, *94*, 4374–4376.
- <sup>4</sup> Taylor, B. L. H.; Swift, E. C.; Waetzig, J. D.; Jarvo, E. R. Stereospecific Nickel-Catalyzed Cross-Coupling Reactions of Alkyl Ethers: Enantioselective Synthesis of Diarylethanes. *J. Am. Chem. Soc.* **2011**, *133*, 389–391.
- <sup>5</sup> Erickson, L. W.; Lucas, E. L.; Tollefson, E. J.; Jarvo, E. R. Nickel Catalyzed Cross-Electrophile Coupling of Alkyl Fluorides: Stereospecific Synthesis of Vinylcyclopropanes. *J. Am. Chem. Soc.* **2016**, *138*, 14006–14011.
- <sup>6</sup> Tollefson, E. J.; Dawson, D. D.; Osborne, C. A.; Jarvo, E. R. Stereospecific Cross-Coupling Reactions of Aryl-Substituted Tetrahydrofurans, Tetrahydropyrans, and Lactones. *J. Am. Chem. Soc.* **2014**, *136*, 14951–14958.
- <sup>7</sup> Dawson, D. D.; Jarvo, E. R. Stereospecific Nickel-Catalyzed Cross-Coupling Reactions of Benzylic Ethers with Isotopically-Labeled Grignard Reagents. *Org. Process Res. Dev.* **2015**, *19*, 1356–1359.
- <sup>8</sup> Taylor, B. L. H.; Harris, M. R.; Jarvo, E. R. Synthesis Of Enantioenriched Triarylmethanes By Stereospecific Cross-Coupling Reactions. *Angew. Chem., Int. Ed.* **2012**, *51*, 7790–7793.
- <sup>9</sup> Nomura, N.; Rajanbabu, T. V. Nickel-Catalyzed Asymmetric Allylation Of Alkyl Grignard Reagents. Effect Of Ligands, Leaving Groups And A Kinetic Resolution With A Hard Nucleophile. *Tetrahedron Lett.* **1997**, *38*, 1713–1716.
- <sup>10</sup> Soni, V.; Sharma, D. M.; Punji, B. Nickel-Catalyzed Regioselective C(2)-H Difluoroalkylation of Indoles with Difluoroalkyl Bromides. *Chem. Asian J.* **2018**, *13*, 2516–2521.
- <sup>11</sup> Guan, B.-T.; Xiang, S.-K.; Wang, B.-Q.; Sun, Z.-P.; Wang, Y.; Zhao, K.-Q.; Shi, Z.-J. Direct Benzylic Alkylation via Ni-Catalyzed Selective Benzylic sp<sup>3</sup> C-O Activation. *J. Am. Chem. Soc.* **2008**, *130*, 3268–3269.
- <sup>12</sup> Han, F. S. Transition-Metal-Catalyzed Suzuki–Miyaura Cross-Coupling Reactions: A Remarkable Advance From Palladium To Nickel Catalysts. *Chem. Soc. Rev.* **2013**, *42*, 5270–5298.
- <sup>13</sup> Kuwano, R.; Shimizu, R. An Improvement of Nickel Catalyst For Cross-Coupling Reaction of Aryl Boronic Acids With Aryl Carbonates by Using a Ferrocenyl Bisphosphine Ligand. *Chem. Lett.* **2011**, *40*, 913–915.
- <sup>14</sup> Trost, B. M.; Spagnol, M. D. Nickel Catalyzed Coupling of Allylamines and Boronic Acids. *J. Chem. Soc., Perkin Trans. 1* **1995**, 2083–2096.
- <sup>15</sup> Li, Y.; Wang, K.; Ping, Y.; Wang, Y.; Kong, W. Nickel-Catalyzed Domino Heck Cyclization/Suzuki Coupling for the Synthesis of 3,3- Disubstituted Oxindoles. *Org. Lett.* **2018**, *20*, 921–924.
- <sup>16</sup> Okuda, Y.; Xu, J.; Ishida, T.; Wang, C.-A.; Nishihara, Y. Nickel-Catalyzed Decarbonylative Alkylation of Aroyl Fluorides Assisted by Lewis-Acidic Organoboranes. *ACS Omega* **2018**, *3*, 13129–13140.

- 
- <sup>17</sup> Zhao, Y.-L.; Li, Y.; Li, Y.; Gao, L.-X.; Han, F.-S. Aryl Phosphoramides: Useful Electrophiles for Suzuki-Miyaura Coupling Catalyzed by a NiCl<sub>2</sub>/dppp System (dppp = 1,3-bis-(diphenylphosphino)propane). *Chem. Eur. J.* **2010**, *16*, 4991–4994.
- <sup>18</sup> Zeng, Z.; Yang, D.; Long, Y.; Pan, X.; Huang, G.; Zuo, X.; Zhou, W. Nickel-Catalyzed Asymmetric Ring Opening of Oxabenzonorborenes with Arylboronic Acids. *J. Org. Chem.* **2014**, *79*, 5249–5257.
- <sup>19</sup> Hu, F.; Lei, X. A Nickel Precatalyst for Efficient Cross-Coupling Reactions of Aryl Tosylates with Aryl Boronic Acids: Vital Role of dppf. *Tetrahedron* **2014**, *70*, 3854–3858.
- <sup>20</sup> Sylvester, K. T.; Wu, K.; Doyle, A. G. Mechanistic Investigation of the Nickel-Catalyzed Suzuki Reaction of N,O-Acetals: Evidence for Boronic Acid Assisted Oxidative Addition and an Iminium Activation Pathway. *J. Am. Chem. Soc.* **2012**, *134*, 16967–16970.
- <sup>21</sup> Johnson, J. B.; Yu, R. T.; Fink, P.; Bercot, E. A.; Rovis, T. Selective Substituent Transfer from Mixed Zinc Reagents in Ni Catalyzed Anhydride Alkylation. *Org. Lett.* **2006**, *8*, 4307–4310.
- <sup>22</sup> Tarui, A.; Shinohara, S.; Sato, K.; Omote, M.; Ando, A. Nickel Catalyzed Negishi Cross-Coupling of Bromodifluoroacetamides. *Org. Lett.* **2016**, *18*, 1128–1131.
- <sup>23</sup> Yu, D.; Wang, C.-S.; Yao, C.; Shen, Q.; Lu, L. Nickel-Catalyzed  $\alpha$ -Arylation of Zinc Enolates with Polyfluoroarenes via C-F Bond Activation under Neutral Conditions. *Org. Lett.* **2014**, *16*, 5544–5547.
- <sup>24</sup> Yamamoto, T.; Yamakawa, T. Nickel-Catalyzed Vinylation of Aryl Chlorides and Bromides with Vinyl ZnBr·MgBrCl. *J. Org. Chem.* **2009**, *74*, 3603–3605.
- <sup>25</sup> Melzig, L.; Metzger, A.; Knochel, P. Room Temperature Crosscoupling of Highly Functionalized Organozinc Reagents with Thiomethylated N-heterocycles by Nickel Catalysis. *J. Org. Chem.* **2010**, *75*, 2131–2133.
- <sup>26</sup> Wisniewska, H. M.; Swift, E. C.; Jarvo, E. R. Functional-Group Tolerant, Nickel-Catalyzed Cross-Coupling Reaction for Enantioselective Construction of Tertiary Methyl-Bearing Stereocenters. *J. Am. Chem. Soc.* **2013**, *135*, 9083–9090.
- <sup>27</sup> Gavryushin, A.; Kofink, C.; Manolikakes, G.; Knochel, P. An Efficient Negishi Cross-Coupling Reaction Catalyzed by Nickel(II) and Diethyl Phosphite. *Tetrahedron* **2006**, *62*, 7521–7533.
- <sup>28</sup> Metzger, A.; Melzig, L.; Knochel, P. Scaled-up Transition-Metal Catalyzed Cross-Coupling Reactions of Thioether-Substituted N-Heterocycles with Organozinc Reagents. *Synthesis* **2010**, 2853–2858.
- <sup>29</sup> Melzig, L.; Dennenwaldt, T.; Gavryushin, A.; Knochel, P. Direct Aminoalkylation of Arenes, Heteroarenes, and Alkenes via Ni Catalyzed Negishi Cross-Coupling Reactions. *J. Org. Chem.* **2011**, *76*, 8891–8906.
- <sup>30</sup> Melzig, L.; Metzger, A.; Knochel, P. Pd- and Ni-Catalyzed Cross-Coupling Reactions of Functionalized Organozinc Reagents with Unsaturated Thioethers. *Chem. Eur. J.* **2011**, *17*, 2948–2956.
- <sup>31</sup> Shirakawa, E.; Yamasaki, K.; Hiyama, T. Nickel-Catalyzed Cross Coupling Reactions of Aryl Halides with Organostannanes. *J. Chem. Soc., Perkin Trans. 1* **1997**, *1*, 2449–2450.
- <sup>32</sup> Clark, J. S. K.; McGuire, R. T.; Lavoie, C. M.; Ferguson, M. J.; Stradiotto, M. Examining the Impact of Heteroaryl Variants of PdAdPhos on Nickel-Catalyzed C(sp<sup>2</sup>)-N Cross-Couplings. *Organometallics* **2019**, *38*, 167–175.
- <sup>33</sup> Clark, J. S. K.; Voth, C. N.; Ferguson, M. J.; Stradiotto, M. Evaluating 1,1'-Bis(phosphino)ferrocene Ancillary Ligand Variants in the Nickel-Catalyzed C-N Cross-Coupling of (Hetero)aryl Chlorides. *Organometallics* **2017**, *36*, 679–686.

- 
- <sup>34</sup> Iwai, T.; Harada, T.; Shimada, H.; Asano, K.; Sawamura, M. A Polystyrene-Cross-Linking Bisphosphine: Controlled Metal Monochelation and Ligand-Enabled First-Row Transition Metal Catalysis. *ACS Catal.* **2017**, *7*, 1681–1692.
- <sup>35</sup> Omar-Amrani, R.; Thomas, A.; Brenner, E.; Schneider, R.; Fort, Y. Efficient Nickel-Mediated Intramolecular Amination of Aryl Chlorides. *Org. Lett.* **2003**, *5*, 2311–2314.
- <sup>36</sup> Harada, T.; Ueda, Y.; Iwai, T.; Sawamura, M. Nickel-Catalyzed Amination of Aryl Fluorides with Primary Amines. *Chem. Commun.* **2018**, *54*, 1718–1721.
- <sup>37</sup> Ackermann, L.; Song, W.; Sandmann, R. Nickel-Catalyzed, Base Mediated Amination/Hydroamination Reaction Sequence for a Modular Synthesis of Indoles. *J. Organomet. Chem.* **2011**, *696*, 195–201.
- <sup>38</sup> Pawlas, J.; Nakao, Y.; Kawatsura, M.; Hartwig, J. F. A General Nickel-Catalyzed Hydroamination of 1,3-Dienes by Alkylamines: Catalyst Selection, Scope, and Mechanism. *J. Am. Chem. Soc.* **2002**, *124*, 3669–3679.
- <sup>39</sup> Green, R. A.; Hartwig, J. F. Nickel-Catalyzed Amination of Aryl Chlorides with Ammonia or Ammonium Salts. *Angew. Chem. Int. Ed.* **2015**, *54*, 3768–3772.
- <sup>40</sup> Borzenko, A.; Rotta-Loria, N. L.; MacQueen, P. M.; Lavoie, C. M.; McDonald, R.; Stradiotto, M. Nickel-Catalyzed Monoarylation of Ammonia. *Angew. Chem. Int. Ed.* **2015**, *54*, 3773–3777.
- <sup>41</sup> Yang, P.; Zhang, C.; Ma, Y.; Zhang, C.; Li, A.; Tang, B.; Zhou, J. S. Nickel-Catalyzed N-Alkylation of Acylhydrazines and Arylamines Using Alcohols and Enantioselective Examples. *Angew. Chem. Int. Ed.* **2017**, *56*, 14702–14706.
- <sup>42</sup> Birkholz, M.-N.; Freixa, Z.; van Leeuwen, P. W. N. M. Bite angle effects of diphosphines in C-C and C-X bond forming cross coupling reactions. *Chem. Soc. Rev.* **2009**, *38*, 1099–1118.
- <sup>43</sup> Rosman, K. J. R.; Taylor, P. D. P Isotopic Compositions of The Elements 1997. *Pure Appl. Chem.* **1998**, *70*, 217–235.
- <sup>44</sup> Shriver, D. F.; Atkins, P. W.; Langford, C. H *Inorganic Chemistry*; Oxford University Press: New York, 1992, pp 212.
- <sup>45</sup> Bren, K. L. *NMR Analysis of Spin Densities*; Wiley-VCH: Hoboken, New Jersey 2015.
- <sup>46</sup> Payard, P.; Perego, L. A.; Grimauad, L.; Ciofini, I. A DFT Protocol for the Prediction of <sup>31</sup>P NMR Chemical Shifts of Phosphine Ligands in First-Row Transition-Metal Complexes. *Organometallics* **2020**, *39*, 3121–3130.
- <sup>47</sup> Kühl, O. *Phosphorus-31 NMR Spectroscopy*; Springer-Verlag, Berlin, 2008; pp 7–12, 16–22.
- <sup>48</sup> Pregosin, P. S.; Kunz, R. Coupling Constants in <sup>31</sup>P and <sup>13</sup>C NMR of Transition Metal Phosphine Complexes; *NMR Basic Principles and Progress Series*; Springer-Verlag: Berlin, 1979; pp 16–46.
- <sup>49</sup> Carlson, A. W.; Primka, D. A.; Douma, E. D.; Bowering, M. A. Evaluation of Air-Free Glassware Using the Ketyl Test. *Dalton Trans.* **2020**, *49*, 15213–15218.
- <sup>50</sup> Air-tolerance and moisture-tolerance of NMR primarily derives from the ability to prepare samples in air and moisture free environments, such as on a nitrogen line or in a glovebox. Air-free NMR tubes, such as J. Young tubes, have been shown to be air-tight for days, such as in ref 50, far longer than the time scale of most NMR spectroscopies.
- <sup>51</sup> Pregosin, P. S. *NMR in Organometallic Chemistry*; Wiley-VCH: Weinheim, 2012; pp 258–264.
- <sup>52</sup> Ramsey, N. F. Electron Coupled Interactions between Nuclear Spins in Molecules. *Phys. Rev.* **1953**, *91*, 303–307.
- <sup>53</sup> Fraser, R. R.; Lemieux, R. V.; Stevens, J. D. Opposite Relative Signs of Geminal and Vicinal Proton-Proton Coupling Constants in Saturated Organic Molecules. *J. Am. Chem. Soc.* **1961**, *83*, 3901–3902.

- 
- <sup>54</sup> Finegold, H. Signs of Nuclear Resonance Coupling Constants in Saturated Aliphatic Systems. *Proc. Chem. Soc.* **1962**, 213–214.
- <sup>55</sup> Karplus, M. Comments on The Signs of Proton Coupling Constants. *J. Am. Chem. Soc.* **1962**, *84*, 2458–2460.
- <sup>56</sup> Freeman, R.; Bhacca, N. S. Relative Signs of Nuclear Spin Coupling Constants: A Refinement of the Double Irradiation Experiment *J. Chem. Phys.* **1963**, *38*, 1088–1093.
- <sup>57</sup> Freeman, R.; McLauchlan, K. A.; Musher, J. I.; Pachler, K. G. R. The Relative Signs of Geminal and Vicinal Proton Spin Coupling Constants. *Mol. Phys.* **1962**, *5*, 321–327.
- <sup>58</sup> Kaplan, F.; Roberts, J. D. Nuclear Magnetic Resonance Spectroscopy. Abnormal Splitting of Ethyl Groups Due to Molecular Asymmetry. *J. Am. Chem. Soc.* **1961**, *83*, 4666–4668.
- <sup>59</sup> Cookson, R. C.; Crabb, T. J.; Frankel, J. J.; Hudec, J. Geminal Coupling Constants in Methylene Groups. *Tetrahedron* **1996**, *22*, 355–390
- <sup>60</sup> Karplus, M. Vicinal Proton Coupling in Nuclear Magnetic Resonance. *J. Am. Chem. Soc.* **1963**, *85*, 2870–2871.
- <sup>61</sup> Thureau, P.; Carvin, I.; Ziarelli, F.; Viel, S.; Mollica, G. A Karplus Equation for the Conformational Analysis of Organic Molecular Crystals. *Angew. Chem. Int. Ed.* **2019**, *58*, 16047–16051
- <sup>62</sup> Thibaudeau, C.; Plavec, J.; Chattopadhyaya, J. A New Generalized Karplus-Type Equation Relating Vicinal Proton-Fluorine Coupling Constants to H-C-C-F Torsion Angles. *J. Org. Chem.* **1998**, *63*, 4967–4984.
- <sup>63</sup> Fukada, Y.; Mayamae, K.; Sasanuma, Y. Computational Design of Polymers: Poly(Esteramide) and Polyurethane. *RSC Advances* **2017**, *7*, 38387–38398.
- <sup>64</sup> Stangler, T.; Hartmann, R.; Willbold, D.; Koenig, B. W. Modern High Resolution NMR for the Study of Structure, Dynamics and Interactions of Biological Macromolecules. *Z. Phys. Chem.* **2009**, *220*, 567–613.
- <sup>65</sup> Bystrov, V. F. Spin—Spin Coupling and the Conformational States Of Peptide Systems. *Prog. Nuc. Mag. Reson. Spectrosc.* **1976**, *10*, 41–82.
- <sup>66</sup> Lee, J. H.; Li, F.; Grishaev, A.; Bax, A. Quantitative Residue-Specific Protein Backbone Torsion Angle Dynamics from Concerted Measurement of  $^3J$  Couplings. *J. Am. Chem. Soc.* **2015**, *137*, 1432–1435.
- <sup>67</sup> Wang, A.; Bax, A. Determination of the Backbone Dihedral Angles  $\phi$  in Human Ubiquitin from Reparametrized Empirical Karplus Equations. *J. Am. Chem. Soc.* **1996**, *118*, 2483–2494.
- <sup>68</sup> J. G. Verkade Spectroscopic Studies of Metal-Phosphorus Bonding in Coordination Complexes. *Coord. Chem. Rev.* **1972**, *9*, 1, 1–106.
- <sup>69</sup> Bertrand, R. D.; Ogilvie, F. B.; Verkade, J. G. Signs of Phosphorus-Phosphorus Coupling Constants in Coordination Compounds. *J. Am. Chem. Soc.* **1970**, *92*, 1908–1915.
- <sup>70</sup> Fontaine, X. L. R.; Kennedy, J. D.; Shaw, B. L.; Vila, J. M. Determination of the Relative Signs of  $^2J(^{31}\text{P}-^{31}\text{P})$  in complexes of Tungsten(0) and Molebdenum(0) using Two-dimensional [ $^{31}\text{P}$ - $^{31}\text{P}$ ]-COSY-45 Nuclear Magnetic Resonance Chemical Shift Correlation. *J. Chem. Soc. Dalton. Trans.* **1987**, 2401–2405.
- <sup>71</sup> Lejkowski, M, L.; Lindner, R.; Kageyama, T.; Bódizs, G. É.; Plessow, P. N.; Müller, I. B.; Schäfer, A.; Rominger, F.; Hofmann, P.; Futter, C.; Schunk, S. A.; Limbach, M. The First Catalytic Synthesis of an Acrylate from CO<sub>2</sub> and an Alkene –A Rational Approach. *Chem. Eur. J.* **2012**, *18*, 14017–14025.

- 
- <sup>72</sup> Plessow, P. N.; Weigel, L.; Lindner, R.; Schäfer, A.; Rominger, F.; Limbach, M.; Hofmann, P. Mechanistic Details of the Nickel-Mediated Formation of Acrylates from CO<sub>2</sub>, Ethylene and Methyl Iodide. *Organometallics* **2013**, *32*, 3327–3338.
- <sup>73</sup> Garcia, J. J.; Brunkan, N. M.; Jones, W. D. Cleavage of Carbon–Carbon Bonds in Aromatic Nitriles Using Nickel(0). *J. Am. Chem. Soc.* **2002**, *124*, 9547–9555.
- <sup>74</sup> Garcia, J. J.; Jones, W. D. Reversible Cleavage of Carbon–Carbon Bonds in Benzonitrile Using Nickel(0). *Organometallics* **2000**, *19*, 5544–5545.
- <sup>75</sup> Waterman, R.; Hillhouse, G. L.  $\eta^2$ -Organoazide Complexes of Nickel and Their Conversion to Terminal Imido Complexes via Dinitrogen Extrusion. *J. Am. Chem. Soc.* **2008**, *130*, 12628–12629.
- <sup>76</sup> Mindiola, D. J.; Waterman, R.; Jenkins, D. M.; Hillhouse, G. L. Synthesis of 1,2-bis(di-tert-butylphosphino)ethane (dtbpe) Complexes of Nickel: Radical Coupling and Reduction Reactions Promoted by the Nickel(I) Dimer [(dtbpe)NiCl]<sub>2</sub>. *Inorg. Chim. Acta* **2003**, *345*, 299–308.
- <sup>77</sup> Ateşin, T. A.; Li, T.; Lachaize, S.; Brennessel, W. W.; García, J. J.; Jones, W. D. Experimental and Theoretical Examination of C–CN and C–H Bond Activations of Acetonitrile Using Zerovalent Nickel. *J. Am. Chem. Soc.* **2007**, *129*, 7562–7569.
- <sup>78</sup> Curley, J. J.; Kitiachvili, K. D.; Waterman, R.; Hillhouse, G. L. Sequential Insertion Reactions of Carbon Monoxide and Ethylene into the Ni–C Bond of a Cationic Nickel(II) Alkyl Complex. *Organometallics* **2009**, *28*, 2568–2571.
- <sup>79</sup> Desnoyer, A. N.; Bowes, E. G.; Patrick, B. O.; Love, J. A. Synthesis of 2-Nickela(II)oxetanes from Nickel(0) and Epoxides: Structure, Reactivity, and a New Mechanism of Formation. *J. Am. Chem. Soc.* **2015**, *137*, 12748–12751.
- <sup>80</sup> Desnoyer, A. N.; He, W.; Behyan, S.; Chiu, W.; Love, J. A.; Kennepohl, P. The Importance of Ligand-Induced Backdonation in the Stabilization of Square Planar d<sup>10</sup> Nickel  $\pi$ -Complexes. *Chem. Eur. J.* **2019**, *25*, 5259–5268.
- <sup>81</sup> Smith, M. L.; Leone, A. K.; Zimmerman, P. M.; McNeil, A. J. Impact of Preferential  $\pi$ -Binding in Catalyst-Transfer Polycondensation of Thiazole Derivatives. *ACS Macro Lett.* **2016**, *5*, 1411–1415.
- <sup>82</sup> Lanni, E. L.; McNeil, A. J. Mechanistic Studies on Ni(dppe)Cl<sub>2</sub>-Catalyzed Chain-Growth Polymerizations: Evidence for Rate-Determining Reductive Elimination. *J. Am. Chem. Soc.* **2009**, *131*, 16573–16579.
- <sup>83</sup> Willot, P.; Koeckelberghs, G. Evidence for Catalyst Association in the Catalyst Transfer Polymerization of Thieno[3,2-*b*]thiophene. *Macromolecules* **2014**, *47*, 8548–8555.
- <sup>84</sup> Reaxys. <https://www.reaxys.com/> (data retrieved on Dec 22, 2020).
- <sup>85</sup> Nett, A. J.; Cañellas, S.; Higuchi, Y.; Robo, M. T.; Kochkodan, J. M.; Haynes, M. T.; Kampf, J. W.; Montgomery, J. Stable, Well-Defined Nickel(0) Catalysts for Catalytic C–C and C–N Bond Formation. *ACS Catalysis* **2018**, *8*, 6606–6611.
- <sup>86</sup> Nattmann, L.; Saeb, R.; Nöthling, N.; Cornella, J. An Air-Stable Binary Ni(0)–Olefin Catalyst. *Nature Cat.* **2020**, *3*, 6–13.
- <sup>87</sup> Bilbrey, J. A.; Bootsma, A. N.; Bartlett, M. A.; Locklin, J.; Wheeler, S. E.; Allen, W. D. Ring-Walking of Zerovalent Nickel on Aryl Halides. *J. Chem. Theory Comput.* **2017**, *13*, 1706–1711.
- <sup>88</sup> D' Accriscio, F.; Ohleier, A.; Nicolas, E.; Demange, M.; Du Boullay, O. T.; Saffon-Merceron, N.; Fustier-Boutignon, M.; Rezabal, E.; Frison, G.; Nebra, N.; Mézailles, N. [(dcpp)Ni( $\eta^2$ -Arene)] Precursors: Synthesis, Reactivity, and Catalytic Application to the Suzuki–Miyaura Reaction. *Organometallics*, **2020**, *39*, 1688–1699.
- <sup>89</sup> Levitt, M. *Spin Dynamics: Basics of Nuclear Magnetic Resonance*; Wiley-VCH, 2008.

- 
- <sup>90</sup> Chalmers, B. A.; Nejman, P. S.; Llewellyn, A. V.; Felaar, A. M.; Griffiths, B. L.; Portman, E. I.; Gordon, E.-J. L.; Fan, K. J. H.; Woolins, J. D.; Bühl, M.; Malinka, O. L.; Cordes, D. B.; Salwin, A. M. Z.; Kilian, P. A Study of Through-Space and Through-Bond  $J_{PP}$  Coupling in a Rigid Nonsymmetrical Bis(phosphine) and its Metal Complexes. *Inorg. Chem.* **2018**, *57*, 3387–3398.
- <sup>91</sup> Pedersoli, S.; Tormena, C. F.; dos Santos, F. P.; Contreras, R. H.; Rittner, R. Stereochemical Behavior of  $^1J_{CH}$  and  $^2J_{CH}$  NMR Coupling Constants in  $\alpha$ -Substituted Acetamides. *J. Mol. Struct.* **2008**, *26*, 508–513.
- <sup>92</sup> Khaliullin, R. Z.; Cobar, E. A.; Lochan, R. C.; Bell, A. T.; Head-Gordon, M. Unravelling the Origin of Intermolecular Interactions Using Absolutely Localized Molecular Orbitals *J. Phys. Chem. A* **2007**, *111*, 8753–8765.
- <sup>93</sup> Horn, P. R.; Head-Gordon, M. Polarization contributions to intermolecular interactions revisited with fragment electric-field response functions. *J. Phys. Chem.* **2015**, *143*, 114111.
- <sup>94</sup> Khaliullin, R. Z.; Bell, A. T.; Head-Gordon, M. Analysis of charge transfer effects in molecular complexes based on absolutely localized molecular orbitals. *J. Chem. Phys.* **2008**, *128*, 184112.
- <sup>95</sup> Horn, P. R.; Mao, Y.; Head-Gordon, M. Probing non-covalent interactions with a second generation energy decomposition analysis using absolutely localized molecular orbitals *Phys. Chem. Chem. Phys.* **2016**, *18*, 23067.
- <sup>96</sup> Huynh, K.; Lough, A. J.; Forgeron, M. A. M.; Bendle, M.; Pressa Soto, A.; Wasylshen, R. E.; Manners, I. Synthesis and Reactivity of Phosphine-Stabilized Phosphoranimine Cations,  $[R_3P \cdot PR'_2NSiMe_3]^+$ . *J. Am. Chem. Soc.* **2009**, *131*, 7905–7916.
- <sup>97</sup> Burk, S.; Götz, K.; Kaupp, M.; Nieger, M.; Weber, J.; Günne, J. S.; Gudat, D. Diphosphines with Strongly Polarized P-P Bonds: Hybrids between Covalent Molecules and Donor-Acceptor Adducts with Flexible Molecular Structures. *J. Am. Chem. Soc.* **2009**, *131*, 10763–10774.
- <sup>98</sup>  $pK_a$  values of the parent arenes were used to quantify the withdrawing strength of each aryl ligand: Shen, K.; Fu, Y.; Li, J.-N.; Liu, L.; Guo, Q.-X. What are the  $pK_a$  values of C–H bonds in aromatic heterocyclic compounds in DMSO? *Tetrahedron* **2007**, *63*, 1568–1576.
- <sup>99</sup> Tolman, C. A. Steric Effects of Phosphorus Ligands in Organometallic Chemistry and Homogeneous Catalysis. *Chem. Rev.* **1977**, *77*, 313–348.
- <sup>100</sup> Contreras, R. H.; Peralta, J. E. Angular Dependence of Spin–Spin Coupling Constants. *Prog. Nucl. Mag. Reson. Spectrosc.* **2000**, *37*, 321–425.
- <sup>101</sup> Balci, M. *Basic  $^1H$ - and  $^{13}C$ -NMR Spectroscopy*; 1<sup>st</sup> ed.; Elsevier B.V, 2005; pp 87–133.
- <sup>102</sup> Grossman, G.; Lang, R.; Ohms, G.; Scheller, D. Dependence of Vicinal  $^{31}P$ - $^{31}P$  and  $^{31}P$ - $^{13}C$  Coupling Constants on the Dihedral Angle of P-Diphosphonates. *Magn. Res. Chem.* **1990**, *28*, 500–504.
- <sup>103</sup> Vitek, A. K.; Jugovic, T. M. E.; Zimmerman, P. M. Z. Revealing the Strong Relationships between Ligand Conformers and Activation Barriers: A Case Study of Bisphosphine Reductive Elimination. *ACS Catal.* **2020**, *10*, 7136–7145.
- <sup>104</sup> Noyori, R.; Takaya, H. BINAP: An Efficient Chiral Element for Asymmetric Catalysis. *Acc. Chem. Res.* **1990**, *23*, 345–350.
- <sup>105</sup> Argüelles, A. J.; Sun, S.; Budaitis, B. G.; Nagorny, P. Design, Synthesis, and Application of Chiral  $C_2$ -Symmetric Spiroketal-Containing Ligands in Transition-Metal Catalysis. *Angew. Chem. Int. Ed.* **2018**, *57*, 5325–5329.



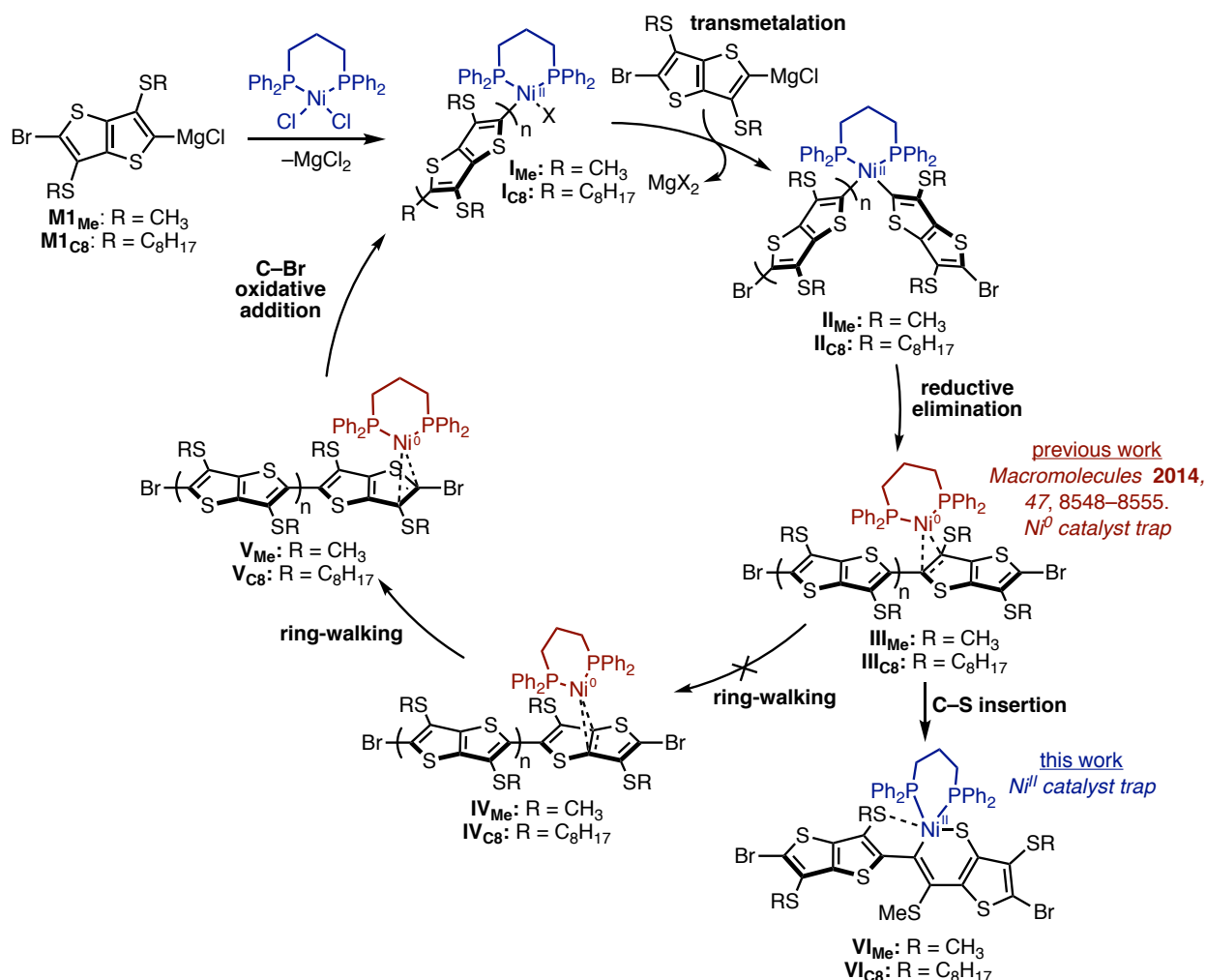
## Chapter 3 Rethinking Catalyst Trapping in Ni-Catalyzed Thieno[3,2-*b*]thiophene Polymerization

### 3.1 Introduction

Catalyst-transfer polymerization (CTP) is a chain-growth polymerization reaction used to generate conjugated polymers,<sup>1,2</sup> enabling control over molar mass,<sup>3</sup> sequence,<sup>4</sup> and end-group identity.<sup>5,6</sup> However, the scope of monomers that can be polymerized using CTP is limited to small, electron-rich arenes.<sup>7,8</sup> Monomers outside this classification, such as larger or electron-deficient arenes, often give higher dispersity or lower molar mass polymers<sup>9–11</sup> due to termination,<sup>12</sup> chain-transfer,<sup>13,14</sup> or catalyst dissociation reactions.<sup>15</sup> Efforts to expand the monomer scope beyond electron-rich, small arenes have therefore focused on identifying catalysts or monomers that prevent these side-reactions, enabling chemists to achieve chain-growth polymerizations.<sup>7</sup>

The mechanism of CTP is similar to many cross-coupling reactions (Scheme 3.1):<sup>2</sup> C–C bonds form through sequential oxidative addition, transmetalation, and reductive elimination steps.<sup>16</sup> After reductive elimination,  $\pi$ -complexes form between the catalyst and product (Scheme 3.1, **III**, **IV**, **V**).<sup>17,18,19</sup> These  $\pi$ -complexes dissociate to regenerate a free  $M^0$  in typical cross-coupling reactions,<sup>16,18</sup> but in CTP the  $M^0$  must remain bound as a  $\pi$ -complex to enable chain-growth.<sup>1,2,4,5,7,9,10,20,21</sup> The  $\pi$ -complexes in CTP interconvert to other  $\pi$ -complexes via ring-walking (Scheme 3.1, **III–V**),<sup>17</sup> to eventually insert into a carbon–halogen bond at the polymer chain end. The binding energy of the  $\pi$ -complex is important for the success of CTP; if the binding energy is low, then unbinding becomes competitive with ring-walking, and the  $\pi$ -complexes may dissociate

leading to step-growth (see Chapter 1).<sup>20</sup> If the binding energy is too strong to a particular site on the arene, the catalyst can be trapped, preventing productive ring-walking.<sup>22,23,24</sup> Lastly, if association is too strong or if electrophilic bonds are present, oxidative addition can occur before reaching the chain-end,<sup>25,26</sup> preventing turnover by forming an off-cycle catalyst trap. Although off-cycle  $M^{II}$  catalyst traps are rarely observed in CTP, such trapping mechanisms exist in small molecule reactions<sup>27,28</sup> and therefore may be applicable in CTP.



**Scheme 3.1** A mechanism for CTP of thienothiophene. For clarity,  $Ni^0$  complexes are colored red, while  $Ni^{II}$  complexes are colored blue.

A prominent example of catalyst trapping in CTP is in the Ni-catalyzed thieno[3,2-*b*]thiophene (TTh) polymerization.<sup>24</sup> In the original report by Willot and Koeckelberghs, Pd catalysts enable access to oligomers and polymers of TTh, while Ni catalysts result in dimers. Koeckelberghs concluded that this behavior with Ni arises from a species that resists turnover (i.e., a catalyst trap) and further claim that an on-cycle  $\pi$ -complex (e.g., **III** or **IV**) serves as the trap due to high-barrier ring-walking and high  $\pi$ -binding affinity. The investigations performed by Koeckelberghs support this structural claim, and also explain why polymerization does not occur via step-growth (as is common for other failed CTP reactions) because the high stability of the  $\pi$ -complex prevents generating a free  $M^0$  species.

At the time of Koeckelberghs' investigation, few if any  $\pi$ -complexes to sulfur-containing heteroarenes had been observed, even in small-molecule reactions. More recently, Kennepohl and coworkers have isolated and characterized the first examples of stable  $\pi$ -complexes between Ni and thiophene.<sup>29</sup> Kennepohl's studies elucidated the structure, binding energy, and reactions of Ni/thiophene  $\pi$ -complexes, showing that ring-walking *and* C–S insertion reactions can occur from these species. While previous work by Jones has shown that C–S insertion of  $Ni^0$  is facile into many sulfur-containing arenes,<sup>30–32</sup> Kennepohl's study is among the first investigations to show that C–S insertion adducts may form *during* CTP.<sup>33</sup> Given the work of both Jones and Kennepohl, we hypothesized that C–S insertion adducts (e.g., **VI** in Scheme 3.1) could potentially form as off-cycle species during TTh polymerization, and provide an alternative explanation for the trapping behavior observed in polymerizing TTh.

We report a computational and experimental investigation into catalyst trapping in CTP of thieno[3,2-*b*]thiophene. We provide evidence that the previously proposed  $Ni^0$  catalyst trap is unlikely based on *J*-coupling constants in <sup>31</sup>P NMR spectra from the polymerization and small-

molecule reactions. Additionally, computational modeling of reaction paths indicates that the C–S insertion adduct is highly stable, and forms with low barrier, implicating C–S insertion adducts as catalyst traps. Implications of similar C–S insertion reactions on the monomer scope of CTP will be discussed.

### 3.2 Reanalyzing the Polymerization of Thieno[3,2-*b*]thiophene

Thieno[3,2-*b*]thiophene is an electron-rich arene that has a similar structure to thiophene, an arene that is readily polymerized via CTP.<sup>2</sup> Therefore, catalysts that enable polymerization of thiophene, such as Ni(dppp)Cl<sub>2</sub> may enable polymerization of TTh. However, when any Ni catalyst is used, no polymer results, only dimers.<sup>24</sup> From in situ <sup>31</sup>P NMR spectroscopy of the Ni(dppp)Cl<sub>2</sub> catalyzed polymerization of **M1** in the presence of LiCl, a set of two doublets with  $|J_{PP}| = 60$  Hz was observed (Figure 3.1), indicating that a single trapped species forms.

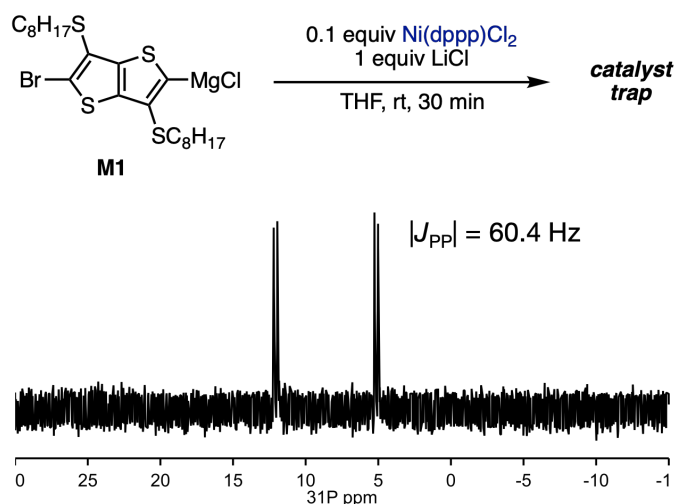


**Figure 3.1** Reaction of **M1** with Ni(dppp)Cl<sub>2</sub>, yielding a catalyst trap that appears in <sup>31</sup>P NMR spectra as two doublets with  $\delta = 12.08$  ppm ( $|J_{PP}| = 60.4$  Hz) and  $\delta = 5.14$  ppm ( $|J_{PP}| = 60.4$  Hz).

Previous work from our groups has established that the  $|J_{PP}|$  of Ni bidentate phosphine complexes depends on the linker length of the phosphine and the oxidation state of the Ni.<sup>34</sup> For complexes with two carbon linkers,  $|J_{PP}| < 30$  Hz is indicative of Ni<sup>II</sup> and  $|J_{PP}| > 40$  Hz is indicative

of Ni<sup>0</sup>. For complexes with three carbons in the phosphine linker, such as Ni(dppp)Cl<sub>2</sub> used here, we found that the trend with oxidation state is reversed, with  $|J_{PP}| > 40$  Hz being indicative of Ni<sup>II</sup> while  $|J_{PP}| < 30$  Hz is indicative of Ni<sup>0</sup>. Given that the observed  $|J_{PP}| = 60$  Hz came from a polymerization using a complex with a 3-carbon linker (i.e., Ni(dppp)Cl<sub>2</sub>), the spectrum observed is consistent with a Ni<sup>II</sup> catalyst trap. This result is in contrast to the original investigation, in which the authors proposed that  $|J_{PP}| = 60$  Hz was consistent with Ni<sup>0</sup>. However, at the time of the original investigation, the dependence of  $|J_{PP}|$  on linker length was not known, so the complexes that were used for comparing  $|J_{PP}|$  values contained phosphines of varied linker length, precluding efforts to reliably assign an oxidation state.

Additional evidence for a Ni<sup>II</sup> catalyst trap comes from simulation of the  $|J_{PP}|$  values of the on-cycle species. Ni<sup>0</sup> complexes all have  $|J_{PP}| < 20$  Hz, while the expected on-cycle Ni<sup>II</sup> complexes have much larger  $|J_{PP}|$ , greater than 60 Hz (Figure 3.2, computational details can be found in the Appendix). Given these results, we sought to evaluate the catalytic cycle of CTP for **M1** to understand if any of the on-cycle reaction paths have a high enough barrier to trap the catalyst as a Ni<sup>II</sup> complex.

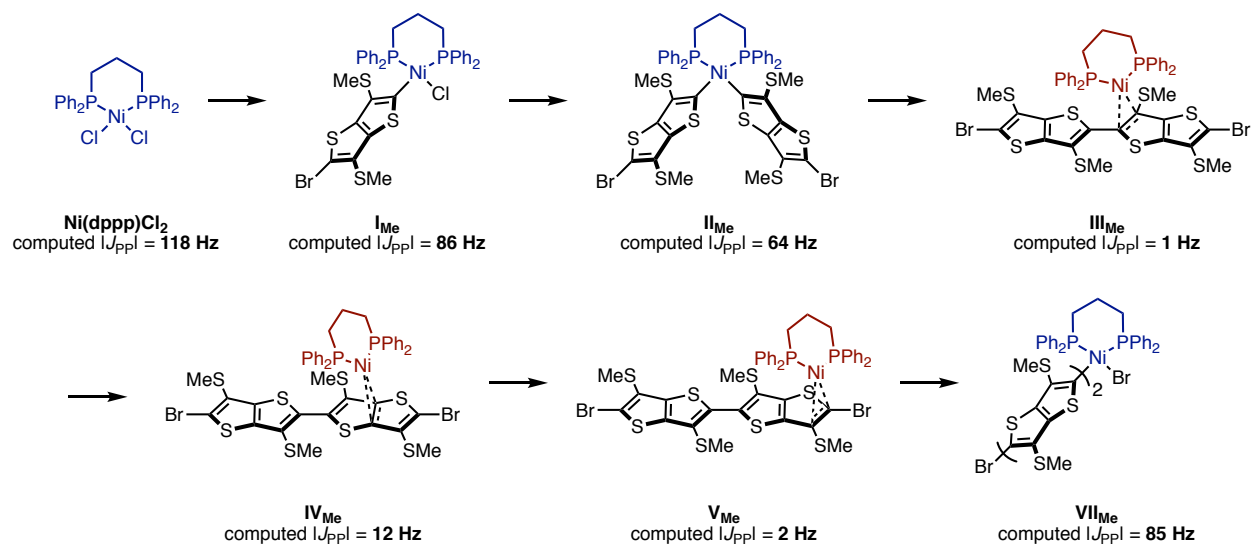


**Figure 3.2** Computed  $|J_{\text{PP}}|$  for all on-cycle species expected in the CTP of  $\text{M1}_{\text{Me}}$ . RMS error for  $|J_{\text{PP}}|$  calculations is  $\sim 11 \text{ Hz}$ . red =  $\text{Ni}^0$ , blue =  $\text{Ni}^{\text{II}}$ .

### 3.3 Reaction Paths for Thienothiophene Catalyst-Transfer Polymerization

To interrogate the catalytic cycle of CTP for TTh, we used computational reaction path discovery algorithms<sup>35–37</sup> given the success of these algorithms in elucidating the other organometallic transformations.<sup>15,38–41</sup> Starting from the  $\text{Ni(dppp)Cl}_2$  precatalyst and a disolvated Grignard monomer,  $\text{M1(THF)}_2$ ,<sup>42</sup> we modeled the transmetalation and found that it proceeds via a concerted mechanism with  $\Delta G^\ddagger_{\text{TM1}} = 17.1 \text{ kcal/mol}$ , consistent with previously reported transmetalation mechanisms (Figure 3.3).<sup>43–45</sup> Transmetalation of another equivalent of  $\text{M1(THF)}_2$  onto  $\text{I}_{\text{Me}}$  proceeded with a higher barrier of  $\Delta G^\ddagger_{\text{TM2}} = 23.5 \text{ kcal/mol}$ , to give  $\text{II}_{\text{Me}}$ . While high, the barrier for the second transmetalation is not high enough to cause trapping,<sup>46</sup> especially given the presence of  $\text{LiCl}$  in the reaction mixture (which tends to increase the rate of transmetalation).<sup>47,48</sup> Reductive elimination from  $\text{II}_{\text{Me}}$  to form  $\pi$ -complex  $\text{III}_{\text{Me}}$  proceeded through a barrier of  $\Delta G^\ddagger_{\text{RE}} = 17.7 \text{ kcal/mol}$ , again, too low to trap the catalyst at species  $\text{II}_{\text{Me}}$ . The relatively

higher barrier for transmetalation versus reductive elimination is consistent with other polymerizations catalyzed by Ni(dppp) where transmetalation is turnover-limiting.<sup>49</sup>

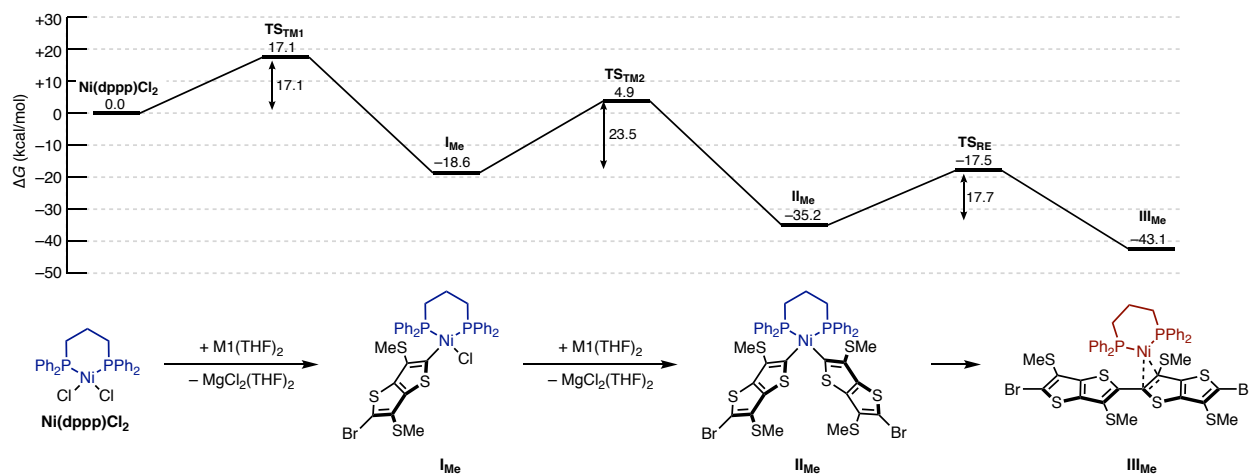


**Figure 3.3** Reaction paths for initiation in Ni(dppp) CTP of **M1** (red = Ni<sup>0</sup>, blue = Ni<sup>II</sup>).

Ring-walking from  $\pi$ -complex **III**<sub>Me</sub> to **IV**<sub>Me</sub> proceeds with a  $\Delta G^{\ddagger}_{RW1} = 18.1$  kcal/mol (Figure 3.4), a higher barrier than other ring-walking reactions over electron-rich arenes.<sup>17,43</sup> Given the low barrier ( $\Delta G^{\ddagger}_{RW2} = 8.1$  kcal/mol) and high exergonicity ( $\Delta G_{RW2} = -14.4$  kcal/mol) of the next ring-walking step from **IV**<sub>Me</sub> to **V**<sub>Me</sub>, it is unlikely that ring-walking is impeded in CTP of thieno[3,2-*b*]thiophene. By the energetic span model,<sup>50</sup> the effective barrier for ring-walking from **III**<sub>Me</sub> to **V**<sub>Me</sub> is  $\Delta G^{\ddagger}_{RW} = 18.5$  kcal/mol (difference between the highest ring-walking transition state and most stable  $\pi$ -complex, **TS**<sub>RW2</sub>-**III**<sub>Me</sub>) indicating that ring-walking is feasible and should occur under the reaction conditions if no side reactions occur (*vide infra*). Lastly, C–Br oxidative addition from **V**<sub>Me</sub> to **VII**<sub>Me</sub> proceeds with a low barrier,  $\Delta G^{\ddagger}_{CBrOA} = 12.1$  kcal/mol, and is highly exergonic, providing the driving force for catalytic turnover.

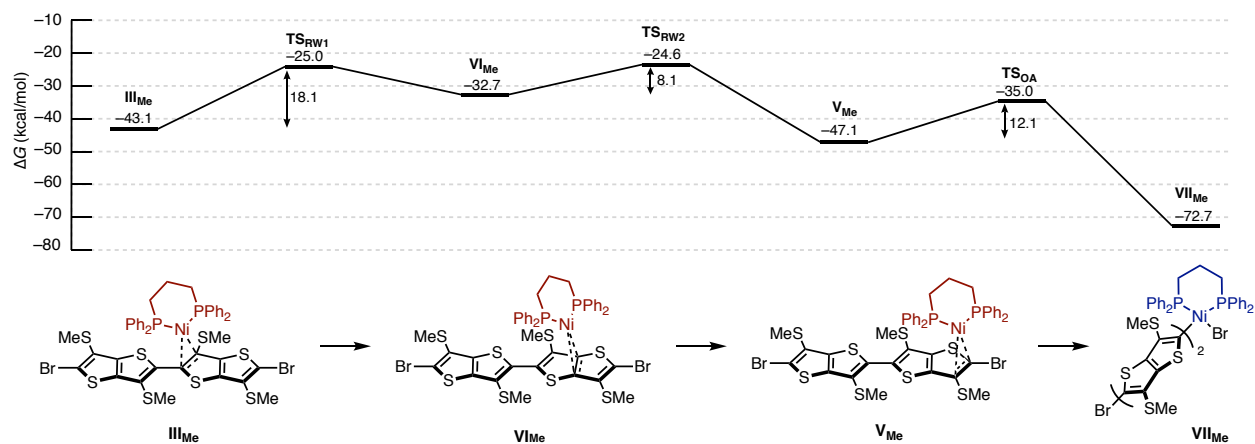


**Figure 3.4** Reaction paths for ring-walking and chain-end oxidative addition during Ni(dppp) catalyzed CTP of **M1** (red = Ni<sup>0</sup>, blue = Ni<sup>II</sup>).

Given the feasibility of the on-cycle reaction paths for reaction of Ni(dppp)Cl<sub>2</sub> with **M1**, on-cycle catalyst traps are unlikely in the CTP of TTh. This result is corroborated by experimental data on the on-cycle Ni<sup>II</sup> complexes. For example, synthesizing **I**<sub>C8</sub> via oxidative addition of Ni<sup>0</sup> into 2,5-dibromo-3,6-dithiooctylthienothiophene leads to <sup>31</sup>P NMR spectra that are inconsistent with the polymerization NMR spectra, ruling out **I** as a catalyst trap. Additionally, polymerization is not observed when we utilize a thienothiophene-containing monomer which has less steric bulk at the site of transmetalation (**M2**), indicating that transmetalation is not turnover-limiting. The other on-cycle Ni<sup>II</sup> species, **II**<sub>Me</sub>, can be ruled out in part by <sup>31</sup>P chemical shifts. Of the few NiAr<sub>2</sub> complexes that have been observed, the chemical shifts of the <sup>31</sup>P atoms differ by less than 2 ppm,<sup>34,47,51–54</sup> indicative of the similar electronic environments of the P atoms. In the case of the catalyst trap, the difference in chemical shifts of P1 and P2 is much larger (**Figure 3.1**, Δδ<sub>P1–P2</sub> = 6.9 ppm), uncharacteristic of NiAr<sub>2</sub> complexes. In addition to the low barriers we calculated, these data indicate that **II**<sub>Me</sub> is unlikely to be the catalyst trap. As such, we explored off-cycle reactions which could explain the catalyst-trapping.



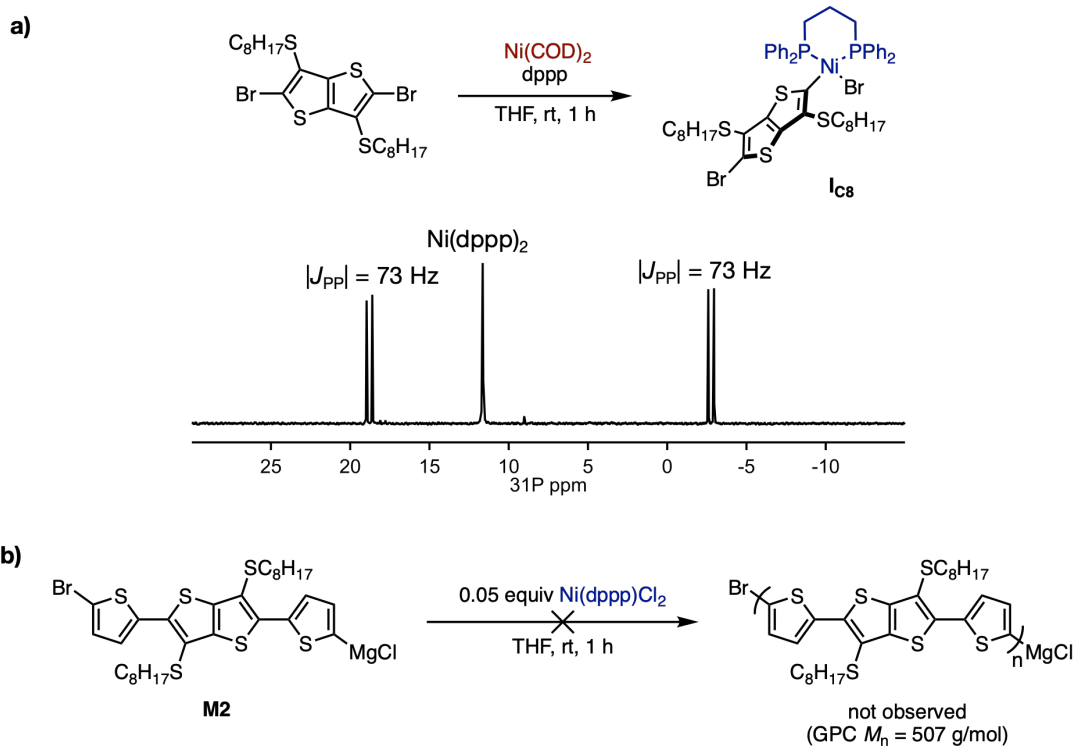


**Figure 3.5** a) Reaction of 2,5-dibromo-3,6-dithiooctylthienothiophene with  $\text{Ni}(\text{COD})_2$  and dppp, yielding  $\text{Ni}(\text{dppp})_2$  at  $\delta = 11.6$  ppm, and a set of doublets assigned to **I** at  $\delta = 18.8$  ppm ( $|J_{\text{PP}}| = 72.8$  Hz) and  $\delta = -2.8$  ppm ( $|J_{\text{PP}}| = 73.1$  Hz) and b) attempted polymerization of **M2** with  $\text{Ni}(\text{dppp})\text{Cl}_2$ .

### 3.4 Off-Cycle Reaction Paths and Catalyst Traps

Experimentally identifying off-cycle reactivity in CTP can be challenging due to the presence of oligomers, additives, excess monomer, and difficulty in characterizing polymeric species.<sup>55,56</sup> However, small molecule reactions can be informative in understanding the off-cycle reactions from a polymerization. Of particular interest was exploring C–S insertion into the thienothiophene ring, partially because of previous investigations by Jones<sup>30–32,57</sup> but also because of simulations in a related system, which unexpectedly showed C–S insertion despite our attempts to model ring-walking (see Appendix A2.8.3). Given the previous studies by Jones and more recent studies by Kennepohl<sup>29</sup> and McNeil<sup>15</sup> where C–S insertion adducts are observed in equilibrium

with  $\pi$ -complexes, C–S insertion seemed like a possible off-cycle reaction. Indeed, by exposing thieno[3,2-*b*]thiophene to a Ni<sup>0</sup> source, C–S insertion products can be observed (Figure 3.6) supporting our hypothesis that C–S insertion is viable.<sup>58</sup>

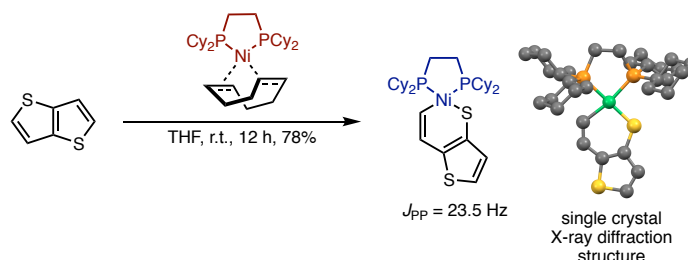


**Figure 3.6** C–S oxidative addition into thienothiophene (C, grey; P, orange; Ni, green; S, yellow). Hydrogens excluded from the crystal structure for clarity.

In previously studied C–S insertion reactions of thiophene,<sup>30–32,57</sup> bithiophene,<sup>32</sup> and thiazole,<sup>15</sup> equilibrium was observed between the C–S insertion adducts and  $\pi$ -complexes ( $K_{\text{eq}} \sim 1$ ). These equilibria suggest that C–S insertion may not be trapping in cross-coupling reactions with these arenes, as the C–S insertion adduct may convert back to the  $\pi$ -complex and then react in on-cycle reactions from the  $\pi$ -complex. However, C–S insertion adducts for fused thiophene derivatives (i.e., benzothiophene and dibenzothiophene) were found by Jones to be much more stable than the C–S insertion adducts for thiophene.<sup>30,32</sup> Given that catalyst traps must be thermodynamically more stable than on-cycle species, the increased stability of C–S insertion adducts into fused arenes is consistent with our hypothesis that C–S insertion may lead to catalyst trapping in CTP of TTh. As such, we investigated the reaction paths of C–S insertion into TTh to elucidate the stability of the C–S insertion adducts relative to the  $\pi$ -complexes.

Indeed, DFT simulations indicate that C–S insertion into thienothiophene may be trapping during the polymerization (Figure 3.7). Insertion from **III**<sub>Me</sub> proceeds with a heat of reaction  $\Delta G_{\text{CSOA}} = -7.8$  kcal/mol, indicating that the C–S insertion adduct (**VI**<sub>Me</sub>) is favored over the  $\pi$ -

complex (with an expected  $K_{\text{eq}} = \sim 10^6$ ). Additionally, the barrier to C–S insertion is much lower than the barrier to ring-walking ( $\Delta G^\ddagger_{\text{CSOA}} = 8.3$  kcal/mol,  $\Delta G^\ddagger_{\text{RW}} = 18.1$  kcal/mol,  $\Delta\Delta G^\ddagger_{\text{RW-CSOA}} = 9.8$  kcal/mol), meaning that C–S insertion is highly favored kinetically. The exergonicity and low barrier to C–S insertion indicates that even if C–S insertion is reversible and  $\pi$ -complexes can form, ring-walking is unlikely due to the large effective barrier to ring-walking from the insertion adduct ( $\Delta G^\ddagger = 25.9$  for  $\text{VI}_{\text{Me}}$  to  $\text{TS}_{\text{RW1}}$ ). Lastly, the computed  $|J_{\text{PP}}|$  coupling constant of  $\text{VI}_{\text{Me}}$  is 56 Hz, which is within error of the  $|J_{\text{PP}}|$  observed from in situ  $^{31}\text{P}$  NMR of the polymerization ( $|J_{\text{PP}}| = 60$  Hz), supporting  $\text{VI}$  as a potential catalyst trap.

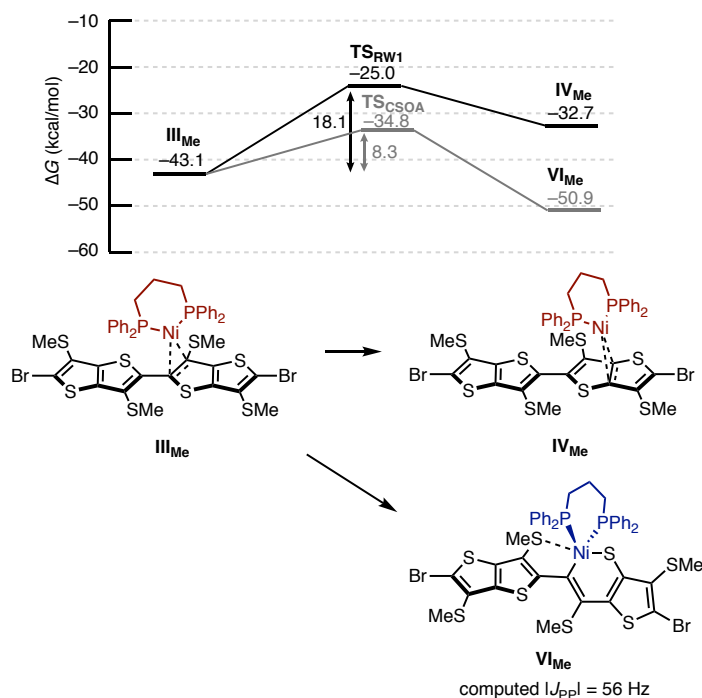
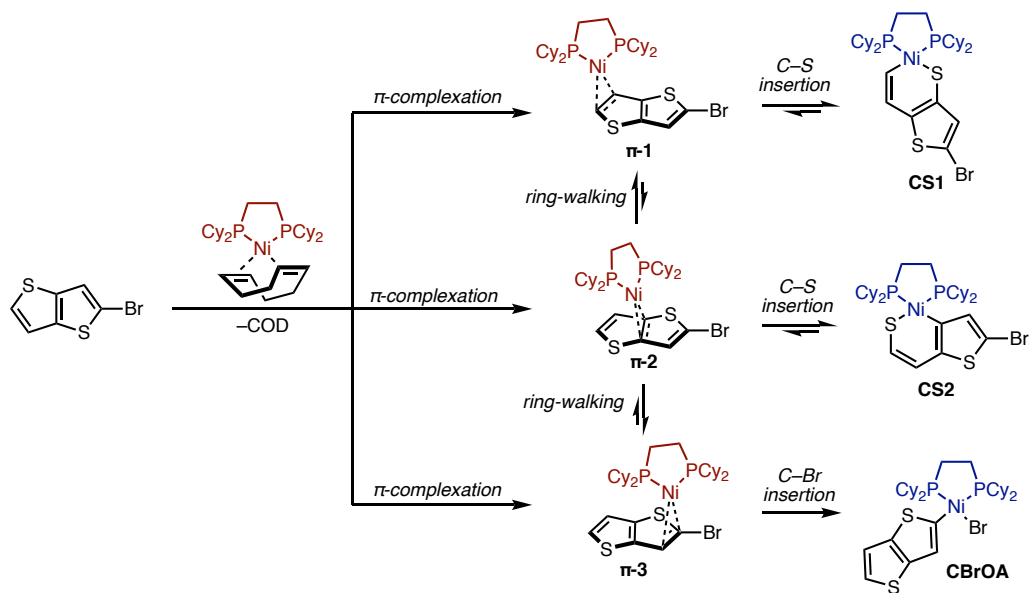


**Figure 3.7** Reaction paths from  $\text{III}_{\text{Me}}$ , showing ring-walking and C–S insertion.

To determine if C–S insertion actually prevents ring-walking, we investigated the reaction of 2-bromothieno[3,2-*b*]thiophene with a  $\text{Ni}^0$  source (Scheme 3.2). We hypothesized that  $\pi$ -complexes would form between  $\text{Ni}^0$  and 2-bromothieno[3,2-*b*]thiophene (i.e.,  $\pi$ -1,  $\pi$ -2, and  $\pi$ -3,

Scheme 3.2), and from these  $\pi$ -complexes, C–S insertion or C–Br insertion would occur to generate Ni<sup>II</sup> complexes **CS1**, **CS2**, and **CBrOA** (Scheme 3.2). If C–S insertion is reversible and ring-walking is facile, then C–S insertion adducts **CS1** and **CS2** would convert to **CBrOA** via the reverse reaction (C–S reductive elimination) and subsequent ring-walking. However, if C–S insertion is irreversible or ring-walking is difficult, then the C–S and C–Br insertion products will persist in the reaction mixture, even at long reaction times.



**Scheme 3.2** Proposed mechanism for reaction of 2-bromothiophene with Ni(1,2-bis(dicyclohexylphosphino)ethane)(cycloocta-1,5-diene) (red = Ni<sup>0</sup>, blue = Ni<sup>II</sup>).

<sup>31</sup>P NMR spectroscopy can be used to differentiate C–S and C–Br insertion adducts by their  $J_{PP}$  values: C–S insertion adducts with 2-carbon linkers typically have  $J_{PP} < 25$  Hz<sup>29–32,34</sup> and C–Br insertion adducts typically have  $J_{PP} > 30$  Hz.<sup>34,59</sup> From this, NMR spectra of the reaction of Ni(1,2-bis(dicyclohexylphosphino)ethane)(cycloocta-1,5-diene) (i.e., Ni(dcppe)(COD)) and 2-bromothieno[3,2-*b*]thiophene reveals three sets of doublets at short reaction times that correspond to C–S and C–Br insertion adducts (Figure 3.8, 0.5 h). At long reaction time, a population of C–S insertion adducts remains (Figure 3.8, 48 h), however, other species form as well, indicating

degradation of some C–S or C–Br insertion adducts.<sup>60</sup> Given the persistence of C–S insertion adducts along with the DFT simulations described above, it seems plausible that C–S insertion adducts inhibit ring-walking to the chain end. Without ring-walking to the chain-end, C–Br insertion reactions required for turnover in CTP cannot occur, explaining the reactivity observed in CTP of **M1** with Ni catalysts.

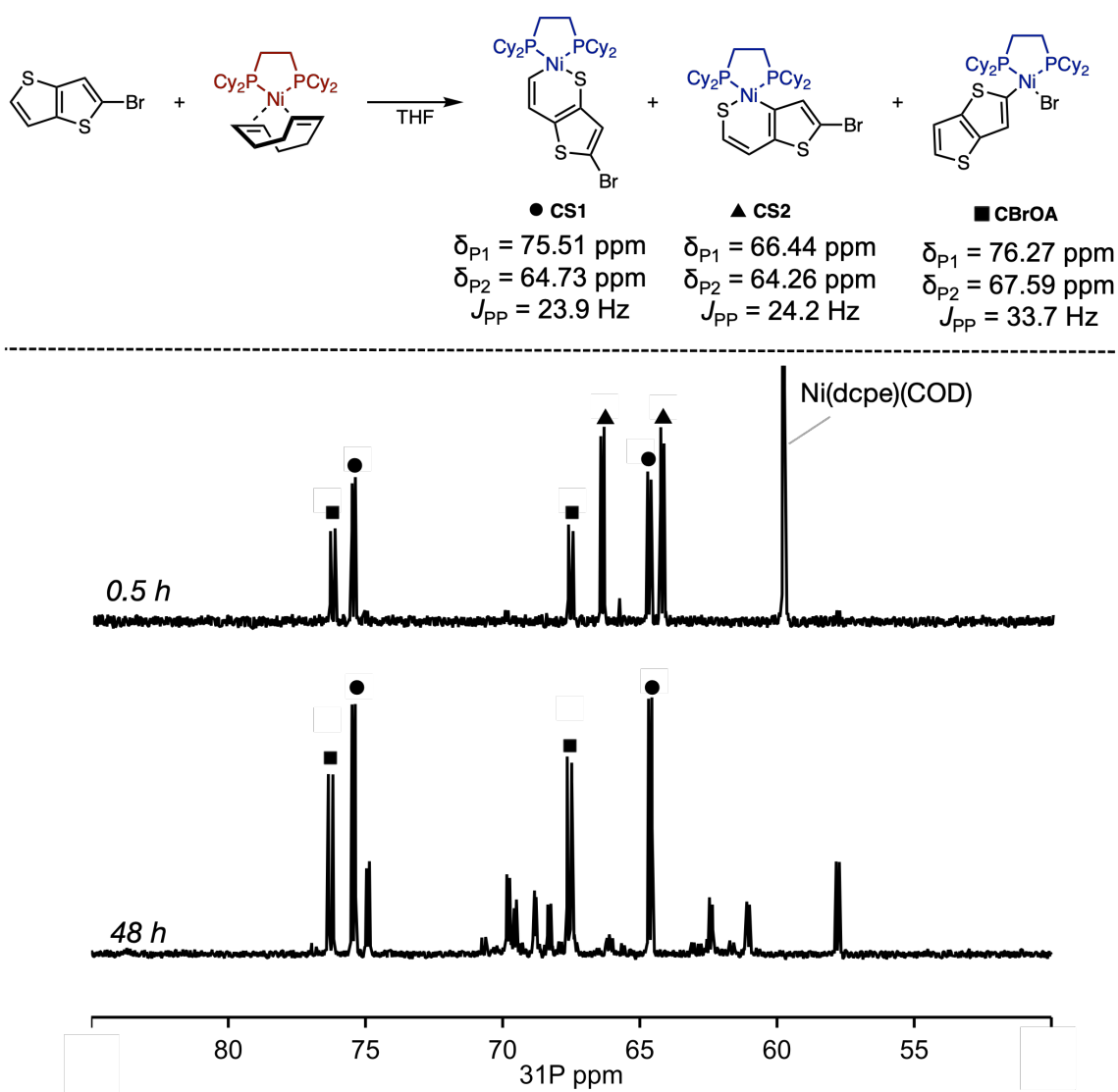


**Figure 3.8** <sup>31</sup>P NMR spectra of the reaction between Ni(dcppe)(COD) and 2-bromothiopheno[3,2-*b*]thiophene at 0.5 h and 48 h. Red = Ni<sup>0</sup>, blue = Ni<sup>II</sup>.

Additionally, exposing  $\text{Ni}^0(1,3\text{-bis}(\text{dicyclohexylphosphino})\text{propane})$  (i.e.,  $\text{Ni}(\text{dcpp})$ ) to 3,6-dioctylthiothienothiophene yields spectra (Figure 3.9) with  $J_{\text{PP}} > 40$  Hz, indicative of  $\text{Ni}^{\text{II}}$  complexes. These species are assigned to the C–S insertion adducts, given the absence of other C–X bonds that would enable the formation of other  $\text{Ni}^{\text{II}}$  species. Notably, the chemical shift and  $J_{\text{PP}}$  of these species are very similar to those observed in the reaction of  $\text{Ni}(\text{dppp})\text{Cl}_2$  with **M1** (Figure 3.5), further supporting the assignment of the catalyst trap as a C–S insertion adduct.

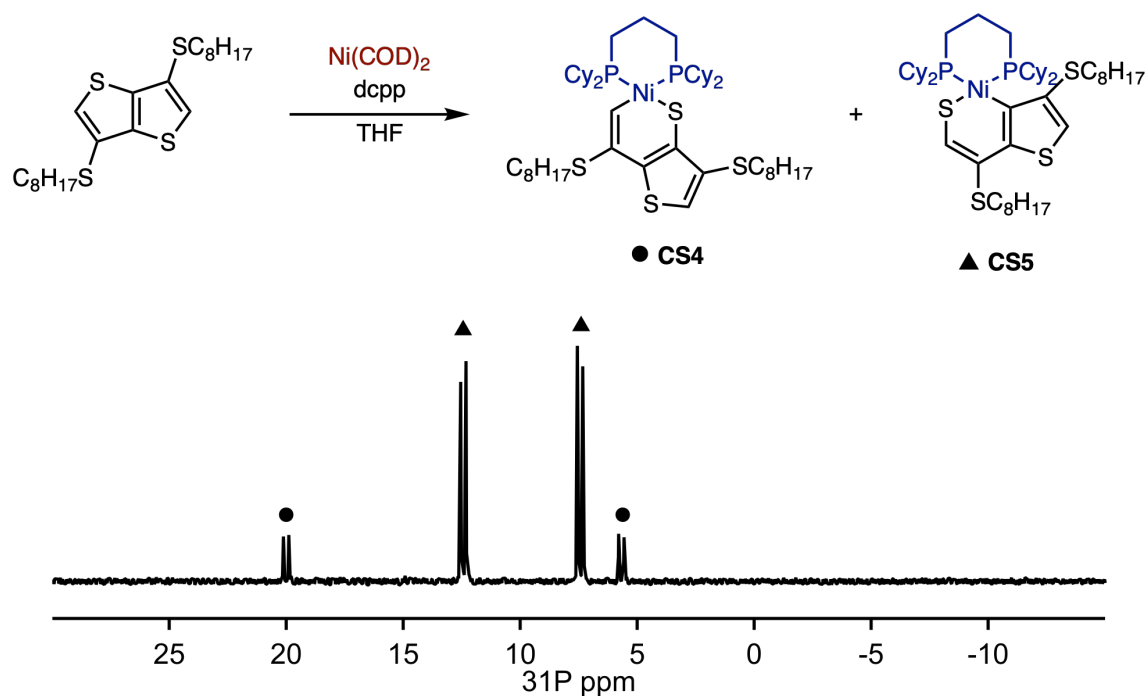


**Figure 3.9** Reaction of  $\text{Ni}$  bis(cycloocta-1,5-diene) with 3,6-dithiooctylthienothiophene and  $\text{dcpp}$ , yielding a set of doublets assigned to **CS4** at  $\delta = 12.0$  ppm ( $|J_{\text{PP}}| = 55.2$  Hz) and  $\delta = 7.02$  ppm ( $|J_{\text{PP}}| = 55.5$  Hz), and another set of doublets assigned to **CS5** at  $\delta = 19.6$  ppm ( $|J_{\text{PP}}| = 56.1$  Hz) and  $\delta = 5.27$  ppm ( $|J_{\text{PP}}| = 55.9$  Hz) Red =  $\text{Ni}^0$ , blue =  $\text{Ni}^{\text{II}}$ .

Given the investigations in the previous sections, C–S insertion is likely to cause trapping in  $\text{Ni}$ -catalyzed thieno[3,2-*b*]thiophene polymerization. A discussion on dissociation reactions

from the  $\pi$ -complexes as well as discussions on the identity of species isolated from the quenched polymerization can be found in the Appendix section A2.4.

### 3.5 Identifying Catalysts That Avoid C–S Insertion

Given these insights into the reaction, we sought to identify catalysts that avoid C–S insertion so as to enable CTP of **M1**. Using DFT simulations, we explored the effect of changing the substituents on the P atoms of the bidentate phosphine to influence the barriers to ring-walking or C–S insertion (Figure 3.10a). We found that bidentate phosphonite ligands with strongly withdrawing alkoxy groups were likely to be selective for ring-walking over C–S insertion (Figure 3.10b).

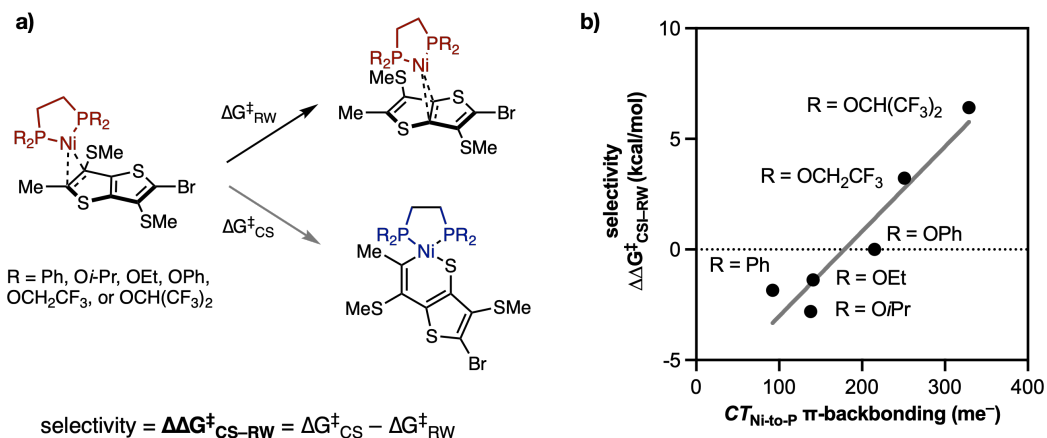


**Figure 3.10** a) Computational ligand screening for enabling TTh polymerization and b) results of the ligand screen, showing the dependence of  $\Delta\Delta G^{\ddagger}$  on the  $\pi$ -backbonding ability of the ligand.

When we generated some of these Ni catalysts bearing bidentate phosphonite ligands, and used them in CTP of TTh, we saw no polymer formation, indicating our catalyst choice was not optimal. We hypothesize that upon reductive elimination, the resulting  $Ni^0$  can undergo P–O insertion into the ligand, causing the catalyst to decompose. The insights gained from the computational ligand screening however suggest that the selectivity for ring-walking over C–S

insertion arose from decreasing the ring-walking barrier (rather than increasing C–S insertion barrier) due to increasing  $\pi$ -accepting ability of phosphonite ligands (Figure 3.10b). Therefore, while phosphonite ligands may not be suitable for the polymerization of **M1**, further investigations aiming to enable CTP of thienothiophene should explore less-electrophilic  $\pi$ -accepting ligands, such as cyclic alkyl amino carbenes, to enable lower barrier ring-walking.

### 3.6 Conclusions and Outlook

Thieno[3,2-*b*]thiophene is an electron-rich arene that cannot be polymerized via Ni-based catalyst-transfer polymerization. Previous investigations concluded that polymerization is hampered by high-barrier ring-walking reactions, preventing turnover in the polymerization, and causing the Ni catalyst to be trapped as a Ni<sup>0</sup>  $\pi$ -complex. This study demonstrated that the polymerization trap may be better assigned as a Ni<sup>II</sup> complex, given the  $J_{PP}$  in <sup>31</sup>P NMR spectra. Small molecule reactions enabled us to rule out the on-cycle species as catalyst traps, and computational investigations into the reactivity of Ni<sup>0</sup>  $\pi$ -complexes of thienothiophene enabled identifying C–S insertion adducts catalyst traps. The reactivity of Ni<sup>0</sup> with thienothiophenes in small-molecule reactions support that C–S insertion species can form and that these species are sufficiently stable to prevent ring-walking, supporting a reassignment of the catalyst trap.

The target polymer, poly(thienothiophene), is not a highly studied polymer, so the inability to access poly(thienothiophene) via CTP is not highly limiting. However, fused sulfur-containing arenes *are* highly prevalent in high-performance conjugated polymers,<sup>61</sup> such as those used in solar cells with record-breaking power conversion efficiencies.<sup>62,63</sup> Expanding the monomer scope of CTP to include fused sulfur-containing arenes like thienothiophene will therefore be highly useful for enhancing the properties of advanced conjugated polymers. The catalyst trapping mechanism proposed in this work may provide insight into the limits of the monomer scope of CTP. Potentially



other fused sulfur-containing arenes can undergo similar C–S insertion reactions, complicating or preventing the synthesis of these polymers. Therefore, we encourage those who study CTP (or those who aim to synthesize high-performance conjugated polymers via controlled chain-growth methods) to consider C–S insertion as a mode of catalyst trapping so as to identify catalysts that can avoid C–S insertion and enable controlled chain-growth polymerization of these monomers.

### 3.7 References

- 
- <sup>1</sup> Yokozawa, T.; Ohta, Y. Transformation of Step-Growth Polymerization into Living Chain-Growth Polymerization. *Chem. Rev.* **2016**, *116*, 1950–1968.
- <sup>2</sup> Bryan, Z. J.; McNeil, A. J. Conjugated Polymer Synthesis via Catalyst-Transfer Polycondensation (CTP): Mechanism, Scope, and Applications *Macromolecules* **2013**, *46*, 8695–8405.
- <sup>3</sup> Gu, K.; Onorato, J.; Xiao, S. S.; Luscombe, C. K.; Loo, Y.-L. Determination of the Molecular Weight of Conjugated Polymers with Diffusion-Ordered NMR Spectroscopy. *Chem. Mater.* **2018**, *30*, 570–576.
- <sup>4</sup> Palermo, E. F.; McNeil, A. J. Impact of Copolymer Sequence on Solid-State Properties for Random, Gradient and Block Copolymers containing Thiophene and Selenophene. *Macromolecules* **2012**, *45*, 5948–5955.
- <sup>5</sup> Lutz, J. P.; Hannigan, M. D.; McNeil, A. J. Polymers Synthesized via Catalyst-Transfer Polymerization and Their Applications *Coord. Chem. Rev.* **2018**, *376*, 225–247.
- <sup>6</sup> Elmalem, E.; Biedermann, F.; Johnson, K.; Friend, R. H.; Huck, W. T. S. Synthesis and Photophysics of Fully  $\pi$ -Conjugated Heterobis-Functionalized Polymeric Molecular Wires via Suzuki Chain-Growth Polymerization. *J. Am. Chem. Soc.* **2012**, *134*, 17769–17777.
- <sup>7</sup> Leone, A. K.; McNeil, A. J. Matchmaking in Catalyst-Transfer Polycondensation: Optimizing Catalysts based on Mechanistic Insight *Acc. Chem. Res.* **2016**, *49*, 2822–2831.
- <sup>8</sup> Yokozawa, T.; Ohta, Y. Transformation of Step-Growth Polymerization into Living Chain-Growth Polymerization. *Chem. Rev.* **2016**, *116*, 1950–1968.
- <sup>9</sup> Senkovskyy, V.; Tkachov, R.; Komber, H.; Sommer, M.; Heuken, M.; Voit, B.; Huck, W. T. S.; Kataev, V.; Petr, A.; Kiriya, A. Chain-Growth Polymerization of Unusual Anion-Radical Monomers Based on Naphthalene Diimide: A New Route to Well-Defined n-Type Conjugated Copolymers *J. Am. Chem. Soc.* **2011**, *133*, 19966–19970.
- <sup>10</sup> Senkovskyy, V.; Tkachov, R.; Komber, H.; John, A.; Sommer, J.-U., Kiriya, A. Mechanistic Insight into Catalyst-Transfer Polymerization of Unusual Anion-Radical Naphthalene Diimide Monomers: An Observation of Ni(0) Intermediates *Macromolecules*, **2012**, *45*, 7770–7777.
- <sup>11</sup> Bridges, C. R.; McCormick, T. M.; Gibson, G. L.; Hollinger, J.; Seferos, D. S. Designing and Refining Ni(II)diimine Catalysts Toward the Controlled Synthesis of Electron-Deficient Conjugated Polymers *J. Am. Chem. Soc.* **2013**, *135*, 13212–13219.
- <sup>12</sup> Pammer, F.; Jager, J.; Rudolf, B.; Sun, Y. Soluble Head-to-Tail Regioregular Polythiazoles: Preparation, Properties, and Evidence for Chain-Growth Behavior in the Synthesis via Kumada-Coupling Polycondensation. *Macromolecules* **2014**, *47*, 5904–5912.
- <sup>13</sup> Takagi, K.; Kawagita, E.; Kouchi, R. Synthesis and Characterization of Polythiophene Derivatives with Nitrogen Heterocycles on the Side Chain. *J. Polym. Sci., Part A: Polym. Chem.* **2014**, *52*, 2166–2174.
- <sup>14</sup> Schiefer, D.; Wen, T.; Wang, Y.; Goursot, P.; Komber, H.; Hanselmann, R.; Braunstein, P.; Reiter, G.; Sommer, M. Nickel Catalyst with a Hybrid P, N Ligand for Kumada Catalyst Transfer Polycondensation of Sterically Hindered Thiophenes. *ACS Macro Lett.* **2014**, *3*, 617–621.
- <sup>15</sup> Smith, M. L.; Leone, A. K.; Zimmerman, P. M.; McNeil, A. J. Impact of Preferential  $\pi$ -Binding in Catalyst-Transfer Polycondensation of Thiazole Derivatives. *ACS Macro Lett.* **2016**, *5*, 1411–1415.

- 
- <sup>16</sup> Jana, R.; Pathak, T. P.; Sigman, M. S. Advances in Transition Metal (Pd,Ni,Fe)-Catalyzed Cross-Coupling Reactions Using Alkyl-organometallics as Reaction Partners. *Chem. Rev.* **2011**, *111*, 1417–1492.
- <sup>17</sup> Bilbrey, J. A.; Bootsma, A. N.; Bartlett, M. A.; Locklin, J.; Wheeler, S. E.; Allen, W. D. Ring-Walking of Zerovalent Nickel on Aryl Halides *J. Chem. Theory. Comput.* **2017**, *13*, 1706–1711.
- <sup>18</sup> Zenkina, O. V.; Karton, A.; Freeman, D.; Shimon, L. J. W.; Martin, J. M. L.; van der Boom, M. E. Directing Aryl–I versus Aryl–Br Bond Activation by Nickel via a Ring Walking Process. *Inorg. Chem.* **2008**, *47*, 5114–5121.
- <sup>19</sup> Sontag, S. K.; Bilbrey, J. A.; Huddleston, N. E.; Sheppard, G. R.; Allen, W. D.; Locklin, J.  $\pi$ -Complexation in Nickel-Catalyzed Cross-Coupling Reactions. *J. Org. Chem.* **2014**, *79*, 1836–1841
- <sup>20</sup> Leone, A. K.; Goldberg, P. K.; McNeil, A. J. Ring-Walking in Catalyst-Transfer Polymerization. *J. Am. Chem. Soc.* **2018**, *140*, 7846–7850.
- <sup>21</sup> Additionally, CTP is differentiated from most other cross-couplings in that the monomer structure in CTP contains both a nucleophilic group (i.e., MgCl, ZnCl, B(OR)<sub>2</sub>, or SnR<sub>3</sub>) and an electrophilic group (i.e., C–Cl, C–Br, or C–I bond) while in cross coupling, the nucleophile and electrophile are different species.
- <sup>22</sup> Nojima, M.; Ohta, Y.; Yokozawa, T. Investigation of Catalyst-Transfer Condensation Polymerization for Synthesis of Poly(p-phenylenevinylene). *J. Polym. Sci. A - Polym. Chem.* **2014**, *52*, 2643–2653.
- <sup>23</sup> Bedi, A.; De Winter, J.; Gerbaux, P.; Koeckelberghs, G. Detrimental Ni(0) Transfer in Kumada Catalyst Transfer Polycondensation of Benzo[2,1-b:3,4-b']dithiophene. *J. Polym. Sci. A - Polym. Chem.* **2016**, *54*, 1706–1712.
- <sup>24</sup> Willot, P.; Koeckelberghs, G. Evidence for Catalyst Association in the Catalyst Transfer Polymerization of Thieno[3,2-*b*]thiophene *Macromolecules* **2014**, *47*, 8548–8555.
- <sup>25</sup> Dewar, M. A Review of  $\pi$ -Complex Theory. *Bull. Soc. Chim. Fr.* **1951**, *1*, C79.
- <sup>26</sup> Chatt, J.; Duncanson, L. A. Olefin Co-ordination Compounds. Part III. Infra-red Spectra and Structure: Attempted Preparation of Acetylene Complexes. *J. Chem. Soc.* **1953**, *0*, 2939–2947.
- <sup>27</sup> Balcells, D.; Nova, A. Designing Pd and Ni Catalysts for Cross-Coupling Reactions by Minimizing Off-Cycle Species *ACS Catal.* **2018**, *8*, 3499–3515.
- <sup>28</sup> Ahneman, D. T.; Estrada, J. G.; Lin, S.; Dreher, S. D.; Doyle, A. G. Predicting Reaction Performance in C–N Cross-Coupling Using Machine Learning. *Science* **2018**, *360*, 186–190.
- <sup>29</sup> He, W.; Patrick, B. O.; Kennepohl, P. Identifying the Missing Link in Catalyst Transfer Polymerization *Nat. Commun.* **2018**, *9*, 3866.
- <sup>30</sup> Vicic, D. A.; Jones, W. D. Room-Temperature Desulfurization of Dibenzothiophene Mediated by [(*i*-Pr<sub>2</sub>PCH<sub>2</sub>)<sub>2</sub>NiH]<sub>2</sub>. *J. Am. Chem. Soc.* **1997**, *119*, 10855–10856.
- <sup>31</sup> Vicic, D. A.; Jones, W. D. Deep Hydrodesulfurization in Homogeneous Solution: Access to a Transition-Metal Insertion Complex of 4,6-Dimethyldibenzothiophene *Organometallics* **1998**, *17*, 3411–3413.
- <sup>32</sup> Vicic, D. A.; Jones, W. D. Modeling the Hydrodesulfurization Reaction at Nickel. Unusual Reactivity of Dibenzothiophenes Relative to Thiophene and Benzothiophene. *J. Am. Chem. Soc.* **1999**, *121*, 7606–7617.
- <sup>33</sup> C–S insertion into thiazole was considered in reference 15, however, they concluded that C–S insertion was unlikely to cause catalyst trapping or off-cycle activity.
- <sup>34</sup> Hannigan, M. D.; McNeil, A. J.; Zimmerman, P. M. Using  $J_{PP}$  to Identify Ni Bidentate Phosphine Complexes In Situ. *Inorganic Chemistry* **2021**,

- 
- <sup>35</sup> Zimmerman, P. M. Single-Ended Transition State Finding with the Growing String Method. *J. Comput. Chem.* **2015**, *36*, 601–611.
- <sup>36</sup> Zimmerman, P. M. Growing String Method with Interpolation and Optimization in Internal Coordinates: Method and Examples. *J. Chem. Phys.* **2013**, *138*, 184102.
- <sup>37</sup> Zimmerman, P. Reliable Transition State Searches Integrated with the Growing String Method. *J. Chem. Theory Comput.* **2013**, *9*, 3043–3050.
- <sup>38</sup> Nett, A. J.; Zhao, W.; Zimmerman, P.; Montgomery, J. Highly Active Nickel Catalysts for C-H Functionalization Identified Through Analysis of Off-Cycle Intermediates. *J. Am. Chem. Soc.* **2015**, *137*, 7636–7639.
- <sup>39</sup> Ellington, B. R.; Paul, B.; Das, D.; Vitek, A. K.; Zimmerman, P. M.; Marsh, E. N. G. An Unusual Iron-Dependent Oxidative Deformylation Reaction Providing Insight into Hydrocarbon Biosynthesis in Nature. *ACS Catal.* **2016**, *6*, 3293–3300.
- <sup>40</sup> Pendleton, I. M.; Pérez-Temprano, M. H.; Sanford, M. S.; Zimmerman, P. M. Experimental and Computational Assessment of Reactivity and Mechanism in C(sp<sup>3</sup>)-N Bond-Forming Reductive Elimination from Palladium(IV). *J. Am. Chem. Soc.* **2016**, *138*, 6049–6060.
- <sup>41</sup> Ludwig, J. R.; Zimmerman, P. M.; Gianino, J. B.; Schindler, C. S. Iron(III)-Catalysed Carbonyl–Olefin Metathesis. *Nature* **2016**, *533*, 374–379.
- <sup>42</sup> Curtis, E. R.; Hannigan, M. D.; Vitek, A. K.; Zimmerman, P. M. Quantum Chemical Investigation of Dimerization in the Schlenk Equilibrium of Thiophene Grignard Reagents. *J. Phys. Chem. A* **2020**, *124*, 1480–1488.
- <sup>43</sup> Pollit, A. A.; Ye, S.; Seferos, D. S. Elucidating the Role of Catalyst Steric and Electronic Effects in Controlling the Synthesis of  $\pi$ -Conjugated Polymers. *Macromolecules* **2020**, *53*, 138–148.
- <sup>44</sup> Vitek, A. K.; Leone, A. K.; McNeil, A. J.; Zimmerman, P. M. Spin-Switching Transmetalation at Ni Diimine Catalysts. *ACS Catal.* **2018**, *8*, 3655–3666.
- <sup>45</sup> Pollit, A. A.; Lough, A. J.; Seferos, D. S. Examining the Spin State and Redox Chemistry of Ni(Diimine) Catalysts during the Synthesis of  $\pi$ -Conjugated Polymers. *Macromol. Chem. Phys.* **2020**, *221*, 2000321.
- <sup>46</sup> Ryu, H.; Park, J.; Kim, H. K.; Park, J. Y.; Kim, S.-T.; Baik, M.-H. Pitfalls in Computational Modeling of Chemical Reactions and How To Avoid Them. *Organometallics* **2018**, *37*, 3228–3239.
- <sup>47</sup> Lanni, E. L.; McNeil, A. J. Mechanistic Studies on Ni(dppe)Cl<sub>2</sub>-Catalyzed Chain-Growth Polymerizations: Evidence for Rate-Determining Reductive Elimination. *J. Am. Chem. Soc.* **2009**, *131*, 16573–16579.
- <sup>48</sup> Wu, S.; Huang, L.; Tian, H.; Geng, Y.; Wang, F. LiCl-Promoted Chain Growth Kumada Catalyst-Transfer Polycondensation of the “Reversed” Thiophene Monomer. *Macromolecules* **2011**, *44*, 7558–7567.
- <sup>49</sup> Lanni, E. L.; McNeil, A. J. Evidence for Ligand-Dependent Mechanistic Changes in Nickel-Catalyzed Chain-Growth Polymerizations. *Macromolecules* **2010**, *43*, 8039–8044.
- <sup>50</sup> Kozuch, S.; Shaik, S. How to Conceptualize Catalytic Cycles? The Energetic Span Model. *Acc. Chem. Rev.* **2011**, *44*, 101–110.
- <sup>51</sup> Ye, S.; Cheng, S.; Pollit, A. A.; Forbes, M. W.; Seferos, D. S. Isolation of Living Conjugated Polymer Chains. *J. Am. Chem. Soc.* **2020**, *142*, 11244–11251.
- <sup>52</sup> Ye, S.; Foster, S. M.; Pollit, A. A.; Cheng, S.; Seferos, D. S. The Role of Halogens in the Catalyst Transfer Polymerization for  $\pi$ -Conjugated Polymers. *Chem. Sci.* **2019**, *10*, 2075–2080.

- 
- <sup>53</sup> Even complexes with (dppp)NiX<sub>2</sub> complexes with electronically distinct carbon-based X-type ligands have small  $\Delta_{\delta P1-\delta P2}$ . For example, in Cámpora, J.; López, J. A.; Maya, C.; Palma, P.; Carmona, E.; Valegra, P. Synthesis and reactivity studies on alkyl-aryloxo complexes of nickel containing chelating diphosphines: cyclometallation and carbonylation reactions *J. Organomet. Chem.* **2002**, *643*, 331–341. The complex 1,3-bis(diisopropylphosphino) propane Ni(CH<sub>2</sub>CMe<sub>2</sub>-o-C<sub>6</sub>H<sub>4</sub>) has a  $\Delta_{\delta P1-\delta P2} = 2.0$  ppm despite having both alkyl and aryl substituents and in Bour, J. R.; Roy, P.; Cauty, A. J.; Kampf, J. W.; Sanford, M. S. Oxidatively Induced Aryl-CF<sub>3</sub> Coupling at Diphosphine Nickel Complexes. *Organometallics* **2020**, *39*, 3–7. The complex (dppp)Ni(CF<sub>3</sub>)(Ph) has a  $\Delta_{\delta P1-\delta P2} = 4.6$  ppm despite the large difference in the electronic properties of CF<sub>3</sub> and Ph ligands.
- <sup>54</sup> Lee, S. R.; Bloom, J. W. G.; Wheeler, S. E.; McNeil, A. J. Accelerating Ni(II) Precatalyst Initiation Using Reactive Ligands and its Impact On Chain-Growth Polymerizations. *Dalton Trans*, **2013**, *42*, 4218–4222.
- <sup>55</sup> Tang, X.; Chen, W.; Li, L. The Tough Journey of Polymer Crystallization: Battling with Chain Flexibility and Connectivity. *Macromolecules* **2019**, *52*, 3575–3591.
- <sup>56</sup> MALDI-TOF MS is used frequently for polymer characterization, but the interpretation of MALDI mass spectra is facilitated by assuming a repeat unit molecular weight and end-group functionality. If side reactions change the molecular weight of even a few repeat units, understanding what reactions caused this change *and* assigning the molecular weight change to species that are not at the polymer chain-ends can be challenging if not impossible.
- <sup>57</sup> Grochowski, M. R.; Li, T.; Brennessel, W. W.; Jones, W. D. Competitive Carbon-Sulfur vs Carbon-Carbon Bond Activation of 2-Cyanothiophene with [Ni(dippe)H]<sub>2</sub>. *J. Am. Chem. Soc.* **2010**, *132*, 12412–12421.
- <sup>58</sup> Ni(dcpe) was used due to the ease of synthesis of Ni(dcpe)COD as well as the tendency for dcpe ligands to mono-ligate to Ni. Similar adducts with Ni(dppp) and Ni(dppe) were attempted however, due to the tendency for these species to form Ni(dppp)<sub>2</sub> and Ni(dppe)<sub>2</sub>, C–S insertion adducts with these ligands could not be isolated.
- <sup>59</sup> Desnoyer, A. N.; He, W.; Behyan, S.; Chiu, W.; Love, J. A.; Kennepohl, P. The Importance of Ligand-Induced Backdonation in the Stabilization of Square Planar d<sup>10</sup> Nickel  $\pi$ -Complexes. *Chem. - Eur. J.* **2019**, *25*, 5259–5268.
- <sup>60</sup> The degradation is expected: degradation of C–S insertion adducts to other species has been reported previously by Jones. C–Br insertion adducts of thiophene are known to undergo disproportionation.
- <sup>61</sup> Lee, C.; Lee, S.; Kim, G.-U.; Lee, W.; Kim, B. J. Recent Advances, Design Guidelines, and Prospects of All-Polymer Solar Cells. *Chem. Rev.* **2019**, *119*, 8028–8086.
- <sup>62</sup> Bin, H.; Gao, L.; Zhang, Z.-G.; Yang, Y.; Zhang, Y.; Zhang, C.; Chen, S.; Xue, L.; Yang, C.; Xiao, M.; Li, Y. 11.4% Efficiency Non-Fullerene Polymer Solar Cells with Trialkylsilyl Substituted 2D-Conjugated Polymers as Donor. *Nature Commun.* **2016**, *7*, 13651.
- <sup>63</sup> Fu, H.; Li, Y.; Yu, J.; Qu, Z.; Fan, Q.; Lin, F.; Woo, H. Y.; Gao, F.; Zhu, Z.; Jen, A. K.-Y. High Efficiency (15.8%) All-Polymer Solar Cells Enabled by a Regioregular Narrow Bandgap Polymer Acceptor. *J. Am. Chem. Soc.* **2021**, *143*, 2665–2670.

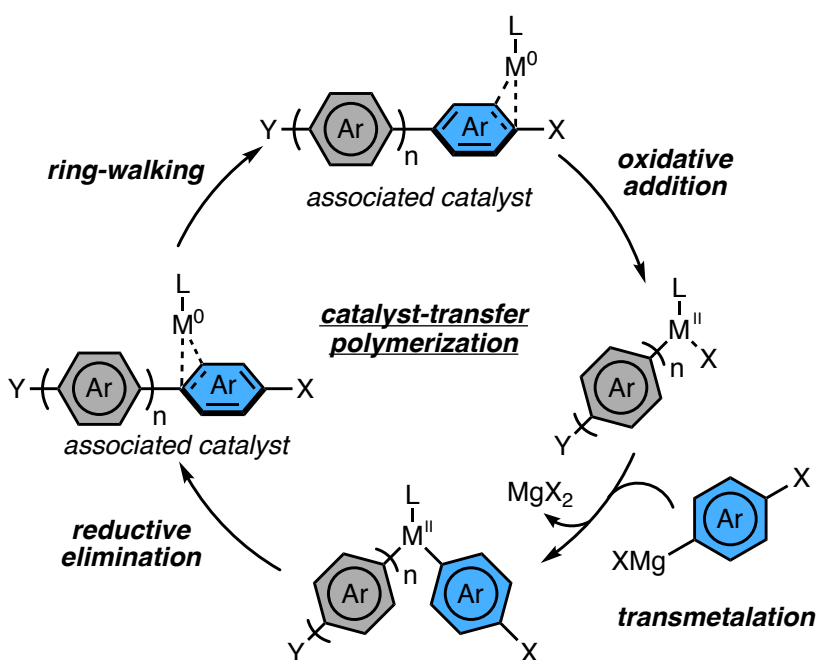
## Chapter 4 Elucidating Ring-Walking in Catalyst-Transfer Polymerization

### 4.1 Introduction

Catalyst-transfer polymerization (CTP) is a polymerization method used to access polymers with higher control over average molar mass, sequence, and end-group identity compared to step-growth polymerization methods.<sup>1-4</sup> As such, CTP has enabled access to polymers useful for chemical sensing, light harvesting, and other applications.<sup>5,6</sup> However, CTP is limited by its monomer scope in; electron-deficient arenes are not commonly polymerized via CTP, while they are commonly polymerized via step-growth polymerizations, and large monomers composed of multiple arenes are also not commonly polymerized via CTP.<sup>1,2,7</sup> Given that the mechanism of CTP invokes persistent  $\pi$ -complexes between the catalyst and polymer (Scheme 4.1),<sup>1,8-17</sup> (while most step-growth polymerizations do not) the limits to the monomer scope of CTP may be due to instability or side-reactions of  $\pi$ -complexes for some classes of arenes. As such, expanding the monomer scope of CTP will require identifying the structure-property relationships that affect  $\pi$ -binding and side-reactions of  $\pi$ -complexes, and will require development of pairing strategies that enable identifying catalysts that avoid side-reactions.

Dissociation is a deleterious reaction in CTP, so catalysts must be chosen to enable  $\pi$ -complexes that are sufficiently stable,<sup>1,2,7,17</sup> However,  $\pi$ -complexes that are *too* stable (i.e., strongly bound) have been proposed to resist ring-walking.<sup>1,18-20</sup> Without ring-walking, the  $M^0$  catalyst cannot undergo oxidative addition at the polymer chain-end, stalling turnover in the polymerization. Therefore, catalysts must be chosen to form  $\pi$ -complexes that are bound enough

to resist dissociation but are not so strongly bound that they impede ring-walking and subsequent catalytic turnover. These requirements suggest that there is a narrow chemical space of catalysts that enable ring-walking (and CTP) and imply that it may be difficult to identify successful CTP reactions by catalyst screening without also understanding structure–property relationships that affect  $\pi$ -binding and ring-walking. Despite the fact that  $\pi$ -complexes are commonly invoked in CTP,  $\pi$ -complexes are difficult to observe during the polymerization, limiting our understanding of the reactivity of these  $\pi$ -complexes.



**Scheme 4.1** The mechanism of Kumada catalyst-transfer polymerization.

In most CTP reactions, the  $\pi$ -complexes are highly reactive toward ring-walking and oxidative addition.<sup>17</sup> While this reactivity is beneficial for enabling polymerization, the resulting short lifetime of  $\pi$ -complexes causes challenges in experimentally studying reactivity. The ease of ring-walking in many  $\pi$ -complexes causes fluxionality,<sup>21</sup> preventing characterization of  $\pi$ -complexes via NMR spectroscopy (even in small molecules).<sup>22</sup> Structural studies such as X-ray

crystallography are impossible on  $\pi$ -complexes from polymerizations both because of their fluxionality and because of the disorder caused by the polymer chain. Small-molecule structural studies are also challenging and are typically only enabled by using bulky phosphine ligands, limiting the types of  $\pi$ -complexes that can be studied using small molecule studies.<sup>23,24</sup> Lastly, CTP of most monomers gives  $M^{II}$  resting states,<sup>25,26</sup> meaning that the  $M^0$  species are in low concentration during the reaction, further precluding studies on the  $M^0$  species. These factors have caused many to use indirect experimental evidence to understand ring-walking and the  $\pi$ -complexes during CTP.

The types of monomers amenable to CTP is one source of indirect evidence for  $\pi$ -complex stability. The dominance of electron-rich monomers in CTP implies that  $\pi$ -complexes to electron-rich arenes are less likely to unbind or get trapped compared to  $\pi$ -complexes to electron-deficient arenes.<sup>7,20</sup> Similarly, the lack of representation of large monomers supports that smaller arenes enable ring-walking to the chain-end more easily.<sup>17</sup> For understanding ring-walking barriers, some indirect evidence can be gleaned from the polymerization behavior of specific monomers. For example, McNeil and coworkers studied the competition between ring-walking and catalyst unbinding in CTP of thiophene and benzene and found that  $\pi$ -complexes to polythiophene did not dissociate.<sup>17</sup> Whether a catalyst dissociated during CTP of benzene depended on catalyst identity indicating that metal, monomer, and ancillary ligand identity are important in stabilizing  $\pi$ -complexes. Additionally, Koeckelberghs and Yokozawa have observed that highly electron-rich monomers are polymerized easily with Pd catalysts, but hindered when Ni catalysts are used.<sup>19,27,28</sup> Based on the difficulty of producing high molar mass polymer with Ni catalysts in these systems, along with the higher  $\pi$ -binding affinity of Ni complexes to arenes, these examples are cited as evidence<sup>7,17,19,20,27-29</sup> that ring-walking is more difficult in highly-bound  $\pi$ -complexes.



Given that computational chemistry enables understanding reaction mechanisms without requiring synthesis or isolation, others have used computations to interrogate ring-walking and the reactions of  $\pi$ -complexes directly. Allen and coworkers have used simulations to investigate ring-walking over a series of arenes.<sup>21</sup> They found that Ni(dppe)–pyrrole  $\pi$ -complexes had lower ring-walking barrier *and* were more strongly bound than Ni(dppe)–thiophene  $\pi$ -complexes, indicating that ring-walking barrier and binding energy are not strongly correlated. Studies on ring-walking by Seferos reveal that  $\pi$ -complexes of thiophene and various Ni bidentate phosphines all have similar binding energies but a wide range of ring-walking barriers,<sup>29</sup> similarly indicating that there may be a low correlation between ring-walking barrier and  $\pi$ -binding energy. Given of the ease of using computation to analyze hard-to-observe species, we propose that simulating ring-walking over a wider set of  $\pi$ -complexes might provide useful insight into the structure-property relationships that govern CTP.

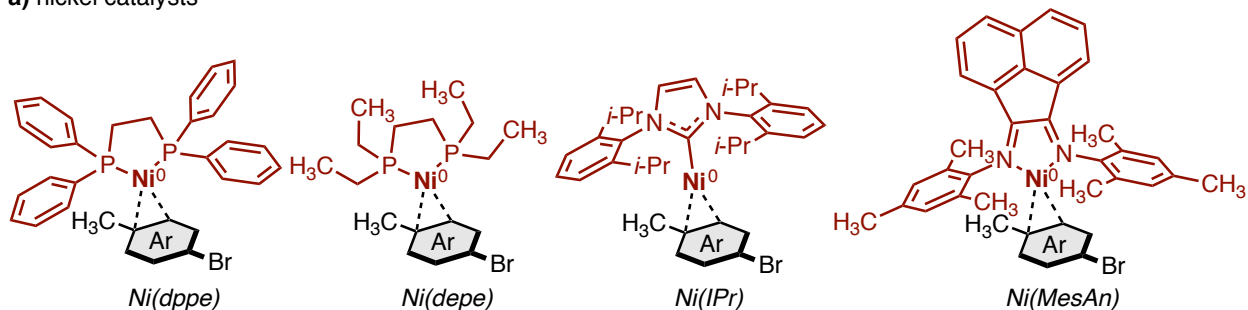
We present an investigation into ring-walking of Ni<sup>0</sup> and Pd<sup>0</sup> complexes over different arenes to understand the effect of catalyst and arene structure on the barriers to ring-walking. We find that the  $\pi$ -binding energy is a poor predictor of the ring-walking barrier. Instead, we find that  $\pi$ -binding energy is influenced by the energy of the arene  $\pi^*$  orbital, while ring-walking barriers correlate with the metal identity and the substitution pattern of the arene. The implications of these findings on catalyst choice in CTP will be discussed.

## 4.2 Dataset Construction

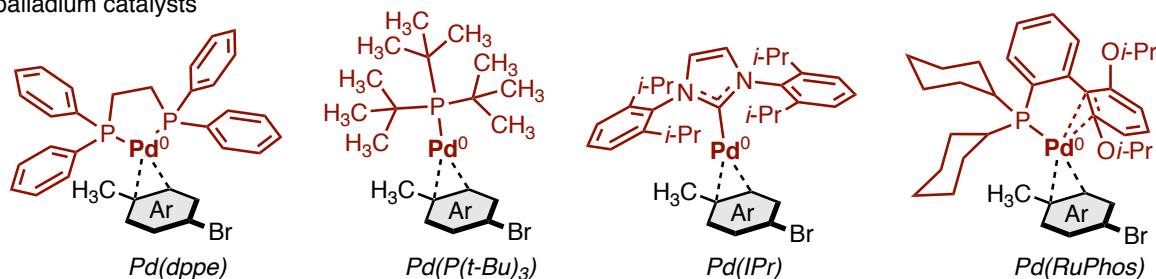
We compiled data on ring-walking for 72  $\pi$ -complexes, derived from eight catalysts and nine arenes (Scheme 4.2). Thiophene, furan, pyrrole, thiazole, benzotriazole, and benzene were chosen because at least one example of CTP of these arenes has been reported.<sup>7,18,30</sup> Other arenes

which were not previously reported in CTP (i.e., oxazole, thienopyrroledione, and ethylenedioxythiophene) were chosen to enable comparisons due to varying electronics or steric encumbrance of the arene. Catalysts were chosen based on their ability to enable CTP for one or more arenes in the dataset.<sup>7,31,32</sup> Ni(depe) and Pd(dppe) are not known to catalyze CTP without significant deviation from chain-growth behavior but were included to enable comparing the effect of metal identity and ligand electronics relative to Ni(dppe).

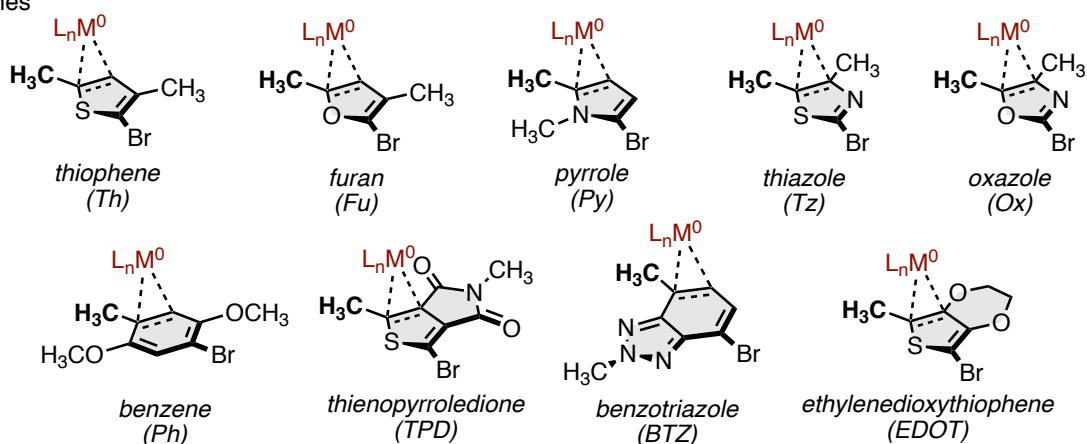
a) nickel catalysts



b) palladium catalysts



c) arenes



**Scheme 4.2** a) Structures of the Ni complexes, b) Pd complexes, and c) arenes that make up the  $\pi$ -complexes in this study. Polymer chains were truncated to methyl groups (bolded). Side chains were truncated to methyl groups (un-bolded).

The  $\pi$ -complexes we studied were constructed to model the final ring-walking step in CTP, ring-walking of the catalyst to the chain-end C–Br bond. To reduce computational cost, the arenes modeled had a methyl group which represents a truncated polymer chain. Additionally, side chains were truncated to methyl groups for the same reason. Reaction paths were modeled using

the single-ended growing string method<sup>33,34</sup> (SE-GSM) due to its success in elucidating other organometallic transformations,<sup>35–37</sup> including CTP.<sup>38,39</sup> SE-GSM explores reaction paths using reactant structures and driving coordinates as inputs (unlike other methods, which require specific product or transition state structures), enabling us to identify intermediates that are non-intuitive or unexplored, ideal for reactions like ring-walking in which experimental mechanistic insight is sparse. Binding energies were calculated by comparing the  $\pi$ -complex binding energy to the energy of the dissociated arene and metal complex. For more details, see Appendix 3.

### 4.3 Trends Between Structure and $\pi$ -Binding Energy

$\pi$ -Complex binding energy can be an important factor in the outcome of CTP, therefore, we were motivated to understand the factors that affect it. The Dewar-Chatt-Duncanson model of  $\pi$ -binding in metal–olefin complexes indicates that for late transition metals (i.e., with filled d-orbitals), the major bonding interactions are  $\pi$ -backbonding interactions between the filled metal d-orbitals (particularly the  $d_{x^2-y^2}$  orbital) and the unoccupied  $\pi^*$  orbitals of the arene (Figure 4.1a). Therefore, maximizing these interactions by increasing the spatial overlap of metal and  $\pi^*$  orbitals or by decreasing the difference in energy between these orbitals should lead to stronger  $\pi$ -complexes. Given the range of orbital energies of arenes (Figure 4.1b) and metal complexes (Figure 4.1c), we expected that there will be large variance in the binding energies due to these orbital interactions.

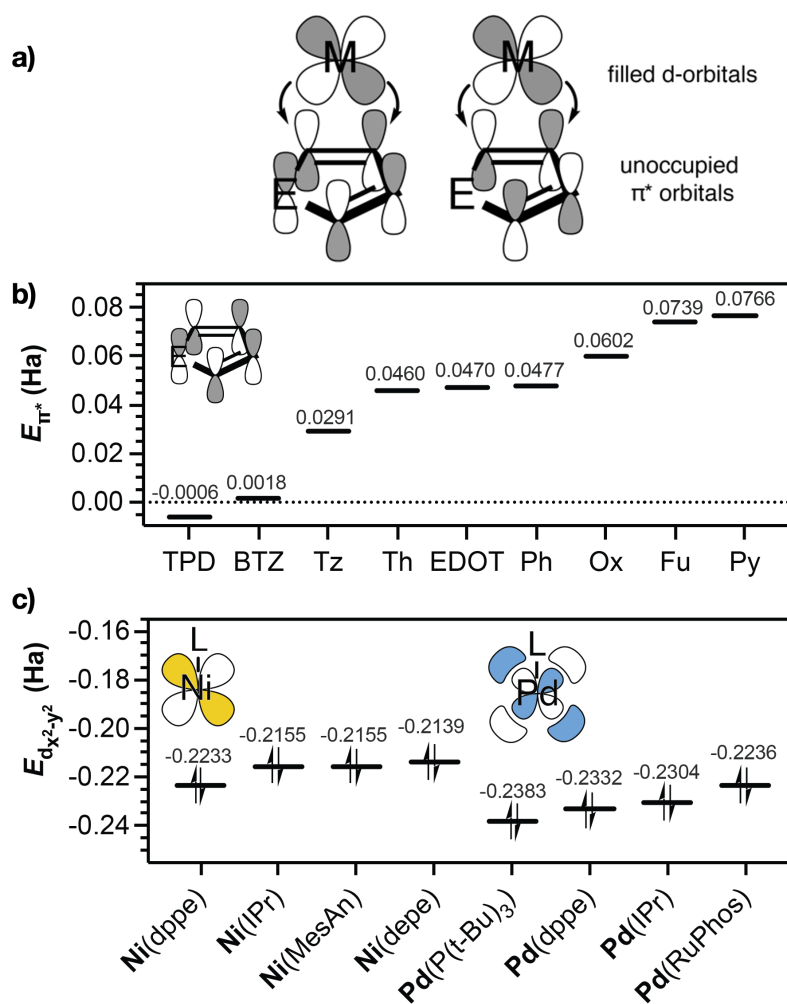


**Figure 4.1** a) Orbitals involved in bonding between arenes and late transition metals, b) Energy of  $\pi^*$  orbital of the arenes and c) energy of the d orbital of the catalyst.

Indeed, we found that the strength of  $\pi$ -bonding varied between 5 kcal/mol and 40 kcal/mol depending on the metal and arene (Figure 4.2). The most strongly bound  $\pi$ -complexes formed between Ni and arenes with lower energy  $\pi^*$  orbitals, such as TPD and BTZ. Other arenes such as pyrrole and furan, which have high energy  $\pi^*$  orbitals, are less able to engage in backbonding with d-orbitals, causing lower binding energies. Quantitatively, when  $\Delta G_{\text{bind}}$  is expressed as a function of the energy gap between the metal and arene orbitals (Figure 4.3), the DCD model seems to be

better at predicting  $\pi$ -binding in Ni complexes, given the larger  $R^2$  for Ni ( $R^2 = 0.68$ ) compared to Pd ( $R^2 = 0.26$ ).

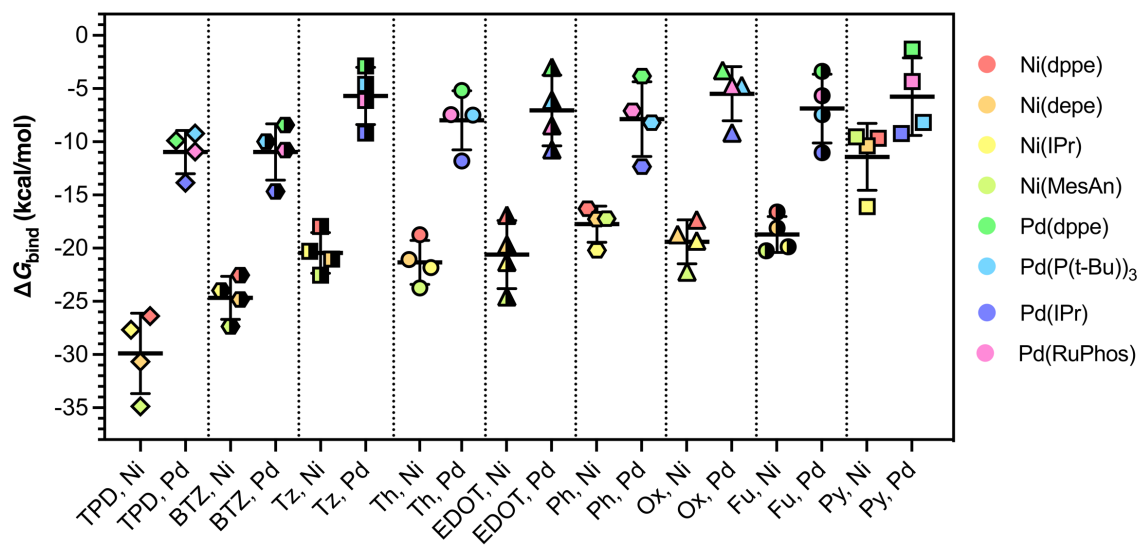


**Figure 4.2**  $\Delta G_{\text{bind}}$  for metal/arene  $\pi$ -complexes, sorted by arene  $\pi^*$  energy (increasing to the right).

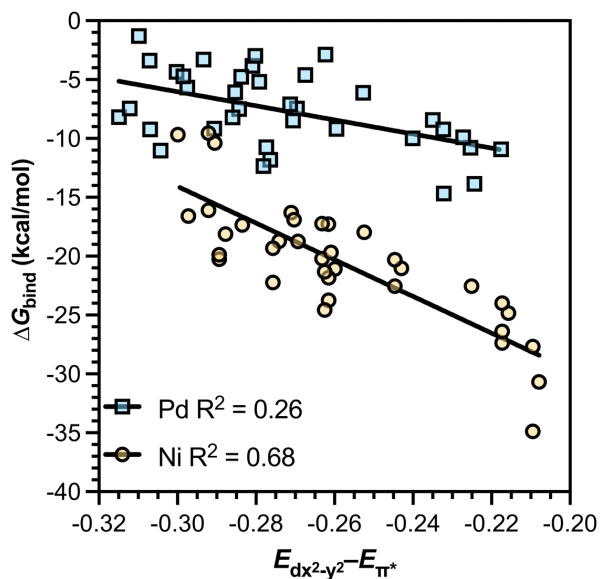


**Figure 4.3**  $\Delta G_{\text{bind}}$  as a function of the energy gap between metal d-orbitals and  $\pi^*$  orbitals.

Metal identity had the most pronounced effect on  $\pi$ -binding energy, with Ni complexes being more strongly bound than Pd complexes by approximately 15 kcal/mol. This strong effect of metal is likely due to the lower energy of Pd's occupied d-orbitals compared to Ni (Figure 4.1c) causing less backbonding between Pd and the  $\pi^*$  orbitals of the arene. Additionally, the larger size of Pd's d-orbitals may lead to less overlap between d and  $\pi^*$  orbitals, leading to weaker interactions between Pd and arenes.

Ancillary ligand did not have as strong of an effect on  $\pi$ -binding energy (Figure 4.4). Ni complexes showed almost no differences in binding energy with varying ancillary ligand. Pd complexes showed a larger effect of ancillary ligand, with an  $\sim 8$  kcal/mol difference between the median binding energy of Pd(dppe) complexes and that of Pd(IPr), but the effects were not as dramatic as the effect of varying metal identity or arene identity. The smaller effect of ancillary ligand on  $\pi$ -binding energy compared to the effect of arene may be due to the strong  $\sigma$ -donating character of all of ligands in this study, causing little variance in the ancillary ligand electronic properties across the dataset. Incorporation weakly  $\sigma$ -donating ligands or other ligands with a wider range of electronic properties may reveal a larger effect of ancillary ligand on  $\pi$ -complex binding energy, in line with the model of ligand-induced  $\pi$ -backbonding proposed by Kennepohl.<sup>40</sup> However, catalysts with weakly  $\sigma$ -donating ligands are not known to catalyze CTP and are therefore outside of the scope of this study.

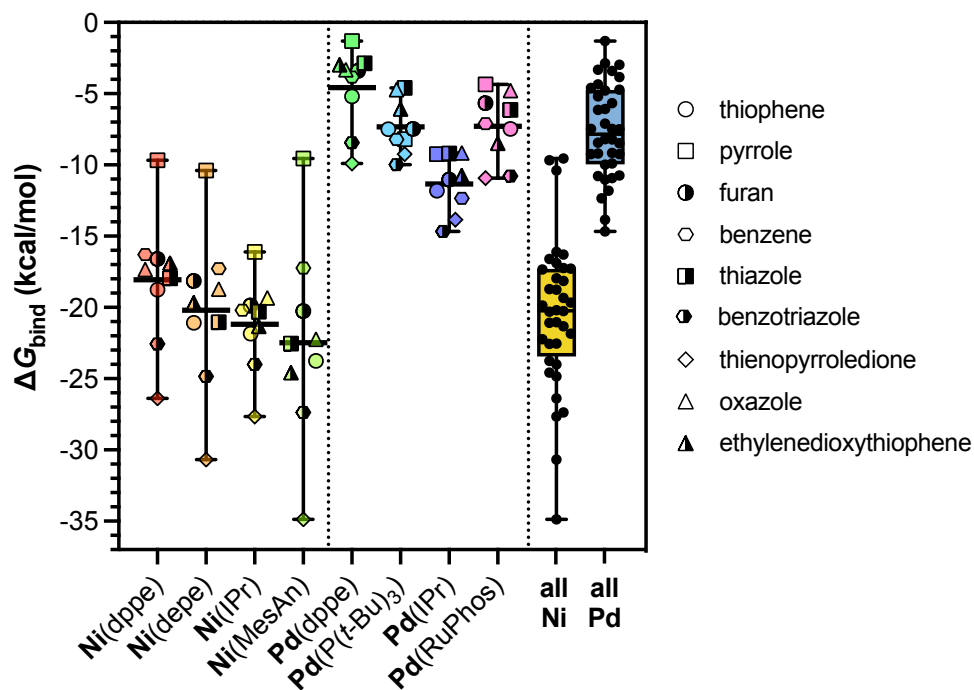


**Figure 4.4**  $\Delta G_{\text{bind}}$  for metal/arene  $\pi$ -complexes, sorted by metal catalyst.

Generally, these trends agree with the Dewar-Chatt-Duncanson model, however, when we plot  $\pi$ -binding energy versus the amount of charge transferred from the metal to the arene ( $CT_{\text{M-to-Ar}}$ , Figure 4.5) we find a moderate correlation ( $R^2 = 0.75$ ) suggesting that other factors may also be affecting the binding energy, such as the steric environment of the arene or metal catalyst.



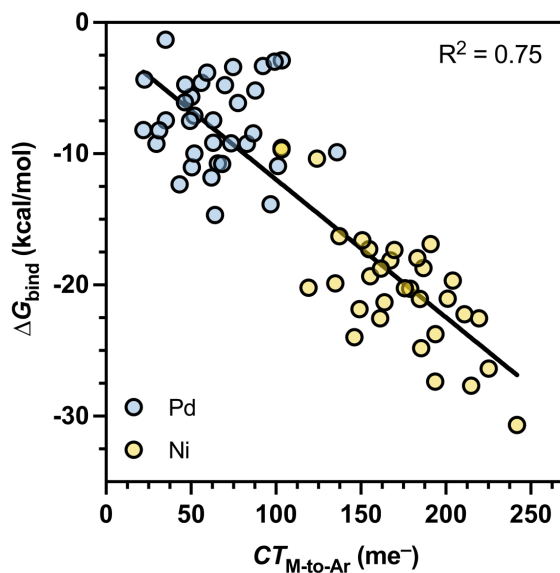


**Figure 4.5**  $\Delta G_{\text{bind}}$  of  $\pi$ -complexes as a function of  $CT_{\text{M-to-Ar}}$ , the charge transfer from the metal to the arene in the  $\pi$ -complex.

Additionally, within some classes of ancillary ligands, the charge transfer from the metal to the ancillary ligand ( $CT_{\text{M-to-L}}$ ) correlated with the  $\pi$ -binding energy (Figure 4.6). Generally, more backbonding charge transfer to the ancillary ligand caused weaker binding energies. This correlation likely is a result of competition for metal donation between the  $\pi$ -accepting orbitals of the ancillary ligand and the  $\pi$ -accepting orbitals of the arene: if more  $\pi$ -backbonding happens between the metal's d-orbitals and the ancillary ligand, then less  $\pi$ -backbonding occurs between the metal and arene, weakening the M–Ar bond and decreasing the binding energy of the  $\pi$ -complex.

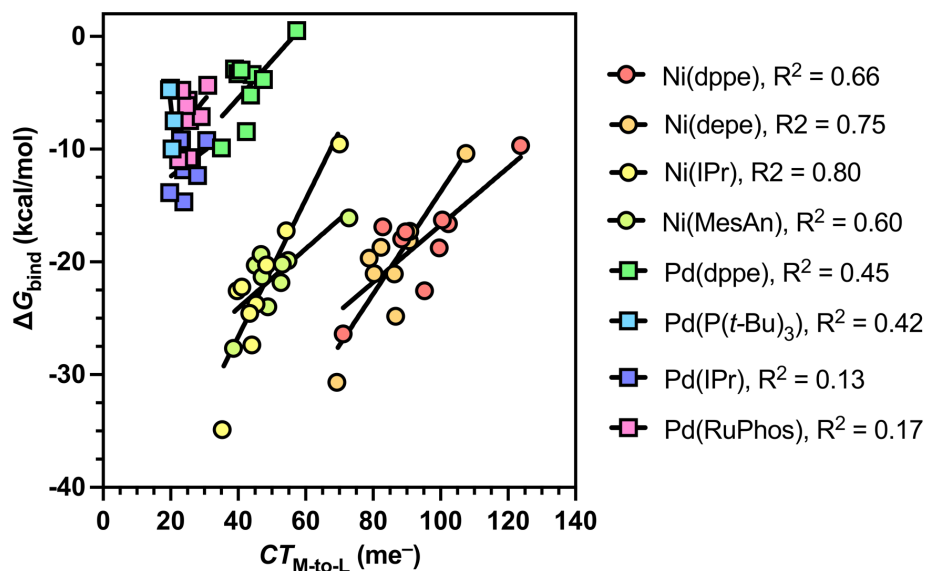


**Figure 4.6**  $\Delta G_{\text{bind}}$  of  $\pi$ -complexes as a function of  $CT_{\text{M-to-L}}$ , the charge transfer from the metal to the ancillary ligand in the  $\pi$ -complex.

Given that the average binding energies of Ni  $\pi$ -complexes are much higher than that of Pd  $\pi$ -complexes, it is unsurprising that Ni catalysts are well represented in CTP because their higher thermodynamic stability. However, success in CTP is also determined by the ability of a catalyst to ring-walk to the polymer chain-end. To gain more insight and determine what structural features enable or prevent ring-walking, simulation of the ring-walking reaction paths was required.

#### 4.4 Ring-Walking in $\pi$ -Complexes

We simulated ring-walking over the  $\pi$ -complexes using reaction discovery tools described in the computational details section. In all cases, we found that ring-walking from the  $\pi$ -complexes proceeded via a one-step mechanism to yield  $\eta^2$   $\pi$ -complex products, however, the structure of the transition state varied depending on the metal. Ring-walking of Ni complexes proceeded through an  $\eta^4$  transition state (Figure 4.7a), with the Ni closer to the centroid of the arene (Figure 4.7c).

Ring walking of Pd complexes instead proceeded through an  $\eta^2$  transition state (Figure 4.7b), with the Pd centered over a C–C bond, further away from the centroid of the ring (Figure 4.7d).

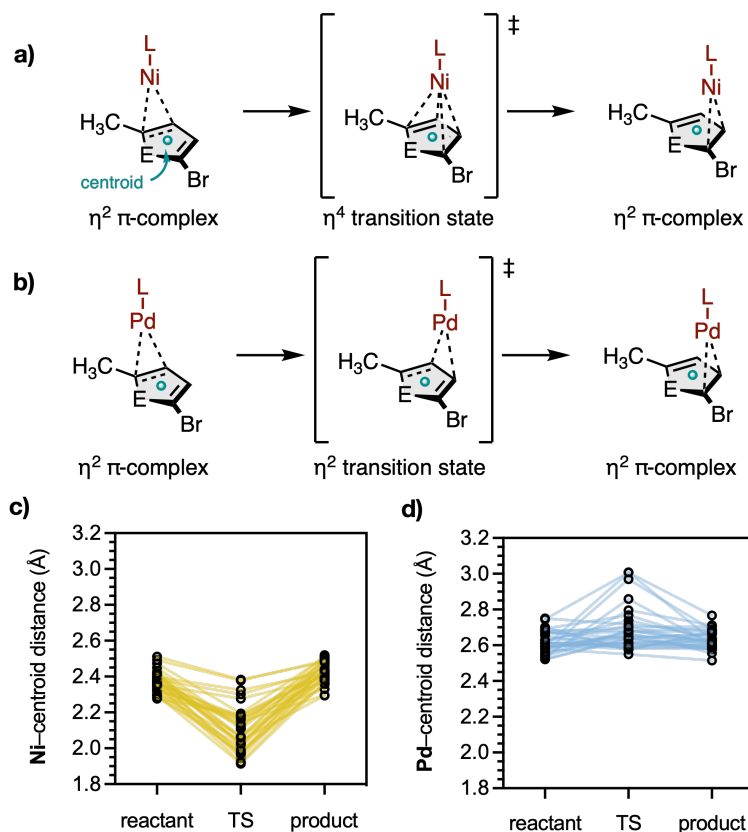
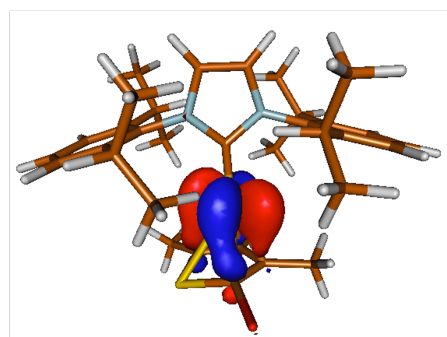
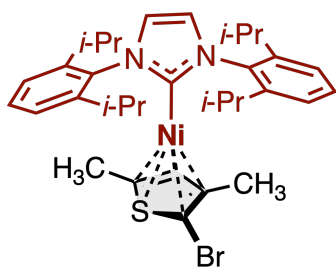


**Figure 4.7** Mechanism of ring-walking for a) Ni  $\pi$ -complexes and b) Pd  $\pi$ -complexes showing differences in the c) Ni-centroid and d) Pd-centroid distances along the reaction path.

The origin of this difference in the geometries of transition states between Ni and Pd likely arises from Ni's increased propensity for backbonding, enabling more donation from Ni to the  $\pi^*$  orbitals during ring-walking. This effect of increased backbonding can be observed in the orbital interactions in the transition states, which show increased overlap of Ni's  $d_{xz}$  orbital (Figure 4.8a) with the arene  $\pi^*$  compared to Pd's  $d_{xz}$  orbital (Figure 4.8b).

a) Ni(IPr) + thiophene



b) Pd(IPr) + thiophene

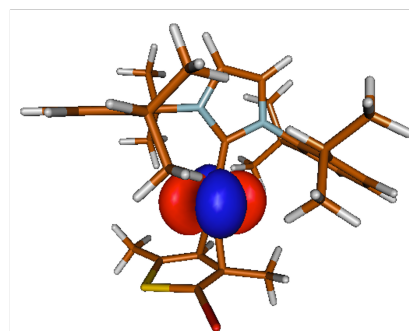
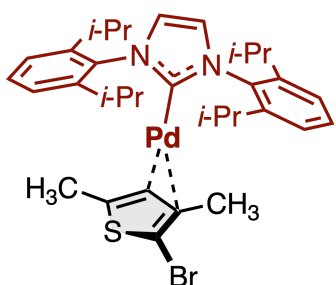


**Figure 4.8** Transition states and backbonding orbitals present in ring-walking of a) Ni(IPr) and b) Pd(IPr) over thiophene. Orbitals are rendered at an isovalue = 0.03.

In addition to the difference in transition state structures of Ni and Pd complexes, the barriers to ring-walking in Pd  $\pi$ -complexes were lower than in Ni  $\pi$ -complexes (Figure 4.9). Given that Ni complexes are more highly bound than Pd complexes, this appears to imply that higher ring-walking barriers result from more strongly bound  $\pi$ -complexes (vide infra). Notably, some of the ring-walking barriers for Pd complexes (particularly for Pd(dppe)) were larger than the  $\pi$ -complex binding energy, indicating that unbinding is preferred to ring-walking in these cases and that CTP would not occur.

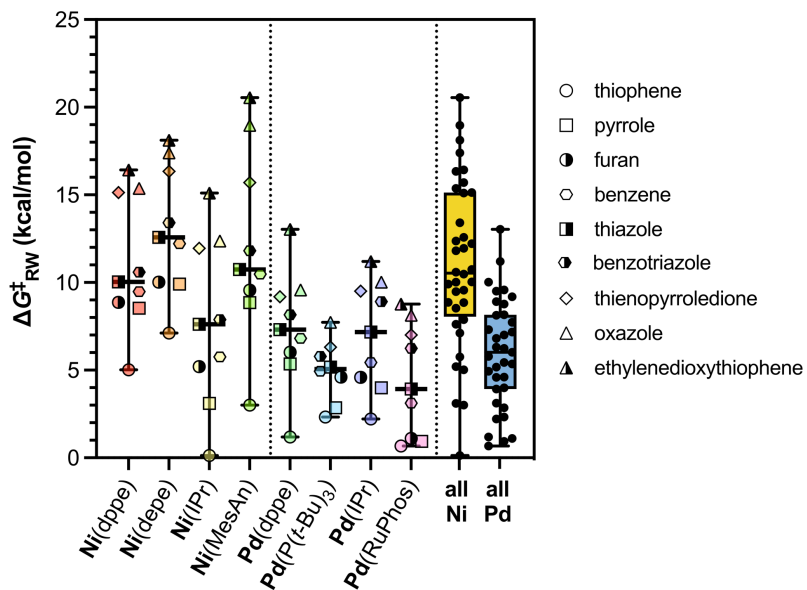


**Figure 4.9** Barriers for ring-walking in Ni and Pd  $\pi$ -complexes.

The relationship between ring-walking barrier and arene identity appears more complicated than the relationship between arene identity and  $\pi$ -binding energy. While the specific cases of TPD (which has high  $\pi$ -binding energy and high ring-walking barriers, Figure 4.10) and pyrrole (which has low  $\pi$ -binding energy and low ring-walking barriers, Figure 4.10) support the idea that more highly-bound  $\pi$ -complexes have higher ring-walking barriers,  $\pi$ -complexes to other arenes do not follow a clear trend. Some pairs of arenes, such as furan and oxazole or thiophene and thiazole, have similar  $\pi$ -binding energies but very different ring-walking barriers. Other arenes, such as benzotriazole and pyrrole, have very different  $\pi$ -binding energies, but similar (low) ring-walking barriers. Indeed, plotting  $\Delta G_{\text{bind}}$  against  $\Delta G_{\text{RW}}^{\ddagger}$  shows that ring-walking barriers are poorly correlated to  $\pi$ -complex binding energies ( $R^2 = 0.39$ , Figure 4.11).

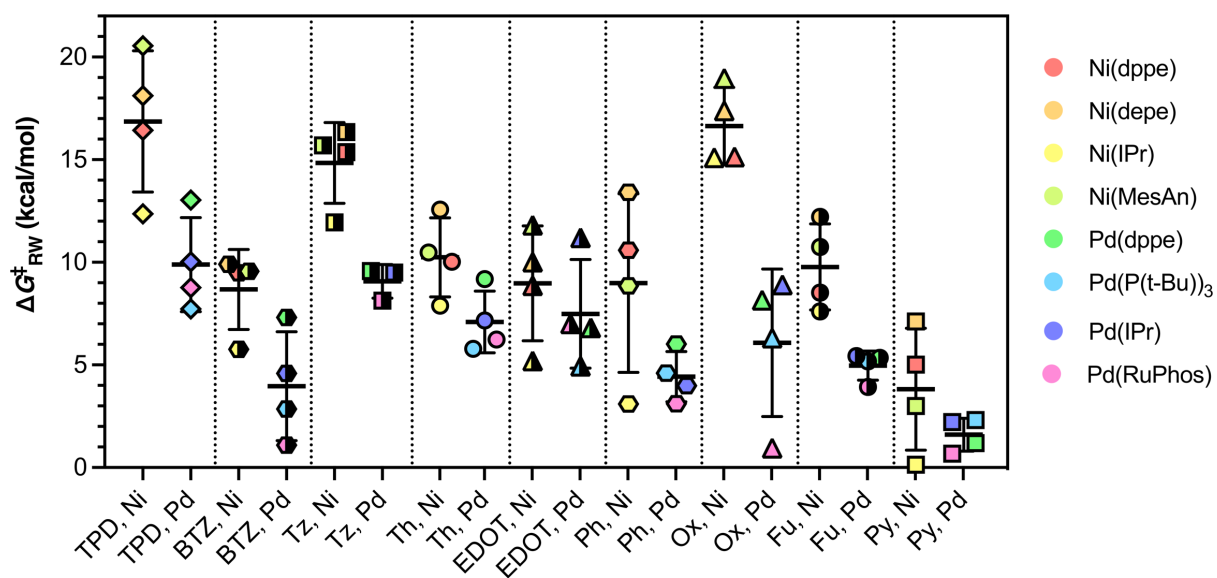


**Figure 4.10**  $\Delta G_{RW}^\ddagger$  for metal/arene  $\pi$ -complexes, sorted by arene  $\pi^*$  energy (increasing to the right).

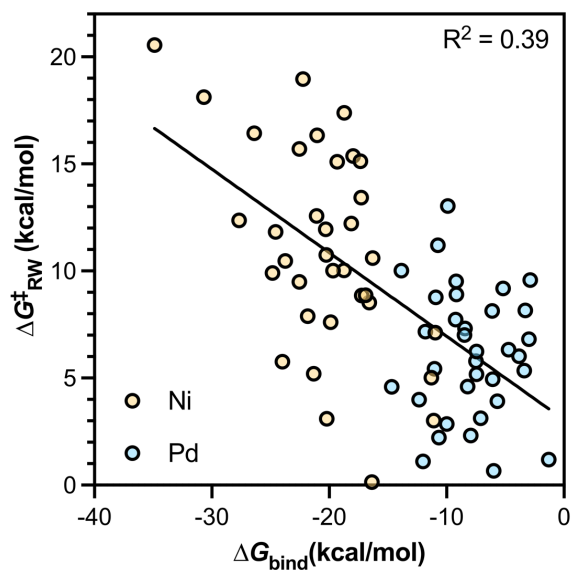


**Figure 4.11**  $\Delta G_{RW}^\ddagger$  vs.  $\Delta G_{bind}$  for the  $\pi$ -complexes in the dataset.

Curiously, the ring-walking barrier had a moderate correlation with the M-to-Ar  $\pi$ -backbonding, indicating that increased  $\pi$ -backbonding from metal to arene is associated with

higher ring-walking barriers (Figure 4.12). Given that  $CT_{M-to-Ar}$  correlates moderately both with the  $\Delta G_{bind}$  and  $\Delta G_{RW}^\ddagger$ , but  $\Delta G_{bind}$  and  $\Delta G_{RW}^\ddagger$  do not correlate with each other, structural features must exist that determine  $\Delta G_{RW}^\ddagger$  that do not affect  $\Delta G_{bind}$  or visa-versa. Given the different substitution patterns of the arenes in our dataset, we attempted to quantify the steric environment of the arenes to understand its effect on ring-walking barriers. However, the buried volume, a common parameter used to describe the size of ligands in metal complexes, correlated poorly with ring-walking barrier (Figure A3.1).

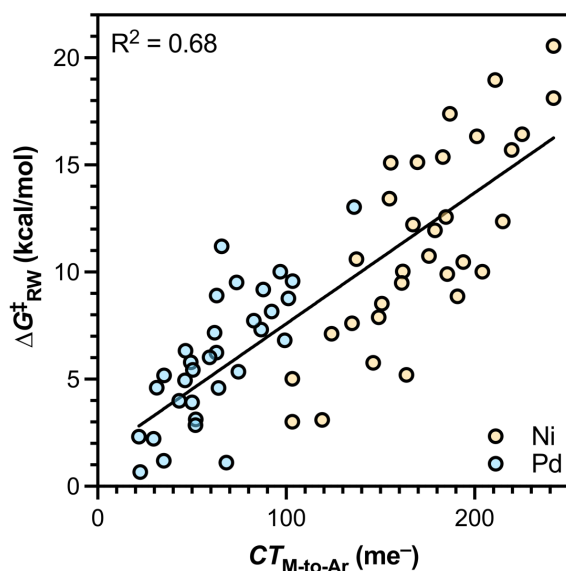


**Figure 4.12**  $\Delta G_{RW}^\ddagger$  of  $\pi$ -complexes as a function of  $CT_{M-to-Ar}$ , the backbonding charge transfer from the metal to the arene in the  $\pi$ -complex.

In contrast, substitution pattern of the ring proved to be useful for describing ring-walking; the complexes in the dataset were broken into 4 classes based on substitution pattern of the arene. Class A contains arenes that have two substituents, Class B corresponded to arenes that have three substituents, Class C contains arenes that have 3 substituents and a N-atom in the ring, and class D contains arenes that have 4 substituents (Figure 4.13a). Moving from class A to class D, we expect the metal catalyst to be more sterically encumbered by the substituents - for class C, the

nitrogen lone pair may provide more bulk given that lone pairs can take up larger volume than bonding electrons.<sup>41</sup> Plotting ring-walking barriers for each class (Figure 4.13b) it seems that the ring-walking barriers increase with the number of substituents on the arene, given that ring-walking for both Ni and Pd complexes is lowest in class A, followed by class B, and highest in classes C and D.

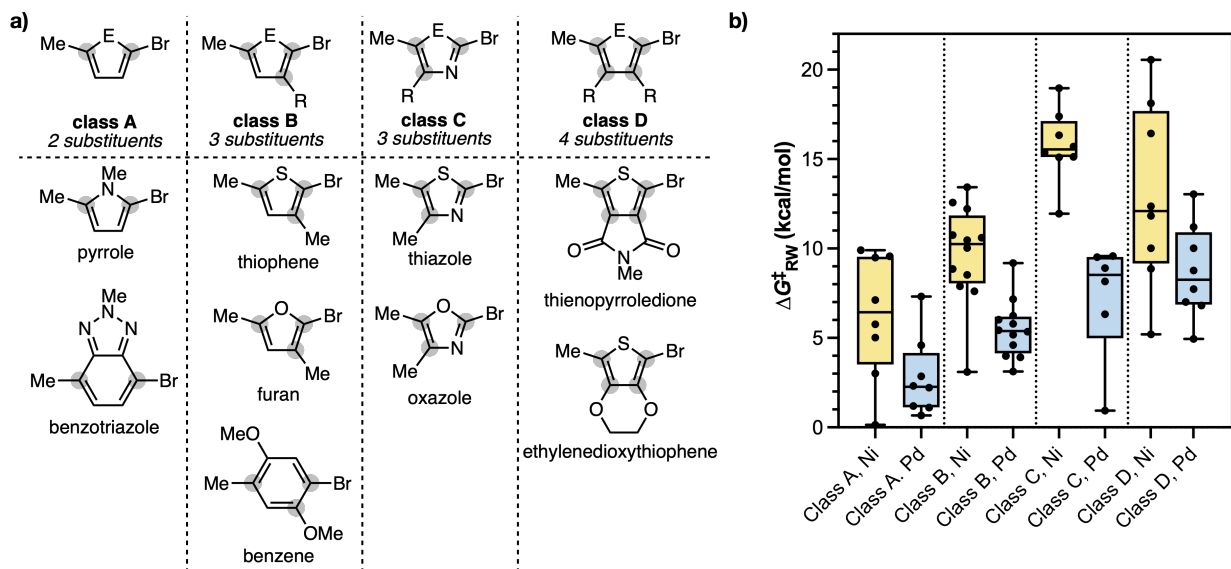


**Figure 4.13** a) classes of arenes based on the number of substituents b) ring-walking barriers within each class.

Potentially, this effect of substituent is also due to the local changes in the electron density with changing substitution. In class A, the  $\pi^*$  orbitals are more highly distributed on the side of the arene closer to the C–Br bond due to the withdrawing effects of halogens, making the  $\pi^*$  orbitals centered on that side of the molecule, therefore enabling attack by the metal d-orbitals. In class B, however, the donating character of the methyl substituent makes the  $\pi^*$  orbitals close to the C–Br bonds less electrophilic, destabilizing the transition state of ring-walking. In class C, the  $\pi^*$  orbital is higher energy due to the presence of the nitrogen, making the incoming  $\pi^*$  bond less susceptible to attack by the metal d-orbitals and therefore destabilizing ring-walking. Lastly, in



class D, the electronic effects of the substituents are cancelled out between reactant and product  $\pi$ -complexes, given the symmetry of substitution, but the increased steric encumbrance potentially causes more steric interactions, destabilizing the transition state. Future studies on ring-walking should therefore consider the substitution of the arene ring as well as the electronic properties of the arenes and catalysts when attempting to understand ring-walking barriers in CTP.

#### 4.5 Conclusions and Outlook

We studied ring-walking in 72  $\pi$ -complexes in CTP to understand the features that affect  $\pi$ -binding energy and ring-walking barriers. We found that  $\pi$ -binding energy correlates with the  $CT_{M-to-Ar}$  (a measure of  $\pi$ -backbonding) and that  $\pi$ -complexes to electron-deficient arenes are more strongly bound than  $\pi$ -complexes to electron-rich arenes. Additionally, we discovered that ring-walking barriers do not correlate strongly with the  $\pi$ -binding energy. Instead, ring-walking barriers mostly correlated with the identity of the metal (with Pd complexes having lower barriers than Ni) and the substitution pattern of the arene, with more highly substituted arenes giving rise to higher barrier ring-walking. These results support the previous hypotheses which stated that Pd-catalysts are more likely to enable CTP in systems where ring-walking is challenging.

The low correlation between ring-walking barrier and binding energy implies that catalysts can be chosen to enable ring-walking without causing catalyst unbinding. Although the barrier to ring-walking is not thought to be problematic in many CTP reactions, using catalysts that enable both high binding energies and low ring-walking barriers may reduce the lifetime of the  $\pi$ -complex, and therefore prevent competitive side reactions that occur from  $\pi$ -complexes. As such, we discourage those who study CTP from assuming that higher  $\pi$ -binding energy results in higher ring-walking barrier, and we encourage others to investigate the structure/property relationships that enable identifying low ring-walking barrier catalysts for CTP.

## 4.6 References

- <sup>1</sup> Bryan, Z. J.; McNeil, A. J. Conjugated Polymer Synthesis via Catalyst-Transfer Polycondensation (CTP): Mechanism, Scope, and Applications. *Macromolecules* **2013**, *46*, 8395–8405.
- <sup>2</sup> Yokoyama, A.; Miyakoshi, R.; Yokozawa, T. Chain-Growth Polymerization for Poly(3-hexylthiophene) with a Defined Molecular Weight and a Low Polydispersity. *Macromolecules* **2004**, *37*, 1169–1171.
- <sup>3</sup> Sheina, E. E.; Liu, J.; Iovu, M. C.; Laird, D. W.; McCullough, R. D. Chain Growth Mechanism for Regioregular Nickel-Initiated Cross-Coupling Polymerizations. *Macromolecules* **2004**, *37*, 3526–3528.
- <sup>4</sup> Yokozawa, T.; Ohta, Y. Transformation of Step-Growth Polymerization into Living Chain-Growth Polymerization. *Chem. Rev.* **2016**, *116*, 1950–1968.
- <sup>5</sup> Lutz, J. P.; Hannigan, M. D.; McNeil, A. J. Polymers synthesized via catalyst-transfer polymerization and their applications *Coord. Chem. Rev.* **2018**, *376*, 225–247.
- <sup>6</sup> Schon, T. B. ; McAllister, B. T. ; Li, P. - F. ; Seferos, D. S. The Rise Of Organic Electrode Materials For Energy Storage. *Chem. Soc. Rev.* **2016**, *45*, 6345 - 6404.
- <sup>7</sup> Leone, A. K.; McNeil, A. J. Matchmaking in Catalyst-Transfer Polycondensation: Optimizing Catalysts based on Mechanistic Insight *Acc. Chem. Res.* **2016**, *49*, 2822–2831.
- <sup>8</sup> Balcells, D.; Nova, A. Designing Pd and Ni Catalysts for Cross-Coupling Reactions by Minimizing Off-Cycle Species *ACS Catal.* **2018**, *8*, 3499–3515.
- <sup>9</sup> Trost, B. M.; Crawley, M. L. Asymmetric Transition-Metal-Catalyzed Allylic Alkylations: Applications in Total Synthesis. *Chem. Rev.* **2003**, *103*, 2921–2944.
- <sup>10</sup> Chen, X., Engle, K. M., Wang, D. H. & Yu, J. Q. Palladium (II)-catalyzed C–H activation/C–C cross-coupling reactions: versatility and practicality. *Angew. Chem., Int. Ed.* **2009**, *48*, 5094–5115.
- <sup>11</sup> Barnard, C. F. J. Palladium-Catalyzed Carbonylation—A Reaction Come of Age. *Organometallics* **2008**, *27*, 5402–5422.
- <sup>12</sup> Lyons, T. W. & Sanford, M. S. Palladium-catalyzed ligand-directed C–H functionalization reactions. *Chem. Rev.* **2010**, *110*, 1147–1169.
- <sup>13</sup> Churchill, D. G.; Janak, K. E.; Wittenberg, J. S.; Parkin, G. Normal and Inverse Primary Kinetic Deuterium Isotope Effects for C–H Bond Reductive Elimination and Oxidative Addition Reactions of Molybdenocene and Tungstenocene Complexes: Evidence for Benzene  $\sigma$ -Complex Intermediates. *J. Am. Chem. Soc.* **2003**, *125*, 1403–1420.
- <sup>14</sup> Hratchian, H. P.; Chowdhury, S. K.; Gutierrez-García, V. M.; Amarasinghe, K. K. D.; Heeg, M. J.; Schlegel, H. B.; Montgomery, J. Combined Experimental and Computational Investigation of the Mechanism of Nickel-Catalyzed Three-Component Addition Processes. *Organometallics* **2004**, *23*, 4636–4646.
- <sup>15</sup> Massera, C.; Frenking, G. Energy Partitioning Analysis of the Bonding in  $L_2TM-C_2H_2$  and  $L_2TM-C_2H_4$  ( $TM = Ni, Pd, Pt$ ;  $L_2 = (PH_3)_2, (PMe_3)_2, H_2PCH_2PH_2, H_2P(CH_2)_2PH_2$ ). *Organometallics* **2003**, *22*, 2758–2765.
- <sup>16</sup> Sontag, S. K.; Bilbrey, J. A.; Huddleston, N. E.; Sheppard, G. R.; Allen, W. D.; Locklin, J.  $\pi$ -Complexation in Nickel-Catalyzed Cross-Coupling Reactions. *J. Org. Chem.* **2014**, *79*, 1836–1841.
- <sup>17</sup> Leone, A. K.; Goldberg, P. K.; McNeil, A. J. Ring-Walking in Catalyst-Transfer Polymerization. *J. Am. Chem. Soc.* **2018**, *25*, 7846–7850.

- 
- <sup>18</sup> Smith, M. L.; Leone, A. K.; Zimmerman, P. M.; McNeil, A. J. Impact of Preferential  $\pi$ -Binding in Catalyst-Transfer Polycondensation of Thiazole Derivatives *ACS Macro Lett.* **2016**, *5*, 1411–1415.
- <sup>19</sup> Willot, P.; Koeckelberghs, G. Evidence for Catalyst Association in the Catalyst Transfer Polymerization of Thieno[3,2-*b*]thiophene. *Macromolecules* **2014**, *47*, 8548–8555.
- <sup>20</sup> Jarrett-Wilkins, C. N.; Pollit, A. A.; Seferos, D. S. Polymerization Catalysts Take A Walk On The Wild Side. *Trends. Chem.* **2020**, *2*, 493–505.
- <sup>21</sup> Bilbrey, J. A.; Bootsma, A. N.; Bartlett, M. A.; Locklin, J.; Wheeler, S. E.; Allen, W. D. Ring-Walking of Zerovalent Nickel on Aryl Halides. *J. Chem. Theory Comput.* **2017**, *13*, 1706–1711.
- <sup>22</sup> D' Accriscio, F.; Ohleier, A.; Nicolas, E.; Demange, M.; Du Boullay, O. T.; Saffon-Merceron, N.; Fustier-Boutignon, M.; Rezabal, E.; Frison, G.; Nebra, N.; Mézailles, N. [(dcpp)Ni( $\eta^2$ -Arene)] Precursors: Synthesis, Reactivity, and Catalytic Application to the Suzuki-Miyaura Reaction. *Organometallics* **2020**, *39*, 1688–1699.
- <sup>23</sup> Lau, S. H.; Chen, L.; Kevlishvili, I.; Davis, K.; Liu, P.; Carrow, B. Capturing the Most Active State of a Palladium(0) Cross-Coupling Catalyst *ChemRxiv* **2021**. DOI: <https://doi.org/10.33774/chemrxiv-2021-477kn>
- <sup>24</sup> He, W.; Patrick, B. O.; Kennepohl, P. Identifying the Missing Link in Catalyst Transfer Polymerization *Nat. Commun.* **2018**, *9*, 3866.
- <sup>25</sup> Lanni, E. L.; McNeil, A. J. Mechanistic Studies on Ni(dppe)Cl<sub>2</sub>-Catalyzed Chain-Growth Polymerizations: Evidence for Rate-Determining Reductive Elimination *J. Am. Chem. Soc.* **2009**, *131*, 16573–16579.
- <sup>26</sup> Lanni, E. L.; McNeil, A. J. Evidence for Ligand-Dependent Mechanistic Changes in Nickel-Catalyzed Chain-Growth Polymerizations. *Macromolecules* **2010**, *43*, 8039–8044.
- <sup>27</sup> Nojjima, M.; Ohta, Y.; Yokozawa, T. Investigation of Catalyst-Transfer Condensation Polymerization for Synthesis of Poly(p-phenylenevinylene) *J. Polym. Sci. A. Polym. Chem.* **2014**, *52*, 2643–2653.
- <sup>28</sup> Bedi, A.; De Winter, J.; Gerbaux, P.; Koeckelberghs, G. Detrimental Ni(0) Transfer in Kumada Catalyst Transfer Polycondensation of Benzo[2,1-*b*:3,4-*b'*]dithiophene. *J. Polym. Sci. A - Polym. Chem.* **2016**, *54*, 1706–1712.
- <sup>29</sup> Pollit, A. A.; Ye, D.; Seferos, D. S. Elucidating the Role of Catalyst Steric and Electronic Effects in Controlling the Synthesis of  $\pi$ -Conjugated Polymers *Macromolecules* **2020**, *53*, 138–148.
- <sup>30</sup> Mueller, E. A.; Leone, A. K.; McNeil, A. J. The History of Palladium-Catalyzed Cross-Couplings Should Inspire the Future of Catalyst-Transfer Polymerization. *J. Am. Chem. Soc.* **2018**, *140*, 15126–15139.
- <sup>31</sup> Magnin, G.; Clifton, J.; Schoenebeck, F. A General and Air-tolerant Strategy to Conjugated Polymers within Seconds under Palladium(I) Dimer Catalysis. *Angew. Chem., Int. Ed.* **2019**, *58*, 10179–10183.
- <sup>32</sup> Lee, J.; Kim, H.; Park, H.; Kim, T.; Hwang, S.-H.; Seo, D.; Chung, T. D.; Choi, T.-L. Universal Suzuki–Miyaura Catalyst-Transfer Polymerization for Precision Synthesis of Strong Donor/Acceptor-Based Conjugated Polymers and Their Sequence Engineering. *J. Am. Chem. Soc.* **2021**, *143*, 11180–11190.
- <sup>33</sup> Zimmerman, P. M. Single-Ended Transition State Finding with the Growing-String Method. *J. Comput. Chem.* **2015**, *36*, 601–611.
- <sup>34</sup> Zimmerman, P. M. Growing String Method with Interpolation and Optimization in Internal Coordinates: Method and Examples. *J. Chem. Phys.* **2013**, *138*, 184102.

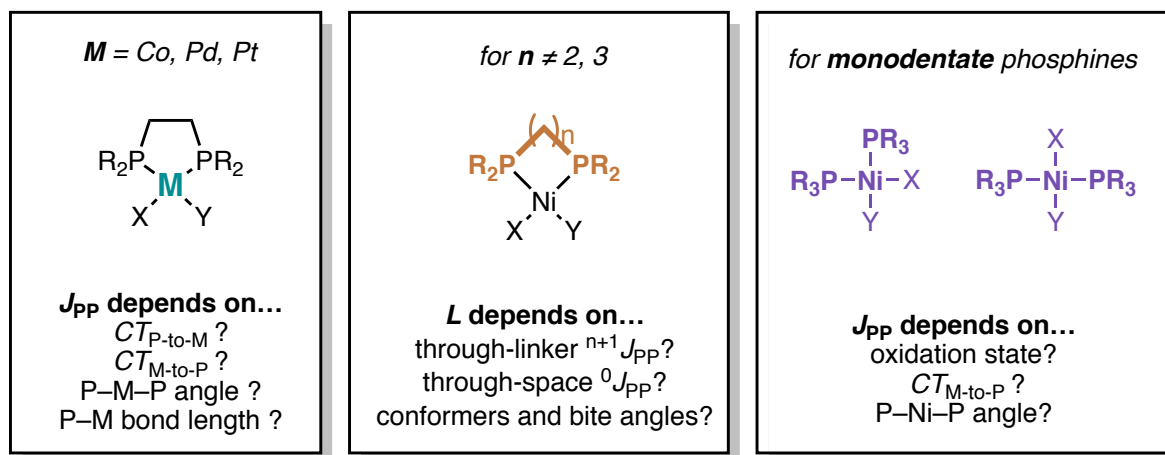
- 
- <sup>35</sup> Nett, A. J.; Zhao, W.; Zimmerman, P. M.; Montgomery, J. Highly Active Nickel Catalysts for C–H Functionalization Identified through Analysis of Off-Cycle Intermediates. *J. Am. Chem. Soc.* **2015**, *137*, 7636–7639
- <sup>36</sup> Ludwig, J. R.; Zimmerman, P. M.; Gianino, J. B.; Schindler, C. S. Iron(III)-Catalysed Carbonyl–Olefin Metathesis. *Nature* **2016**, *533*, 374–379.
- <sup>37</sup> Pendleton, I. M.; Perez-Temprano, M. H.; Sanford, M. S.; Zimmerman, P. M. Experimental and Computational Assessment of Reactivity and Mechanism in C(sp<sup>3</sup>)–N Bond-Forming Reductive Elimination from Palladium(IV). *J. Am. Chem. Soc.* **2016**, *138*, 6049–6060.
- <sup>38</sup> Smith, M. L.; Leone, A. K.; Zimmerman, P. M.; McNeil, A. J. Impact of Preferential  $\pi$ -Binding in Catalyst-Transfer Polycondensation of Thiazole Derivatives. *ACS Macro Lett.* **2016**, *5*, 1411–1415.
- <sup>39</sup> Vitek, A. K.; Leone, A. K.; McNeil, A. J.; Zimmerman, P. M. Spin-Switching Transmetalation at Ni Diimine Catalysts. *ACS Catal.* **2018**, *8*, 3655–3566.
- <sup>40</sup> Desnoyer, A. N.; He, W.; Behyan, S.; Chiu, W.; Love, J. A.; Kennepohl, P. The Importance of Ligand-Induced Backdonation in the Stabilization of Square Planar d<sup>10</sup> Nickel  $\pi$ -Complexes. *Chem. Eur. J.* **2019**, *25*, 5259–5268.
- <sup>41</sup> Rouse, R. A. The Physical Nature of The Lone Pair. *Theo. Chim. Acta* **1976**, *41*, 149–156.

## Chapter 5 Conclusions and Outlook

Conjugated polymers have many uses in organic electronic materials, but the limited scope of chain-growth polymerizations that exist for synthesizing conjugated polymers limits chemists from understanding how polymer structure impacts properties and performance. Expanding catalyst-transfer polymerization into a more general method of conjugated polymer synthesis would likely enable insight into these structure-performance relationships, however, efforts to expand the monomer scope of CTP are rarely successful. Part of this lies in the difficulty of *characterizing* key intermediates, such as the  $\pi$ -complexes or off-cycle complexes. Additionally, our inability to interrogate the reactions that lead to off-cycle reactivity precludes rational catalyst design. Studies described in this dissertation provide new insights into CTP that will benefit researchers by expanding our ability to characterize intermediates and understand the reactions that have prevented expanding the monomer scope.

In Chapter 2, we discussed the effect of the structure of Ni bidentate phosphine complexes on spectral properties. Particularly, we identified that complexes with different phosphine linker lengths have different values of  $J_{PP}$ , and that the sign and magnitude of  $J_{PP}$  are related to the structure of the complex.  $Ni^0$  complexes have more positive values of  $J_{PP}$  than  $Ni^{II}$  complexes, and complexes with 3-carbon linkers have more negative  $J_{PP}$  than complexes with 2-carbon linkers. Due to the differences between the  $J$ -couplings of complexes with different oxidation states and linker lengths, we were able to show that  $J_{PP}$  can be a reliable indicator of oxidation state if the

linker length is known. However, open questions remain with regard to  $J_{PP}$  in metal complexes, discussed below (Scheme 5.1).



**Scheme 5.1** Areas of investigation for future studies into  $J_{PP}$  of metal complexes.

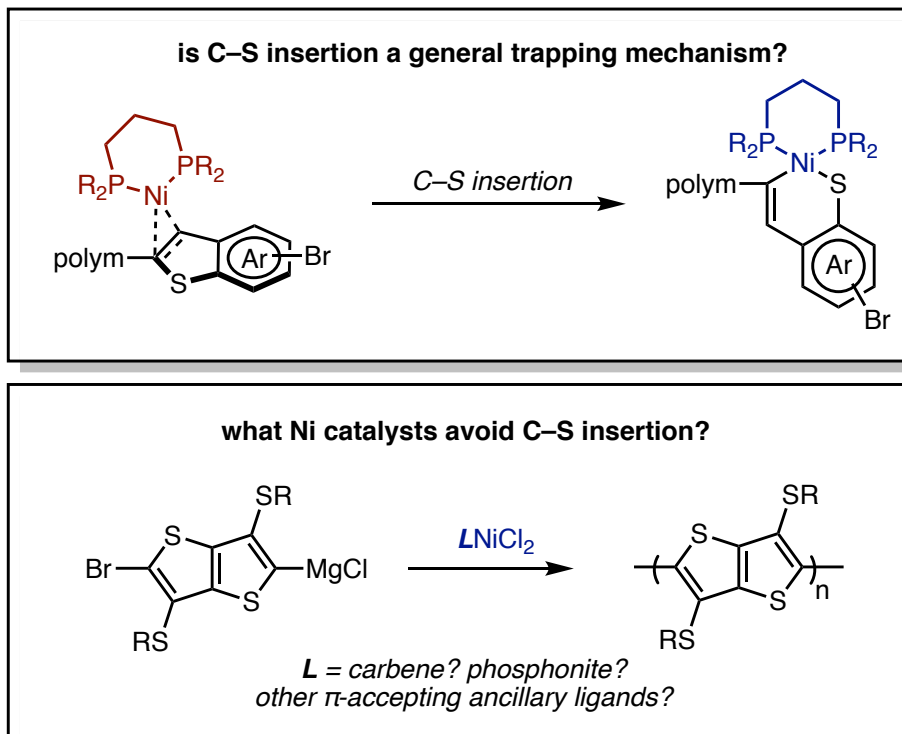
With regard to coordination chemistry, it is unknown if the results from our study (i.e., the dependence on phosphorus donation and linker length) are transferable to other systems, such as Co or Pd complexes, or whether the  $J_{PP}$  constants in other systems will require new models which incorporate terms describing backbonding, P–M bond length, bite angle, or other features. Additionally, while the  $L$  term enabled us to account for the differences in through-linker coupling due to differences in linker length, but it arose from empirically observing the trends in our dataset. Expanding the utility of a  $J_{PP}$  analysis for Ni complexes with different linkers would likely require deliberately studying the  $L$ -term and quantifying the effect of through-space  $J$ -coupling of P-atoms, the effect of bite angle on  $J_{PP}$ , or even conformer effects that would be present in ligands with flexible linkers.

While Ni bidentate phosphine complexes make up a large class of complexes, Ni complexes with monodentate phosphines make up an even larger class, especially when considering the types of complexes used in synthetic reactions. Given that all of the complexes in

our study had P-atoms *cis* on the Ni, but many monodentate phosphine complexes have geometries in which phosphine ligands are *trans*, it is unclear whether the relationships disclosed in our study are applicable to monodentate phosphine systems, and further studies on monodentate complexes will be needed to address the effects of ligand electronics on their  $J_{PP}$ .

Lastly, for catalyst-transfer polymerization, many of the catalysts that enable CTP are Ni bidentate phosphines (for which  $J_{PP}$  analysis is feasible), but many catalysts with other metal or ligand identities also catalyze CTP. Therefore, identifying similar *in situ* analysis methods for other complexes would be highly useful for analyzing CTP, especially for Ni and Pd carbene complexes which are commonly used in CTP.

In Chapter 3, we elucidated the structure of the catalyst trap that forms in the polymerization of thienothiophene.  $J_{PP}$  values observed in  $^{31}\text{P}$  NMR were key to assigning the oxidation state of the catalyst trap and computational reaction path discovery tools enabled us to reveal that C–S insertion causes trapping. C–S insertion mechanisms has not been observed to cause trapping in other CTP reactions, but experimental evidence from this study as well as the results of previous studies on small molecules support the viability of this trapping mechanism. Given that thienothiophenes are common in many high-performing conjugated polymers, future efforts aimed at developing catalysts that undergo ring-walking and avoid C–S insertion would be necessary for enabling the synthesis of high-performance conjugated polymers via CTP. Additionally, related fused arenes like benzothiophene have been shown to undergo C–S insertion in small molecule systems, indicating it is possible that C–S insertion may represent a more general trapping mechanism for fused arene systems. Further investigations into expanding the monomer scope of CTP therefore must evaluate the relevance of C–S insertion in CTP, as well as analogous insertions into non-traditional electrophiles, to understand whether these limit the monomer scope.

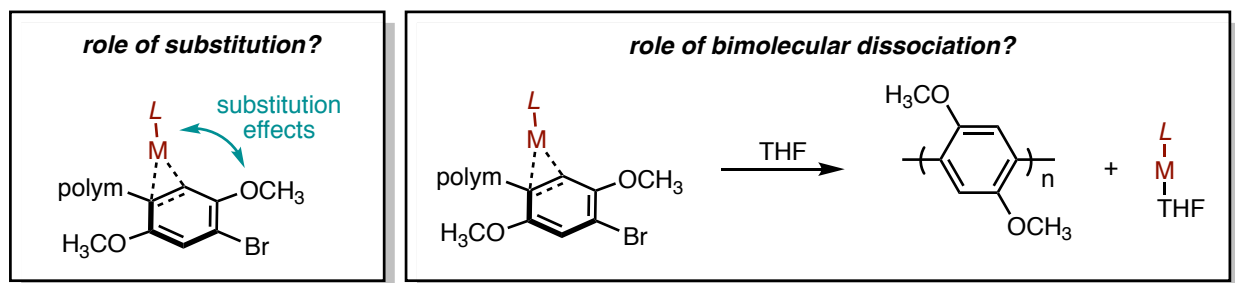


**Scheme 5.2** Areas of investigation for future studies into CTP of fused arenes.

Lastly, in Chapter 4 we explored the effect of monomer and catalyst structure on  $\pi$ -binding and ring-walking. We found that  $\pi$ -binding energies followed the Dewar-Chatt-Duncanson model, indicating that Ni  $\pi$ -complexes are more strongly bound than Pd  $\pi$ -complexes, and  $\pi$ -complexes to electron-deficient arenes are more strongly bound than  $\pi$ -complexes to electron-rich arenes. Additionally, we screened ring-walking barriers over these arenes. While we found that Ni  $\pi$ -complexes generally have higher ring-walking barriers than Pd  $\pi$ -complexes, we also found that there was only a weak correlation between ring-walking barrier and  $\pi$ -complex binding energy. Instead, our computations suggest that ring-walking barrier may have a steric dependence or a dependence on the substitution of the ring, with  $\pi$ -complexes to less-substituted rings having lower ring-walking barriers. Open questions remain (Scheme 5.3) - while we found that there was a dependence of ring-walking barrier on the steric encumbrance of the arene, it is still unclear what



steric parameters are best for quantifying its effect on ring-walking. Buried volume was a poor predictor of ring-walking barrier, and similar parameters (such as cone angle) are poorly defined for some classes of complexes used in CTP (i.e., bidentate ligands). Substitution pattern was marginally correlated with ring-walking but limiting given that substitution is a discrete (i.e., not continuous) variable and generally the substitution pattern of the arene is difficult to modulate without affecting other parts of the catalytic cycle. Additionally, our study does not address the competition between ring-walking barrier and *bimolecular* dissociation, which is likely a mode of dissociation in some of the  $\pi$ -complexes in our study. To obtain a model that more accurately predicts the success of a monomer/catalyst pair based on ring-walking barriers and  $\pi$ -binding energies, then both unimolecular and bimolecular dissociation mechanisms need to be considered.



**Scheme 5.3** Areas of investigation for future studies into ring-walking and reactions of  $M^0$  complexes in CTP.

Catalyst-transfer polymerization poses many challenging problems, requiring broad expertise (i.e., in organometallic, analytical, organic, and physical chemistry) to elucidate its mechanism, key intermediates, or monomer scope limitations. I anticipate that the challenges of analyzing CTP or expanding its monomer scope will remain for some time. However, I also anticipate that the studies described herein will enable future investigators to more easily understand the species that form during CTP as well as the on-cycle or off-cycle reactivity of these species. Hopefully future investigations will eventually result in expanded monomer scope of CTP,

or result in new post-CTP methods of chain-growth polymerizations for conjugated polymer synthesis that enable broader access to precision materials.

## Appendices

## Appendix 1 Supporting Information for Using *J*<sub>PP</sub> to Identify Ni Bidentate Phosphine Complexes in Situ

### A1.1 Dataset Construction and Processing

All of the Ni bidentate phosphine complexes used in this analysis were reported in the literature before December 22<sup>nd</sup> 2020. The process used to identify complexes is described below.

#### A1.1.1 Two-carbon linker dataset

The complexes containing 2-carbon linkers were found via a substructure search of the Reaxys database. The MarvinJS structure editor was used, and the specific structure query is shown in Figure A1.1.

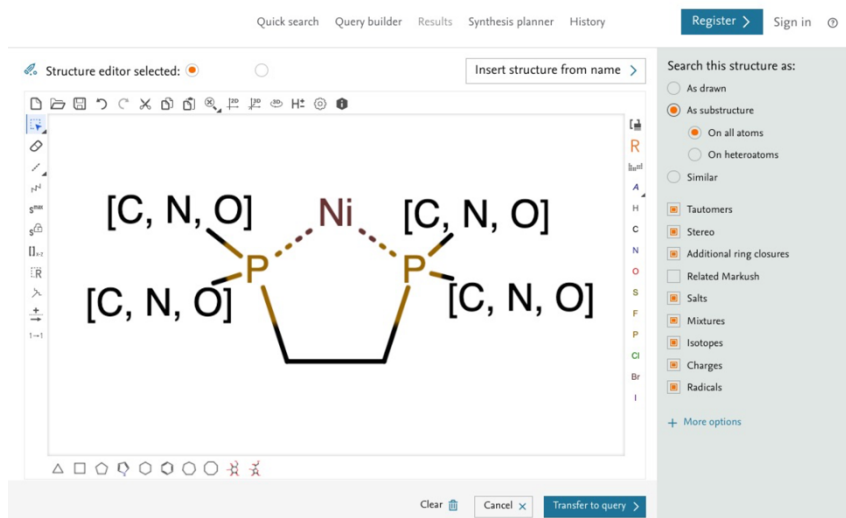


**Figure A1.1** The query used for identifying complexes with 2-carbon backbones. The dotted bonds between P and Ni correspond to “any” bond. The [C,N,O] group attached to the P atoms enables search for structures with P–C, P–N, and P–O bonds.

The results of this query were limited to structures that contain “Interatomic Distances and Angles” (Figure A1.2) as available data, effectively narrowing the dataset to complexes that have single-crystal X-ray diffraction structures reported. This dataset had 812 complexes.

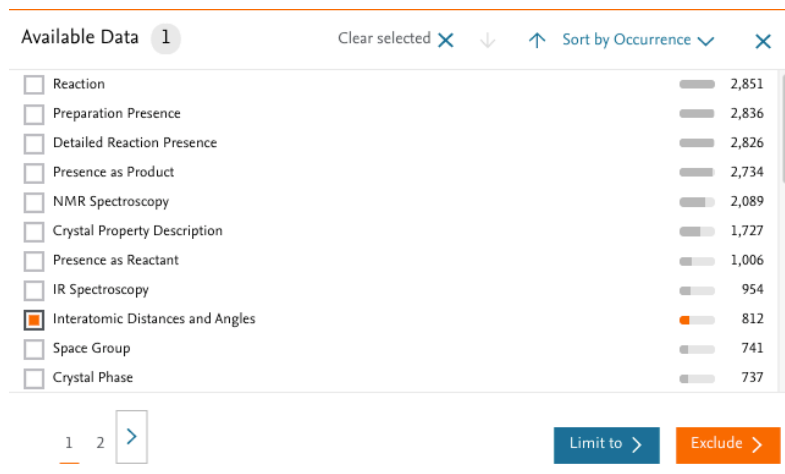


**Figure A1.2** Narrowing the query results by using available data; specifically, only those substances that contain single-crystal X-ray structures by selecting only "Interatomic Distances and Angles".

An additional filter was applied to limit the dataset to complexes that contain “NMR Spectroscopy” (Figure A1.4) as available data, narrowing the dataset to complexes that have been analyzed by NMR spectroscopy (although, this includes NMR spectra of any nucleus). This dataset had 509 complexes.

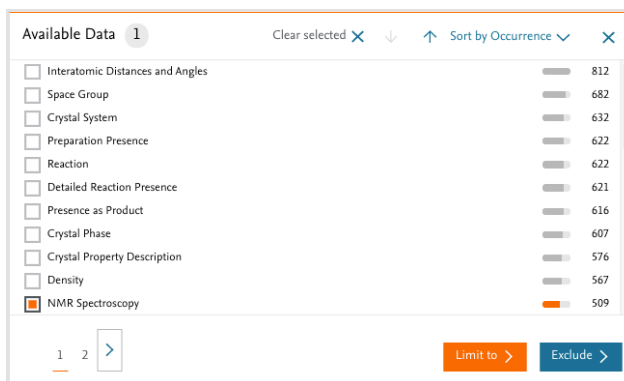


**Figure A1.3** Narrowing down the query results by using available data; specifically, only those substances that contain reported NMR Spectroscopy by selecting only "NMR Spectroscopy".

Lastly, using the filter by structure option, complexes that contain the following substructures were excluded, resulting in 449 substances.



**Figure A1.4** Substructures used as filters to exclude tridentate P ligands.

### A1.1.2 Three-carbon linker dataset

The complexes containing 3-carbon linkers were found via a substructure search using the MarvinJS structure editor in Reaxys. The structure query is shown in Figure A1.5 and yielded 790 substances:

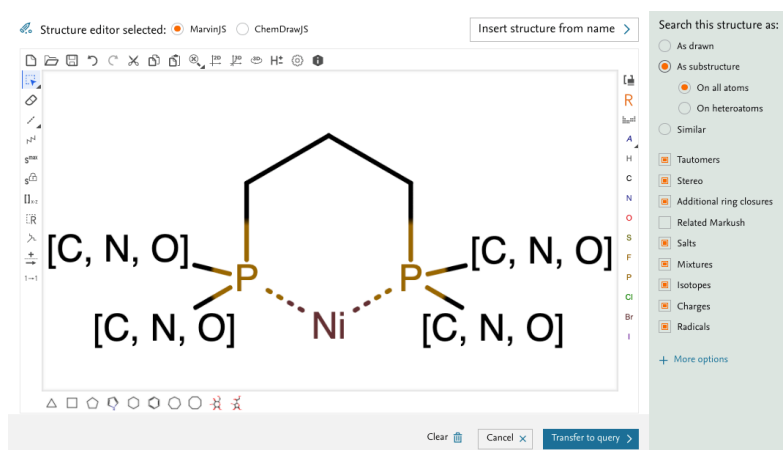


**Figure A1.5** The query used for the substructure search for Ni complexes with 3-carbon linkers. Dotted lines correspond to "any" bond between P and Ni, and the [C,N,O] enables a search for any substructures that have P–C, P–N, or P–O bonds.

The dataset was limited to substances that contain "NMR Spectroscopy" as available data (Figure A1.6), yielding 388 substances.

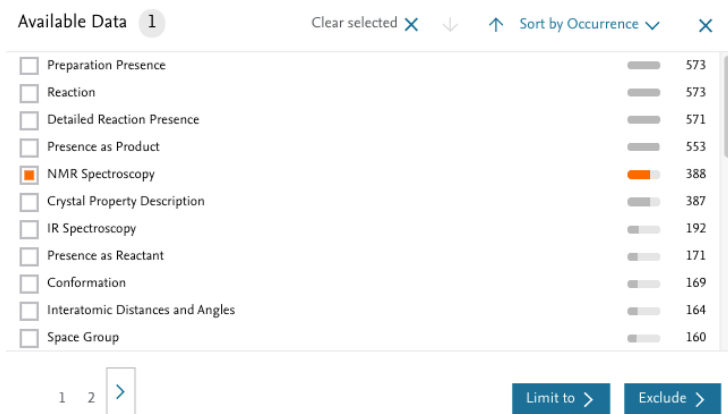


**Figure A1.6** Narrowing down the query results by using available data; specifically, only those substances that contain reported NMR Spectroscopy.

At this point, for the 2C dataset, we applied an interatomic distances and angles filter. However, when the 3-carbon linker dataset was limited to structures that also had reported "Interatomic Distances and Angles" (i.e. the same filters as for the 2-carbon linker dataset) the size of the resulting 3-carbon linker dataset was only 52 complexes, the majority of which did not contain a  $J_{PP}$  due to symmetry of the P-atoms across the metal center. After manually processing the dataset to remove complexes that did not have a  $J_{PP}$  (vide infra), the final 3-carbon linker dataset only contained 20 complexes (17 Ni<sup>II</sup> complexes, 3 Ni<sup>0</sup> complexes). Given the low statistical significance of such a small dataset, the interatomic distances and angles filter was not applied to construct the final 3-carbon dataset. However, because the number of structures in the 2-carbon dataset was sufficiently large with this filter included, and crystal structures enable more reliable assignment of structure and oxidation state, this filter was kept for the 2-carbon dataset.

Lastly, using the "filter by structure" option, tridentate structures were excluded. This filter excludes many substances that have tetrahedral Ni (such as complexes bearing triphos type ligands), narrowing the dataset to 272 substances.

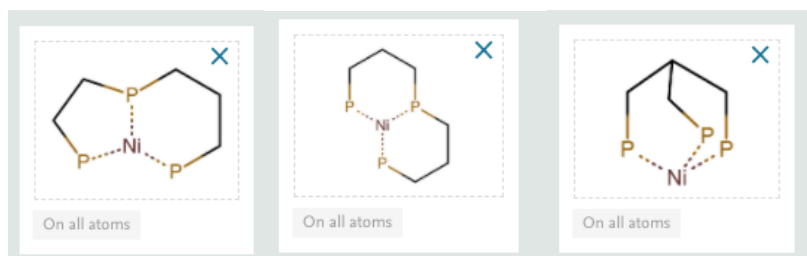


**Figure A1.7** Tridentate substructures used as filter structures to exclude phosphine complexes with trans  $J_{PP}$  values.

### ***A1.1.3 Manual dataset processing***

The results of both searches were exported from Reaxys as Microsoft Excel spreadsheets, containing the structure; identifiers; molecular formula; molecular weight; "interatomic distance and angle" information; parameters for NMR spectroscopy such as nucleus, temperature, magnet strength, and solvent; and the references to papers that report the substance. The sheet was sorted in order of increasing molecular weight, then compounds in these sheets were numbered with an ID of the form 2-2#### (starting from 2-2001) for 2C complexes and 3-3#### (starting from 3-3001) for 3C complexes. Then, this sheet was edited to only include structures that contained  $^{31}\text{P}$  NMR data (by using the "Nucleus NMR Spectroscopy" column in the exported excel sheet) because the "NMR Spectroscopy" filter applied in the initial substructure search only does not consider the nucleus reported. Numbering the complexes before processing is the reason the compounds in Tables S4 and S5 are not numbered sequentially.

Reaxys does not store NMR data itself in the database, so the  $J_{PP}$  and chemical shifts for each complex were obtained by reading the original journal articles and associated supporting information files. Reaxys did provide information on the "Coupling Nuclei" in the exported Excel sheet, but we found that there were many examples in the datasets where no coupling nucleus was listed, but the actual journal article detailing the compound reported a  $J_{PP}$ . Similarly, there were examples where the coupling nucleus listed in the excel sheet was not  $^{31}\text{P}$ , but a  $J_{PP}$  was reported



in the journal article. This error in coupling nucleus most often occurred when P atoms were coupled to multiple nuclei such as in the case of compounds containing  $^{19}\text{F}$ , where there was observable  $J_{\text{FP}}$  coupling and  $J_{\text{PP}}$  coupling in the  $^{31}\text{P}$  NMR spectra. Therefore, we do not recommend using the “coupling nucleus” data provided by Reaxys as a means to filter results in future investigations.

Single crystal XRD data (.cif files) were downloaded from the original journal articles or the Cambridge Crystallographic Data Centre. The oxidation state of the Ni in each complex was determined by searching for the presence of counterions in the crystal structure and/or counting electrons for each complex based on the Lewis structure.<sup>1</sup> For the complexes in the 3-carbon linker dataset that did not have single crystal XRD data, the oxidation state at Ni was evaluated by counting electrons for the reported Lewis structure in the original journal articles. Structures were excluded from the datasets if they satisfied any of the following criteria:

- The complex was symmetric with respect to  $C_2$  rotation or reflection of the P atoms across the metal center, such as for square-planar complexes like  $\text{Ni}(\text{dppe})\text{Cl}_2$ , tetrahedral complexes like  $\text{Ni}(\text{dppp})(\text{CO})_2$ , or trigonal-planar complexes like  $\text{Ni}(\text{dippe})(\text{ethylene})$ . These types of complexes were excluded because  $J$ -coupling between P atoms is not observed in  $^{31}\text{P}$  NMR spectra if P-atoms are equivalent. Note: Few tetrahedral complexes remained after this filter because tetrahedral Ni complexes with symmetric bidentate phosphine ligands have equivalent P atoms regardless of the identities of the *trans* ligands.
- The complex contained a non-innocent ligand. These complexes were excluded because oxidation state is poorly defined in these systems.
- The  $^{31}\text{P}$  NMR spectra contained broad peaks. These complexes were excluded

because  $J$ -coupling is not resolvable.

- The only  $J_{PP}$  observed was a *trans* or exocyclic  $^2J_{PP}$ , such as in Ni(dcppe)PCy<sub>3</sub> or Ni(dppe)(dppp)Cl<sub>2</sub>. These complexes were excluded because these  $J_{PP}$  are expected to arise from different orbital interactions than *cis*  $J_{PP}$  and are therefore outside the scope of our study.
- The <sup>31</sup>P NMR spectra contained only one singlet. These complexes were excluded because the presence of only one singlet indicates the structure in solution has a tetrahedral geometry, is not diamagnetic, or is fluxional with respect to geometry at the metal. Treatment of spectra that contained two singlets is detailed below.
- For the 2-carbon case only, data was excluded if a single crystal X-ray structure could not be found. This occurred when there was an entry for the structure in the Cambridge Crystallographic Database, but no coordinates were available for the entry.

Some structures in the dataset only contained two singlets of equal intensity in reported <sup>31</sup>P NMR spectra, but were square planar at Ni and non-symmetric (i.e., contained P atoms in the bidentate ligand that had different chemical shifts). In these cases, the  $J$ -coupling was recorded as 0.0 Hz. These structures are indicated in Tables S4 and S5 with an asterisk next to the reported  $J_{PP}$  value (e.g., compound **2-2003**).

Many journal articles that were found via the Reaxys substructure search contained additional Ni complexes not already in our Reaxys dataset. When these complexes were found, the structures and relevant information were added to our dataset if they satisfied the criteria outlined above (usually with an ID number that contains a trailing letter, e.g., compound **2-2021b**). Based on the existence of complexes not included in the original Reaxys search, it is likely that

there are many more examples of complexes in literature that belong in this database, but for unknown reasons, these were not found via the Reaxys search.

The final 2-carbon linker dataset contained information on **181** bidentate phosphine Ni complexes in. The final 3-carbon linker dataset contained information on **51** bidentate phosphine Ni complexes.

### **A1.2 Correlations with experimental $^{31}\text{P}$ chemical shift**

To have an observable  $J_{\text{PP}}$  via 1-D  $^{31}\text{P}$  NMR spectra, the P atoms in a complex must not be related by symmetry (However, see reference S2 for a method for obtaining  $J_{\text{PP}}$  for symmetric complexes).<sup>2</sup> Therefore, all complexes in our datasets have two  $^{31}\text{P}$  chemical shifts. The  $^{31}\text{P}$  chemical shift of 2C and 3C complexes are plotted on violin plots (Figure A1.8).

The results indicate  $^{31}\text{P}$  chemical shift is a poor indicator of the oxidation state of Ni bidentate phosphine complexes, given p-values  $> 0.05$  for comparisons between the 2C  $\text{Ni}^0/\text{Ni}^{\text{II}}$  datasets and 3C  $\text{Ni}^0/\text{Ni}^{\text{II}}$  datasets, which indicate the distributions are not significantly different. Additionally, the high overlap in  $^{31}\text{P}$  chemical shift ranges of  $\text{Ni}^0$  and  $\text{Ni}^{\text{II}}$  complexes with the same linker length further indicates that  $^{31}\text{P}$  chemical shift is a poor indicator of oxidation state.

Small p-values and small overlap of ranges was noted when comparing complexes of different linker lengths (2C vs 3C) indicating that chemical shift may be an indicator of the linker length. Therefore, use of chemical shift for assignment of linker length may be possible in cases where linker length is unknown (e.g. if ligands with multiple binding modes are used, or if there are multiple ligands of different linker lengths present in the reaction medium).

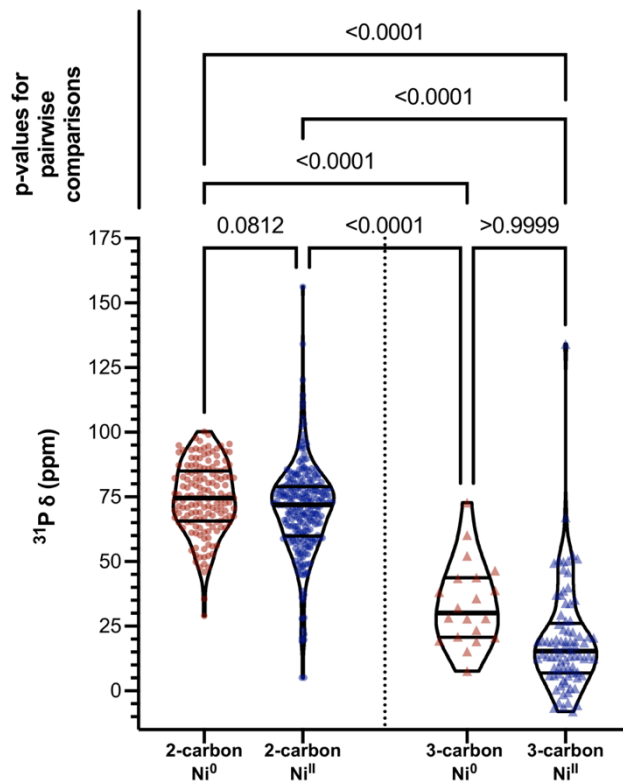


**Figure A1.8** Violin plot of chemical shifts of 2C and 3C complexes. All complexes in these datasets showed two separate  $^{31}\text{P}$  chemical shifts - both shifts are included in the data above.

No correlation was observed between  $|J_{\text{PP}}|$  or  $^{31}\text{P}$  chemical shifts (Figure A1.9), difference in chemical shifts  $|\delta_{\text{P1}} - \delta_{\text{P2}}|$  (Figure A1.10), or average chemical shift  $(\delta_{\text{P1}} + \delta_{\text{P2}})/2$  (Figure A1.11).

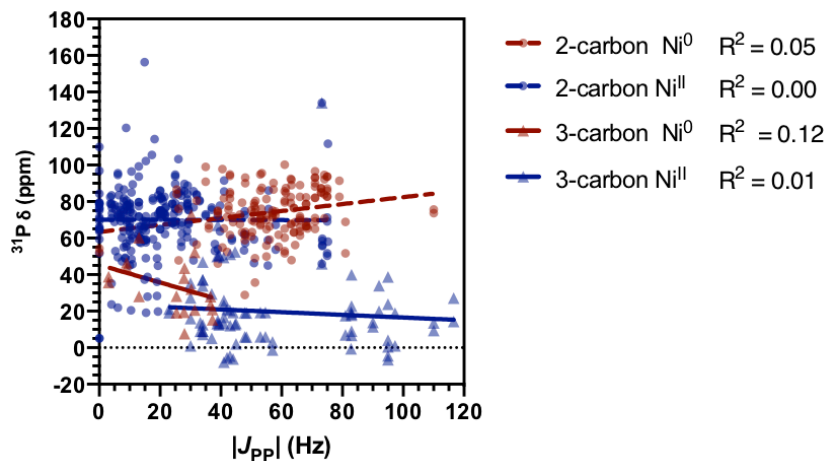


**Figure A1.9**  $^{31}\text{P}$  chemical shift versus  $|J_{\text{PP}}|$  for all complexes in the 2C and 3C datasets.

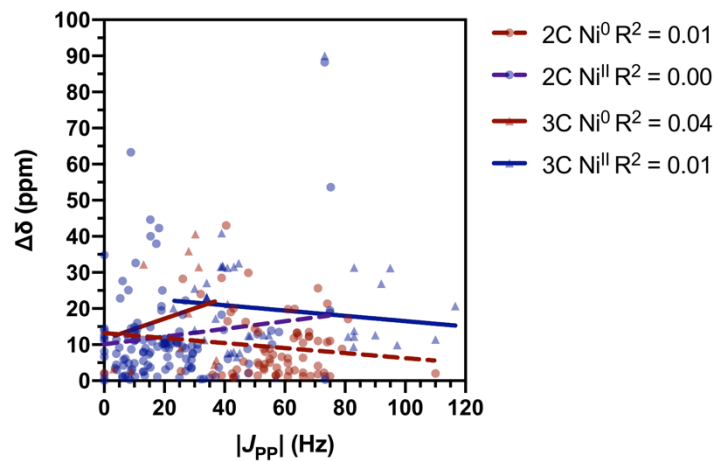


**Figure A1.10** Difference in the two  $^{31}\text{P}$  chemical shifts of each complex versus  $|J_{\text{PP}}|$  in the 2C and 3C datasets.

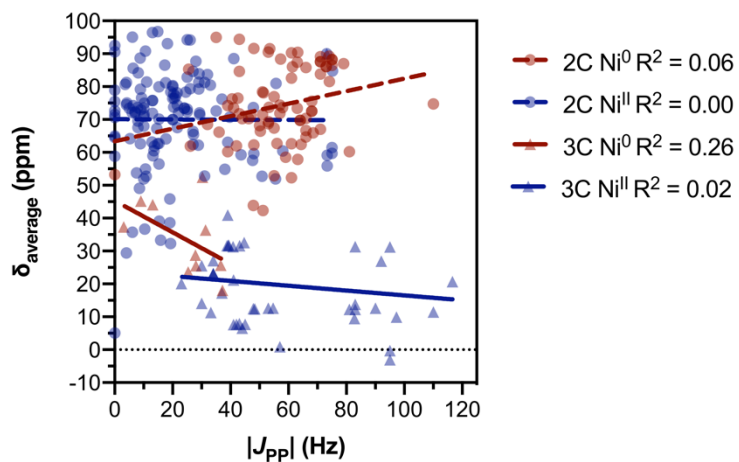


**Figure A1.11** average of the two  $^{31}\text{P}$  chemical shifts versus  $|J_{\text{PP}}|$  for each complex in the 2C and 3C datasets.

## A1.3 Computational details

### *A1.3.1 Geometry optimization*

All structures were optimized using Q-Chem 5.1<sup>3</sup> at the DFT level of theory using the O3LYP functional<sup>4</sup> with the LANL2DZ basis sets and corresponding electron core potentials.<sup>5</sup> If a crystal structure was available for the desired complex, this structure was used as the input geometry for optimization. If a crystal structure was unavailable, then the proposed Lewis structure for the complex was converted into a 3-dimensional XYZ structure by drawing the structure in Avogadro, and subsequently optimized using the level of theory above. All structures were optimized as singlets - accuracy of this spin state is evidenced by the availability of well-resolved NMR spectra for all complexes in the dataset.

### *A1.3.2 Internuclear spin-spin coupling ( $J$ -coupling) calculations*

Levels of theory were screened to identify appropriate functional/basis set combinations for internuclear spin-spin coupling calculations (i.e.,  $J_{PP}$  calculations). Given the high cost of benchmarking against the entire dataset, a subset of complexes was used for these benchmarks. The results of the benchmarking below led us to the O3LYP functional<sup>4</sup> for Internuclear spin-spin coupling (ISSC) calculations, with the aug-cc-pVTZ-J basis set on P atoms<sup>6</sup> and the cc-pVDZ basis set on all other atoms.<sup>7</sup> Based on analysis of Ramsey contributors,<sup>8</sup> the Fermi contact contributor to the total  $J_{PP}$  was found to be the largest contributor, and therefore was the only contributor computed for the majority of complexes in the 2C and 3C datasets (Tables S4 and S5). Only isotropic  $J_{PP}$  values were used, because only the isotropic  $|J_{PP}|$  value is observed in solution phase NMR spectroscopy.

**A1.3.2.1 DFT Functional Benchmarking:** For benchmarking against DFT functionals, Fermi contact  $J_{PP}$  of complexes **2-2002**, **2-2003**, **2-2004** and **2-2025** were computed. The basis sets used for these functional screenings consisted of cc-pVDZ<sup>7</sup> on all atoms, except phosphorus which had aug-cc-pVTZ-J.<sup>6</sup> All metaGGA functionals available in Q-Chem 5.1 were used for functional screening (functionals from higher rungs of DFT, such as hybrid GGA or hybrid-meta GGA functionals are not compatible with ISSC calculations as implemented in QChem 5.1). Results are in Table A1.1. RMS error is evaluated based on the differences between the absolute value of the computed  $J_{PP}$  and the value of the observed  $J_{PP}$  (because most experiments only give the magnitude of the  $J_{PP}$ , not the sign). This screen revealed that O3LYP was most accurate for these complexes (RMSE = 5.31 Hz); the only other functional to give an RMSE less than 10 Hz was the B97-2 functional (RMSE = 6.43 Hz). While O3LYP and B97-2 are known to be competent functionals for geometry and property prediction in some classes of molecules, it is unknown why these perform particularly well compared to other functionals in computation of  $J_{PP}$  in these systems.

**Table A1.1** Density functional screen for  $J_{PP}$  calculations, sorted in order of most accurate to least accurate. O3LYP, the functional used for all other  $J_{PP}$  calculations, is highlighted in green.

DFT Functional	$J_{PP}$ for 2-2002 (Hz)	Error for 2-2002 (Hz)	$J_{PP}$ for 2-2003 (Hz)	Error for 2-2003 (Hz)	$J_{PP}$ for 2-2004 (Hz)	Error for 2-2004 (Hz)	$J_{PP}$ for 2-2025 (Hz)	Error for 2-2025 (Hz)	RMS error
experiment observed $ J_{PP} $	9.0	-	0.0	-	4.0	-	20.4	-	-
O3LYP <sup>4</sup>	-4.51	-4.50	7.41	7.41	9.61	5.61	-17.88	-2.52	5.31
B97-2 <sup>9</sup>	-8.72	-0.28	5.74	5.74	14.22	10.22	-25.70	5.30	6.43
B97 <sup>10</sup>	-3.90	-5.10	9.31	9.31	22.40	18.40	-19.76	-0.64	10.63
WP04 <sup>11</sup>	0.89	-8.11	15.48	15.48	15.40	11.40	-16.11	-4.29	10.65
B97-1 <sup>12</sup>	-3.29	-5.72	10.17	10.17	25.61	21.61	-19.79	-0.61	12.28
B3PW91 <sup>13</sup>	5.40	-3.60	20.55	20.55	30.16	26.16	-13.62	-6.78	17.07
B3P86 <sup>13</sup>	6.09	-2.91	20.75	20.75	31.06	27.06	-12.05	-8.35	17.61
revPBE0 <sup>14</sup>	1.66	-7.34	20.09	20.09	32.99	28.99	-22.20	1.80	18.04
B97-3 <sup>15</sup>	3.17	-5.83	15.56	15.56	35.51	31.51	-14.67	-5.73	18.04
PBE0 <sup>14</sup>	3.44	-5.56	21.29	21.29	34.82	30.82	-19.12	-1.28	18.95
B1PW91 <sup>16</sup>	4.43	-4.57	22.82	22.82	35.94	31.94	-19.09	-1.31	19.77
MPW1PBE <sup>17</sup>	4.63	-4.37	23.01	23.01	36.22	32.22	-18.63	-1.77	19.94
MPW1PW91 <sup>17</sup>	4.70	-4.30	23.04	23.04	36.52	32.52	-18.56	-1.84	20.06
B3LYP5 <sup>13,18</sup>	10.58	1.58	24.51	24.51	36.68	32.68	-6.92	-13.48	21.52
B3LYP <sup>13,18</sup>	10.83	1.83	24.58	24.58	36.73	32.73	-6.51	-13.89	21.63
SOGGA11-X <sup>19</sup>	23.26	14.26	29.55	29.55	32.58	28.58	15.92	-4.48	21.87
X3LYP <sup>20</sup>	10.89	1.89	25.38	25.38	39.16	35.16	-7.44	-12.96	22.65
B1LYP <sup>16</sup>	11.16	2.16	27.61	27.61	44.48	40.48	-10.01	-10.39	25.07
MPW1LYP <sup>17</sup>	11.39	2.39	27.80	27.80	45.00	41.00	-9.55	-10.85	25.38
PBEh-3C <sup>21</sup>	-11.06	2.06	17.50	17.50	45.15	41.15	-48.76	28.36	26.50
MPW1K <sup>22</sup>	-6.95	-2.05	27.83	27.83	53.71	49.71	-52.87	32.47	32.80
B97-K <sup>23</sup>	22.25	13.25	31.07	31.07	61.16	57.16	-7.61	-12.79	33.81
B5050LYP <sup>24</sup>	-9.22	0.22	27.09	27.09	59.03	55.03	-64.99	44.59	37.91
BHLYP	-6.06	-2.94	33.30	33.30	64.10	60.10	-64.94	44.54	40.97
PBE50 <sup>25</sup>	-10.80	1.80	48.27	48.27	60.29	56.29	-81.19	60.79	47.95

**A1.3.2.2 Basis set benchmarking:** Basis set benchmarking at the O3LYP level of theory was achieved using a larger set of complexes: **2-2002**, **2-2003**, **2-2004**, **2-2025**, **2-2038**, **2-2086**, **2-2086b**, **2-2089**, **2-2143b**, **2-2143c**. The basis sets ANO-R0, cc-pVDZ, def2-svp, and pc-1, cc-pVDZ + aug-cc-pVTZ-J on P, cc-pVDZ + pcJ-1 on P, and cc-pVDZ + pcJ-2 on P were used with the O3LYP functional in ISSC calculations - exclusion of common basis sets such as 6-31G\* and



LANL2DZ was due to limitations of Q-Chem 5.1, because the ISSC module is not compatible with basis sets with SP shells or basis sets that require ECPs. Results are in Table A1.2 - RMS error is evaluated based on the differences between the absolute value of the computed  $J_{PP}$  and the value of the observed  $|J_{PP}|$  (because most experiments only give the magnitude of the  $J_{PP}$ , not the sign). The screen revealed that O3LYP/cc-pVDZ + aug-cc-pVTZ-J for P gave the most accurate  $|J_{PP}|$  values compared to experimental values.

**Table A1.2** Benchmarks of basis sets for  $J_{PP}$  calculations (O3LYP functional).

<b>Basis set</b>	$J_{PP}$ for 2- 2002	$J_{PP}$ for 2- 2003	$J_{PP}$ for 2- 2004	$J_{PP}$ for 2- 2025	$J_{PP}$ for 2- 2038	$J_{PP}$ for 2- 2086	$J_{PP}$ for 2- 2086 b	$J_{PP}$ for 2- 2089	$J_{PP}$ for 2- 2143 b	$J_{PP}$ for 2- 2143 c	<b>RMS error</b>
Experiment $ J_{PP} $	9.0	0.0	4.0	20.4	71.0	33.0	0.0	21.5	48.0	4.0	-
ANO-R0	119.9	167.1	202.5	169.1	432.6	303.2	126.2	165.4	359.9	126.2	<b>213.1</b>
cc-pVDZ	-5.0	2.7	-7.6	-18.5	63.1	27.9	-3.7	-18.7	34.8	2.2	<b>5.7</b>
def2-svp <sup>30</sup>	-14.3	-5.2	-4.6	-26.8	37.0	7.6	-15.4	-27.5	15.3	-10.6	<b>18.1</b>
pc-1	-12.1	-1.1	-5.4	-27.4	57.9	19.5	-11.1	-28.3	27.6	-6.0	<b>10.0</b>
cc-pVDZ + aug-cc- pVTZ-J on P	-6.0	4.4	3.0	-19.8	68.1	26.0	-5.6	-20.4	36.9	0.3	<b>5.1</b>
cc-pVDZ + pcJ-1 on P	-4.2	5.9	6.0	-20.1	67.1	24.6	-7.3	-21.0	34.6	-1.4	<b>6.2</b>
cc-pVDZ + pcJ-2 on P	-6.1	4.1	2.0	-20.5	67.6	25.5	-6.4	-21.3	34.7	-0.3	<b>5.7</b>

**A1.3.2.3 Contributors to  $J_{PP}$ :** There are four contributors to  $J$ -coupling: The Fermi contact (FC) contribution, the paramagnetic spin-orbit contribution (PSO), the diamagnetic spin-orbit contribution (DSO), and the spin-dipole contribution (SD).<sup>8</sup> The sum of all four contributors gives the total  $J$ -coupling value. For 43 complexes in our dataset, we utilized Q-Chem to calculate all four contributors to  $J_{PP}$  (Table A1.3). SD and PSO terms were positive for most 2C complexes, but negative for 3C complexes, however, the magnitude of these terms was small, never larger

than 2 Hz. The FC term dominated the total, with the remaining terms (PSO, DSO, and SD) combined making up less than  $\sim 3$  Hz total contribution to the  $J_{PP}$ . This dominance of Fermi contact agrees with other  $J_{PP}$  computations.<sup>26,27,28</sup> Therefore, only the Fermi Contact term was computed for the remaining complexes.

**Table A1.3** Ramsey contributors to  $J_{PP}$  for a subset of complexes in this study.

<b>Compound #</b>	<b>FC (Hz)</b>	<b>SD (Hz)</b>	<b>PSO (Hz)</b>	<b>DSO (Hz)</b>	<b>Total <math>J_{PP}</math> = FC + SD + PSO + DSO (Hz)</b>	<b>SD + PSO + DSO (Hz)</b>
2-2002	-5.990	0.956	1.237	0.260	-3.537	2.453
2-2003	4.431	0.808	1.638	0.255	7.132	2.701
2-2004	3.030	0.957	1.075	0.224	5.286	2.256
2-2005	-13.838	0.708	1.979	0.256	-10.895	2.943
2-2019	43.279	1.700	0.482	0.226	45.687	2.408
2-2020	-20.084	0.727	1.748	0.249	-17.360	2.724
2-2021	73.619	1.976	0.111	0.229	75.935	2.316
2-2021b	-7.703	0.999	1.109	0.268	-5.327	2.376
2-2022	-31.203	0.321	2.416	0.268	-28.198	3.005
2-2023	47.012	1.642	0.476	0.231	49.361	2.349
2-2025	-19.794	0.849	1.612	0.284	-17.049	2.745
2-2032	6.963	1.031	1.411	0.277	9.682	2.719
2-2035	-26.216	0.360	2.325	0.270	-23.261	2.955
2-2038	68.147	1.525	-0.188	0.223	69.707	1.560
2-2046d	61.451	1.967	0.258	0.232	63.908	2.457
2-2046e	-15.624	0.658	1.667	0.270	-13.029	2.595
2-2086	25.984	1.157	0.281	0.240	27.662	1.678
2-2086b	-5.643	0.249	0.905	0.262	-4.227	1.416
2-2088	-1.791	0.716	1.488	0.280	0.693	2.484
2-2089	-20.362	0.871	1.670	0.288	-17.533	2.829
2-2090	-1.941	0.650	1.180	0.278	0.167	2.108
2-2094	45.844	1.431	0.200	0.245	47.720	1.876
2-2106	49.323	1.581	0.186	0.246	51.336	2.013
2-2107	-19.333	0.551	1.842	0.272	-16.668	2.665
2-2110	-22.716	0.554	1.835	0.255	-20.072	2.644
2-2121	-14.408	0.809	1.755	0.255	-11.589	2.819
2-2122	-15.929	0.719	1.852	0.258	-13.100	2.829
2-2143b	34.763	1.151	0.360	0.253	36.527	1.764
2-2143c	0.300	0.494	1.047	0.262	2.103	1.803
2-2143e	47.056	1.313	0.110	0.246	48.725	1.669
2-2150	-14.943	0.606	1.171	0.290	-12.876	2.067
2-2151	-6.861	0.647	1.179	0.287	-4.748	2.113
2-2172	-2.009	1.016	1.766	0.298	1.071	3.080
2-2174	-22.914	0.653	1.669	0.302	-20.290	2.624
2-2177	-11.466	0.622	1.922	0.287	-8.635	2.831
2-2202	-16.242	0.499	1.181	0.314	-14.248	1.994
2-2296	-17.196	0.475	1.513	0.321	-14.887	2.309
3-3002	-9.314	-0.227	0.069	0.135	-9.337	-0.023
3-3007	22.927	-0.284	0.710	0.151	23.504	0.577
3-3008	-25.463	-0.148	-0.441	0.215	-25.837	-0.374
3-3009	-40.897	-0.157	-0.903	0.202	-41.755	-0.858
3-3029	-84.576	0.421	-1.289	0.276	-85.168	-0.592
3-3030	-114.755	0.137	-1.356	0.233	-115.741	-0.986

### A1.3.3 Charge transfer calculations

Charge transfer was evaluated using the second-generation energy decomposition analysis with absolutely localized molecular orbitals described by Head-Gordon and coworkers and implemented in Q-Chem 5.1. Calculations were performed with the  $\omega$ B97M-V functional<sup>29</sup> and def2-SVP basis set.<sup>30</sup> All molecules in the dataset were fragmented along the P–Ni bonds, giving two fragments: fragment 1, containing the bidentate phosphine, and fragment 2, containing the Ni and all other ligands (Figure A1.12). Many cationic complexes were assumed to have a positive charge localized on Ni, therefore, any non-coordinating ions present (such as the BARF anion in **3-3011**), were included in Fragment 2 for those structures. Some complexes contain ionic moieties in the phosphine, such as for complex **2-2428**, so non-coordinating counterions were included in Fragment 1 in these cases. The spin states of both fragments were assumed singlets. This spin state assignment for the fragments is based on recognizing the unfragmented complexes are singlets due to the existence of well resolved NMR spectra, and that free phosphines (i.e., fragment 1) are generally ground state singlets. Due to the fragmentation scheme, charge transfer values could not be computed for ligands of denticity greater than  $\kappa^2$ , such as complex **2-2051** and **2-2051a** which contain a tridentate ligand.

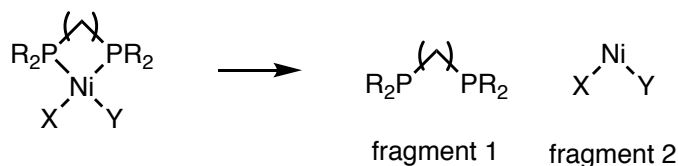


**Figure A1.12** Fragmentation scheme for charge transfer analysis of most complexes.

The P-to-Ni charge transfer ( $CT_{\text{P-to-Ni}}$ ) in Tables A1.4 and A1.5 refer to the total amount of charge donated from fragment 1 to fragment 2. The Ni-to-P charge transfer ( $CT_{\text{Ni-to-P}}$ ) refers to the total charge donated from fragment 2 to fragment 1.

## A1.4 Backbonding $CT_{Ni-to-P}$ vs $J_{PP}$

There was a weaker correlation observed between  $J_{PP}$  and the Ni-to-P charge transfer (Figure A1.13) than for the correlation of  $J_{PP}$  and  $CT_{P-to-Ni}$  (Figure 2.4 in the manuscript). This lower correlation indicates that Ni-to-P backbonding charge transfer is not as good a descriptor of  $J_{PP}$  as the  $\sigma$ -bonding P-to-Ni charge transfer.

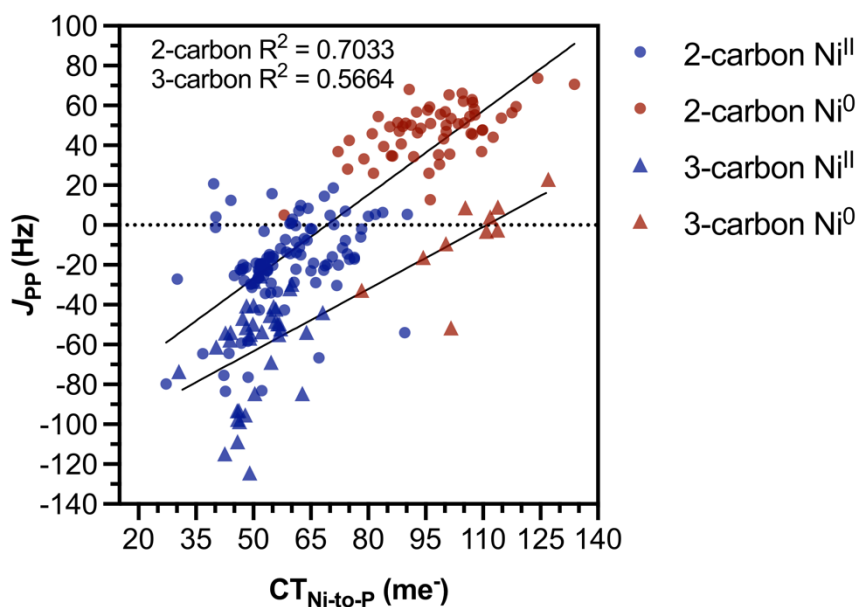


**Figure A1.13** Ni-to-P charge transfer versus  $|J_{PP}|$  with regression lines shown in black.

## A1.5 Correlations with bite angle and linker identity

### A1.5.1 Bite angle measurements

The bite angles discussed below are P-Ni-P angles measured from the available crystal structures. If no crystal structure was available, as was the case with many 3C complexes, then the P-Ni-P bite angle from the DFT optimized structure was used.

### A1.5.2 Linker identity and correlations with bite angle

Linker identity and bite angle are clearly linked; when comparing the bite angles of 2C complexes to bite angles of 3C complexes the distributions differ significantly ( $p < 0.0001$ ), with 3C complexes generally having much larger bite angles (Figure A1.14):

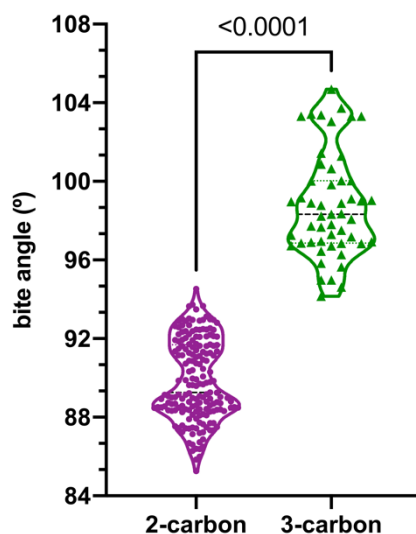


**Figure A1.14** P-Ni-P Bite angle for 2C and 3C complexes.

Within each dataset, however, there was less significant correlation with linker identity. When comparing 2C complexes containing aliphatic linkers (i.e. all carbons are  $sp^3$  hybridized, e.g., ethane linkers) to 2C complexes containing olefinic linkers (i.e., all carbons are  $sp^2$  hybridized, e.g., ethylene and benzene linkers), the distributions overlap significantly (Figure A1.15) and only differ to a  $p$ -value = 0.2692. Similar results are observed when comparing 3C complexes with aliphatic linkers (e.g., propane linkers) to complexes with olefinic linkers (e.g., naphthalene linkers, acenaphthene linkers, and ligands with fused cyclopentadienyl groups in the backbone like JosiPhos), where the  $p$ -value = 0.1831. These results indicate that the P-Ni-P bite angle is most affected by the number of carbons, and less so by their hybridization.

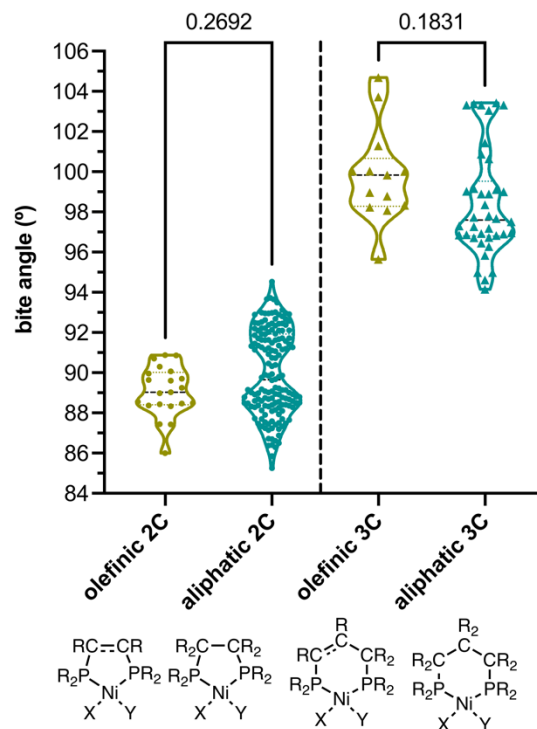


**Figure A1.15** Violin plots for comparison of bite angles between complexes with olefinic and aliphatic 2C or 3C linkers.

### A1.5.3 Chemical shift correlations with bite angle

For other types of transition metal complexes, there are notable effects of the bite angle on the observed  $^{31}\text{P}$  NMR chemical shift.<sup>31</sup> We investigated the effect of bite angle on the  $^{31}\text{P}$  chemical shifts of the complexes in our datasets (Figure A1.16).

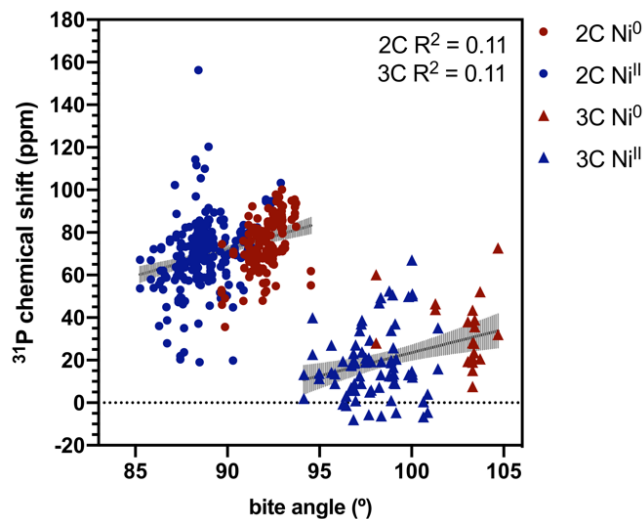


**Figure A1.16** Plot of bite angle vs. chemical shift for 2C and 3C complexes

The effect of linker length on chemical shift is low and is consistent with the results in Figure A1.8. Correlations with bite angle are often discussed in terms of ring-size effects,<sup>3233</sup> with larger bite angles being observed at larger ring sizes. Therefore, the low bite angle/chemical shift correlations observed here likely result from small sampling of ring sizes (i.e., only 2 ring sizes, 5-membered and 6-membered, make up the entire dataset).

#### ***A1.5.4 $J_{PP}$ correlations with Bite Angle***

Correlations between bite angle and calculated  $J_{PP}$  were used to investigate if  $J_{PP}$  is accurately described as a  ${}^2J$ , geminal coupling (Figure A1.17).



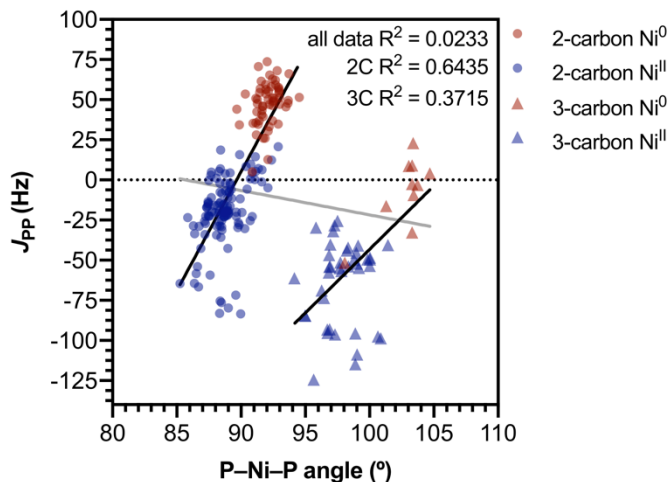


**Figure A1.17** Calculated  $J_{PP}$  versus P–Ni–P bite angle. Lines of best fit for the 2C and 3C datasets in black, line of best fit for the 2C+3C combined dataset in grey.

Within each dataset, the bite angle correlated moderately with  $J_{PP}$ , with worse correlation in the 3C dataset. This correlation is positive, which is the opposite correlation needed to explain the difference in  $J_{PP}$  between 2C and 3C complexes (because the 3C complexes have more negative  $J_{PP}$  and larger bite angles) indicating that the difference in  $J_{PP}$  between 2C and 3C complexes is not related to bite angle. If we add the value of  $L$  in Eq. 2 (where  $L = 0$  Hz for 2C complexes and  $L = -48.47$  Hz for 3C complexes) to all  $J_{PP}$  values to correct for differences in through-linker  $J_{PP}$ , we can probe the angular dependence of the through-Ni coupling (Figure A1.18). Still, even when corrected for differences in through-linker coupling by adding  $L$ ,  $R^2$  for the combined dataset is quite low (0.0915) indicating that  $J_{PP}$  has a poor dependence on bite angle.

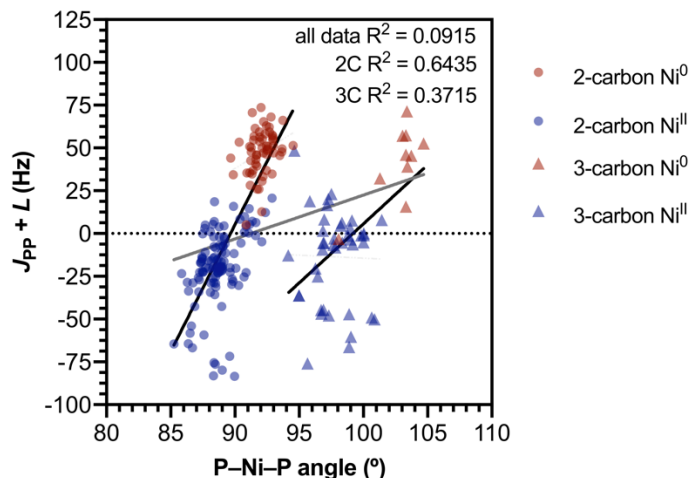


**Figure A1.18** P-Ni-P Bite angle versus  $J_{PP} + L$ . Lines of best fit for the 2C and 3C datasets in black, line of best fit for the 2C+3C combined dataset in grey.

We propose that the correlation of bite angle with  $J_{PP}$  within each dataset arises from the dependence of metal complex geometry on oxidation state, rather than through an angular dependence of  $J_{PP}$ . Most  $\text{Ni}^0$  complexes in our 2C and 3C datasets have a  $\text{NiL}_3$  structure, favoring trigonal planar geometries, with bite angles  $> 100^\circ$ . Most  $\text{Ni}^{\text{II}}$  complexes however have a  $\text{NiL}_2\text{X}_2$  structure, favoring square planar geometries with bite angles  $\sim 90^\circ$ . Given that  $\text{Ni}^0$  complexes favor larger bite angles, and  $\text{Ni}^{\text{II}}$  complexes favor smaller bite angles near  $90^\circ$ , the bite angles are partitioned based on oxidation state at Ni, similar to how  $J_{PP}$  partitions by oxidation state, causing an apparent dependence of  $J_{PP}$  and bite angle. This hypothesis of partitioning of the bite angles based on oxidation state is supported by correlations between P-to-Ni charge transfer and P-Ni-P bite angle (Figure A1.19), which show that complexes with  $\text{Ni}^0$  have higher bite angles and lower  $CT_{\text{P-to-Ni}}$  values than  $\text{Ni}^{\text{II}}$  complexes but shows little correlation beyond oxidation state (i.e. low correlation within each oxidation state/linker length pair).

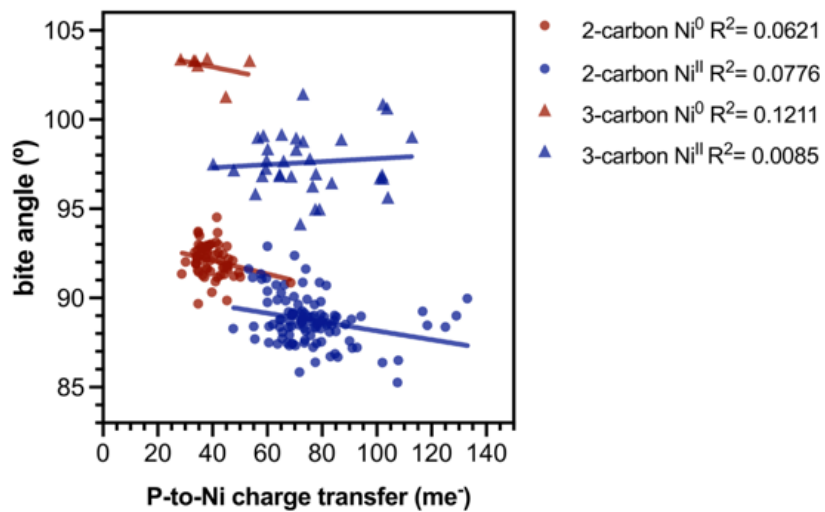


**Figure A1.19** P-Ni-P Bite angle versus P-to-Ni charge transfer.

### A1.6 XYZ coordinates

The database of information containing the  $J_{PP}$  and structures of all 2C and 3C complexes, as well as all XYZ coordinates of all complexes can be found online at the published journal article:

*Inorg. Chem.* **2021**, *60*, 13400–13408. <https://doi.org/10.1021/acs.inorgchem.1c01720>

## A1.7 References

<sup>1</sup> Hartwig, J. F. *Organotransition Metal Chemistry: From Bonding to Catalysis*, 1st ed.; University Science Books: California, 2010; pp 1–26.

<sup>2</sup> “The  $J_{PP}$  of symmetric transition metal phosphine complexes can be resolved, but via a combination of NMR spectroscopies.  $^{31}\text{P}$  and  $^{13}\text{C}$  NMR spectra enable resolving the  $J_{PP}$  of symmetric complexes, as detailed in: Bertrand, R. D.; Ogilvie, F. B.; Verkade, J. G. Signs of Phosphorus-Phosphorus Coupling Constants in Coordination Compounds. *J. Am. Chem. Soc.* **1970**, *92*, 1908–1915. Additionally,  $^1\text{H}$  NMR spectra can also be used to assign  $J_{PP}$ , as detailed in” Ogilvie, F. B.; Jenkins, J. M.; Verkade, J. G.  $^{31}\text{P}$ – $^{31}\text{P}$  Spin-Spin Coupling in Complexes Containing Two Phosphorus Ligands. *J. Am. Chem. Soc.* **1970**, *92*, 1916–1923.

<sup>3</sup> Shao, Y.; Gan, Z.; Epifanovsky, E.; Gilbert, A. T. B.; Wormit, M.; Kussmann, J.; Lange, A. W.; Behn, A.; Deng, J.; Feng, X.; Ghosh, D.; Goldey, M.; Horn, P. R.; Jacobson, L. D.; Kaliman, I.; Khaliullin, R. Z.; Kúš, T.; Landau, A.; Liu, J.; Proynov, E. I.; Rhee, Y. M.; Richard, R. M.; Rohrdanz, M. A.; Steele, R. P.; Sundstrom, E. J.; Woodcock III, H. L.; Zimmerman, P. M.; Zuev, D.; Albrecht, B.; Alguire, E.; Austin, B.; Beran, G. J. O.; Bernard, Y. A.; Berquist, E.; Brandhorst, K.; Bravaya, K. B.; Brown, S. T.; Casanova, D.; Chang, C.-M.; Chen, Y.; Chien, S. H.; Closser, K. D.; Crittenden, D. L.; Diedenhofen, M.; DiStasio Jr., R. A.; Dop, H.; Dutoi, A. D.; Edgar, R. G.; Fatehi, S.; Fusti-Molnar, L.; Ghysels, A.; Golubeva-Zadorozhnaya, A.; Gomes, J.; Hanson-Heine, M. W. D.; Harbach, P. H. P.; Hauser, A. W.; Hohenstein, E. G.; Holden, Z. C.; Jagau, T.-C.; Ji, H.; Kaduk, B.; Khistyayev, K.; Kim, J.; Kim, J.; King, R. A.; Klunzinger, P.; Kosenkov, D.; Kowalczyk, T.; Krauter, C. M.; Lao, K. U.; Laurent, A.; Lawler, K. V.; Levchenko, S. V.; Lin, C. Y.; Liu, F.; Livshits, E.; Lochan, R. C.; Luenser, A.; Manohar, P.; Manzer, S. F.; Mao, S.-P.; Mardirossian, N.; Marenich, A. W.; Maurer, S. A.; Mayhall, N. J.; Oana, C. M.; Olivares-Amaya, R.; O’Neill, D. P.; Parkhill, J. A.; Perrine, T. M.; Peverati, R.; Pieniazek, P. A.; Prociuk, A.; Rehn, D. R.; Rosta, E.; Russ, N. J.; Sergueev, N.; Sharada, S. M.; Sharma, S.; Small, D. W.; Sodt, A.; Stein, T.; Stück, D.; Su, Y.-C.; Thom, A. J. W.; Tsuchimochi, T.; Vogt, L.; Vydrov, O.; Wang, T.; Watson, M. A.; Wenzel, J.; White, A.; Williams, C. F.; Vanovschi, V.; Yeganeh, S.; Yost, S. R.; You, Z.-Q.; Zhang, I. Y.; Zhang, X.; Zhou, Y.; Brooks, B. R.; Chan, G. K. L.; Chipman, D. M.; Cramer, C. J.; Goddard III, W. A.; Gordon, M. S.; Hehre, W. J.; Klamt, A.; Schaefer III, H. F.; Schmidt, M. W.; Sherrill, C. D.; Truhlar, D. G.; Warshel, A.; Xue, X.; Aspuru-Guzik, A.; Baer, R.; Bell, A. T.; Besley, N. A.; Chai, J. D.; Dreuw, A.; Dunietz, B. D.; Furlani, T. R.; Gwaltney, S. R.; Hsu, C.-P.; Jung, Y.; Kong, J.; Lambrecht, D. S.; Liang, W.; Ochsenfeld, C.; Rassolov, V. A.; Slipchenko, L. V.; Subotnik, J. E.; Van Voorhis, T.; Herbert, J. M.; Krylov, A. I.; Gill, P. M. W.; Head-Gordon, M. Advances in Molecular Quantum Chemistry Contained in the Q-Chem 4 Program Package. *Mol. Phys.* **2015**, *113*, 184–215.

<sup>4</sup> Handy, N. C.; Cohen, A. J. Dynamic Correlation. *Mol. Phys.* **2001**, *99*, 607–615.

<sup>5</sup> a) Dunning, T. H.; Hay, P. J. Gaussian Basis Sets for Molecular Calculations in 'Methods of Electronic Structure Theory *Modern Theoretical Chemistry* 1<sup>st</sup> ed.; Springer: Berlin, 1977, pp 1–27.

b) Hay, P. J.; Wadt, W. R. Ab Initio Effective Core Potentials for Molecular Calculations. Potentials for K to Au Including the Outermost Core Orbitals. *J. Chem. Phys.* **1985**, *82*, 299–310.

c) Wadt, W. R.; Hay, P. J. Ab Initio Effective Core Potentials For Molecular Calculations. Potentials for Main Group Elements Na to Bi. *J. Chem. Phys.* **1985**, *82*, 284–298.

- 
- <sup>6</sup> Provasi, P. F.; Sauer, S. P. A. Optimized Basis Sets for the Calculation of Indirect Nuclear Spin-Spin Coupling Constants Involving the Atoms B, Al, Si, P, and Cl. *J. Chem. Phys.* **2010**, *133*, 054308.
- <sup>7</sup> a) Balabanov, N. B.; Peterson, K. A. Systematically Convergent Basis Sets for Transition Metals. I. All-Electron Correlation Consistent Basis Sets for the 3d Elements Sc–Zn. *J. Chem. Phys.* **2005**, *123*, 064107.
- b) Balabanov, N. B.; Peterson, K. A. Basis Set Limit Electronic Excitation Energies, Ionization Potentials, and Electron Affinities for the 3d Transition Metal Atoms: Coupled Cluster and Multireference Methods. *J. Chem. Phys.* **2006**, *125*, 074110.
- c) Dunning, T. H. Gaussian Basis Sets for Use in Correlated Molecular Calculations. I. The Atoms Boron Through Neon and Hydrogen. *J. Chem. Phys.* **1989**, *90*, 1007–1023.
- d) Prascher, B. P.; Woon, D. E.; Peterson, K. A.; Dunning, T. H.; Wilson, A. K. Gaussian Basis Sets for Use in Correlated Molecular Calculations. VII. Valence, Core-Valence, and Scalar Relativistic Basis Sets for Li, Be, Na, and Mg. *Theor. Chem. Acc.* **2011**, *128*, 69–82.
- e) Wilson, A. K.; Woon, D. E.; Peterson, K. A.; Dunning, T. H. Gaussian Basis Sets for Use in Correlated Molecular Calculations. IX. The Atoms Gallium through Krypton. *J. Chem. Phys.* **1999**, *110*, 7667–7676.
- f) Woon, D. E.; Dunning, T. H. Gaussian Basis Sets for Use in Correlated Molecular Calculations. III. The Atoms Aluminum Through Argon. *J. Chem. Phys.* **1993**, *98*, 1358–1371.
- <sup>8</sup> Ramsey, N. F. Electron Coupled Interactions between Nuclear Spins in Molecules. *Phys. Rev.* **1953**, *91*, 303–307.
- <sup>9</sup> Wilson, P. J.; Bradley, T. J.; Tozer, D. J. Tozer Hybrid Exchange-Correlation Functional Determined from Thermochemical Data and Ab Initio Potentials. *J. Chem. Phys.* **2001**, *115*, 9233–9242.
- <sup>10</sup> Becke, A. D. Density-Functional Thermochemistry. V. Systematic Optimization of Exchange-Correlation Functionals. *J. Chem. Phys.* **1997**, *107*, 8554–8560.
- <sup>11</sup> Wiitala, K. W.; Hoyer, T. R.; Cramer, C. J. Hybrid Density Functional Methods Empirically Optimized for the Computation of <sup>13</sup>C and <sup>1</sup>H Chemical Shifts in Chloroform Solution. *J. Chem. Theory Comput.* **2006**, *2*, 1085–1092.
- <sup>12</sup> Hamprecht, F. A.; Cohen, A. J.; Tozer, D. J.; Handy, N. C. Handy Development and Assessment of New Exchange-Correlation Functionals. *J. Chem. Phys.* **1998**, *109*, 6264–6271.
- <sup>13</sup> Becke, A. D. Density-Functional Thermochemistry. III. The Role of Exact Exchange. *J. Chem. Phys.* **1993**, *98*, 5648–5652.
- <sup>14</sup> Adamo, C. Toward Reliable Density Functional Methods Without Adjustable Parameters: The PBE0 Model. *J. Chem. Phys.* **1999**, *110*, 6158–6170.
- <sup>15</sup> Keal, T. W.; Tozer, D. J. Semiempirical Hybrid Functional with Improved Performance in an Extensive Chemical Assessment. *J. Chem. Phys.* **2005**, *123*, 121103.
- <sup>16</sup> Adamo, C.; Barone, V. Toward Reliable Adiabatic Connection Models Free from Adjustable Parameters. *Chem. Phys. Lett.* **1997**, *274*, 242–250.
- <sup>17</sup> Adamo, C.; Barone, V. Exchange Functionals with Improved Long-Range Behavior and Adiabatic Connection Methods Without Adjustable Parameters: The mPW and mPW1PW Models. *J. Chem. Phys.* **1998**, *108*, 664–675.

- 
- <sup>18</sup> Stephens, P. J.; Devlin, F. J.; Chabalowski, C. F.; Frish, M. J. Ab Initio Calculation of Vibrational Absorption and Circular Dichroism Spectra Using Density Functional Force Fields. *J. Phys. Chem.* **1994**, *98*, 11623–11627.
- <sup>19</sup> Peverati, R.; Truhlar, D. G. Communication: a Global Hybrid Generalized Gradient Approximation to the Exchange-Correlation Functional that Satisfies the Second-Order Density-Gradient Constraint and has Broad Applicability In Chemistry. *J. Chem. Phys.* **2011**, *135*, 191102.
- <sup>20</sup> Xu, X.; Goddard III, W. A. The X3LYP Extended Density Functional for Accurate Descriptions of Nonbond Interactions, Spin States, and Thermochemical Properties. *Proc. Natl. Acad. Sci. U.S.A.* **2003**, *101*, 2673–2677.
- <sup>21</sup> Grimme, S.; Brandenburg, J. G.; Bannwarth, C.; Hansen, A. Consistent Structures and Interactions by Density Functional Theory with Small Atomic Orbital Basis Sets. *J. Chem. Phys.* **2015**, *143*, 054107.
- <sup>22</sup> Lynch, B. J.; Fast, P. L.; Harris, M.; Truhlar, D. G. Adiabatic Connection for Kinetics. *J. Phys. Chem. A* **2000**, *104*, 4811–4815.
- <sup>23</sup> Boese, A. D.; Martin, J. M. L. Development of Density Functionals for Thermochemical Kinetics. *J. Chem. Phys.* **2004**, *121*, 3405–3416.
- <sup>24</sup> Shao, Y.; Head-Gordon, M.; Krylov, A. I. The Spin-Flip Approach Within Time-Dependent Density Functional Theory: Theory and Applications to Diradicals. *J. Chem. Phys.* **2003**, *118*, 4807–4818.
- <sup>25</sup> Bernard, Y. A.; Shao, Y.; Krylov, A. I. General Formulation of Spin-Flip Time-Dependent Density Functional Theory Using Non-Collinear Kernels: Theory, Implementation, and Benchmarks. *J. Chem. Phys.* **2012**, *136*, 204103.
- <sup>26</sup> Burk, S.; Götz, K.; Kaupp, M.; Nieger, M.; Weber, J.; Schmedt auf der Günne, J.; Gudat, D. Diphosphines with Strongly Polarized P-P Bonds: Hybrids between Covalent Molecules and Donor-Acceptor Adducts with Flexible Molecular Structures. *J. Am. Chem. Soc.* **2009**, *131*, 10763–10774.
- <sup>27</sup> Forgeron, M. A. M.; Gee, M.; Wasylishen, R. E. A Theoretical Investigation of One-Bond Phosphorus-Phosphorus Indirect Nuclear Spin-Spin Coupling Tensors,  $^1J(^{31}\text{P}, ^{31}\text{P})$ , Using Density Functional Theory. *J. Phys. Chem. A* **2004**, *108*(22), 4895–4908.
- <sup>28</sup> Huynh, K., Lough, A. J.; Forgeron, M. A. M.; Bendle, M.; Soto, A. P.; Wasylishen, R. E.; Manners, I. Synthesis and Reactivity of Phosphine-Stabilized Phosphoranimine Cations,  $[\text{R}_3\text{P}\cdot\text{PR}'_2\text{dNSiMe}_3]^+$ . *J. Am. Chem. Soc.* **2009**, *131*, 7905–7916.
- <sup>29</sup> Mardirossian, N.; Head-Gordon, M.  $\omega$ B97M-V: A Combinatorially Optimized, Range-Separated Hybrid, Meta-GGA Density Functional With VV10 Nonlocal Correlation. *J. Chem. Phys.* **2016**, *144*, 214110.
- <sup>30</sup> a) Metz, B.; Stoll, H.; Dolg, M. Small-Core Multiconfiguration-Dirac-Hartree-Fock-Adjusted Pseudopotentials for Post-*d* Main Group Elements: Application to PbH And PbO. *J. Chem. Phys.* **2000**, *113*, 2563–2569. b) Peterson, K. A.; Figgen, D.; Goll, E.; Stoll, H.; Dolg, M. Systematically Convergent Basis Sets with Relativistic Pseudopotentials. II. Small-Core Pseudopotentials and Correlation Consistent Basis Sets for the Post-*d* Group 16-18 Elements. *J. Chem. Phys.* **2003**, *119*, 11113–11123. c) Weigend, F.; Alrichs, R. Balanced Basis Sets of Split Valence, Triple Zeta Valence and Quadruple Zeta Valence Quality for H To Rn: Design and Assessment of Accuracy. *J. Phys. Chem. Chem. Phys.* **2005**, *7*, 3297–3305.

- 
- <sup>31</sup> For an example, compare the <sup>31</sup>P NMR chemical shifts of complexes in: Petzold, H.; Görls, H.; Weigand, W. A simple and efficient synthesis of bisphosphine platinum(0) complexes with various P–Pt–P angles. *J. Organomet. Chem.* **2007**, *262*, 2736–2742.
- <sup>32</sup> Kühl, O. *Phosphorus-31 NMR Spectroscopy*; Springer-Verlag, Berlin, 2008; pp 7–12, 16–22.
- <sup>33</sup> Pregosin, P. S. *NMR in Organometallic Chemistry*; Wiley-VCH: Weinheim, 2012; pp 168–170.

## Appendix 2 Supporting Information for Rethinking Catalyst Trapping in Ni-Catalyzed Polymerization of Thieno[3,2-*b*]thiophenes

### A2.1 Materials

Flash chromatography was performed on SiliCycle silica gel (40–63  $\mu\text{m}$ ). Isopropyl magnesium chloride (iPrMgCl) was purchased as a 2 M solution in THF from Millipore Sigma and titrated against salicylaldehyde phenylhydrazone.<sup>1</sup> Ni(dppp)Cl<sub>2</sub> (dppp = 1,3-bis(diphenylphosphinopropane)) was purchased from Strem Chemicals Inc. Thieno[3,2-*b*]thiophene and 3,6-dibromothieno[3,2-*b*]thiophene were purchased from BLDPharm. All other materials and solvents were purchased from Millipore Sigma, Acros, or Fisher and were used without further purification unless otherwise noted. Reactions that were performed in the glovebox with tetrahydrofuran (THF) used THF that was dried and deoxygenated using an Innovative Technology (IT) solvent purification system composed of activated alumina, copper catalyst, and molecular sieves. The glovebox in which specified procedures were carried out was an MBraun LABmaster 130 with a N<sub>2</sub> atmosphere.



## A2.2 General Experimental Details

NMR Spectroscopy: Unless otherwise noted, all spectra were acquired at room temperature (rt). NMR of all organometallic species were taken in air-tight J. Young tubes. Spectra were acquired on either a Varian Vnmrs 500 spectrometer with a Varian 5 mm PFG OneNMR probe (operating at 500 MHz for  $^1\text{H}$  NMR spectra, 126 MHz for  $^{13}\text{C}$  NMR spectra, and 202 MHz for  $^{31}\text{P}$  NMR spectra), a Varian Vnmrs 600 spectrometer with a Varian 4mm PFF AutoX dual broadband probe (operating at 600 MHz for  $^1\text{H}$  NMR spectra, 151 MHz for  $^{13}\text{C}$  NMR spectra, and 242 MHz for  $^{31}\text{P}$  NMR spectra), or a Varian Vnmrs 700 spectrometer with a Varian 5 mm PFG AutoX Broadband Probe (operating at 700 MHz for  $^1\text{H}$  NMR spectra, 176 MHz for  $^{13}\text{C}$  NMR spectra, and 283 MHz for  $^{31}\text{P}$  NMR spectra), denoted next to the spectra.  $^1\text{H}$  spectra were  $^{13}\text{C}$ -decoupled;  $^{13}\text{C}$  spectra were  $^1\text{H}$  decoupled;  $^{31}\text{P}$  spectra were  $^1\text{H}$  decoupled. Chemical shift data are reported in units of  $\delta$  (ppm). For  $^1\text{H}$  and  $^{13}\text{C}$  spectra, chemical shifts were calibrated by referencing the residual protic solvent peaks to their chemical shifts relative to tetramethylsilane.<sup>2</sup> For  $^{31}\text{P}$  NMR spectra, chemical shifts were calibrated using an external 85%  $\text{H}_3\text{PO}_4$  reference. Multiplicities are reported as follows: singlet (s), doublet (d), triplet (t), quartet (q), multiplet (m), broad resonance (br). Residual water is denoted by an asterisk (\*).

High Resolution Mass Spectrometry: High-resolution mass spectrometry data were obtained on a Agilent 6230 TOF HPLC-MS. Unless otherwise specified, the method used was an ESI+ (i.e., positive mode) method.

Gel-Permeation Chromatography (GPC): Polymer molar masses were determined by comparison with polystyrene standards (Varian, EasiCal PS-2 MW 580–377,400) at 40 °C in THF on a

Malvern Viscotek GPCMax VE2001 equipped with two Viscotek LT- 5000L 8 mm (ID) × 300 mm (L) columns and analyzed with Viscotek TDA 305 (with RI, UV-PDA Detector Model 2600 (190–500 nm), RALS/LALS, and viscometer). Data presented correspond to the absorbance at S4 254 nm normalized to the highest peak.

Polymer work-up for GPC: Polymerizations were quenched using aq. HCl (12 M). The organic layer was extracted with CHCl<sub>3</sub>, dried over MgSO<sub>4</sub>, and filtered through a PTFE filter (0.2 μm), concentrated under reduced pressure to dryness and then redissolved in THF/toluene (99:1 v/v) with mild heating and filtered through a PTFE filter (0.2 μm) into a GPC vial.

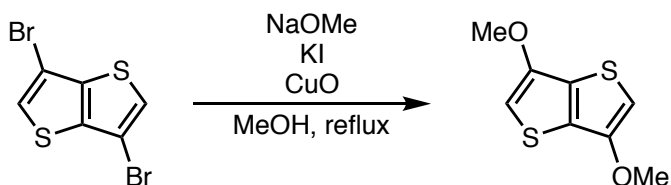
Gas Chromatography: Gas chromatographic (GC) analysis was done using a Shimadzu GC 2010 containing a Shimadzu SHRX5 (crossbound 5% diphenyl – 95% dimethyl polysiloxane; 15 m, 0.25 mm ID, 0.25 μm df) column. The GC method had an initial temperature of 100 °C and increased in temperature at a ramp rate of 15 °C/min until 270 °C (21.3 minutes), then the temperature was held at 270 °C for 30 additional minutes.

Polymer work-up for GC: Polymerizations were quenched using aq. HCl (12 M). The organic layer was extracted with CHCl<sub>3</sub>, dried over MgSO<sub>4</sub>, and filtered through a PTFE filter (0.2 μm). 0.1–0.2 mL were placed into a 2 mL GC vial, and diluted with chloroform.

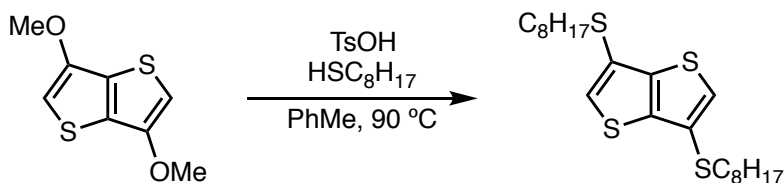
iPrMgCl titration: In a glovebox, an amount of salicylaldehyde phenylhydrazone was massed and dissolved in a known amount of THF such that the concentration of salicylaldehyde phenylhydrazone was ~0.1 M. For titration, iPrMgCl was added dropwise using a 100 μL syringe

into the salicylaldehyde phenylhydrazone solution. Titration was complete when the solution turned bright orange.

### A2.3 Synthetic Procedures



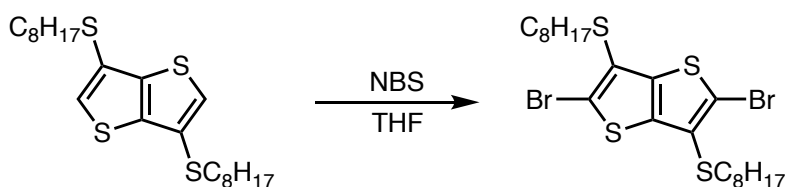
**3,6-dimethoxythiopheno[3,2-*b*]thiophene.** In a 250 mL round bottom flask, 3,6-dibromothiopheno[3,2-*b*]thiophene (1.302 g, 4.37 mmol), potassium iodide (0.0699 g, 0.420 mmol, 0.096 equiv.), and copper (II) oxide (0.7525 g, 9.47 mmol, 2.17 equiv.) were added to a 25 wt% solution of NaOMe in MeOH (100 mL). The reaction, black, was fitted with a reflux condenser and stirred under reflux for 16 h. The reaction mixture was cooled to rt and stirred with water (40 mL) and dichloromethane (50 mL) for 10 minutes, before pouring into a separatory funnel. The organic layer, purple, was collected and the aqueous layer, black, was extracted with DCM (2 x 50 mL) then ether (50 mL x 3). The combined organic layers, pink, were dried over magnesium sulfate, filtered through a 1 inch celite plug, and concentrated in vacuo to give a solid, orange, that was redissolved in DCM (10 mL) and deposited onto silica (5 g) for purification via column chromatography (25 g silica, eluting with a gradient from 100% hexanes to 20% DCM, 80% hexanes) to isolate 0.5882 g 3,6-dimethoxythiopheno[3,2-*b*]thiophene as a white, crystalline solid (67 % yield). HRMS (ESI<sup>+</sup>): calculated for C<sub>8</sub>H<sub>9</sub>O<sub>2</sub>S<sub>2</sub> [M+H]<sup>+</sup> = 201.0039, found = 201.0040. <sup>1</sup>H NMR (500 MHz, CDCl<sub>3</sub>) δ 6.26 (s, 1H), 3.92 (s, 3H). <sup>13</sup>C NMR (126 MHz, CDCl<sub>3</sub>) δ 151.02, 128.61, 97.52, 57.71.



**3,6-dithiooctylthiopheno[3,2-*b*]thiophene.** In a 50 mL round bottom flask, 3,6-dimethoxythiopheno[3,2-*b*]thiophene (0.5010 g, 2.505 mmol), *p*-toluenesulfonic acid hydrate (0.0110 g, 0.064 mmol, 0.025 equiv.), and octane thiol (1.0 mL, 5.753 mmol, 2.29 equiv.) were added to stirring toluene (30 mL). The reaction, colorless, was allowed to stir open to the atmosphere at 90 °C for 12 h.

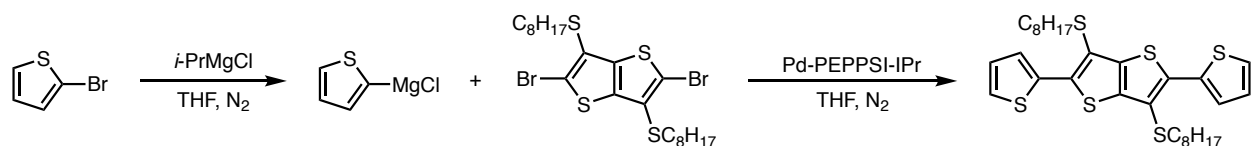
Afterwards, the reaction mixture, red, was cooled to rt and stirred with sodium bicarbonate (10 mL, 20 mol% in water). The organic layer, orange, was collected and the aqueous layer was extracted with DCM (2 x 30 mL) and the combined organic layers, orange, were dried over magnesium sulfate, filtered, and concentrated in vacuo to give a yellow oil. This oil was placed on high vacuum (< 100 mtorr) and while heating (50 °C) for 20 min to remove remaining octane thiol. The resulting brown solid was dissolved in hexanes (6 mL) and was loaded onto a silica column for purification (eluting with 100% hexanes) to isolate 0.9064 g 3,6-dithiooctylthieno[3,2-*b*]thiophene as a white, waxy solid (85 % yield). HRMS (ESI+): calculated for C<sub>22</sub>H<sub>37</sub>S<sub>4</sub> [M+H]<sup>+</sup> = 429.1773, found = 429.1773. <sup>1</sup>H NMR (700 MHz, CDCl<sub>3</sub>) δ 7.28 (s, 2H), 2.90 (t, *J* = 7.2 Hz, 4H), 1.65 – 1.57 (m, 4H), 1.40 (m, 4H), 1.31 – 1.20 (m, 16H), 0.87 (t, *J* = 7.1 Hz, 6H). δ <sup>13</sup>C NMR (176 MHz, cdcl<sub>3</sub>) δ 141.31, 127.11, 125.11, 34.76, 31.93, 29.80, 29.31, 29.24, 28.71, 22.79, 14.24.

---

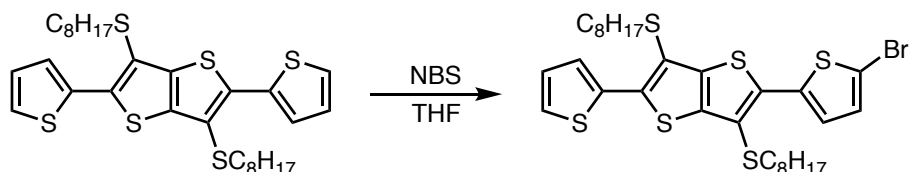


**2,5-dibromo-3,6-dithiooctylthieno[3,2-*b*]thiophene.** In a 40 mL vial, 3,6-dithiooctylthieno[3,2-*b*]thiophene (1.251 g, 2.923 mmol), *N*-bromosuccinimide (1.091 g, 6.129 mmol, 2.097 equiv,) were added to stirring unstabilized tetrahydrofuran (25 mL). The reaction, yellow, was allowed to stir closed at rt for 3h. Afterwards, the reaction mixture, red, was quenched with water (20 mL) and poured into a separatory funnel containing DCM (25 mL). The organic layer, yellow, was collected and the aqueous layer was extracted with DCM (4 x 30 mL) and the combined organic layers, yellow, were dried over magnesium sulfate, filtered, and concentrated in vacuo to give a yellow solid. This solid was dissolved in DCM (5 mL) and recrystallized by layering with acetonitrile (10 mL) and leaving in an open flask overnight. The resulting crystals, colorless, were collected by decanting the supernatant, and the crystals washed with ethanol (~ 5 mL) to give 1.360 g of 2,5-dibromo-3,6-dithiooctylthieno[3,2-*b*]thiophene as clear crystals (79% yield). <sup>1</sup>H NMR (500 MHz, CDCl<sub>3</sub>) δ 2.87 (t, *J* = 7.3 Hz, 4H), 1.54 (q, *J* = 7.6 Hz, 4H), 1.44 – 1.36 (m, 4H), 1.32 – 1.17 (m, 16H), 0.87 (t, *J* = 6.9 Hz, 6H). <sup>13</sup>C NMR (126 MHz, CDCl<sub>3</sub>) δ 139.69, 125.95, 119.50, 35.09, 32.17, 30.38, 29.54, 29.44, 28.82, 23.04, 14.50.

---

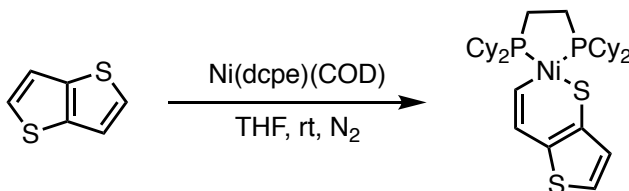


**2,5-di(2-thienyl)-3,6-dioctylthiothieno[3,2-*b*]thiophene.** To 20 mL septum-sealed Schlenk flask connected to a nitrogen line, 2-bromothiophene (0.180 mL, 0.303 g, 1.86 mmol, 2.17 equiv.) was added along with dry THF (20 mL), and isopropyl magnesium chloride (2 M in THF, 0.9 mL, 1.8 mmol, 2.1 equiv.). The reaction mixture was allowed to stir at rt under nitrogen for 30 minutes. Then, a solution of 3,6-dioctylthiothieno[3,2-*b*]thiophene (0.1710 M in THF, 0.5011 g, 0.8551 mmol, 1.0 equiv.) and Pd-PEPPSI-IPr (0.0177 M in THF, 60.4 mg, 0.0889 mmol, 0.104 equiv.) were added via syringe, and the reaction was heated to 60 °C and allowed to stir for 24 h. The reaction was allowed to cool to rt, then quenched with water (10 mL) and poured into a separatory funnel containing DCM (30 mL). The organic layer, brown, was collected and the aqueous layer was extracted once more with DCM (30 mL). The combined organic layers were dried over magnesium sulfate, filtered, and concentrated in vacuo to give a brown oil. This oil was purified via column chromatography (50 g silica, eluted with 100% hexanes) to yield 0.4540 g of 2,5-di(2-thienyl)-3,6-dioctylthiothieno[3,2-*b*]thiophene as a yellow, flaky solid (89% yield). HRMS (ESI<sup>+</sup>): calculated for C<sub>30</sub>H<sub>41</sub>S<sub>6</sub> [M+H]<sup>+</sup> = 593.1528, found = 593.1529. <sup>1</sup>H NMR (500 MHz, *d*<sub>2</sub>-DCM) δ 7.48 (dd, *J* = 3.7, 1.2 Hz, 2H), 7.41 (dd, *J* = 5.1, 1.2 Hz, 2H), 7.09 (dd, *J* = 5.1, 3.7 Hz, 2H), 2.91 (t, *J* = 7.3 Hz, 4H), 1.57 (p, *J* = 7.3 Hz, 4H), 1.36 (p, *J* = 7.2 Hz, 4H), 1.31 – 1.18 (m, 16 H), 0.85 (t, *J* = 7.0 Hz, 6H). <sup>13</sup>C NMR (126 MHz, *d*<sub>2</sub>-DCM) δ 141.13, 140.69, 136.30, 127.52, 127.48, 127.19, 120.24, 35.92, 32.35, 30.55, 29.70, 29.61, 29.14, 23.20, 14.42.



**2-(5'-bromothiophen-2'-yl)-5-(2''-thienyl)-3,6-dioctylthiothieno[3,2-*b*]thiophene.** In a 20 mL vial, 2,5-di(2-thienyl)-3,6-dioctylthiothieno[3,2-*b*]thiophene (0.3060 g, 0.5160 mmol), *N*-bromosuccinimide (0.0653 g, 0.3669 mmol, 0.7110 equiv.) were added to stirring unstabilized tetrahydrofuran (10 mL). The reaction, yellow, was allowed to stir closed at rt for 3h. Afterwards, the reaction mixture, yellow, was quenched with water (20 mL) and poured into a separatory funnel containing DCM (20 mL). The organic layer, yellow, was collected and the aqueous layer was

extracted again with DCM (20 mL) and the combined organic layers, yellow, were dried over magnesium sulfate, filtered, and concentrated in vacuo to give a yellow solid. This solid was dry-loaded onto a silica column (100 g) and eluted with 100% hexanes and leaving in an open flask overnight. The resulting crystals, colorless, were collected by decanting the supernatant, and the crystals were dry-loaded onto 1 g of silica and purified via column chromatography (100 g silica, eluted with 100% hexanes) to yield 0.1580 g of 2,5-di(2-thienyl)-3,6-dioctylthiothieno[3,2-*b*]thiophene as a yellow, flaky solid (45% yield). <sup>1</sup>H NMR (500 MHz, Methylene Chloride-*d*<sub>2</sub>) δ 7.47 (dd, *J* = 3.7, 1.2 Hz, 1H), 7.40 (dd, *J* = 5.1, 1.2 Hz, 1H), 7.19 (d, *J* = 4.0 Hz, 1H), 7.08 (dd, *J* = 5.1, 3.7 Hz, 1H), 7.04 (d, *J* = 4.0 Hz, 1H), 2.95 – 2.83 (m, 4H), 1.56 (dp, *J* = 10.4, 7.4 Hz, 4H), 1.36 (d, *J* = 7.2 Hz, 4H), 1.29 – 1.15 (m, 16H), 0.84 (td, *J* = 7.0, 1.9 Hz, 6H). <sup>13</sup>C NMR (126 MHz, cd<sub>2</sub>cl<sub>2</sub>) δ 141.27, 140.93, 140.13, 137.94, 136.19, 130.14, 127.63, 127.55, 127.29, 126.79, 120.56, 120.24, 114.78, 36.13, 35.95, 32.35, 30.56, 29.72, 29.69, 29.62, 29.16, 29.13, 23.22, 14.42.



**Nickel(1,2-bis(dicyclohexylphosphino)ethane)[(C,S-κ<sup>2</sup>)-thieno[3,2-*b*]thiophene].**

Procedure 1: To a 20 mL vial in a nitrogen glovebox, thieno[3,2-*b*]thiophene (23.7 mg, 0.169 mmol, 1.00 equiv) tetrahydrofuran (2.5 mL), and Ni(dcpe)(1,5-cyclooctadiene) (101.0 mg, 0.1712 mmol, 1.014 equiv) were added along with a stir bar, forming a yellow solution that was stirred. After 24 h, volatiles were removed under vacuum, resulting in a red powder that was redissolved in dichloromethane (5 mL) and then crashed out by addition of pentanes (15 mL) giving a red powder. The supernatant was decanted, and the solid was washed twice more with pentanes and dried under high-vacuum, giving 13 (74.4 mg, 0.120 mmol, 70.9% yield).

Procedure 2, X-ray crystals: To a 20 mL vial in a nitrogen glovebox, a solution of thieno[3,2-*b*]thiophene (151 mg, 1.08 mmol, 1.00 equiv) and 1,2-bis(dicyclohexylphosphino)ethane (458 mg, 1.02 mmol, 0.94 equiv.) in tetrahydrofuran (4 mL) was added to nickel bis(1,5-cyclooctadiene) (280 mg, 0.1712 mmol, 1.014 equiv) forming a yellow solution upon stirring. After 24 h, NMR of the solution was taken in THF, and the remaining reaction mixture was treated with hexanes (layered atop the red THF solution) and allowed to sit, undisturbed, at –30°C for three months,

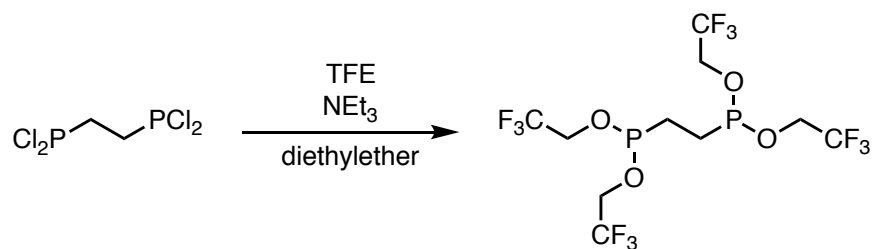
yielding X-ray quality cubic orange crystals.  $^1\text{H}$  NMR (500 MHz, THF)  $\delta$  7.16 (ddd,  $J = 22.5$ , 10.2, 6.2 Hz, 2H), 6.97 (d,  $J = 5.1$  Hz, 1H), 6.79 (d,  $J = 5.0$  Hz, 1H), 2.22 (s, 8H), 1.39 – 0.79 (m, 26H).  $^{31}\text{P}$  NMR (202 MHz, THF)  $\delta$  74.88 (d,  $J = 23.4$  Hz), 64.06 (d,  $J = 23.5$  Hz), 59.70 (impurity, Ni(dcpe)(COD)).

---



**2-bromothieno[3,2-*b*]thiophene.** To a round-bottomed flask (100 mL), thieno[3,2-*b*]thiophene (1.029 g, 7.350 mmol, 1.0 equiv.) was added followed by dimethylformamide (50 mL) and *N*-bromosuccinimide (1.091 g, 6.198 mmol, 0.84 equiv.). The reaction was capped and allowed to stir at rt for 3 h. The reaction was quenched with water (40 mL), poured into a separatory funnel, and extracted with dichloromethane (5 x 30 mL). The combined organic layers were then washed with aqueous LiCl (1 M, 2 x 30 mL), and then washed with water (10 x 50 mL) to remove the residual DMF. The combined organic layers were dried over magnesium sulfate, filtered, and condensed via rotovap to give a yellow oil. This oil was purified by placing atop a silica column (100 g, pre-wetted with hexanes) and eluting with hexanes. Fractions were analyzed by TLC and the pure fractions were combined and condensed in vacuo to give the desired product as a clear, colorless oil (0.6183 g, 38% yield).  $^1\text{H}$  NMR (500 MHz, Methylene Chloride- $d_2$ )  $\delta$  7.44 (d,  $J = 5.3$  Hz, 1H), 7.31 (s, 1H), 7.20 (d,  $J = 5.3$  Hz, 1H).  $^{13}\text{C}$  NMR (126 MHz,  $\text{cd}_2\text{cl}_2$ )  $\delta$  140.02, 138.60, 127.32, 122.76, 122.47, 119.60, 113.90, 110.58.

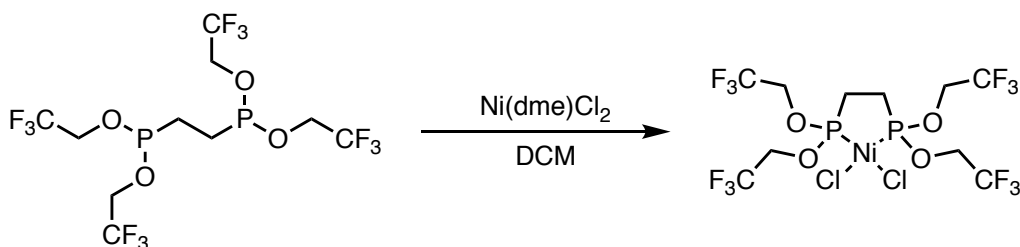
---



**Tetrakis(2,2,2-trifluoroethyl)ethane-1,2-diylbis(phosphonite).** To a flask (250 mL) inside of a nitrogen filled glovebox, trifluoroethanol (3.1 mL, 4.25 g, 42.5 mmol, 4.3 equiv.) was added followed by triethylamine (7.3 mL, 5.29 g, 52.4 mmol, 5.25 equiv.) and diethyl ether (150 mL) forming a clear, colorless solution. To this, a stir bar was added, followed by 1,2-bis(dichlorophosphino)ethane (1.5 mL, 2.30 g, 9.9 mmol, 1.0 equiv.) dropwise over the course of

10 minutes causing a white solid to form. The flask was sealed with a septum, and the reaction was allowed to stir in the glovebox. After 18 h, the reaction was filtered to remove triethylammonium chloride, and the resulting colorless solution was condensed under vacuum in the glovebox, giving a clear, colorless oil. The oil was purified by dissolving in DCM (1 mL) and recrystallizing at  $-35\text{ }^{\circ}\text{C}$ , washing the resulting solid with hexanes and recrystallizing from DCM once more to yield the desired product (1.34 g, 34% yield).  $^1\text{H}$  NMR (500 MHz, THF)  $\delta$  4.03 (ddq,  $J = 16.2, 7.9, 3.5$  Hz, 8H), 1.61 (t,  $J = 7.2$  Hz, 4H).  $^{13}\text{C}$  NMR (126 MHz, THF)  $\delta$  123.13 (q,  $J = 278.8, 278.3$  Hz), 76.85 (t,  $J = 32.1$  Hz), 66.10 – 63.79 (m).  $^{19}\text{F}$  NMR (471 MHz, THF)  $\delta$   $-75.77$  (t,  $J = 8.2$  Hz).  $^{31}\text{P}$  NMR (202 MHz, THF)  $\delta$  198.83 (s).

---

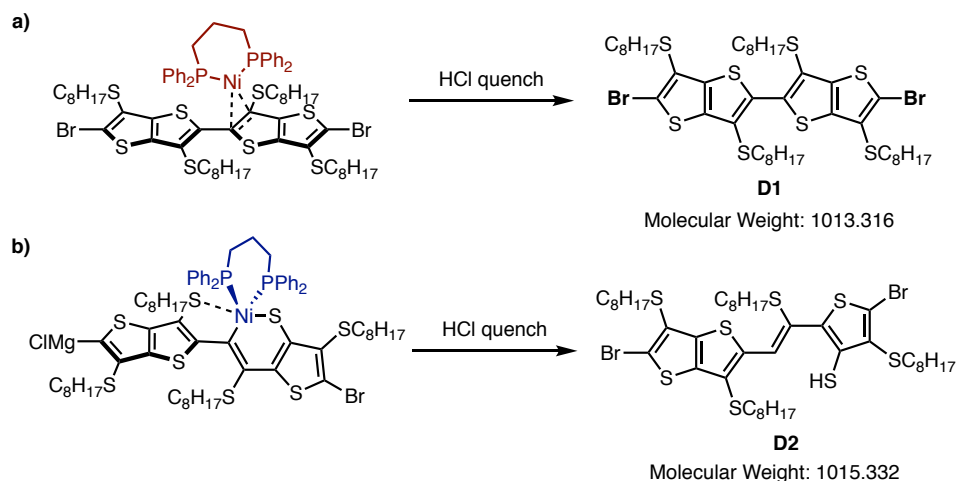


**Nickel Tetrakis(2,2,2-trifluoroethyl)ethane-1,2-diylbis(phosphonite) dichloride.** To a 20 mL vial in the glovebox,  $\text{NiCl}_2(\text{dimethoxyethane})$  (0.1981 g, 0.9046 mmol, 2.089 equiv.) was added. To this, a solution of Tetrakis(2,2,2-trifluoroethyl)ethane-1,2-diylbis(phosphonite) (0.2104 g, 0.4786 mmol, 1.00 equiv.) in THF (8 mL) was added, causing the reaction mixture to turn brown. The reaction was allowed to stir for 10 minutes, and was then filtered through a syringe-tip PTFE mesh filter. The dark red solution was condensed in vacuo to give a brown solid, which was then redissolved in DCM (2 mL) and hexanes (8 mL), then exposed to vacuum to remove DCM, causing a brown solid to crash out. The supernatant was removed, and the brown solid was dried under vacuum to give a flaky brown solid (0.2520 g, 94% yield).  $^1\text{H}$  NMR (500 MHz, Chloroform-*d*)  $\delta$  5.23 (s, 4H), 4.75 (s, 4H), 2.03 (d,  $J = 21.6$  Hz, 4H).  $^{19}\text{F}$  NMR (471 MHz, Chloroform-*d*)  $\delta$   $-74.91$  (d,  $J = 8.3$  Hz).  $^{31}\text{P}$  NMR (202 MHz, Chloroform-*d*)  $\delta$  175.46.



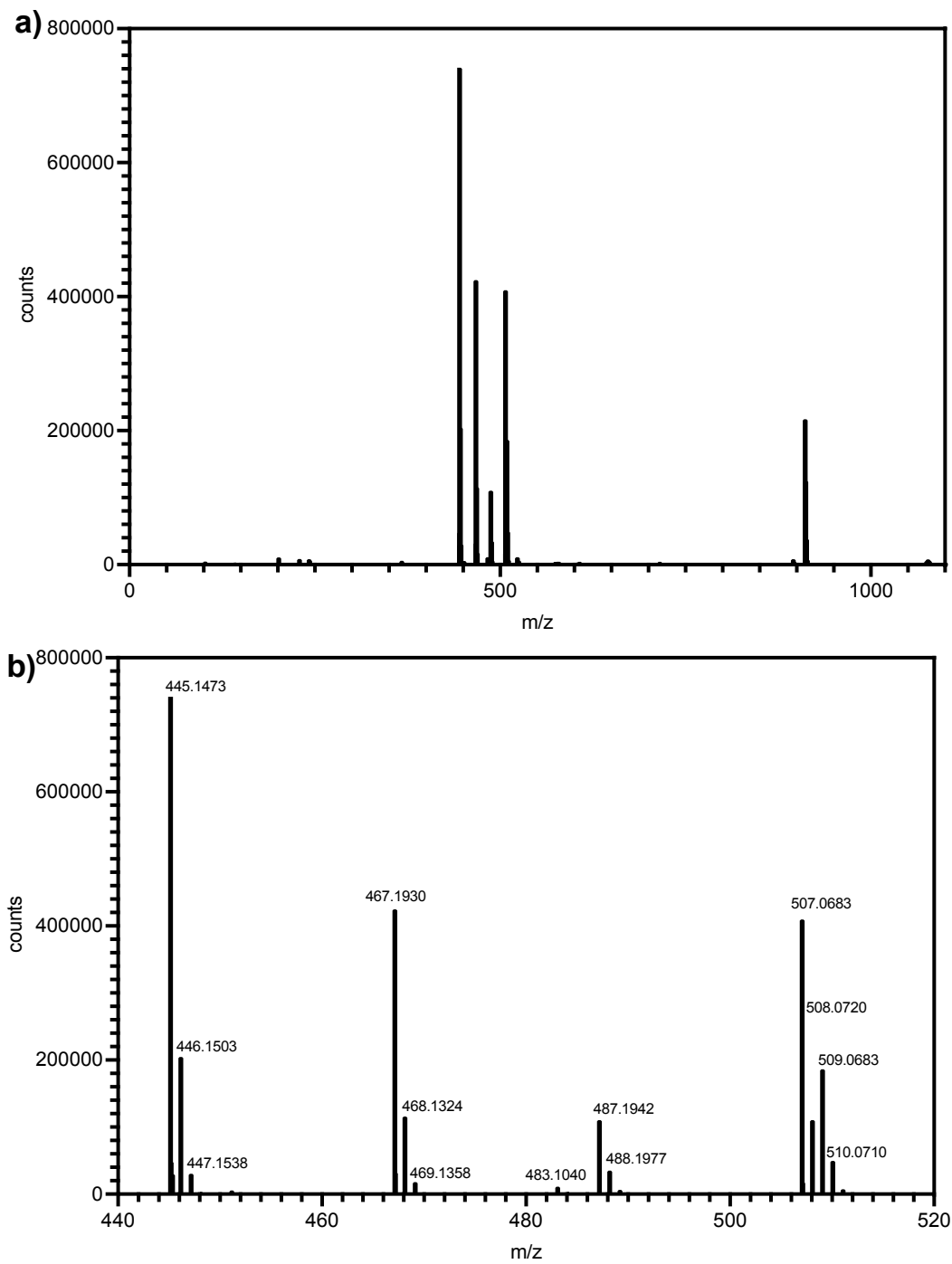
## A2.4 Explaining Dimers in the Quenched Reaction Mixture

In the original investigation by Koeckelberghs, dibromo dimers (such as **D1**, Figure A2.1a) were isolated from the acid-quenched polymerization indicating that the catalyst could not undergo C–Br oxidative addition at the chain end, consistent with quenching the Ni off from a  $\pi$ -complex. In our mechanism, dimers must also form to generate the Ni<sup>0</sup> species which can undergo C–S insertion. However, quenching with acid from the C–S insertion adduct would yield a non-symmetric species with a mass  $\sim 2$  g/mol larger (**D2**, Figure A2.1b) inconsistent with what Koeckelberghs observed from the polymerization.



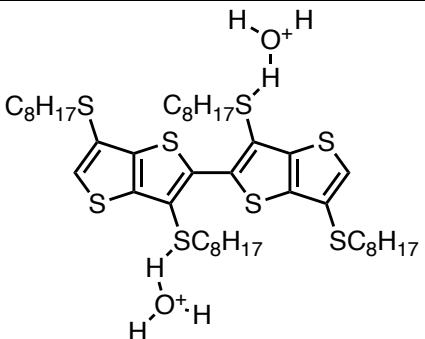
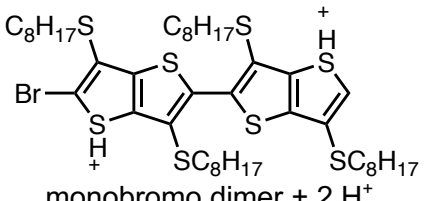
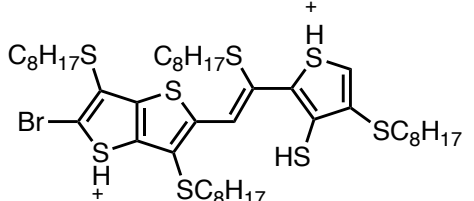
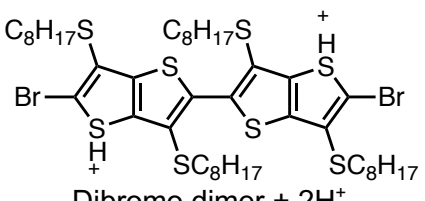
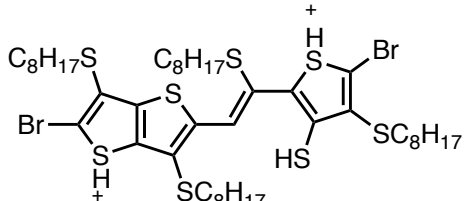
**Figure A2.1** species that result from a) quenching of a  $\pi$ -complex and b) quenching of the C–S insertion adduct.

To explain how dimers such as **D1** form within our mechanism, we analyzed the polymerization to determine if other dimers or other species were present (for experimental details, see Appendix A2.6.1). In these studies, we observed that greater than 10 equivalents of monomer (relative to catalysts) were consumed during polymerizations with Ni(dppp)Cl<sub>2</sub> (Table A2.3). Additionally, dimers such as **D1**, **D2**, and debrominated species had formed, according to the ESI+ mass spectrum (Figure A2.2, Table A2.1).



**Figure A2.2** a) full and b) zoomed-in ESI+ mass spectra from the quenched polymerization mixture, with peaks arising from ring-opened and debrominated species as well as **D1**.

**Table A2.1** Peak assignments for mass spectra in Figure A2.2

Observed peak	Assigned Species	Calculated Mass
446.1503	 <p>no bromo dimer + 2 H<sub>3</sub>O<sup>+</sup></p>	$C_{44}H_{76}O_2S_8^{2+} =$ $M+H_6O_2^{++} =$ 446.1800
467.1286	 <p>monobromo dimer + 2 H<sup>+</sup></p>	$C_{44}H_{71}BrS_8^{2+} =$ $M+2H^+ =$ 467.1247
468.1324	 <p>Ring-opened monobromo dimer + 2 H<sup>+</sup></p>	$C_{44}H_{71}BrS_8^{2+} =$ $M+2H^+ =$ 468.1325
507.0683	 <p>Dibromo dimer + 2H<sup>+</sup></p>	$C_{44}H_{70}Br_2S_8^{2+} =$ $M+2H^+ =$ 507.0789
508.0720	 <p>ring-opened dibromo dimer + 2H<sup>+</sup></p>	$C_{44}H_{72}Br_2S_8^{2+} =$ $M+2H^+ =$ 508.0868

Given that both the  $\pi$ -complex and C–S insertion catalyst traps are proposed to form after the catalyst reacts with only two equivalents of monomer, monomer consumption of greater than

2 equivalents is inconsistent with both mechanisms. Additionally, the formation of non-halogenated dimers is inconsistent with both mechanisms, given the inability of either catalyst to reach the chain-end. However, a mechanism of catalyst trapping in which both dissociation and C–S insertion can occur may be consistent with these observations, as such a mechanism would allow for generation of free Ni<sup>0</sup> which could insert into C–Br bonds and react with excess equivalents of monomer. Indeed, when we calculate the binding energies of the on-cycle  $\pi$ -complexes, we find that the catalyst is weakly bound, with  $\Delta G_{\text{binding}}$  as low as 12.1 kcal/mol (Figure A2.3), potentially enabling dissociation of the  $\pi$ -complex.

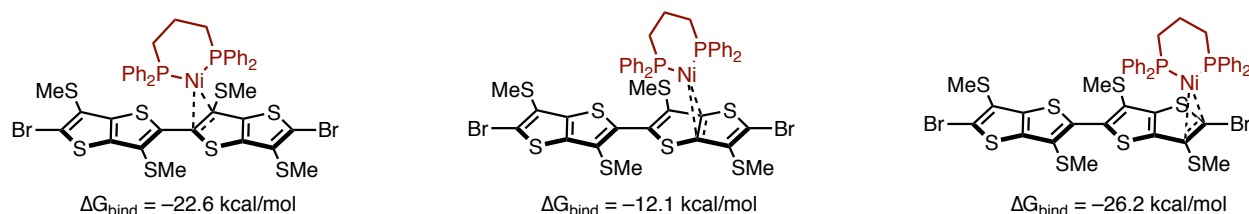


**Figure A2.3** binding energies of the on-cycle  $\pi$ -complexes relative to free **D1** + Ni(dppp). Note, SC<sub>8</sub>H<sub>17</sub> have been truncated to SMe groups to reduce computational complexity.

Given these observations and binding energies, we propose the following mechanism for dimer generation in CTP of TTh (Figure A2.4). After generation of  $\pi$ -complexes via sequential transmetalation and reductive elimination, an equilibrium between C–S insertion adducts, and  $\pi$ -complexes is established. While the catalysts resting state is the C–S insertion adduct (based on computations in the previous section), equilibrium with the  $\pi$ -complexes enable dissociation from the  $\pi$ -complex. Once dissociation occurs, additional equivalents of monomer may be consumed via C–Br or C–S insertion reactions (Figure A2.4), generating debrominated dimers such as **D3**.

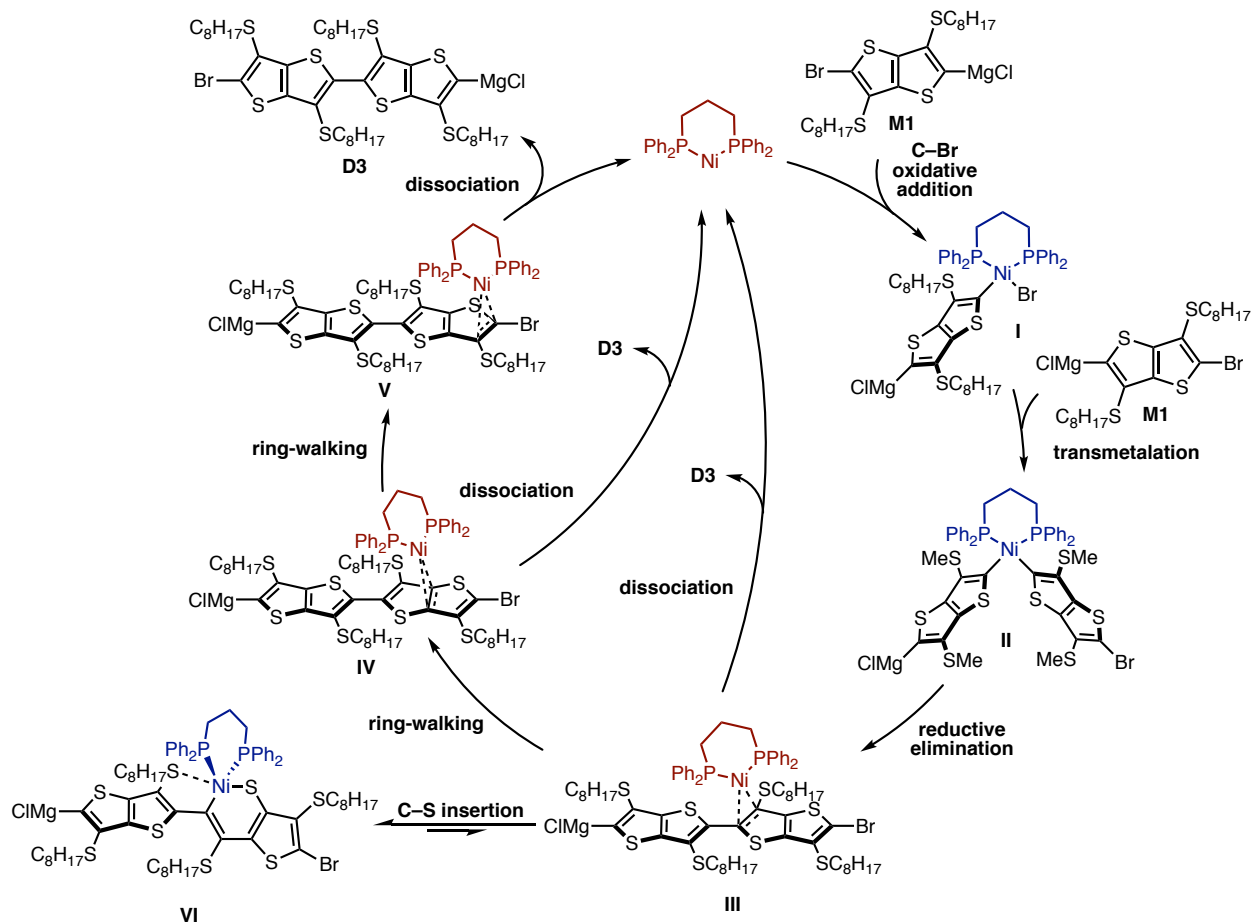


**Figure A2.4** A mechanism for catalyst trapping in CTP, showing the pathways that enable dimer formation and C–S insertion. Note, initiation is not shown.

In addition to dissociation from the  $\pi$ -complex, Vicic and Jones<sup>3,4,5</sup> have also studied the degradation reactions from C–S insertion adducts of thiophene derivatives (Figure A2.5).<sup>32</sup> They find that for benzothiophene and dibenzothiophene, a number of different complexes result from degradation, including free Ni species and demetalated arenes products. Although we have not investigated the relevance of similar degradation pathways from the C–S insertion adducts in TTh, it is possible that dimers of TTh or free Ni species (which may initiate new dimerizations) may form from similar degradation processes.

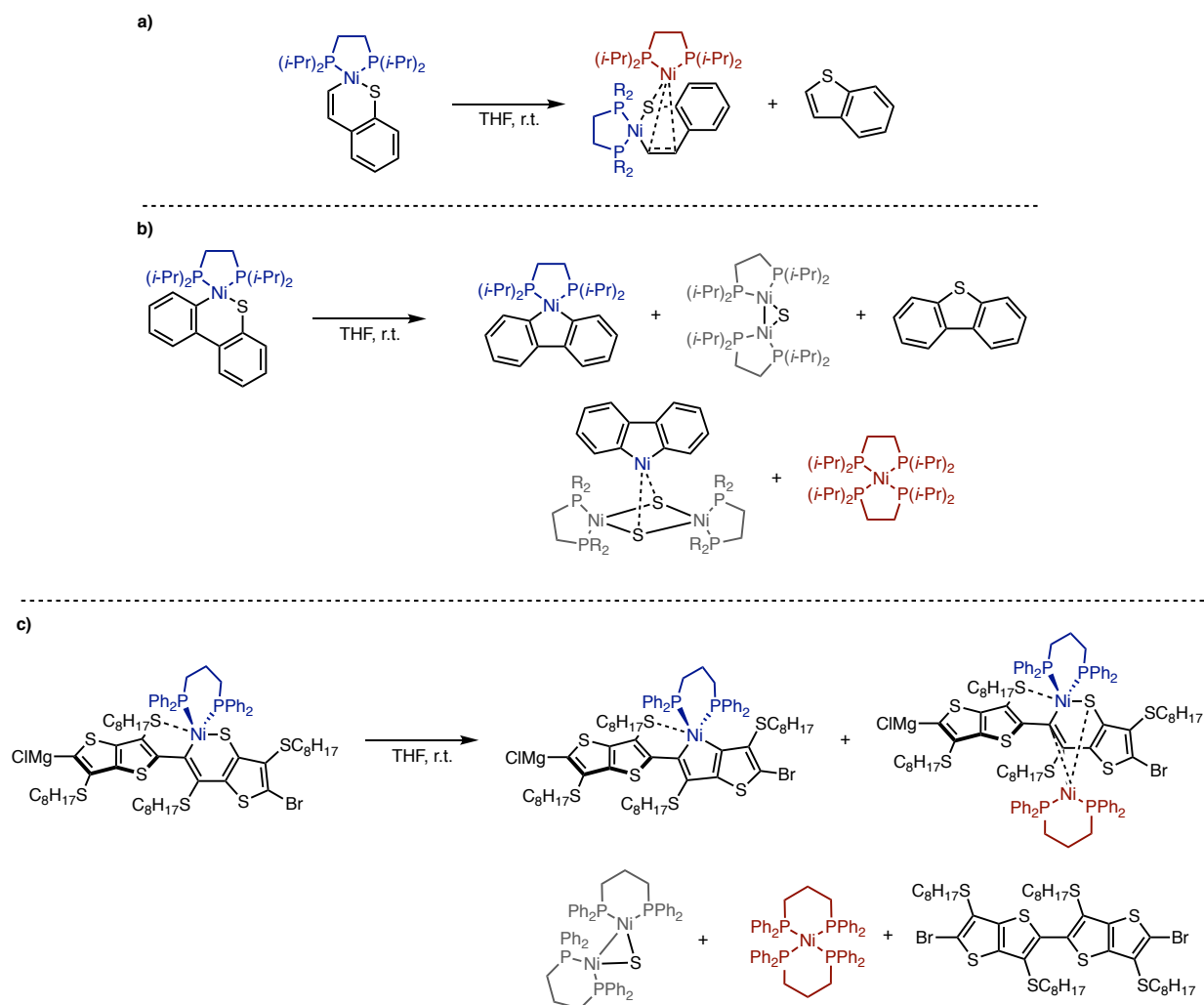
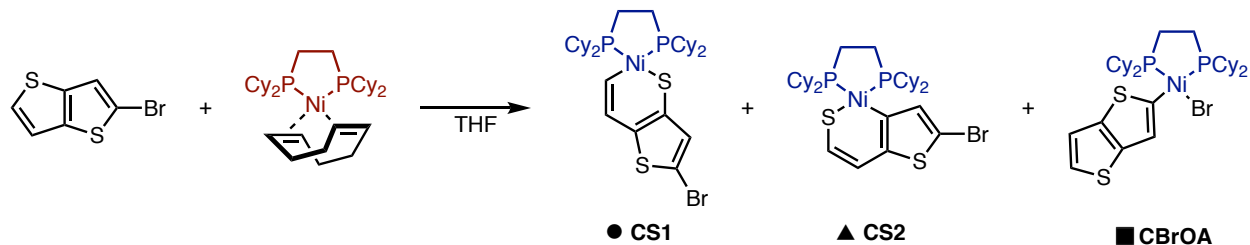


**Figure A2.5** Degradation products observed by Vicic and Jones for a) benzothiophene and b) dibenzothiophene C–S insertion adducts. c) analogous degradation products that may be present in the current system.

## A2.5 Small Molecule NMR Studies

### A2.5.1 NMR study of reaction of 2-bromothiophene with Ni(dcp)(COD)



Procedure: To a 4 mL vial in the glovebox, Ni(COD)(dcp) (76.8 mg, 0.130 mmol, 1.0 equiv.) was added along with a stir bar. To this, a solution of 2-bromothiophene (28.5 mg, 0.130 mmol, 1.0 equiv) in THF (2.2 mL) was added, causing the reaction to turn orange. The reaction was allowed to stir until solids dissolved, then was transferred to a J. Young tube for  $^{31}\text{P}$  NMR analysis. The  $^{31}\text{P}$  NMR taken at different time points are shown below in Figure A2.6.

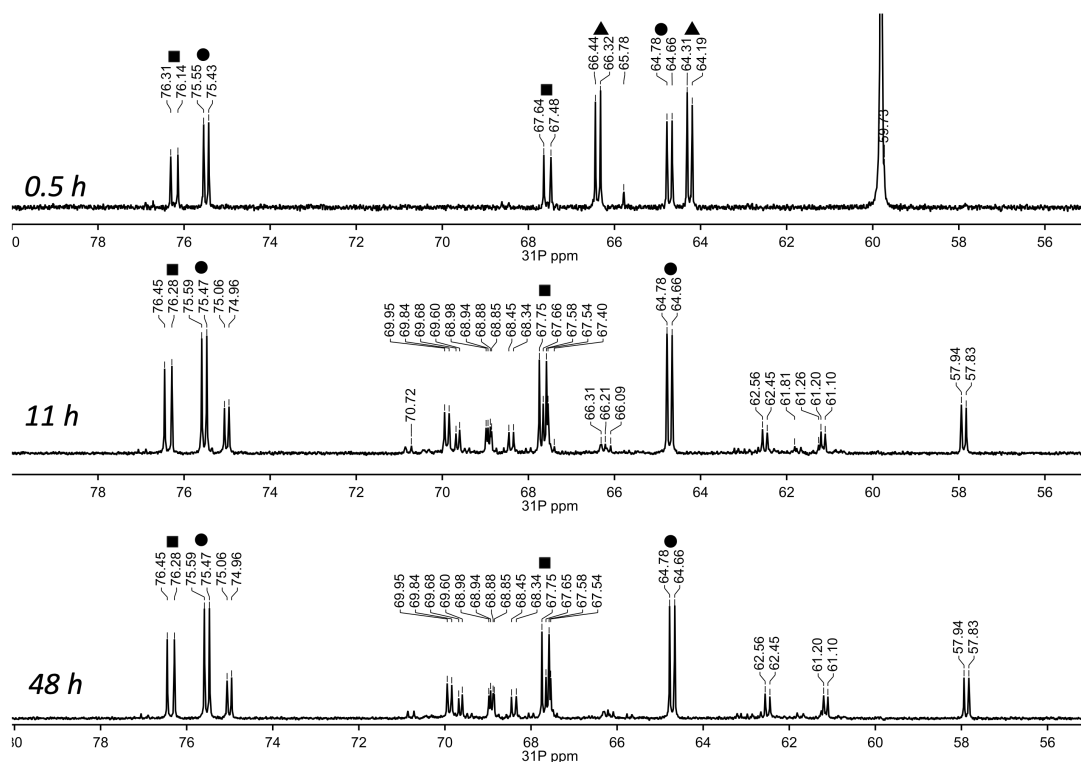
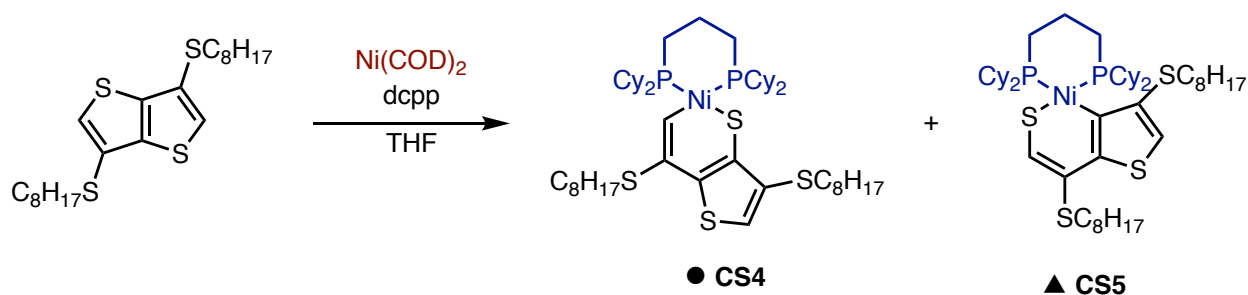


**Figure A2.6**  $^{31}\text{P}$  NMR (202 MHz, THF) spectra taken at different time points for the reaction of Ni(COD)(dcp) with 2-bromothiophene.

We attempted to grow crystals from the reaction mixture via slow vapor diffusion with hexanes, however, no crystals formed. NMR assignments are based on similarity with Nickel(1,2-bis(dicyclohexylphosphino)ethane)[(C,S- $\kappa^2$ )-thieno[3,2-*b*]thiophene] and on similarity with previously reported compounds such as those reported by Jones and Vicic, where C–S insertion into dibenzothiophene yielded C–S insertion adducts with chemical shifts that were close together, while insertion into benzothiophene and thiophene yielded chemical shifts that were further apart.<sup>3–5</sup>

#### A2.5.2 NMR study of reaction of 3,6-dioctylthiethiophene with Ni(COD)<sub>2</sub> and dcpp



Procedure: To a 4 mL vial in the glovebox, Ni(COD)<sub>2</sub> (31.6 mg, 0.114 mmol, 1.0 equiv.) was added along with a stir bar. To this, a solution of 3,6-dioctylthiethiophene (50.4 mg, 0.117 mmol, 1.02 equiv.) and 1,3-bis(dicyclohexylphosphino)propane (51.5 mg, 0.118 mmol, 1.03 equiv.) in THF (2 mL) was added, causing the reaction to turn orange then brown. After 90 minutes, the solution was transferred to a J. Young tube for <sup>31</sup>P NMR analysis. The <sup>31</sup>P NMR taken at different time points are shown below in Figure A2.7.



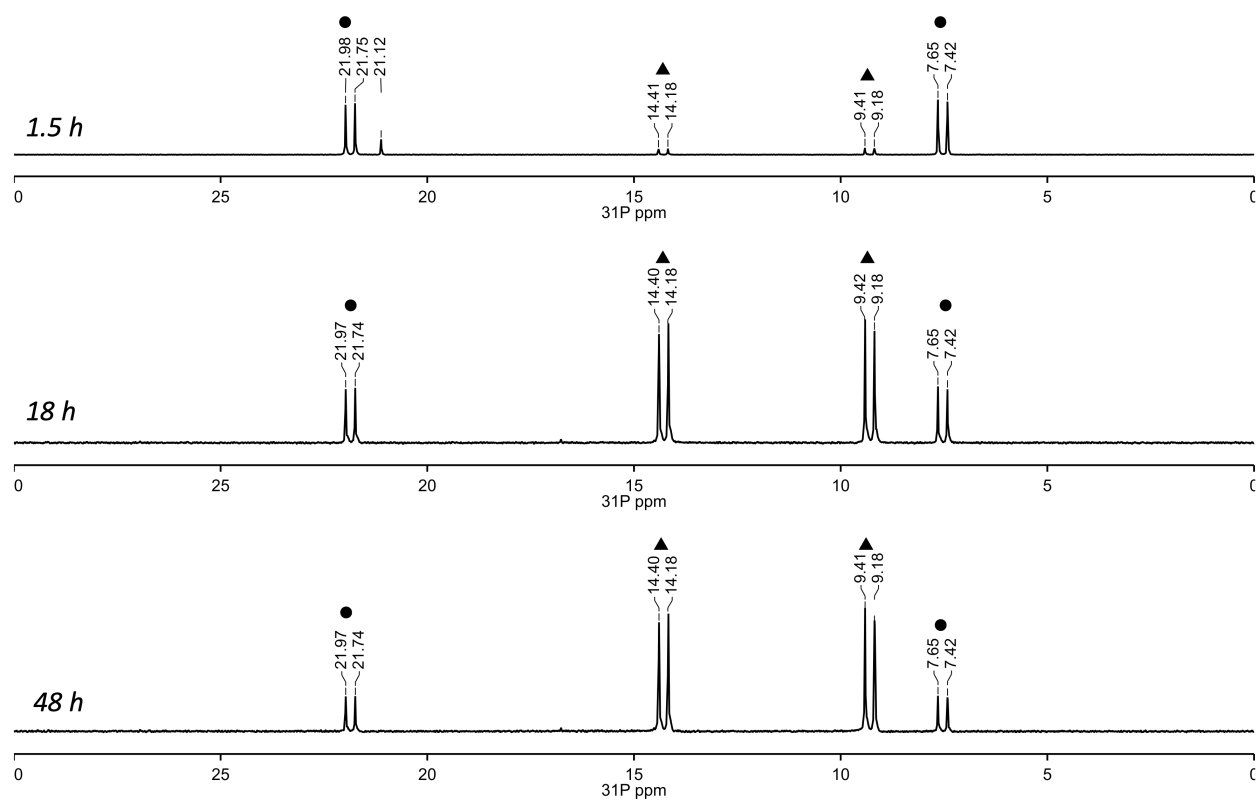
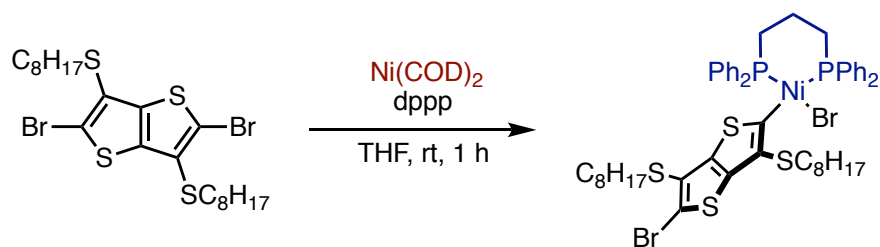


**Figure A2.7**  $^{31}\text{P}$  NMR (243 MHz, THF) spectra taken at different time points for the reaction of  $\text{Ni}(\text{COD})_2$  with dcpp and 3,6-dioctylthienothiophene.

Assignments for the specific C4 and C5 species were based on similarities to chemical shifts of C–S insertion adducts previously reported by Jones and Vicic.<sup>3–5</sup>

### A2.5.3 Reaction of $\text{Ni}(\text{COD})_2$ with 2,5-dibromo-3,6-dithiooctylthienothiophene



Procedure: to a 4 mL vial in the glovebox,  $\text{Ni}(\text{COD})_2$  (11.5 mg, 0.0418 mmol, 1.0 equiv,) was added along with a stir bar. To this, a solution of 2,5-dibromo-3,6-dithiooctylthienothiophene

(26.6 mg, 0.0454 mmol, 1.09 equiv.) and 1,3-bis(diphenylphosphino)propane (17.7 mg, 0.0430 mmol, 1.02 equiv.) in *d*<sub>8</sub>-THF (0.5 mL) was added along with a stir bar, forming a yellow suspension which turned into a dark orange solution after ~5 min. The reaction was analyzed via <sup>1</sup>H and <sup>31</sup>P NMR spectroscopy.

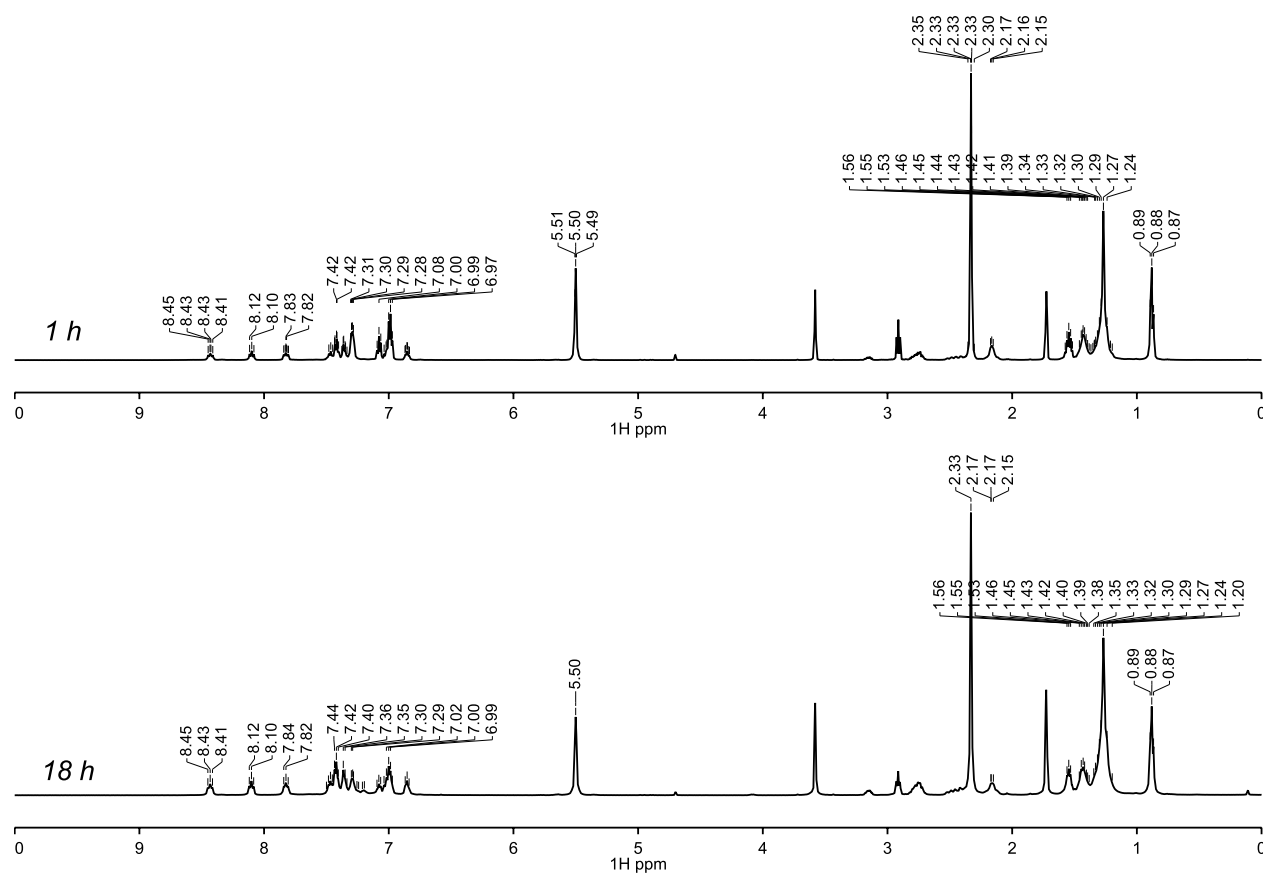


**Figure A2.8** <sup>1</sup>H NMR spectra at 1 h (top) and 18 h (bottom) reaction times.

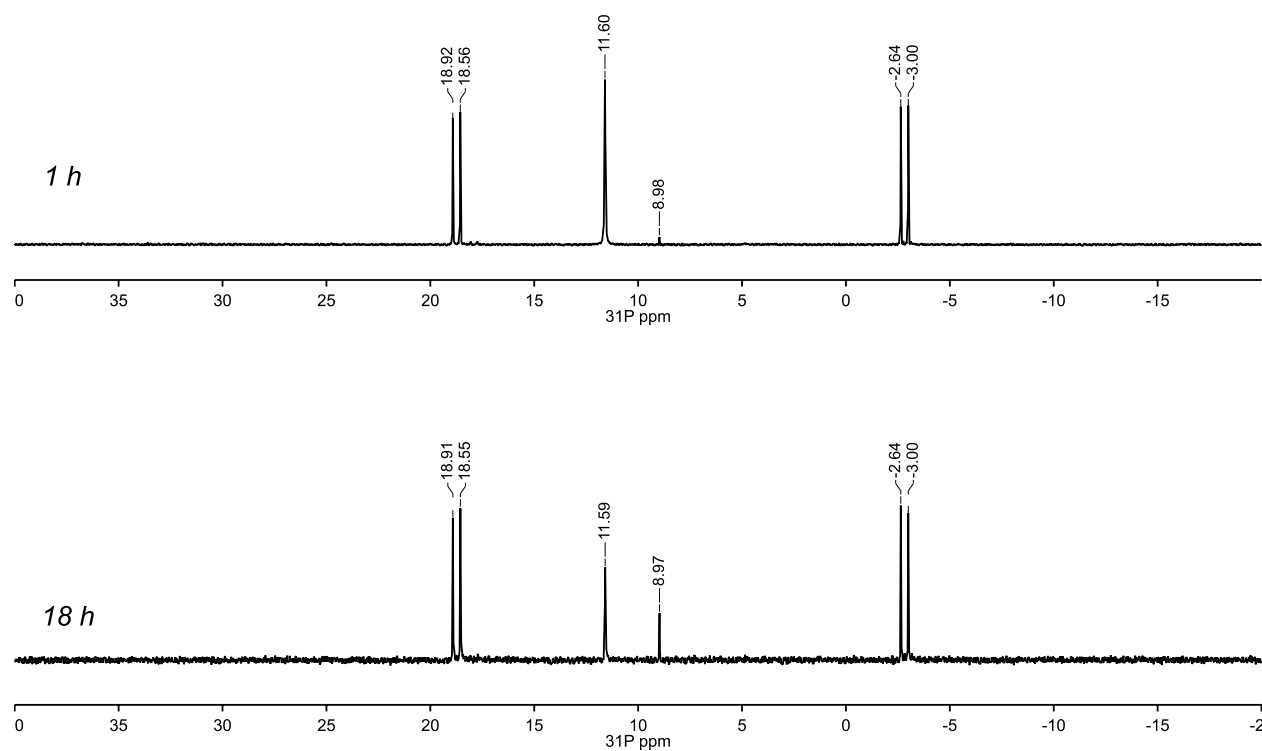
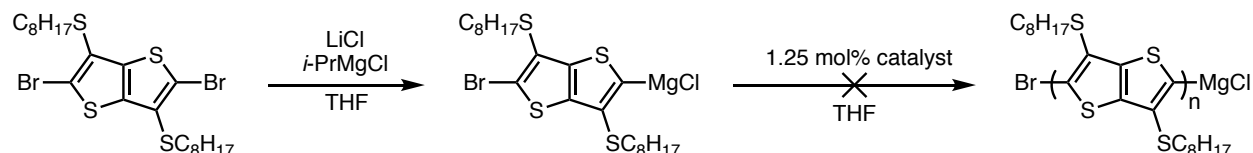


**Figure A2.9**  $^{31}\text{P}$  NMR spectra at 1 h (top) and 18 h (bottom) reaction times, showing peaks at  $\delta$  18.74 (d,  $J = 72.8$  Hz), 11.60, 8.97, -2.82 (d,  $J = 73.1$  Hz). Peaks at 11.6 and 8.97 are assigned to  $\text{Ni}(\text{dppp})_2$  and  $\text{Ni}(\text{dppp})(\text{COD})$  respectively.

$^{31}\text{P}$  NMR spectra show a set of doublets with  $J_{\text{PP}} = 73$  Hz - given the reactivity of  $\text{Ni}^0$  complexes with C-Br containing arenes, we assigned these peaks to species **Ic8**.

## A2.6 Polymerization Reactions

### A2.6.1 Polymerization of 2-magnesioclboro-5-dibromo-3,6-dithiooctylthieno[3,2-*b*]thiophene, M1 with Ni(*dppe*) and Ni(*dppp*).



#### Monomer stock solution preparation:

Monomer solution A (no LiCl): To a 20 mL vial in a nitrogen glovebox, 2,5-dibromo-3,6-dithiooctylthieno[3,2-*b*]thiophene (106.0 mg, 0.1808 mmol, 1.0 equiv.) was added along with C<sub>22</sub>H<sub>46</sub> (GC standard, 4.0 mg), THF (2.0 mL) and *i*PrMgCl (2.0 M in THF, 81  $\mu$ L, 0.90 equiv.) and was left to stir for 30 minutes.

Monomer solution B (w/ LiCl):, 1.0 mL of monomer solution A was removed, and added to a 20 mL vial containing LiCl (3.6 mg, 0.086 mmol, 1.0 equiv.) while the other portion of monomer solution A was left untouched.

Both monomer solutions were left to stir for 30 more minutes. Afterwards, 0.1 mL of each solution was removed and quenched with water, and analyzed by GC analysis. The remaining solutions were then immediately used in polymerizations.

#### Catalyst stock solution preparation:

Ni(*dppp*)Cl<sub>2</sub> stock solution: Ni(*dppp*)Cl<sub>2</sub> (1.1 mg, 2.0  $\mu$ mol) was added to a 20 mL vial in a nitrogen glovebox, along with a stir bar and tetrahydrofuran (4 mL). The solution was allowed to stir for 30 minutes.

Ni(*dppe*)Cl<sub>2</sub> stock solution: Ni(*dppe*)Cl<sub>2</sub> (1.1 mg, 2.1  $\mu$ mol) was added to a 20 mL vial in a nitrogen glovebox, along with a stir bar and tetrahydrofuran (4 mL). The solution was allowed to stir for 30 minutes.

#### Polymerizations:

Polymerization 1 (Ni(*dppp*)Cl<sub>2</sub>, no LiCl): monomer solution A (0.45 mL, 0.0814 mmol) was added to Ni(*dppp*)Cl<sub>2</sub> stock solution (2.0 mL, 1.0  $\mu$ mol, 0.012 equiv) while stirring. The reaction mixture turned orange upon addition and was allowed to stir for 2 h.

Polymerization 2 (NidpppCl<sub>2</sub>, LiCl): monomer solution B (0.45 mL, 0.0814 mmol) was added to Ni(dppp)Cl<sub>2</sub> stock solution (2.0 mL, 1.0 μmol, 0.012 equiv) while stirring. The reaction mixture turned dark orange upon addition and was allowed to stir for 2 h.

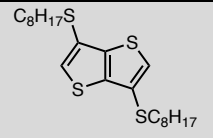
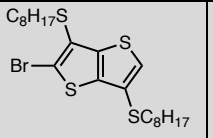
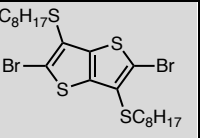
Polymerization 3 (NidppeCl<sub>2</sub>, no LiCl): monomer solution A (0.45 mL, 0.0814 mmol) was added to Ni(dppe)Cl<sub>2</sub> stock solution (2.0 mL, 1.1 μmol, 0.013 equiv) while stirring. The reaction mixture turned orange upon addition and was allowed to stir for 2 h.

Polymerization 4 (NidppeCl<sub>2</sub>, LiCl): monomer solution B (0.45 mL, 0.0814 mmol) was added to Ni(dppe)Cl<sub>2</sub> stock solution (2.0 mL, 1.1 μmol, 0.013 equiv) while stirring. The reaction mixture turned dark orange upon addition and was allowed to stir for 2 h.

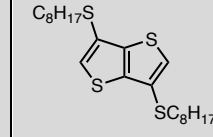
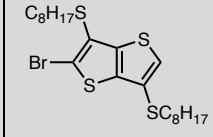
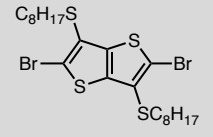
After 2h, all polymerizations were brought out of the glovebox and quenched with H<sub>2</sub>O (1 mL), shaken for 30s, then extracted with CHCl<sub>3</sub> (1 mL) and analyzed via GC and GPC.

Gas Chromatography Data:

**Table A2.2** Monomer activation data from GC analysis of the quenched monomer solution

Monomer activation	 retention time = 20.82 min	 retention time = 26.05 min	 retention time = 32.76 min
	% composition	% composition	% composition
Solution A (no LiCl)	n.d.	87.7 %	12.3 %
Solution B (w/ LiCl)	n.d.	91.0 %	9.0 %

**Table A2.3** Monomer consumption from GC analysis of the quenched polymerizations

polymerization	 retention time = 20.82 min	 retention time = 26.05 min	 retention time = 32.76 min

	% composition	% consumed	% composition	% consumed	% composition	% consumed
1 Nidppp	2.5 %	-100 %	82.9 %	18.3 %	14.6 %	-3.0 %
2 Nidppp, LiCl	3.2 %	-100 %	91.0 %	25.6 %	9.0 %	-9.1 %
3 Nidppe	2.2 %	-100 %	83.6 %	13.9 %	14.2 %	-4.7 %
4 Nidppe, LiCl	3.4 %	-100 %	77.9 %	34.2 %	18.7 %	-12.7 %
Note: a negative value in the % consumed column denotes species that were generated during the reaction						

Gel Permeation Chromatography Data:

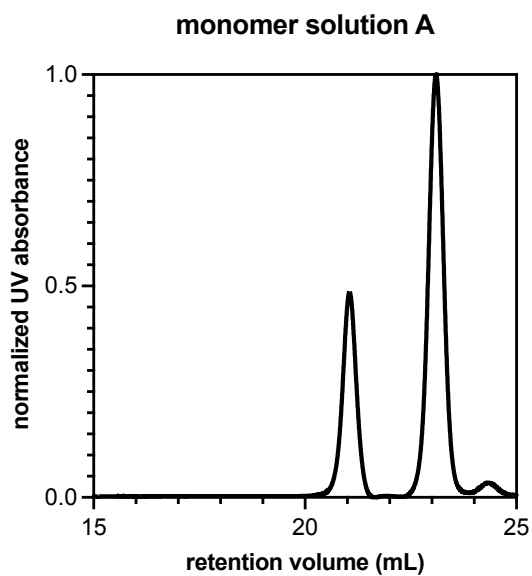


**Figure A2.10** GPC of the monomer solution A,  $M_n = 1099$ ,  $M_w = 1138$ ,  $\bar{D} = 1.03$

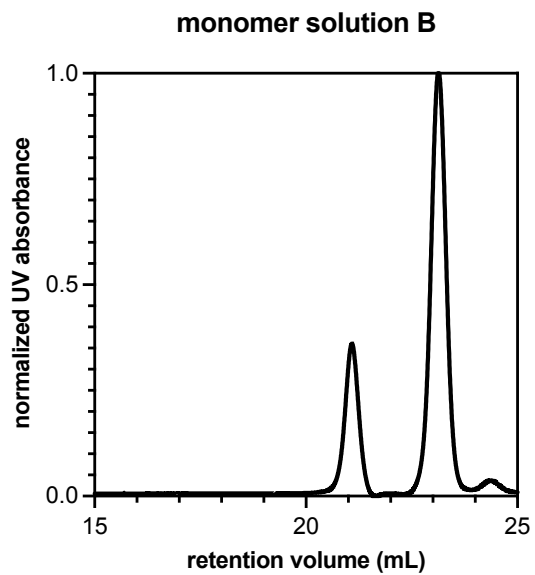


**Figure A2.11** GPC of the monomer solution B,  $M_n = 1069$ ,  $M_w = 1112$ ,  $D = 1.04$

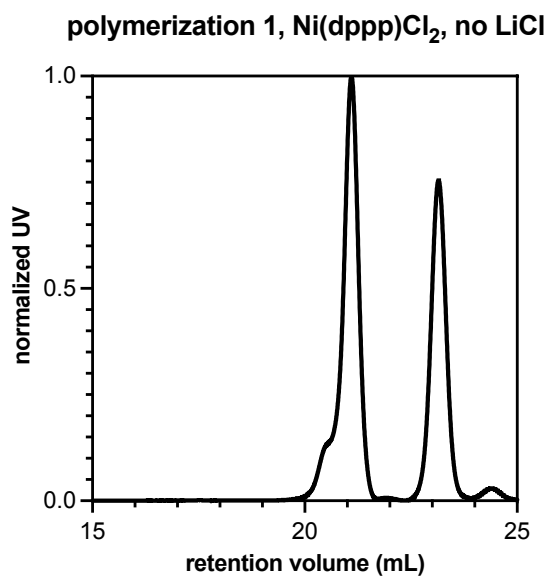


**Figure A2.12** GPC of the polymerization 1,  $M_n = 1107$ ,  $M_w = 1208$ ,  $D = 1.09$

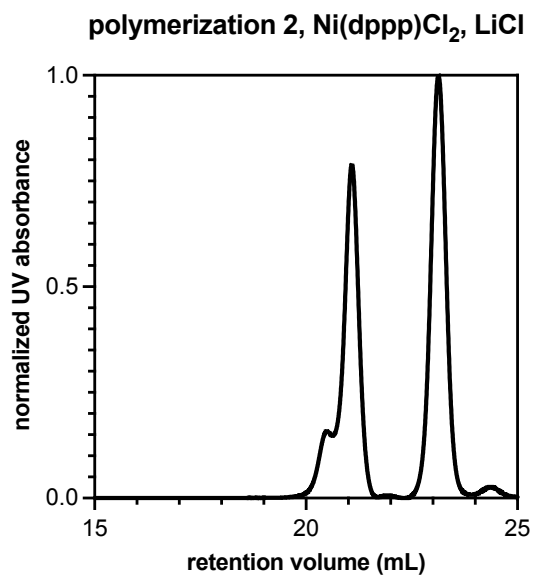


Figure A2.13 GPC of the polymerization 2,  $M_n = 1157$ ,  $M_w = 1281$ ,  $\bar{D} = 1.11$

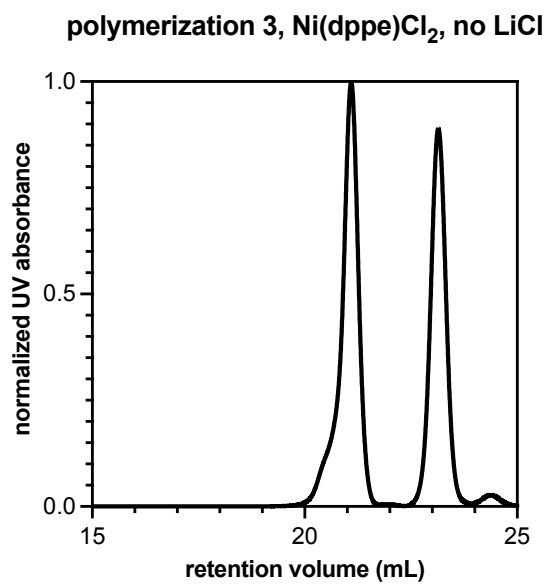
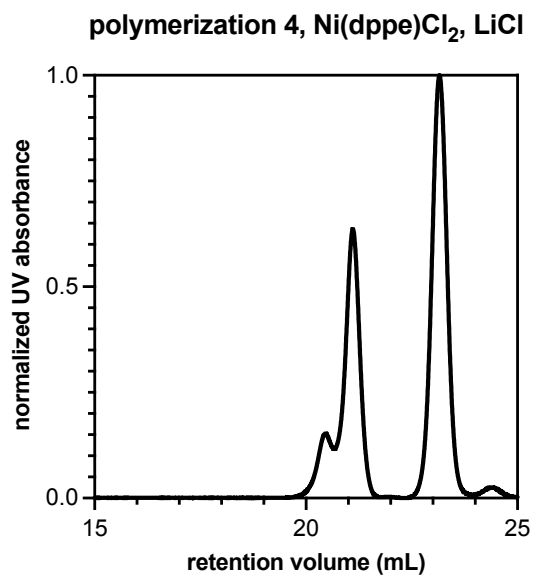


Figure A2.14 GPC of the polymerization 3,  $M_n = 1108$ ,  $M_w = 1204$ ,  $\bar{D} = 1.09$

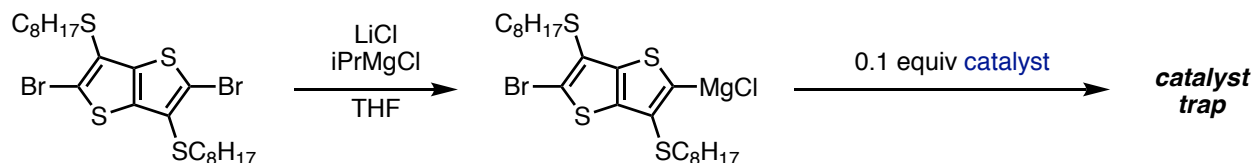




**Figure A2.15** GPC of the polymerization 4,  $M_n = 1154$ ,  $M_w = 1304$ ,  $\bar{D} = 1.13$

Lastly, ESI mass spectra were taken from the quenched polymerization solution for the polymerization 1 (Ni(dppp)Cl<sub>2</sub>, no LiCl) and are shown above in Appendix section A2.4.

**A2.6.2 Polymerization of 2-magnesioclboro-5-dibromo-3,6-dithiooctylthieno[3,2-*b*]thiophene, M1 with Ni(dppp) and Ni(dppe) for NMR studies**



**Monomer stock solution preparation:**

**Monomer solution A (no LiCl):** To a 20 mL vial in a nitrogen glovebox, 2,5-dibromo-3,6-dithiooctylthieno[3,2-*b*]thiophene (104.3 mg, .178 mmol, 1.0 equiv.) was added along with C<sub>22</sub>H<sub>46</sub> (GC standard, 10 mg), THF (1.7 mL) and *i*PrMgCl (2.0 M in THF, 77  $\mu$ L, 0.90 equiv.) and was left to stir for 30 minutes.

**Monomer solution B (w/ LiCl):** 0.85 mL of monomer solution A was removed, and added to a 20 mL vial containing LiCl (3.3 mg, 0.089 mmol, 1.0 equiv.) while the other portion of monomer solution A was left untouched.

Both monomer solutions were left to stir for 30 more minutes. Afterwards, 0.2 mL of each solution was removed and quenched with water and analyzed by GC analysis. The remaining solutions were then immediately used in polymerizations.

**Catalyst stock solution preparation:**

**Ni(dppp)Cl<sub>2</sub> stock solution:** Ni(dppp)Cl<sub>2</sub> (2.7 mg, 5.0  $\mu$ mol) was added to a 20 mL vial in a nitrogen glovebox, along with a stir bar and tetrahydrofuran (2.1 mL). The solution was allowed to stir for 30 minutes.

**Ni(dppe)Cl<sub>2</sub> stock solution:** Ni(dppe)Cl<sub>2</sub> (2.4 mg, 4.5  $\mu$ mol) was added to a 20 mL vial in a nitrogen glovebox, along with a stir bar and tetrahydrofuran (1.8 mL). The solution was allowed to stir for 30 minutes.

**Polymerizations:**

**Polymerization 1 (Ni(dppp)Cl<sub>2</sub>, no LiCl):** monomer solution A (0.2 mL, 0.022 mmol) was added to Ni(dppp)Cl<sub>2</sub> stock solution (0.9 mL, 2.1  $\mu$ mol, 0.09 equiv.) while stirring. The reaction mixture turned orange upon addition and was allowed to stir for 2 h.

**Polymerization 2 (Ni(dppp)Cl<sub>2</sub>, LiCl):** monomer solution B (0.2 mL, 0.022 mmol) was added to Ni(dppp)Cl<sub>2</sub> stock solution (0.9 mL, 2.1  $\mu$ mol, 0.09 equiv) while stirring. The reaction mixture turned dark orange upon addition and was allowed to stir for 2 h.

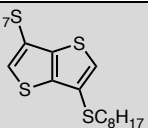
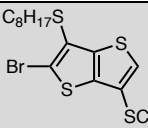
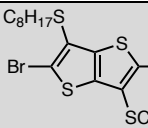
Polymerization 3 (NidppeCl<sub>2</sub>, no LiCl): monomer solution A (0.2 mL, 0.022 mmol) was added to Ni(dppe)Cl<sub>2</sub> stock solution (0.9 mL, 2.2 μmol, 0.10 equiv) while stirring. The reaction mixture turned orange upon addition and was allowed to stir for 2 h.

Polymerization 4 (NidppeCl<sub>2</sub>, LiCl): monomer solution B (0.2 mL, 0.022 mmol) was added to Ni(dppe)Cl<sub>2</sub> stock solution (0.9 mL, 2.2 μmol, 0.10 equiv) while stirring. The reaction mixture turned dark orange upon addition and was allowed to stir for 2 h.

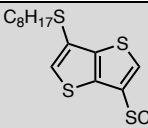
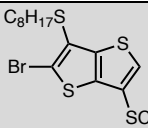
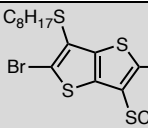
At 30 minutes, J. young tubes were loaded with the polymerization solutions. After 2h, all polymerizations were brought out of the glovebox and quenched with H<sub>2</sub>O (1 mL), shaken for 30s, then extracted with CHCl<sub>3</sub> (1 mL) and analyzed via GC and GPC.

Gas Chromatography Data:

**Table A2.4** Monomer activation data from GC analysis of the quenched monomer solution

Monomer activation	 retention time = 20.82 min	 retention time = 26.05 min	 retention time = 32.76 min
	% composition	% composition	% composition
Solution A (no LiCl)	n.d.	85.3 %	14.6 %

**Table A2.5** Monomer consumption from GC analysis of the quenched polymerizations

polymerization	 retention time = 20.82 min	 retention time = 26.05 min	 retention time = 32.76 min			
	% composition	% consumed	% composition	% consumed	% composition	% consumed
1 Nidppp	21.6 %	-100 %	78.4 %	41.0 %	n.d.	100%

2 Nidppp, LiCl	34.3 %	-100 %	65.7 %	66.8 %	n.d.	100%
3 Nidppe	26.0 %	-100 %	74.0 %	41.2 %	n.d.	100%
4 Nidppe, LiCl	33.5 %	-100%	66.5%	65.5%	n.d.	100 %
Note: a negative value in the % consumed column denotes species that were generated during the reaction						

NMR Data: All spectra were taken on a 600 MHz NMR spectrometer in THF at rt.  $^{31}\text{P}$  NMR resonance frequency was 243 MHz.

Polymerization 1: Ni(dppp)Cl<sub>2</sub> catalyzed polymerization, no LiCl: at short reaction times, the  $^{31}\text{P}$  NMR (Figure A2.16) reveals a set of peaks that match the peaks observed for **I<sub>C8</sub>** in Figure A2.9. At longer reaction times (18 h) a set of doublets grow in that match the chemical shift and  $J_{\text{PP}}$  observed by Koeckelberghs.<sup>6</sup>

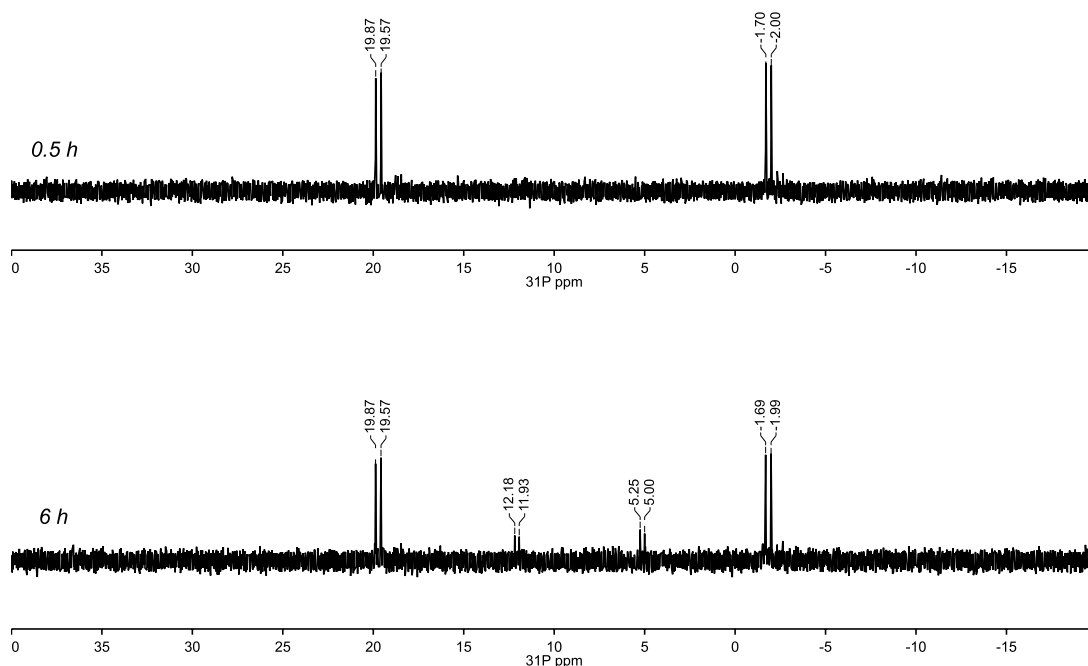


**Figure A2.16**  $^{31}\text{P}$  NMR spectra of polymerization 1 with  $\text{Ni}(\text{dppp})\text{Cl}_2$  at 0.5 h (top) with two peaks at 19.72 (d,  $J = 72.9$  Hz), -1.85 (d,  $J = 73.0$  Hz) and 6 h (bottom), with peaks at  $\delta$  19.72 (d,  $J = 73.0$  Hz), 12.06 (d,  $J = 60.1$  Hz), 5.12 (d,  $J = 60.3$  Hz), -1.84 (d,  $J = 72.9$  Hz).

Polymerization 2:  $\text{Ni}(\text{dppp})\text{Cl}_2$  catalyzed polymerization, with  $\text{LiCl}$ : the  $^{31}\text{P}$  NMR (Figure A2.17) reveals a set of peaks that match the peaks observed by Koeckelberghs, indicating that the catalyst trap was formed.<sup>7</sup>

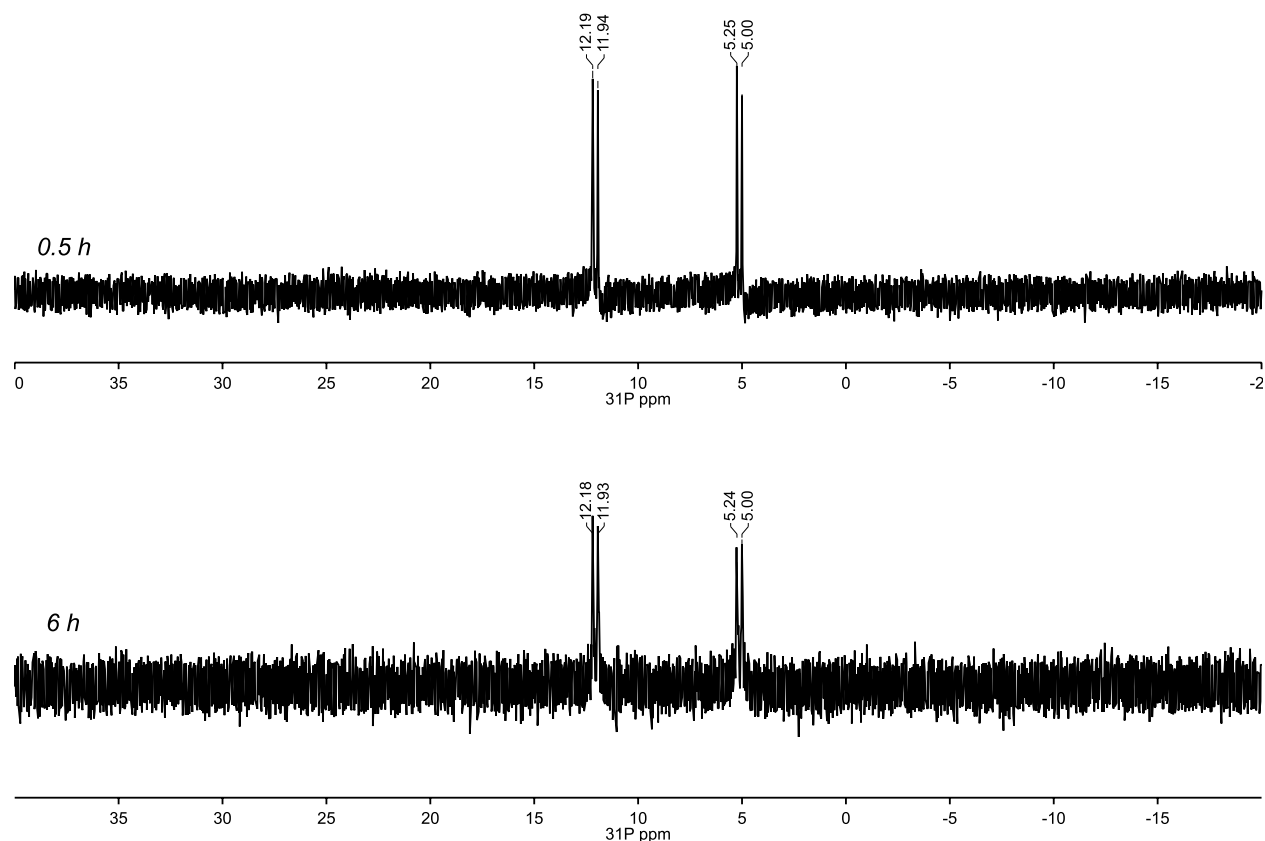


**Figure A2.17**  $^{31}\text{P}$  NMR spectra of polymerization 2, with  $\text{Ni}(\text{dppp})\text{Cl}_2$  and  $\text{LiCl}$ , at 0.5 h (top) and 6 h (bottom) showing peaks at 12.06 (d,  $J = 60.4$  Hz), 5.12 (d,  $J = 60.4$  Hz).

Polymerization 3:  $\text{Ni}(\text{dppe})\text{Cl}_2$  catalyzed polymerization, without  $\text{LiCl}$ : the  $^{31}\text{P}$  NMR (Figure A2.18) reveals two doublets with  $J_{\text{PP}} = 41.2$  Hz. By analogy to Polymerization 1, this species is assigned to:

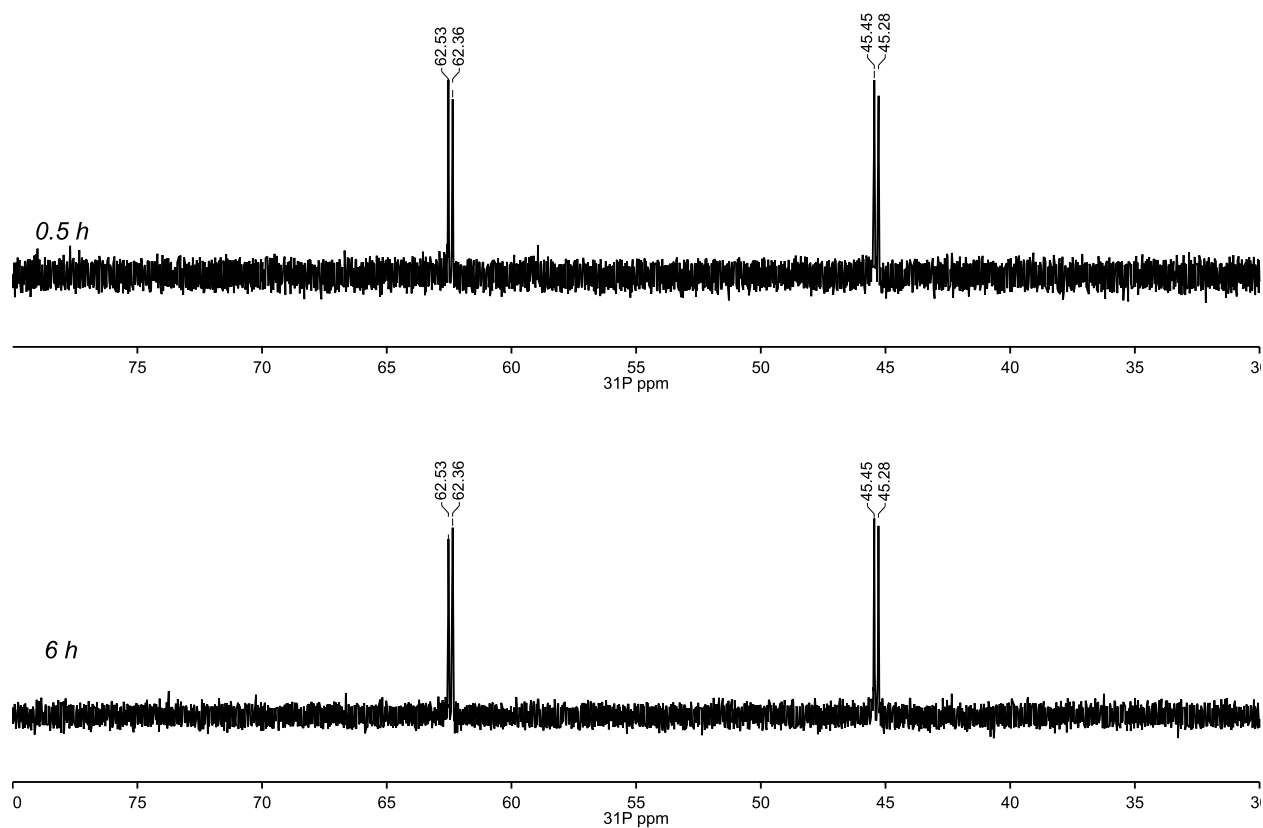
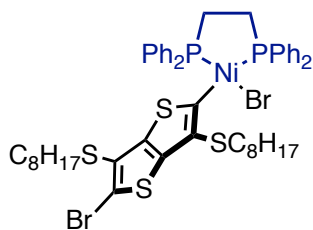
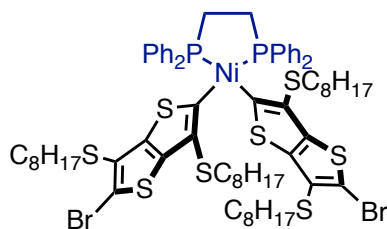


**Figure A2.18**  $^{31}\text{P}$  NMR spectra of polymerization 3, with  $\text{Ni}(\text{dppe})\text{Cl}_2$  at 0.5 h (top) and 6 h (bottom) showing the same peaks at  $\delta$  62.44 (d,  $J = 41.7$  Hz), 45.36 (d,  $J = 41.2$  Hz).

Polymerization 4:  $\text{Ni}(\text{dppe})\text{Cl}_2$  catalyzed polymerization, with  $\text{LiCl}$ : at short reaction times, the  $^{31}\text{P}$  NMR (Figure A2.19) reveals two sets of set of peaks at  $\delta$  51.44 (d,  $J = 30.9$  Hz), 49.28 (d,  $J = 10.9$  Hz), 46.42 (d,  $J = 10.9$  Hz), 44.02 (d,  $J = 31.3$  Hz). At longer reaction times, only the peaks with  $J_{\text{PP}} = 31$  remain. Given the low  $J_{\text{PP}}$ , the peaks at 46.42 and 44.02 are assigned to a  $\text{Ni}^{\text{II}}$  species,

and the small difference in the chemical shift indicates that it may be the species that precedes reductive elimination :



The other set of peaks at 51 and 44ppm are assigned to a Ni<sup>II</sup> complex based on  $J_{PP}$  - and given the persistence, we assign these peaks to the catalyst trap for the Ni(dppe) polymerization, potentially having a structure:

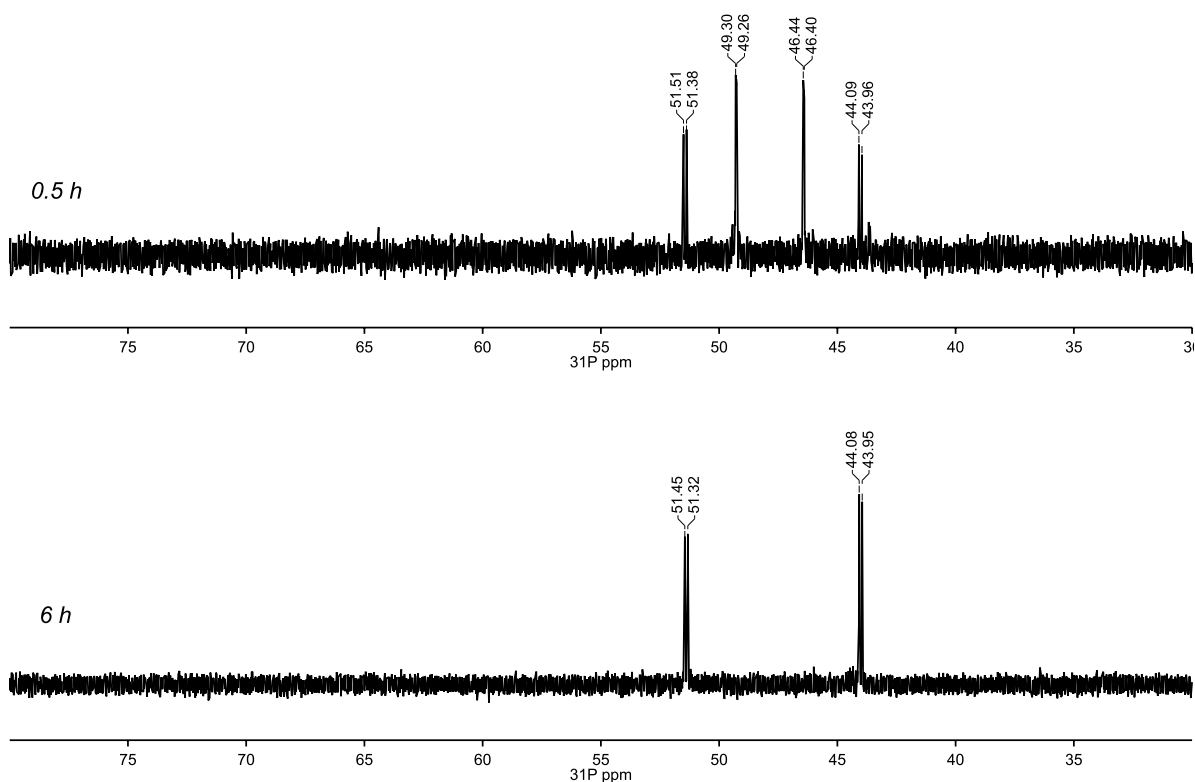
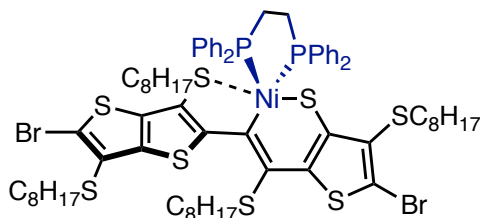
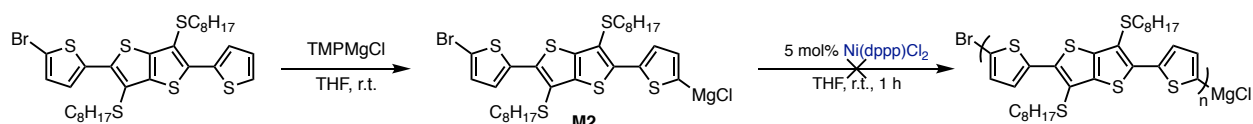


**Figure A2.19**  $^{31}\text{P}$  NMR spectra of polymerization 4, at 0.5 h (top) with peaks at  $\delta$  51.44 (d,  $J = 30.9$  Hz), 49.28 (d,  $J = 10.9$  Hz), 46.42 (d,  $J = 10.9$  Hz), 44.02 (d,  $J = 31.3$  Hz). And at 6 h (bottom) with  $\delta$  51.44 (d,  $J = 30.9$  Hz) and 44.02 (d,  $J = 31.3$  Hz).

### A2.6.3 Polymerization of 2-(5'-bromothien-2'-yl)-5-(5''-chloromagnesiethien-2''-yl)-3,6-dithiooctylthieno[3,2-*b*]thiophene, M2.



#### Monomer stock solution preparation:

To a 20 mL vial in the glovebox, 2-(5'-bromothien-2-yl)-5-thien-2-yl-3,6-dioctylthiothieno[3,2-*b*]thiophene (50.1 mg, 0.075 mmol, 1.0 equiv) was added along with a stir bar, THF (0.74 mL) and N-magnesiochloro-2,2,6,6-tetramethylpiperidine (98  $\mu\text{L}$ , 0.61 M, 0.060 mmol, 0.80 equiv). The reaction was allowed to stir for 1 h.

#### Catalyst stock solution preparation:

Ni(dppp)Cl<sub>2</sub> stock solution: Ni(dppp)Cl<sub>2</sub> (4.4 mg, 8.2  $\mu\text{mol}$ ) was added to a 20 mL vial in a nitrogen glovebox, along with a stir bar and tetrahydrofuran (1 mL). The solution was allowed to stir for 30 minutes.

Polymerizations: The monomer solution (0.13 mL, 0.013 mmol) was added to THF (1.5 mL), and then Ni(dppp)Cl<sub>2</sub> stock solution (78  $\mu\text{L}$ , 0.0006  $\mu\text{mol}$ , 0.05 equiv.) while stirring. The reaction mixture turned orange upon addition and was allowed to stir for 2 h.

GPC analysis: GPC does not reveal polymer:  $M_n = 507$  g/mol



## A2.7 Small Molecule NMR Spectra

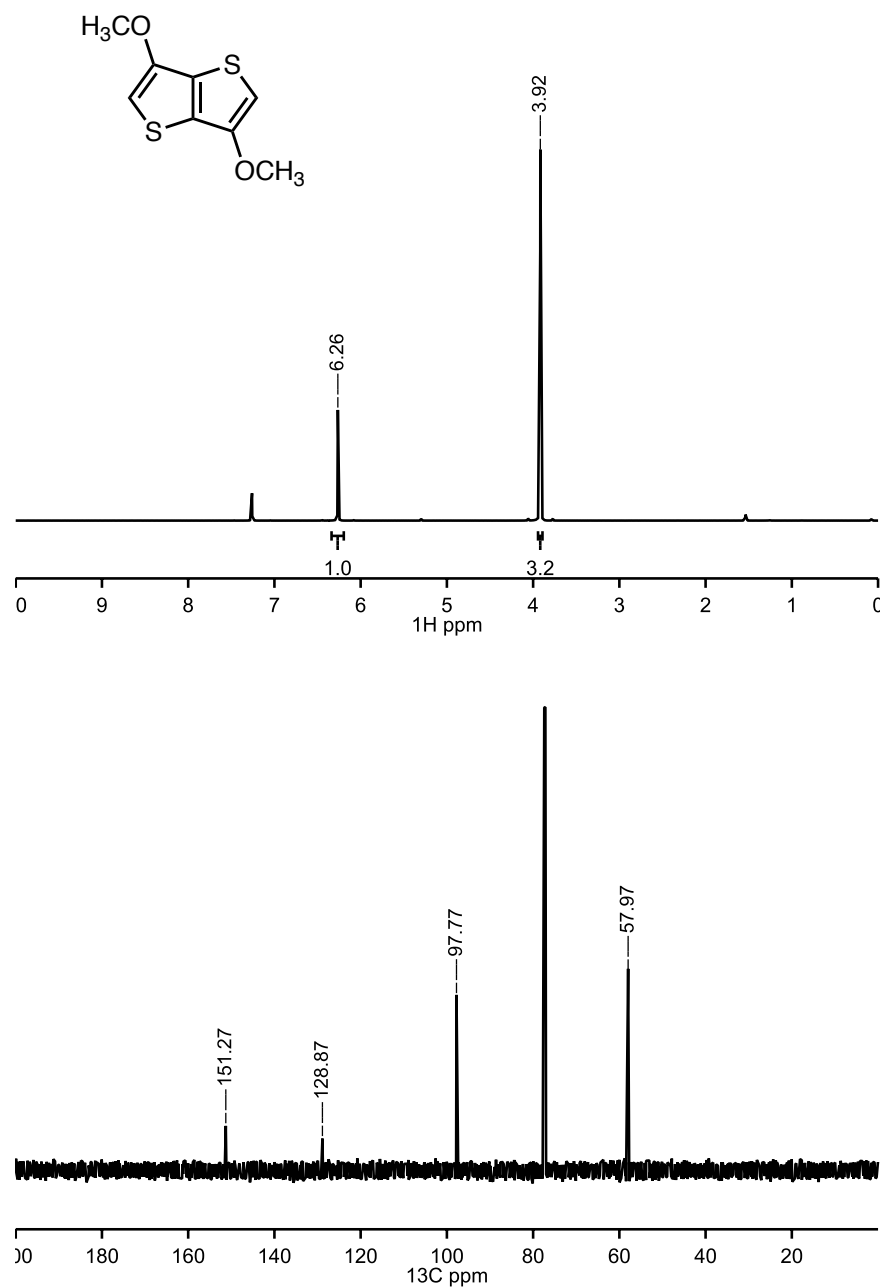


**Figure A2.20**  $^1\text{H}$  and  $^{13}\text{C}$  NMR spectra of 3,6-dimethoxythieno[3,2-*b*]thiophene.  $^1\text{H}$  NMR (500 MHz,  $\text{CDCl}_3$ )  $\delta$  6.26 (s, 1H), 3.92 (s, 3H).  $^{13}\text{C}$  NMR (126 MHz,  $\text{CDCl}_3$ )  $\delta$  151.02, 128.61, 97.52, 57.71.

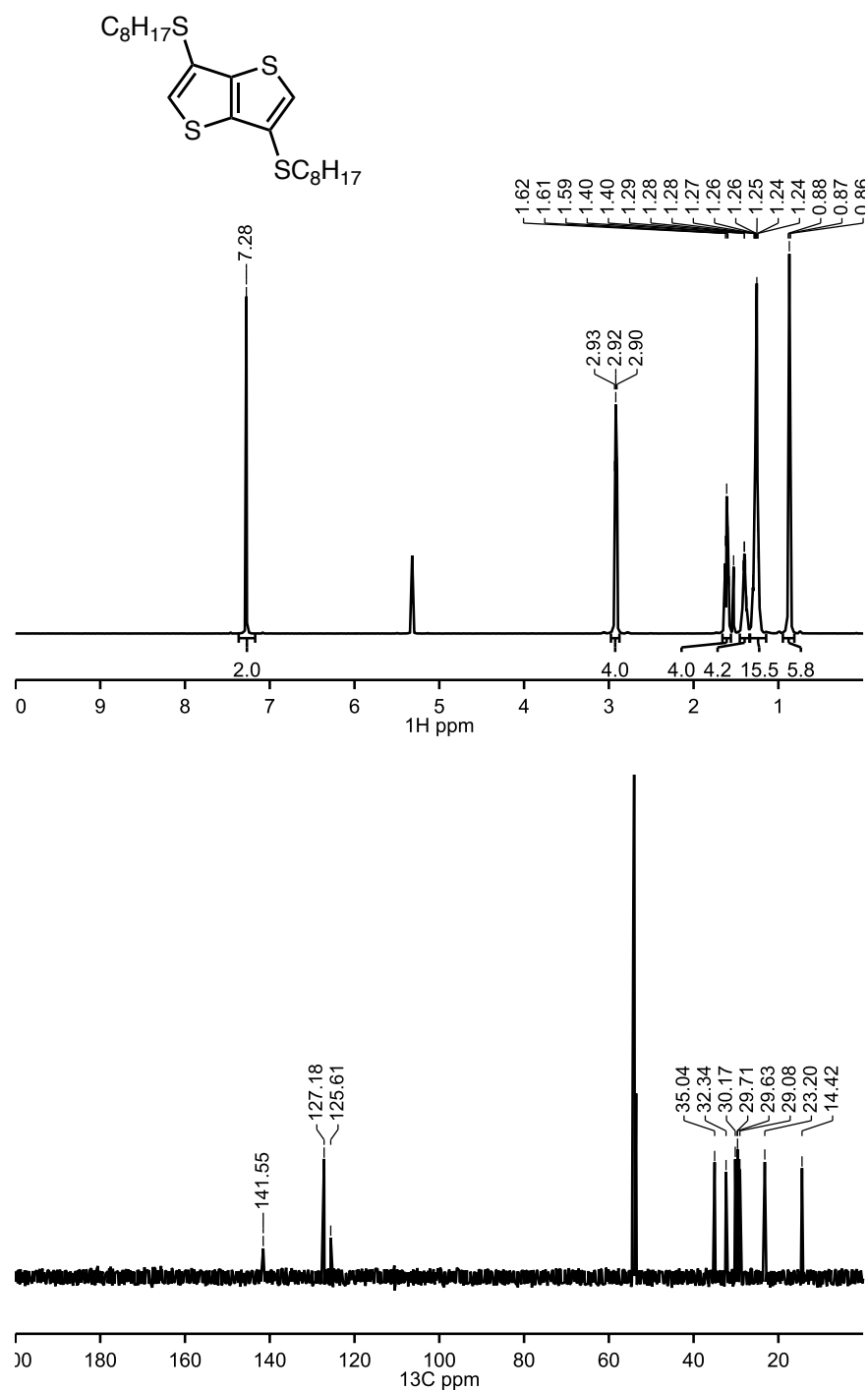


**Figure A2.21**  $^1\text{H}$  and  $^{13}\text{C}$  NMR spectra of 3,6-dioctylthiothieno[3,2-*b*]thiophene.  $^1\text{H}$  NMR (700 MHz,  $\text{CD}_2\text{Cl}_2$ )  $\delta$  7.28 (s, 2H), 2.90 (t,  $J = 7.2$  Hz, 4H), 1.65 – 1.57 (m, 4H), 1.40 (m, 4H), 1.31 – 1.20 (m, 16H), 0.87 (t,  $J = 7.1$  Hz, 6H).  $\delta$   $^{13}\text{C}$  NMR (176 MHz,  $\text{CD}_2\text{Cl}_2$ )  $\delta$  141.31, 127.11, 125.11, 34.76, 31.93, 29.80, 29.31, 29.24, 28.71, 22.79, 14.24.

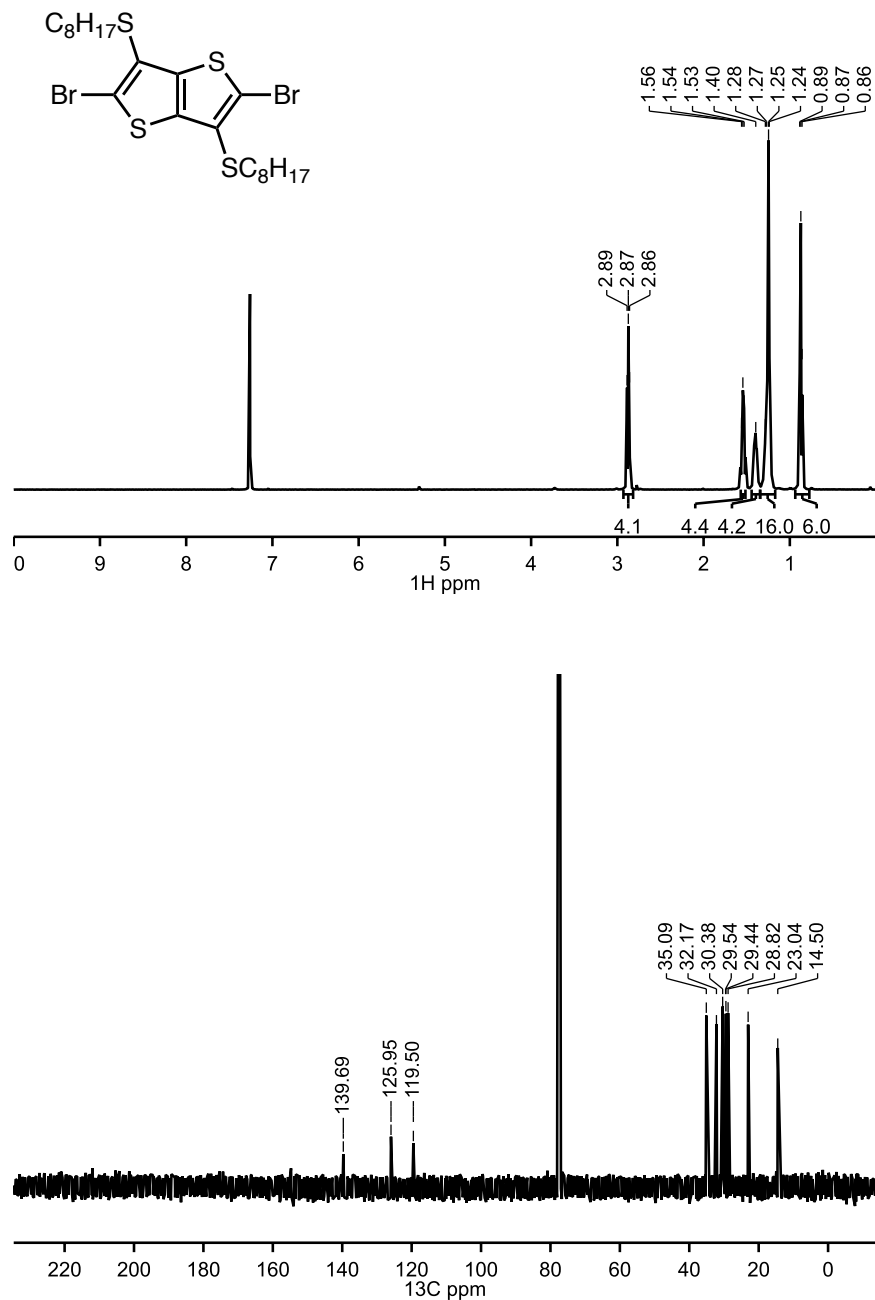


**Figure A2.22**  $^1\text{H}$  and  $^{13}\text{C}$  NMR spectra of 2,5-dibromo-3,6-dioctylthiothieno[3,2-*b*]thiophene.  $^1\text{H}$  NMR (500 MHz,  $\text{CDCl}_3$ )  $\delta$  2.87 (t,  $J = 7.3$  Hz, 4H), 1.54 (q,  $J = 7.6$  Hz, 4H), 1.44 – 1.36 (m, 4H), 1.32 – 1.17 (m, 16H), 0.87 (t,  $J = 6.9$  Hz, 6H).  $^{13}\text{C}$  NMR (126 MHz,  $\text{CDCl}_3$ )  $\delta$  139.69, 125.95, 119.50, 35.09, 32.17, 30.38, 29.54, 29.44, 28.82, 23.04, 14.50.

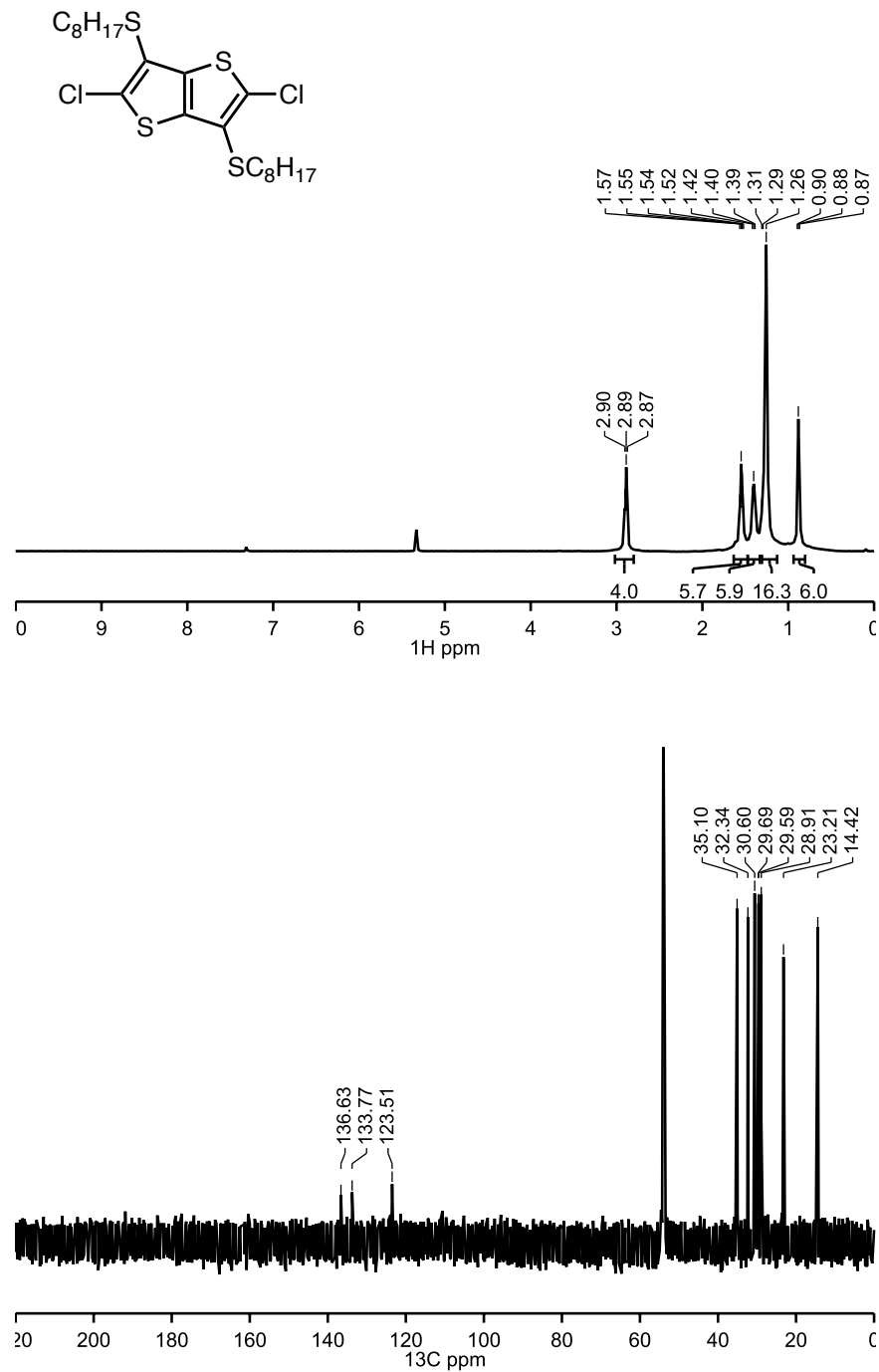


**Figure A2.23** <sup>1</sup>H and <sup>13</sup>C NMR spectra of 2,5-dichloro-3,6-dioctylthiothieno[3,2-*b*]thiophene. <sup>1</sup>H NMR (500 MHz, CD<sub>2</sub>Cl<sub>2</sub>) δ 2.88 (t, *J* = 7.5 Hz, 4H), 1.54 (t, *J* = 7.5 Hz, 4H), 1.43 – 1.35 (m, 4H), 1.24 (s, 16H), 0.87 (t, *J* = 7.3, 6H). <sup>13</sup>C NMR (126 MHz, CD<sub>2</sub>Cl<sub>2</sub>) δ 136.63, 133.77, 123.51, 35.10, 32.34, 30.60, 29.69, 29.59, 28.91, 23.21, 14.42.

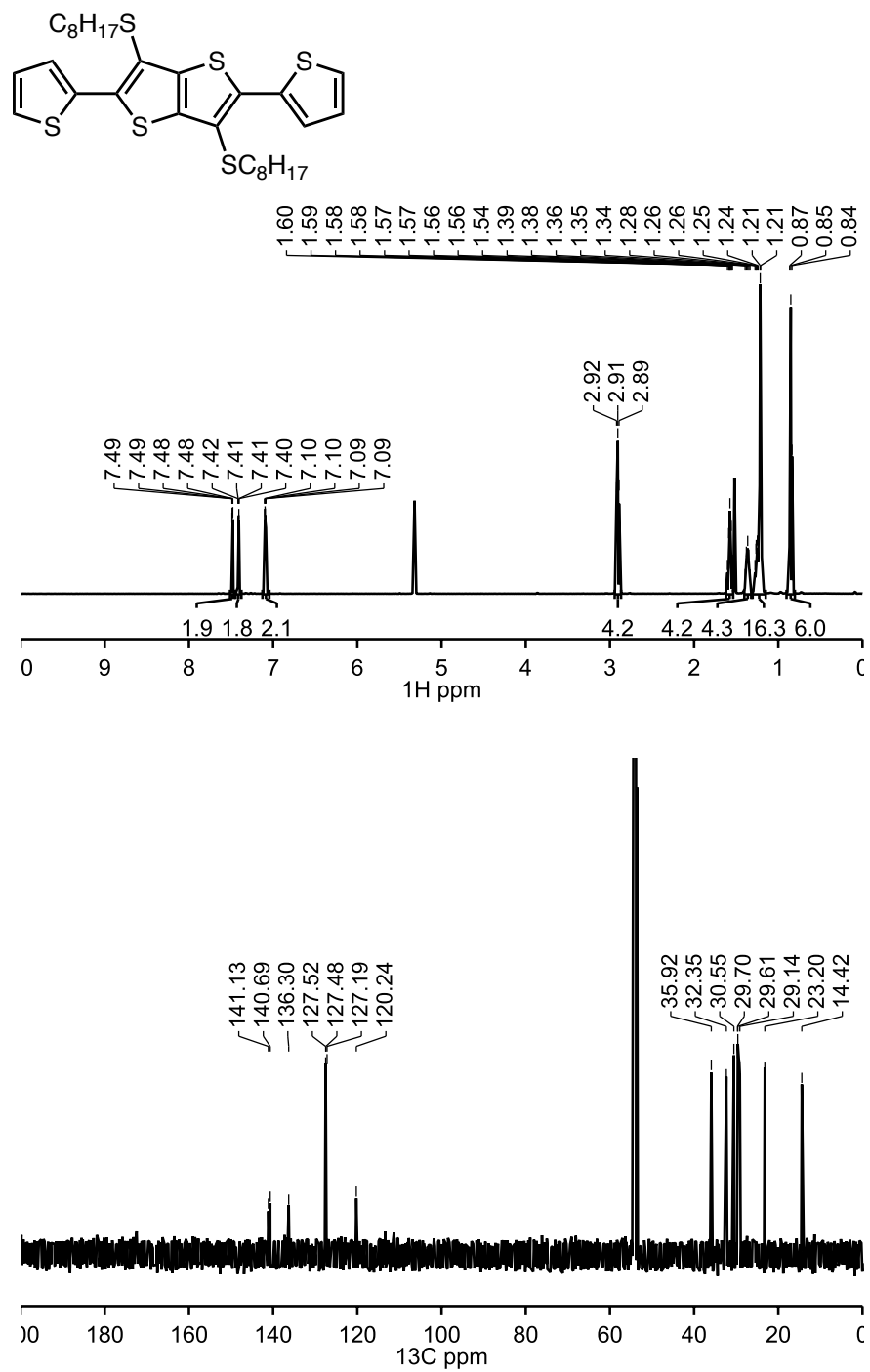


**Figure A2.24** <sup>1</sup>H and <sup>13</sup>C NMR spectra of 2,5-di(2-thienyl)-3,6-dioctylthiothieno[3,2-*b*]thiophene. <sup>1</sup>H NMR (500 MHz, CD<sub>2</sub>Cl<sub>2</sub>) δ 7.48 (dd, *J* = 3.7, 1.2 Hz, 2H), 7.41 (dd, *J* = 5.1, 1.2 Hz, 2H), 7.09 (dd, *J* = 5.1, 3.7 Hz, 2H), 2.91 (t, *J* = 7.3 Hz, 4H), 1.57 (p, *J* = 7.3 Hz, 4H), 1.36 (p, *J* = 7.2 Hz, 4H), 1.31 – 1.18 (m, 16 H), 0.85 (t, *J* = 7.0 Hz, 6H). <sup>13</sup>C NMR (126 MHz, CD<sub>2</sub>Cl<sub>2</sub>) δ 141.13, 140.69, 136.30, 127.52, 127.48, 127.19, 120.24, 35.92, 32.35, 30.55, 29.70, 29.61, 29.14, 23.20, 14.42.

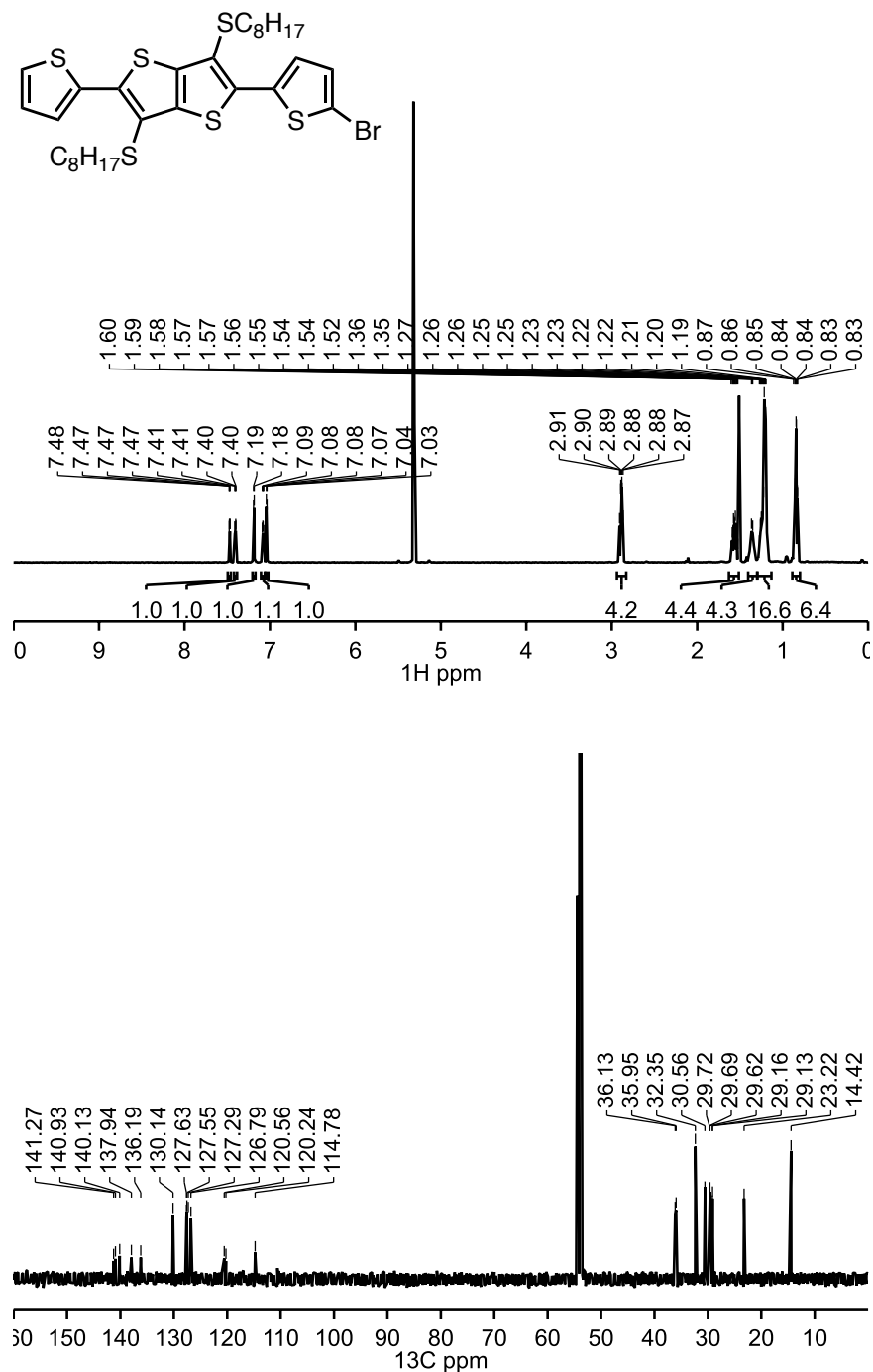


**Figure A2.25** <sup>1</sup>H and <sup>13</sup>C NMR spectra of 2-(5'-bromothien-2'-yl)-5-(2''-thienyl)-3,6-dioctylthiothieno[3,2-*b*]thiophene. <sup>1</sup>H NMR (500 MHz, CD<sub>2</sub>Cl<sub>2</sub>) δ 7.47 (dd, *J* = 3.7, 1.2 Hz, 1H), 7.40 (dd, *J* = 5.1, 1.2 Hz, 1H), 7.19 (d, *J* = 4.0 Hz, 1H), 7.08 (dd, *J* = 5.1, 3.7 Hz, 1H), 7.04 (d, *J* = 4.0 Hz, 1H), 2.95 – 2.83 (m, 4H), 1.56 (dp, *J* = 10.4, 7.4 Hz, 4H), 1.36 (d, *J* = 7.2 Hz, 4H), 1.29 – 1.15 (m, 16H), 0.84 (td, *J* = 7.0, 1.9 Hz, 6H). <sup>13</sup>C NMR (126 MHz, CD<sub>2</sub>Cl<sub>2</sub>) δ 141.27, 140.93, 140.13, 137.94, 136.19, 130.14, 127.63, 127.55, 127.29, 126.79, 120.56, 120.24, 114.78, 36.13, 35.95, 32.35, 30.56, 29.72, 29.69, 29.62, 29.16, 29.13, 23.22, 14.42.

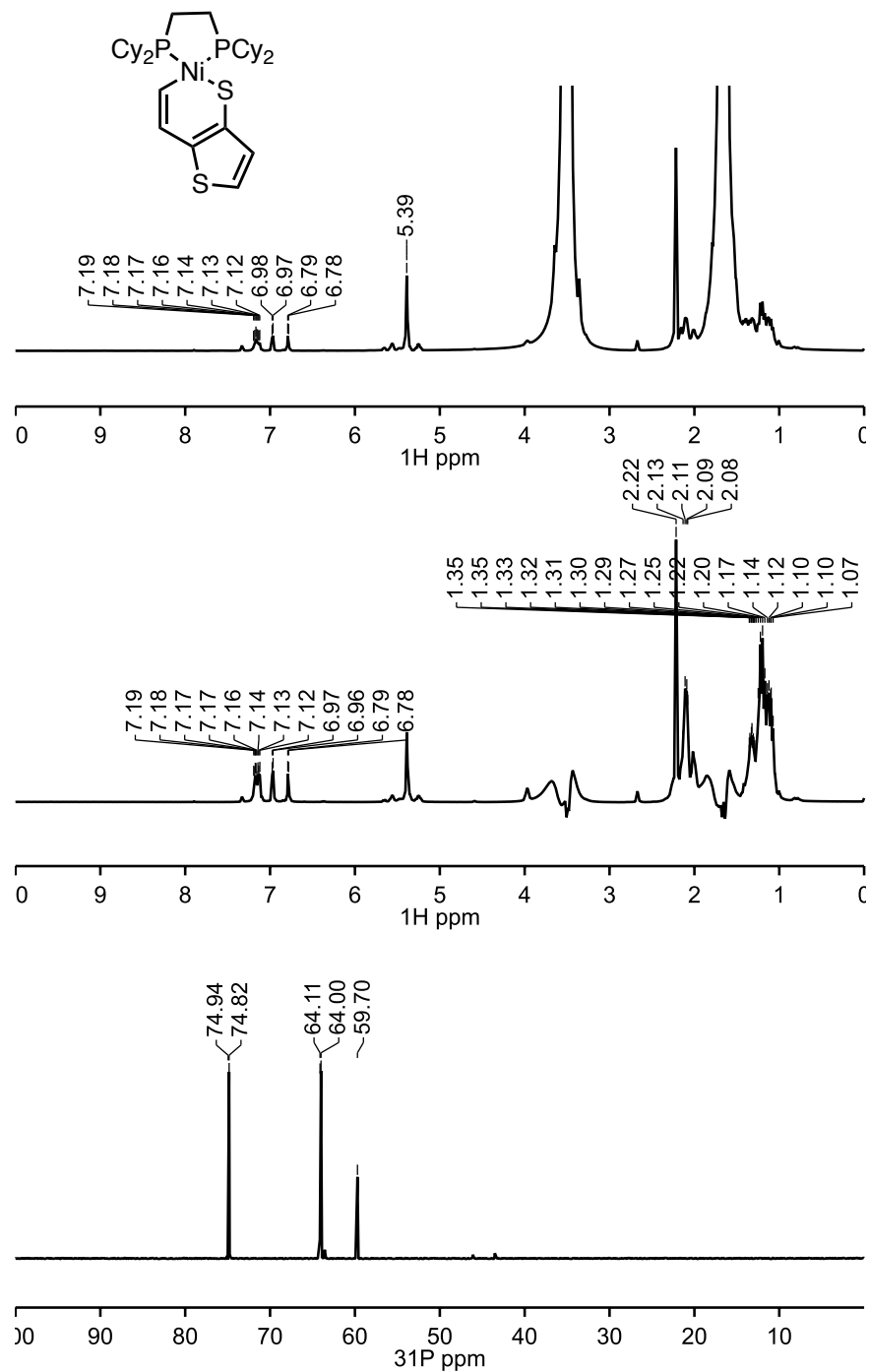


**Figure A2.26**  $^1\text{H}$ , solvent-suppressed  $^1\text{H}$ , and  $^{31}\text{P}$  NMR spectra of nickel(1,2-bis(dicyclohexylphosphino)ethane)[(C,S- $\kappa^2$ )-thieno[3,2-b]thiophene].  $^1\text{H}$  NMR (500 MHz, THF)  $\delta$  7.16 (ddd,  $J = 22.5, 10.2, 6.2$  Hz, 2H), 6.97 (d,  $J = 5.1$  Hz, 1H), 6.79 (d,  $J = 5.0$  Hz, 1H), 2.22 (s, 8H), 1.39 – 0.79 (m, 26H).  $^{31}\text{P}$  NMR (202 MHz, THF)  $\delta$  74.88 (d,  $J = 23.4$  Hz), 64.06 (d,  $J = 23.5$  Hz), 59.70 (impurity, Ni(dcp)(COD)).

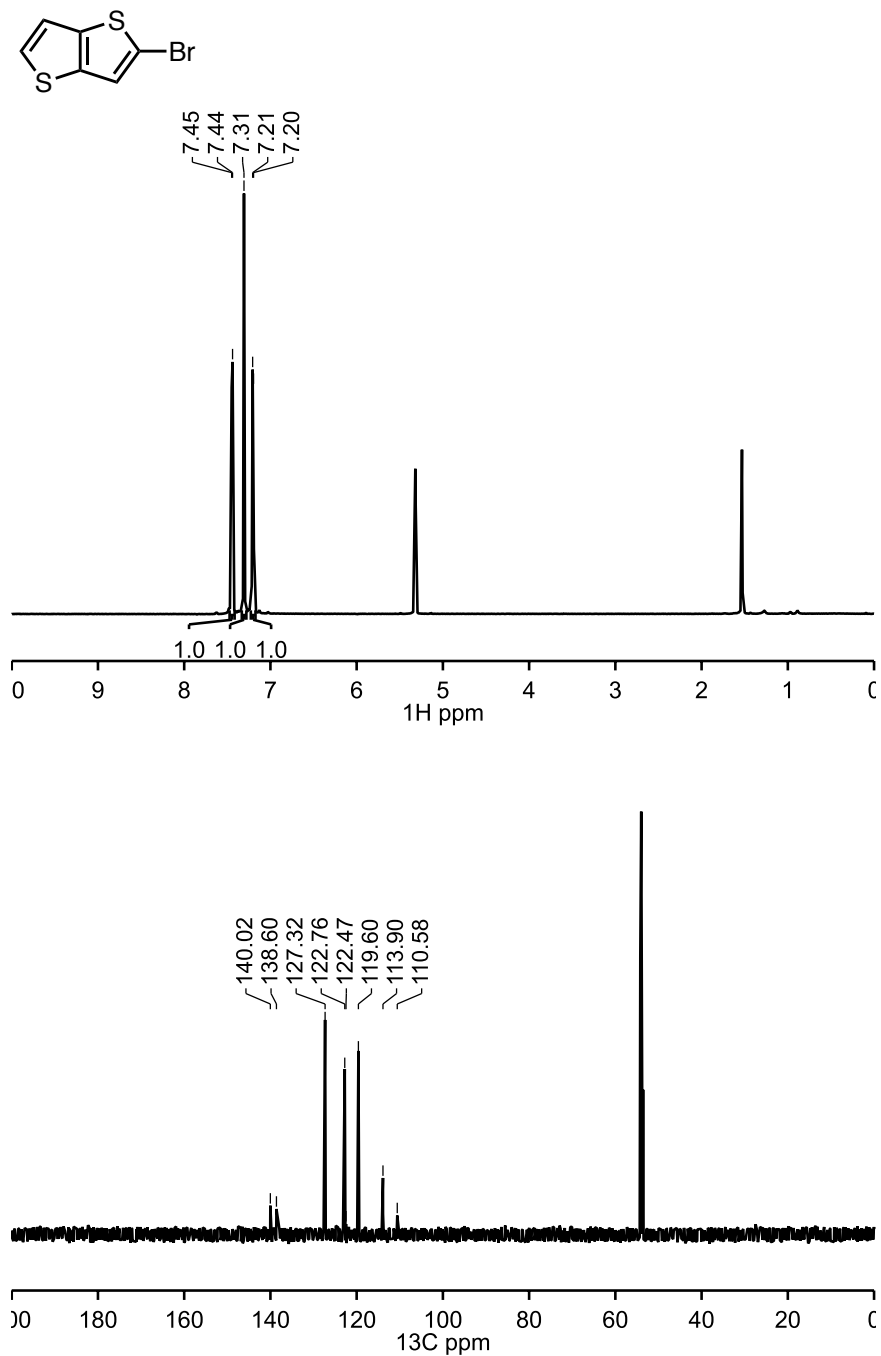


**Figure A2.27** <sup>1</sup>H and <sup>13</sup>C NMR of 2-bromothieno[3,2-*b*]thiophene. <sup>1</sup>H NMR (500 MHz, CD<sub>2</sub>Cl<sub>2</sub>) δ 7.44 (d, *J* = 5.3 Hz, 1H), 7.31 (s, 1H), 7.20 (d, *J* = 5.3 Hz, 1H). <sup>13</sup>C NMR (126 MHz, CD<sub>2</sub>Cl<sub>2</sub>) δ 140.02, 138.60, 127.32, 122.76, 122.47, 119.60, 113.90, 110.58.



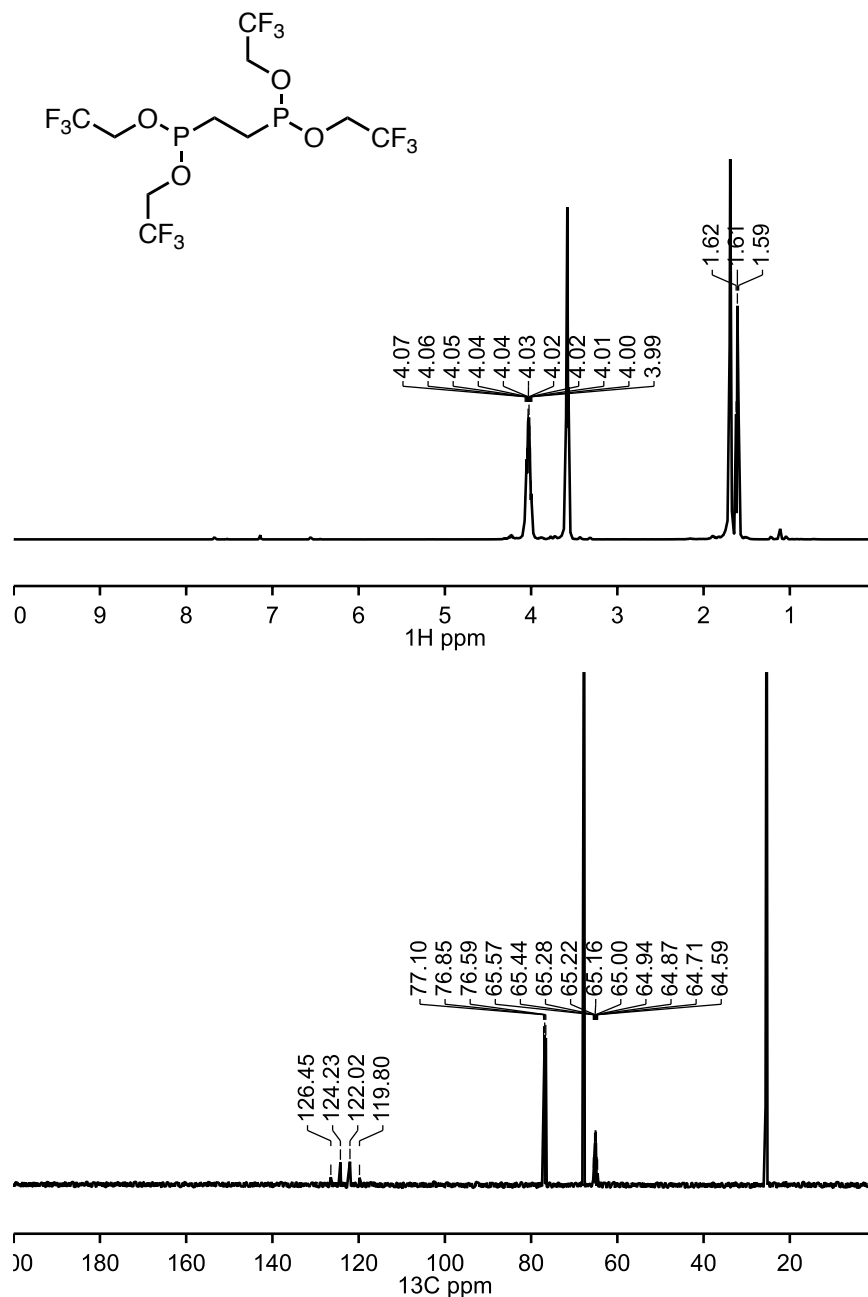


**Figure A2.28**  $^1\text{H}$  and  $^{13}\text{C}$  NMR spectra of tetrakis(2,2,2-trifluoroethyl) ethane-1,2-diylbis(phosphonite).  $^1\text{H}$  NMR (500 MHz, THF)  $\delta$  4.03 (ddq,  $J = 16.2, 7.9, 3.5$  Hz, 8H), 1.61 (t,  $J = 7.2$  Hz, 4H).  $^{13}\text{C}$  NMR (126 MHz, THF)  $\delta$  123.13 (q,  $J = 278.8, 278.3$  Hz), 76.85 (t,  $J = 32.1$  Hz), 66.10 – 63.79 (m).

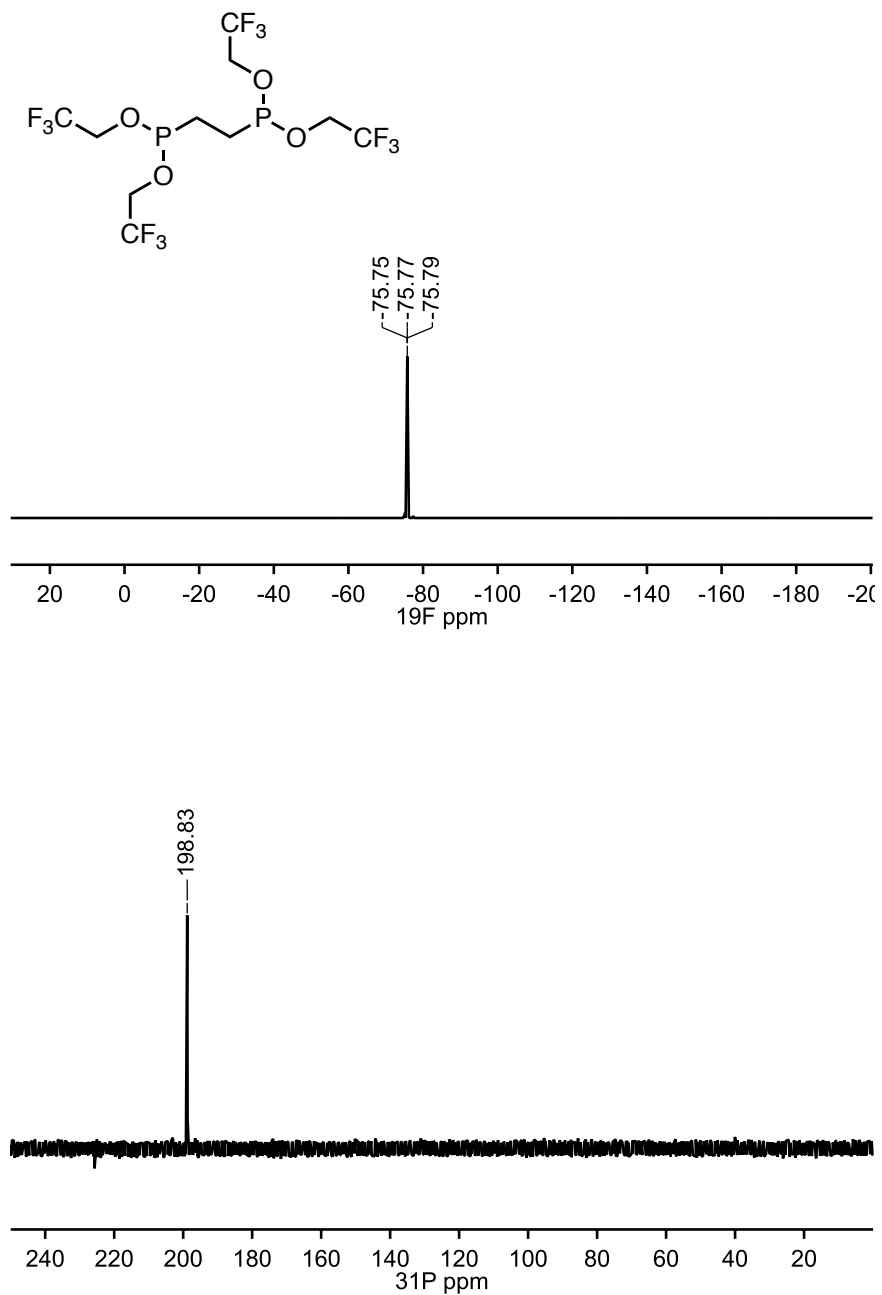


**Figure A2.29**  $^{19}\text{F}$  and  $^{31}\text{P}$  NMR spectra of tetrakis(2,2,2-trifluoroethyl) ethane-1,2-diylbis(phosphonite).  $^{19}\text{F}$  NMR (471 MHz, THF)  $\delta -75.77$  (t,  $J = 8.2$  Hz).  $^{31}\text{P}$  NMR (202 MHz, THF)  $\delta 198.83$  (s).

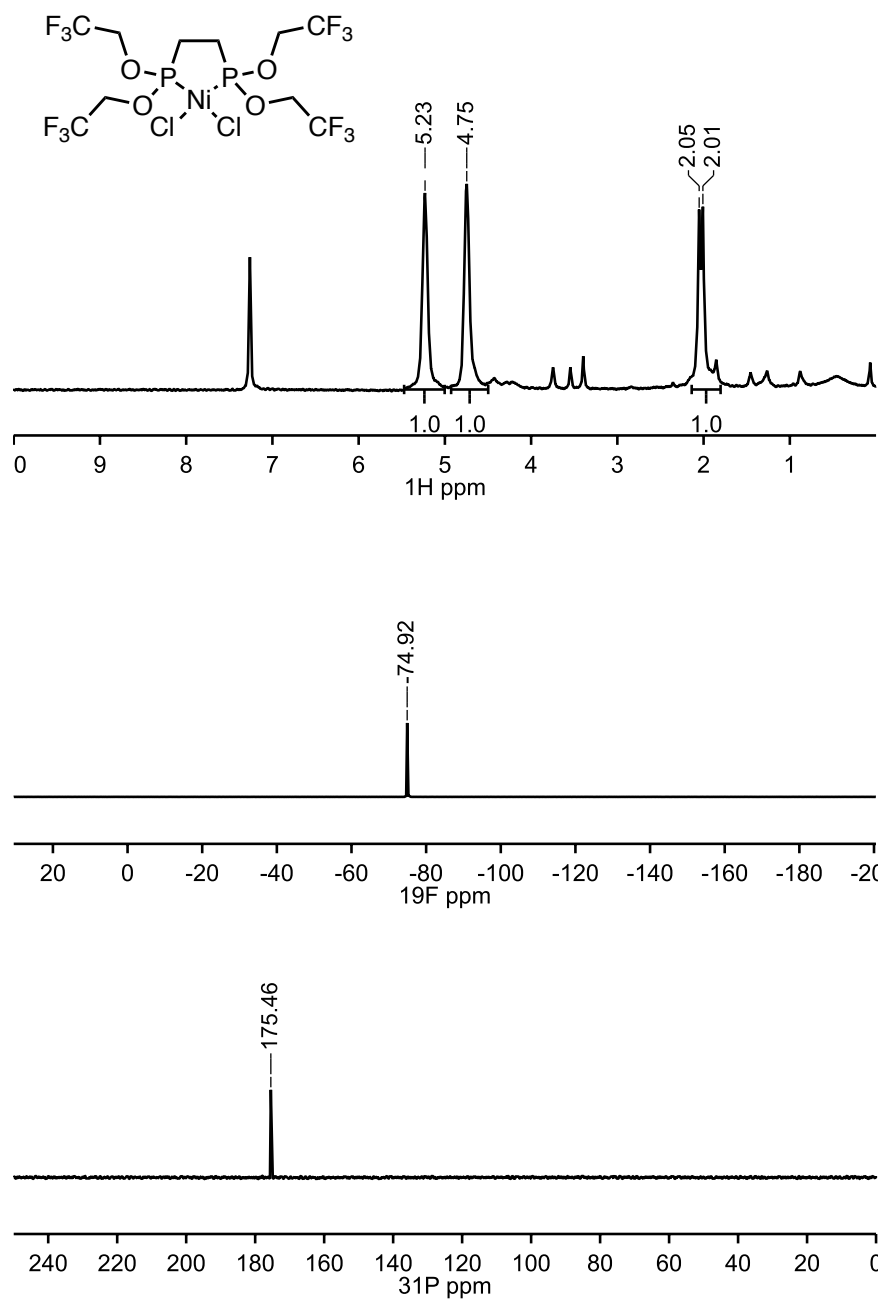


**Figure A2.30** <sup>1</sup>H, <sup>19</sup>F and <sup>31</sup>P NMR spectra of nickel tetrakis(2,2,2-trifluoroethyl)ethane-1,2-diylbis(phosphonite) dichloride. <sup>1</sup>H NMR (500 MHz, Chloroform-*d*) δ 5.23 (s, 4H), 4.75 (s, 4H), 2.03 (d, *J* = 21.6 Hz, 4H). <sup>19</sup>F NMR (471 MHz, Chloroform-*d*) δ -74.91 (d, *J* = 8.3 Hz). <sup>31</sup>P NMR (202 MHz, Chloroform-*d*) δ 175.46.

## A2.8 Computational Details

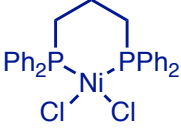
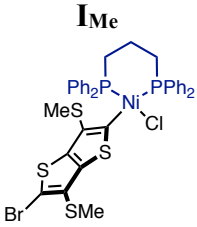
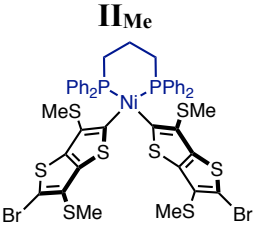
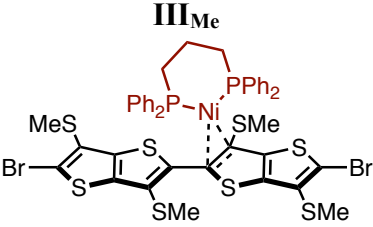
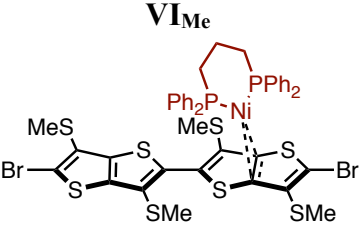
### A2.8.1 Simulations for On-Cycle and Off-Cycle reactions with Ni(dppp)Cl<sub>2</sub>

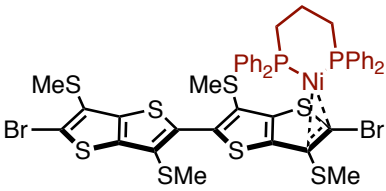
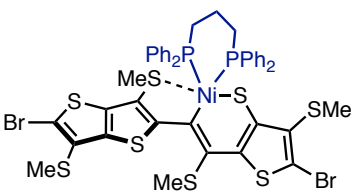
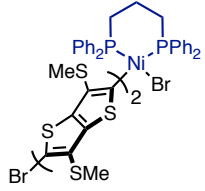
All calculations were performed with Q-Chem 5.1 at the DFT level of theory. Structures were initially constructed in Avogadro and preoptimized in Avogadro using the UFF force field. Coordinates of these structures were then optimized in Q-Chem, using the B3LYP functional and 6-31G\* basis set and singlet spin state. Reaction path searches were performed at the same level of theory using the sing-ended growing-string method described by Zimmerman. Transition state structures and products from the growing-string runs were optimized at the same level of theory. Stationary points were confirmed by the number of negative vibrational modes from frequency calculations at the B3LYP level of theory with the basis set described above: all reactants and products had 0 negative frequencies, all transition states had 1 negative frequency. Final energies were evaluated at the wB97X level of theory, with the def2-TZVP basis set, and SMD solvation in THF. Thermodynamic corrections to the energies were applied at 298 K with the entropy and enthalpy values obtained from frequency calculations. *J*-coupling calculations were performed using the ISSC jobtype in Q-Chem, at the O3LYP level of theory<sup>4</sup> with the aug-cc-pVTZ-J basis set on P atoms<sup>8</sup> and the cc-pVDZ basis set on all other atoms.<sup>9</sup>

### A2.8.2 Signed *J<sub>PP</sub>* values for Ni complexes

The computed  $|J_{PP}|$  values in Figure 3.3 and elsewhere in Chapter 3 are reported as absolute values of the *real*  $J_{PP}$ , because only the magnitude of  $J_{PP}$  is observed in 1-dimensional <sup>31</sup>P NMR spectra. Additionally, they were rounded to the nearest integer. The signed  $J_{PP}$  values that we calculated are reported in Table A2.6.

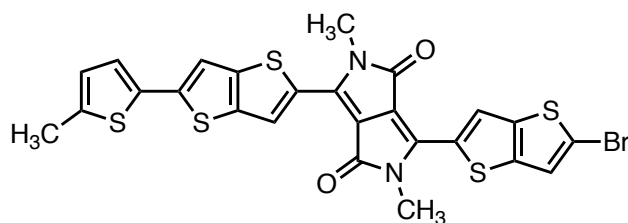
**Table A2.6** Computed  $J_{PP}$  values for complexes in Chapter 3.

Complex	Computed, signed $J_{PP}$	Unsigned $ J_{PP} $
<p><b>Ni(dppp)Cl<sub>2</sub></b></p> 	-118.202 Hz	118.202 Hz
<p><b>I<sub>Me</sub></b></p> 	-85.611 Hz	85.611 Hz
<p><b>II<sub>Me</sub></b></p> 	-64.282 Hz	64.282 Hz
<p><b>III<sub>Me</sub></b></p> 	+0.791 Hz	0.791 Hz
<p><b>VI<sub>Me</sub></b></p> 	+12.487 Hz	12.487 Hz

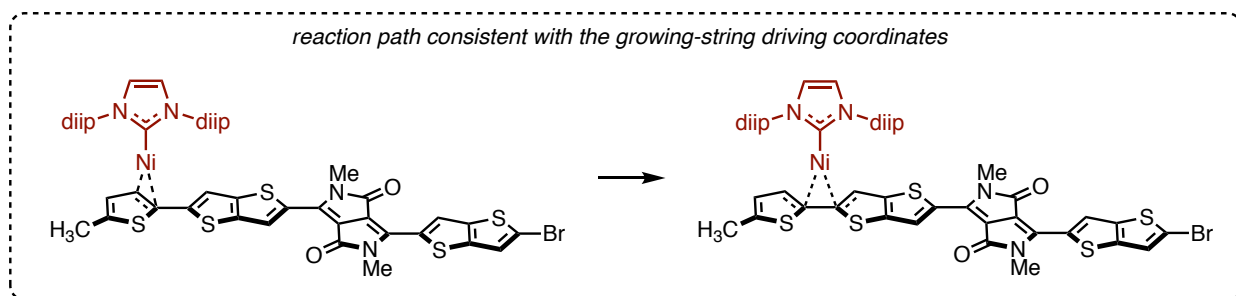
<p style="text-align: center;"><b>V<sub>Me</sub></b></p> 	-1.655 Hz	1.655 Hz
<p style="text-align: center;"><b>VI<sub>Me</sub></b></p> 	-55.752 Hz	55.752 Hz
<p style="text-align: center;"><b>VII<sub>Me</sub></b></p> 	-84.899 Hz	84.899 Hz

### A2.8.3 Discovery of C–S insertion in a TTh containing molecule

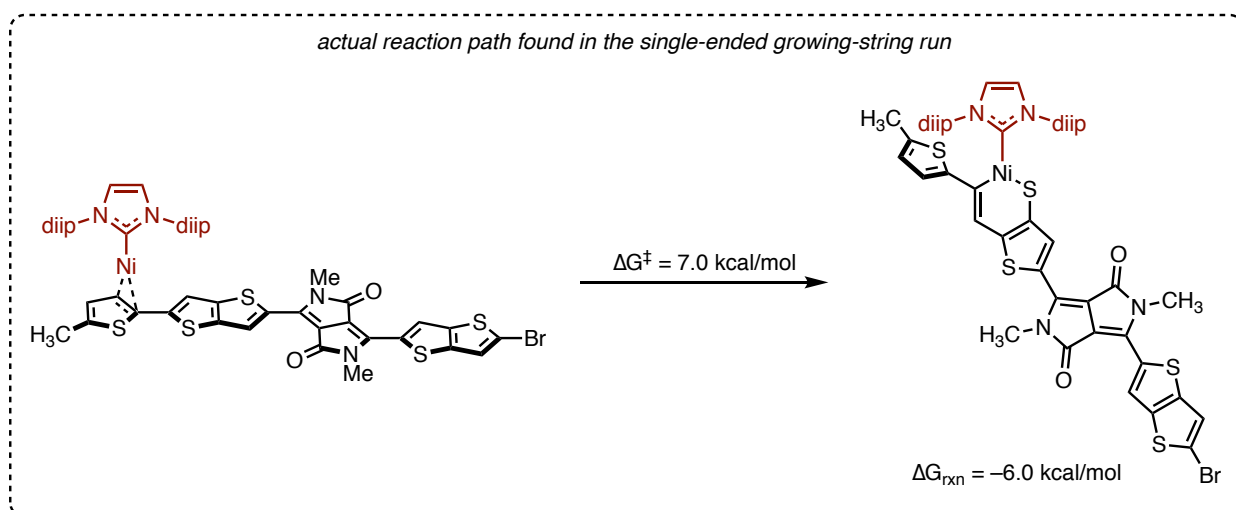
For an unrelated investigation, we were looking at ring-walking of Ni(NHC) catalysts over larger arenes. One of the arenes is a diketopyrrolopyrrole compound shown below:



We intended to understand the barriers to ring-walking in this molecule. We found that for one ring-walking step, when we input driving coordinates that correspond to ring-walking from the terminal thiophene to an internal thienothiophene, shown below:



the single-ended growing string found a reaction path in which the Ni performed C–S insertion into the thienothiophene instead of ring-walking:



Given that the reaction proceeded with a low barrier and was exergonic, this seemed to imply that C–S insertion could occur into thienothiophenes, causing us to investigate the polymerization of thienothiophene and the relevance of C–S insertion to the reaction.

#### ***A2.8.4 Simulations for Catalyst Screening***

Given that C–S insertion has a lower barrier and is more exergonic than ring-walking, C–S insertion will always be favored over ring-walking for Ni(dppp)Cl<sub>2</sub>. As such, we developed a computational model to screen ring-walking and C–S insertion with other ligands with different electronic and steric properties to give insight into how we can prevent C–S insertion. Given that C–S insertion involved oxidation of the metal center from Ni<sup>0</sup> to Ni<sup>II</sup> we expected that using a less

electron-rich Ni complex would be less reducing, and therefore less able to undergo oxidative addition. Therefore, we screened ring-walking and C–S insertion in a series of Ni bidentate phosphonites, depicted in Figure A2.31.

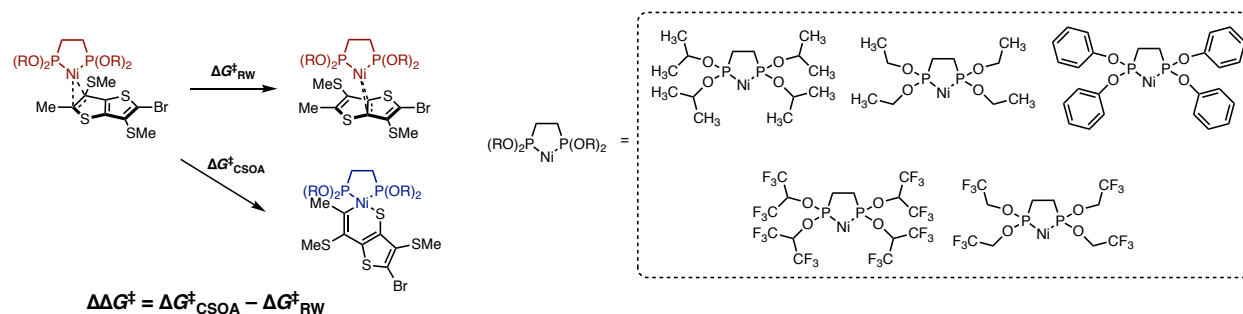


**Figure A2.31** Reactions and catalysts examined for catalyst screening.

We found that, indeed, the preference for ring-walking vs. C–S insertion (measured by  $\Delta\Delta G^\ddagger$  between the two reactions, Figure A2.31) could be affected by the catalyst identity, with catalysts bearing more strongly electron-withdrawing groups causing a greater preference for ring-walking. When we examined the trend in  $\Delta\Delta G^\ddagger$  we found that this primarily arose from a decrease in the  $\Delta G^\ddagger_{\text{RW}}$  with more withdrawing catalysts, which was contrary to our hypothesis. This decrease in  $\Delta G^\ddagger_{\text{RW}}$  with  $\pi$ -backbonding was most obvious when we plotted the  $\Delta G^\ddagger_{\text{RW}}$ ,  $\Delta G^\ddagger_{\text{CSOA}}$ , and  $\Delta\Delta G^\ddagger$  against the charge transferred from Ni-to-P (as a proxy for how withdrawing the phosphine ligand is, Figure A2.32)



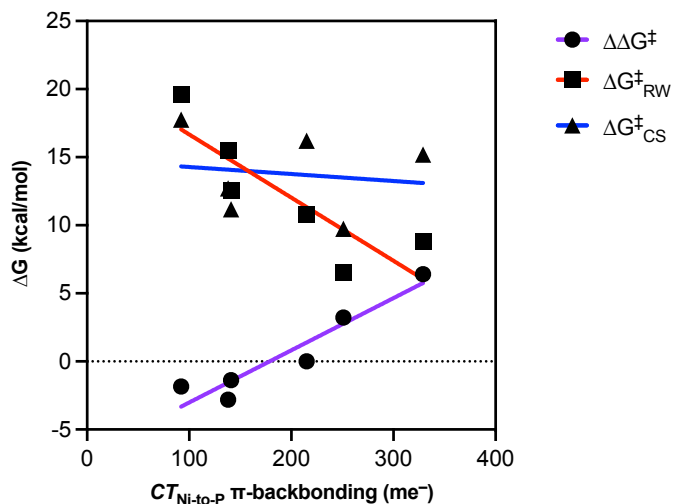


**Figure A2.32** Plot of barriers vs.  $\pi$ -backbonding charge transfer

## A2.9 X-Ray Crystallography Data

### A2.9.1 Structure Determination

Orange blocks of Nickel(1,2-bis(dicyclohexylphosphino)ethane)[(C,S- $\kappa^2$ )-thieno[3,2-b]thiophene], were grown from a tetrahydrofuran/hexanes solution of the compound at 25 °C. A crystal of dimensions 0.15 x 0.12 x 0.12 mm was mounted on a Rigaku AFC10K Saturn 944+ CCD-based X-ray diffractometer equipped with a low temperature device and Micromax-007HF Cu-target micro-focus rotating anode ( $\lambda = 1.54187 \text{ \AA}$ ) operated at 1.2 kW power (40 kV, 30 mA). The X-ray intensities were measured at 85(1) K with the detector placed at a distance 42.00 mm from the crystal. A total of 2028 images were collected with an oscillation width of 1.0° in  $\omega$ . The exposure times were 1 sec. for the low angle images, 4 sec. for high angle. Rigaku d\*trek images were exported to CrysAlisPro for processing and corrected for absorption. The integration of the data yielded a total of 54634 reflections to a maximum  $2\theta$  value of 138.80° of which 6674 were independent and 6561 were greater than  $2\sigma(I)$ . The final cell constants (Table 1) were based on the

xyz centroids of 29253 reflections above  $10\sigma(I)$ . Analysis of the data showed negligible decay during data collection. The structure was solved and refined with the Bruker SHELXTL (version 2018/3) software package, using the space group  $P2(1)/c$  with  $Z = 4$  for the formula  $C_{36}H_{60}P_2S_2Ni$ . All non-hydrogen atoms were refined anisotropically with the hydrogen atoms placed in idealized positions. The bis-thiadienyl ligand is disordered over two positional binding modes. Full matrix least-squares refinement based on  $F^2$  converged at  $R1 = 0.0428$  and  $wR2 = 0.1046$  [based on  $I > 2\sigma(I)$ ],  $R1 = 0.0434$  and  $wR2 = 0.1053$  for all data. Additional details are presented in Table 1 and are given as Supporting Information in a CIF file. Acknowledgement is made for funding from NSF grant CHE-0840456 for X-ray instrumentation.<sup>1011</sup>

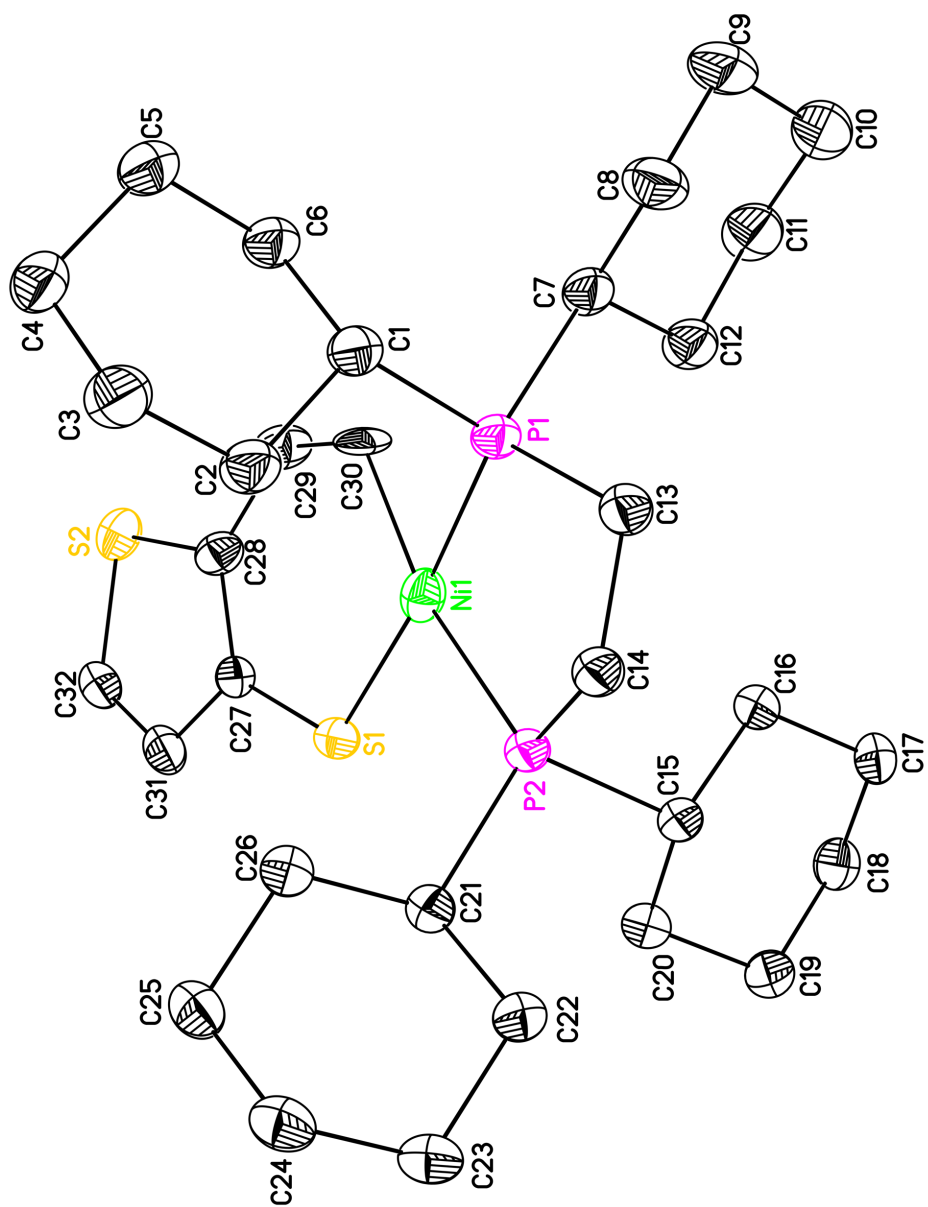


**Figure A2.33** ORTEP of Ni(1,2-bis(dicyclohexylphosphino)ethane)[(C,S-κ2)-thieno[3,2-*b*]thiophene].

**Table A2.7** Crystal data and structure refinement for Ni(1,2-bis(dicyclohexylphosphino)ethane)[(C,S- $\kappa$ 2)-thieno[3,2-*b*]thiophene].

Empirical formula	C36 H60 Ni O P2 S2
Formula weight	693.61
Temperature	85(2) K
Wavelength	1.54184 Å
Crystal system, space group	Monoclinic, P2(1)/c
Unit cell dimensions	a = 12.17790(10) Å alpha = 90 deg.
	b = 17.92990(10) Å beta = 98.8120(10) deg.
	c = 16.6010(2) Å gamma = 90 deg.
Volume	3582.02(6) Å <sup>3</sup>
Z, Calculated density	4, 1.286 Mg/m <sup>3</sup>
Absorption coefficient	2.908 mm <sup>-1</sup>
F(000)	1496
Crystal size	0.150 x 0.120 x 0.120 mm
Theta range for data collection	3.652 to 69.401 deg.
Limiting indices	-14 ≤ h ≤ 14, -21 ≤ k ≤ 21, -20 ≤ l ≤ 19
Reflections collected / unique	54634 / 6674 [R(int) = 0.0388]
Completeness to theta = 67.684	100.00%
Absorption correction	Semi-empirical from equivalents
Max. and min. transmission	1.00000 and 0.82756
Refinement method	Full-matrix least-squares on F <sup>2</sup>
Data / restraints / parameters	6674 / 135 / 452
Goodness-of-fit on F <sup>2</sup>	1.067
Final R indices [I > 2σ(I)]	R1 = 0.0428, wR2 = 0.1046
R indices (all data)	R1 = 0.0434, wR2 = 0.1053
Extinction coefficient	n/a
Largest diff. peak and hole	0.640 and -0.570 e.Å <sup>-3</sup>

## A2.9.2 Coordinates and Angles

**Table A2.8** Atomic coordinates ( $\text{\AA} \times 10^4$ ) and equivalent isotropic displacement parameters ( $\text{\AA}^2 \times 10^3$ ) for Ni(1,2-bis(dicyclohexylphosphino)ethane)[(C,S- $\kappa$ 2)-thieno[3,2-*b*]thiophene].  
U(eq) is defined as one third of the trace of the orthogonalized Uij tensor

	<b>x</b>	<b>y</b>	<b>z</b>	<b>U(eq)</b>
P(1)	2331(1)	7748(1)	8423(1)	23(1)
P(2)	4790(1)	7905(1)	8315(1)	21(1)
Ni(1)	3409(1)	7277(1)	7615(1)	25(1)
S(1)	4494(3)	6712(2)	6979(2)	24(1)
C(27)	3855(5)	6021(3)	6329(3)	23(1)
C(28)	2726(5)	5903(3)	6183(4)	25(1)
C(29)	1858(3)	6328(2)	6456(2)	31(1)
C(30)	1964(11)	6869(9)	7003(8)	26(2)
C(31)	4438(3)	5514(2)	5894(2)	29(1)
C(32)	3768(6)	5025(5)	5421(6)	29(2)
S(2)	2389(1)	5163(1)	5506(1)	30(1)
Ni(1A)	3409(1)	7277(1)	7615(1)	25(1)
S(1A)	2111(5)	6817(4)	6858(3)	27(1)
C(27A)	2410(8)	6079(5)	6237(6)	20(2)
C(28A)	3469(8)	5878(5)	6161(5)	22(2)
C(29A)	4500(6)	6223(3)	6499(4)	23(1)
C(30A)	4628(18)	6819(13)	6989(15)	36(6)
C(31A)	1550(4)	5632(3)	5754(3)	18(1)
C(32A)	2005(8)	5082(7)	5342(8)	39(3)
S(2A)	3442(3)	5113(2)	5505(2)	26(1)
C(1)	1873(2)	7072(1)	9147(1)	26(1)
C(2)	2850(2)	6577(1)	9524(2)	32(1)
C(3)	2497(2)	6009(2)	10125(2)	37(1)
C(4)	1525(2)	5537(1)	9735(2)	37(1)
C(5)	551(2)	6034(1)	9382(2)	36(1)
C(6)	901(2)	6583(1)	8765(1)	30(1)
C(7)	1039(2)	8225(1)	7968(1)	27(1)
C(8)	417(2)	8611(2)	8591(2)	37(1)
C(9)	-661(2)	8965(2)	8158(2)	45(1)
C(10)	-428(2)	9511(2)	7498(2)	43(1)
C(11)	178(2)	9125(2)	6882(2)	41(1)
C(12)	1258(2)	8770(1)	7298(2)	32(1)
C(13)	3077(2)	8466(1)	9089(1)	26(1)
C(14)	4331(2)	8326(1)	9221(1)	25(1)

C(15)	5274(2)	8715(1)	7770(1)	23(1)
C(16)	4284(2)	9140(1)	7305(1)	25(1)
C(17)	4645(2)	9820(1)	6852(1)	28(1)
C(18)	5486(2)	9611(1)	6294(1)	30(1)
C(19)	6473(2)	9210(1)	6781(1)	28(1)
C(20)	6096(2)	8510(1)	7188(1)	26(1)
C(21)	6084(2)	7416(1)	8747(1)	23(1)
C(22)	6934(2)	7922(1)	9264(1)	26(1)
C(23)	8000(2)	7490(1)	9580(1)	29(1)
C(24)	7744(2)	6806(1)	10068(1)	31(1)
C(25)	6910(2)	6299(1)	9551(1)	29(1)
C(26)	5840(2)	6719(1)	9226(1)	26(1)
O(1)	2376(2)	4445(2)	3449(2)	76(1)
C(33)	2426(2)	4053(2)	2698(2)	48(1)
C(34)	1978(3)	3276(2)	2792(2)	54(1)
C(35)	1077(2)	3427(2)	3307(2)	46(1)
C(36)	1524(2)	4038(2)	3846(2)	45(1)

**Table A2.9** Bond lengths [Å] and angles [deg] for Ni(1,2-bis(dicyclohexylphosphino)ethane)[(C,S- $\kappa$ 2)-thieno[3,2-*b*]thiophene].

Atoms	Bond length or angle
P(1)-C(13)	1.845(2)
P(1)-C(7)	1.847(2)
P(1)-C(1)	1.853(2)
P(1)-Ni(1)	2.1849(7)
P(1)-Ni(1A)	2.1849(7)
P(2)-C(14)	1.844(2)
P(2)-C(21)	1.849(2)
P(2)-C(15)	1.854(2)
P(2)-Ni(1A)	2.2025(6)
P(2)-Ni(1)	2.2025(6)
Ni(1)-C(30)	2.029(14)
Ni(1)-S(1)	2.078(2)
S(1)-C(27)	1.746(6)
C(27)-C(28)	1.375(7)
C(27)-C(31)	1.417(6)
C(28)-C(29)	1.432(6)
C(28)-S(2)	1.746(6)
C(29)-C(30)	1.322(11)

C(29)-H(29)	0.95
C(30)-H(30)	0.95
C(31)-C(32)	1.362(9)
C(31)-H(31)	0.95
C(32)-S(2)	1.724(7)
C(32)-H(32)	0.95
Ni(1A)-S(1A)	2.037(5)
Ni(1A)-C(30A)	2.105(18)
S(1A)-C(27A)	1.750(9)
C(27A)-C(28A)	1.363(10)
C(27A)-C(31A)	1.457(10)
C(28A)-C(29A)	1.434(8)
C(28A)-S(2A)	1.748(9)
C(29A)-C(30A)	1.338(16)
C(29A)-H(29A)	0.95
C(30A)-H(30A)	0.95
C(31A)-C(32A)	1.364(11)
C(31A)-H(31A)	0.95
C(32A)-S(2A)	1.731(10)
C(32A)-H(32A)	0.95
C(1)-C(6)	1.530(3)
C(1)-C(2)	1.538(3)
C(1)-H(1)	1
C(2)-C(3)	1.533(3)
C(2)-H(2A)	0.99
C(2)-H(2B)	0.99
C(3)-C(4)	1.517(3)
C(3)-H(3A)	0.99
C(3)-H(3B)	0.99
C(4)-C(5)	1.526(3)
C(4)-H(4A)	0.99
C(4)-H(4B)	0.99
C(5)-C(6)	1.529(3)
C(5)-H(5A)	0.99
C(5)-H(5B)	0.99
C(6)-H(6A)	0.99
C(6)-H(6B)	0.99
C(7)-C(12)	1.534(3)
C(7)-C(8)	1.537(3)
C(7)-H(7)	1
C(8)-C(9)	1.535(3)
C(8)-H(8A)	0.99
C(8)-H(8B)	0.99
C(9)-C(10)	1.529(4)
C(9)-H(9A)	0.99

C(9)-H(9B)	0.99
C(10)-C(11)	1.516(4)
C(10)-H(10A)	0.99
C(10)-H(10B)	0.99
C(11)-C(12)	1.528(3)
C(11)-H(11A)	0.99
C(11)-H(11B)	0.99
C(12)-H(12A)	0.99
C(12)-H(12B)	0.99
C(13)-C(14)	1.529(3)
C(13)-H(13A)	0.99
C(13)-H(13B)	0.99
C(14)-H(14A)	0.99
C(14)-H(14B)	0.99
C(15)-C(16)	1.533(3)
C(15)-C(20)	1.538(3)
C(15)-H(15)	1
C(16)-C(17)	1.531(3)
C(16)-H(16A)	0.99
C(16)-H(16B)	0.99
C(17)-C(18)	1.528(3)
C(17)-H(17A)	0.99
C(17)-H(17B)	0.99
C(18)-C(19)	1.523(3)
C(18)-H(18A)	0.99
C(18)-H(18B)	0.99
C(19)-C(20)	1.530(3)
C(19)-H(19A)	0.99
C(19)-H(19B)	0.99
C(20)-H(20A)	0.99
C(20)-H(20B)	0.99
C(21)-C(26)	1.535(3)
C(21)-C(22)	1.536(3)
C(21)-H(21)	1
C(22)-C(23)	1.533(3)
C(22)-H(22A)	0.99
C(22)-H(22B)	0.99
C(23)-C(24)	1.527(3)
C(23)-H(23A)	0.99
C(23)-H(23B)	0.99
C(24)-C(25)	1.527(3)
C(24)-H(24A)	0.99
C(24)-H(24B)	0.99
C(25)-C(26)	1.530(3)
C(25)-H(25A)	0.99



C(25)-H(25B)	0.99
C(26)-H(26A)	0.99
C(26)-H(26B)	0.99
O(1)-C(33)	1.441(4)
O(1)-C(36)	1.501(4)
C(33)-C(34)	1.514(4)
C(33)-H(33A)	0.99
C(33)-H(33B)	0.99
C(34)-C(35)	1.515(4)
C(34)-H(34A)	0.99
C(34)-H(34B)	0.99
C(35)-C(36)	1.465(4)
C(35)-H(35A)	0.99
C(35)-H(35B)	0.99
C(36)-H(36A)	0.99
C(36)-H(36B)	0.99
C(13)-P(1)-C(7)	103.43(10)
C(13)-P(1)-C(1)	103.69(10)
C(7)-P(1)-C(1)	104.24(10)
C(13)-P(1)-Ni(1)	110.56(7)
C(7)-P(1)-Ni(1)	118.82(8)
C(1)-P(1)-Ni(1)	114.52(7)
C(13)-P(1)-Ni(1A)	110.56(7)
C(7)-P(1)-Ni(1A)	118.82(8)
C(1)-P(1)-Ni(1A)	114.52(7)
C(14)-P(2)-C(21)	103.01(10)
C(14)-P(2)-C(15)	103.69(10)
C(21)-P(2)-C(15)	104.13(9)
C(14)-P(2)-Ni(1A)	109.73(7)
C(21)-P(2)-Ni(1A)	119.90(7)
C(15)-P(2)-Ni(1A)	114.64(7)
C(14)-P(2)-Ni(1)	109.73(7)
C(21)-P(2)-Ni(1)	119.90(7)
C(15)-P(2)-Ni(1)	114.64(7)
C(30)-Ni(1)-S(1)	98.0(3)
C(30)-Ni(1)-P(1)	83.7(3)
S(1)-Ni(1)-P(1)	171.57(11)
C(30)-Ni(1)-P(2)	169.3(4)
S(1)-Ni(1)-P(2)	91.39(8)
P(1)-Ni(1)-P(2)	87.72(2)
C(27)-S(1)-Ni(1)	113.7(2)
C(28)-C(27)-C(31)	112.1(5)
C(28)-C(27)-S(1)	123.9(5)
C(31)-C(27)-S(1)	124.0(4)

C(27)-C(28)-C(29)	129.0(6)
C(27)-C(28)-S(2)	111.1(5)
C(29)-C(28)-S(2)	119.7(5)
C(30)-C(29)-C(28)	127.5(7)
C(30)-C(29)-H(29)	116.3
C(28)-C(29)-H(29)	116.3
C(29)-C(30)-Ni(1)	126.5(8)
C(29)-C(30)-H(30)	116.7
Ni(1)-C(30)-H(30)	116.7
C(32)-C(31)-C(27)	113.8(4)
C(32)-C(31)-H(31)	123.1
C(27)-C(31)-H(31)	123.1
C(31)-C(32)-S(2)	111.4(5)
C(31)-C(32)-H(32)	124.3
S(2)-C(32)-H(32)	124.3
C(32)-S(2)-C(28)	91.5(4)
S(1A)-Ni(1A)-C(30A)	94.4(5)
S(1A)-Ni(1A)-P(1)	93.04(13)
C(30A)-Ni(1A)-P(1)	171.6(7)
S(1A)-Ni(1A)-P(2)	172.1(2)
C(30A)-Ni(1A)-P(2)	85.5(5)
P(1)-Ni(1A)-P(2)	87.72(2)
C(27A)-S(1A)-Ni(1A)	117.3(4)
C(28A)-C(27A)-C(31A)	114.5(7)
C(28A)-C(27A)-S(1A)	122.6(8)
C(31A)-C(27A)-S(1A)	122.9(6)
C(27A)-C(28A)-C(29A)	129.3(9)
C(27A)-C(28A)-S(2A)	109.7(6)
C(29A)-C(28A)-S(2A)	120.9(7)
C(30A)-C(29A)-C(28A)	126.6(11)
C(30A)-C(29A)-H(29A)	116.7
C(28A)-C(29A)-H(29A)	116.7
C(29A)-C(30A)-Ni(1A)	125.9(13)
C(29A)-C(30A)-H(30A)	117
Ni(1A)-C(30A)-H(30A)	117
C(32A)-C(31A)-C(27A)	111.1(6)
C(32A)-C(31A)-H(31A)	124.5
C(27A)-C(31A)-H(31A)	124.5
C(31A)-C(32A)-S(2A)	112.2(7)
C(31A)-C(32A)-H(32A)	123.9
S(2A)-C(32A)-H(32A)	123.9
C(32A)-S(2A)-C(28A)	92.5(5)
C(6)-C(1)-C(2)	109.83(18)
C(6)-C(1)-P(1)	113.30(15)
C(2)-C(1)-P(1)	110.49(15)

C(6)-C(1)-H(1)	107.7
C(2)-C(1)-H(1)	107.7
P(1)-C(1)-H(1)	107.7
C(3)-C(2)-C(1)	111.78(19)
C(3)-C(2)-H(2A)	109.3
C(1)-C(2)-H(2A)	109.3
C(3)-C(2)-H(2B)	109.3
C(1)-C(2)-H(2B)	109.3
H(2A)-C(2)-H(2B)	107.9
C(4)-C(3)-C(2)	111.7(2)
C(4)-C(3)-H(3A)	109.3
C(2)-C(3)-H(3A)	109.3
C(4)-C(3)-H(3B)	109.3
C(2)-C(3)-H(3B)	109.3
H(3A)-C(3)-H(3B)	107.9
C(3)-C(4)-C(5)	110.4(2)
C(3)-C(4)-H(4A)	109.6
C(5)-C(4)-H(4A)	109.6
C(3)-C(4)-H(4B)	109.6
C(5)-C(4)-H(4B)	109.6
H(4A)-C(4)-H(4B)	108.1
C(4)-C(5)-C(6)	110.66(19)
C(4)-C(5)-H(5A)	109.5
C(6)-C(5)-H(5A)	109.5
C(4)-C(5)-H(5B)	109.5
C(6)-C(5)-H(5B)	109.5
H(5A)-C(5)-H(5B)	108.1
C(5)-C(6)-C(1)	111.61(19)
C(5)-C(6)-H(6A)	109.3
C(1)-C(6)-H(6A)	109.3
C(5)-C(6)-H(6B)	109.3
C(1)-C(6)-H(6B)	109.3
H(6A)-C(6)-H(6B)	108
C(12)-C(7)-C(8)	111.01(19)
C(12)-C(7)-P(1)	111.07(15)
C(8)-C(7)-P(1)	114.21(16)
C(12)-C(7)-H(7)	106.7
C(8)-C(7)-H(7)	106.7
P(1)-C(7)-H(7)	106.7
C(9)-C(8)-C(7)	110.2(2)
C(9)-C(8)-H(8A)	109.6
C(7)-C(8)-H(8A)	109.6
C(9)-C(8)-H(8B)	109.6
C(7)-C(8)-H(8B)	109.6
H(8A)-C(8)-H(8B)	108.1

C(10)-C(9)-C(8)	111.2(2)
C(10)-C(9)-H(9A)	109.4
C(8)-C(9)-H(9A)	109.4
C(10)-C(9)-H(9B)	109.4
C(8)-C(9)-H(9B)	109.4
H(9A)-C(9)-H(9B)	108
C(11)-C(10)-C(9)	110.7(2)
C(11)-C(10)-H(10A)	109.5
C(9)-C(10)-H(10A)	109.5
C(11)-C(10)-H(10B)	109.5
C(9)-C(10)-H(10B)	109.5
H(10A)-C(10)-H(10B)	108.1
C(10)-C(11)-C(12)	111.0(2)
C(10)-C(11)-H(11A)	109.4
C(12)-C(11)-H(11A)	109.4
C(10)-C(11)-H(11B)	109.4
C(12)-C(11)-H(11B)	109.4
H(11A)-C(11)-H(11B)	108
C(11)-C(12)-C(7)	111.12(19)
C(11)-C(12)-H(12A)	109.4
C(7)-C(12)-H(12A)	109.4
C(11)-C(12)-H(12B)	109.4
C(7)-C(12)-H(12B)	109.4
H(12A)-C(12)-H(12B)	108
C(14)-C(13)-P(1)	111.10(15)
C(14)-C(13)-H(13A)	109.4
P(1)-C(13)-H(13A)	109.4
C(14)-C(13)-H(13B)	109.4
P(1)-C(13)-H(13B)	109.4
H(13A)-C(13)-H(13B)	108
C(13)-C(14)-P(2)	111.82(15)
C(13)-C(14)-H(14A)	109.3
P(2)-C(14)-H(14A)	109.3
C(13)-C(14)-H(14B)	109.3
P(2)-C(14)-H(14B)	109.3
H(14A)-C(14)-H(14B)	107.9
C(16)-C(15)-C(20)	109.90(17)
C(16)-C(15)-P(2)	110.54(14)
C(20)-C(15)-P(2)	113.93(14)
C(16)-C(15)-H(15)	107.4
C(20)-C(15)-H(15)	107.4
P(2)-C(15)-H(15)	107.4
C(17)-C(16)-C(15)	112.34(17)
C(17)-C(16)-H(16A)	109.1
C(15)-C(16)-H(16A)	109.1

C(17)-C(16)-H(16B)	109.1
C(15)-C(16)-H(16B)	109.1
H(16A)-C(16)-H(16B)	107.9
C(18)-C(17)-C(16)	111.86(17)
C(18)-C(17)-H(17A)	109.2
C(16)-C(17)-H(17A)	109.2
C(18)-C(17)-H(17B)	109.2
C(16)-C(17)-H(17B)	109.2
H(17A)-C(17)-H(17B)	107.9
C(19)-C(18)-C(17)	109.97(18)
C(19)-C(18)-H(18A)	109.7
C(17)-C(18)-H(18A)	109.7
C(19)-C(18)-H(18B)	109.7
C(17)-C(18)-H(18B)	109.7
H(18A)-C(18)-H(18B)	108.2
C(18)-C(19)-C(20)	110.91(18)
C(18)-C(19)-H(19A)	109.5
C(20)-C(19)-H(19A)	109.5
C(18)-C(19)-H(19B)	109.5
C(20)-C(19)-H(19B)	109.5
H(19A)-C(19)-H(19B)	108
C(19)-C(20)-C(15)	110.42(17)
C(19)-C(20)-H(20A)	109.6
C(15)-C(20)-H(20A)	109.6
C(19)-C(20)-H(20B)	109.6
C(15)-C(20)-H(20B)	109.6
H(20A)-C(20)-H(20B)	108.1
C(26)-C(21)-C(22)	110.96(17)
C(26)-C(21)-P(2)	111.50(14)
C(22)-C(21)-P(2)	113.51(14)
C(26)-C(21)-H(21)	106.8
C(22)-C(21)-H(21)	106.8
P(2)-C(21)-H(21)	106.8
C(23)-C(22)-C(21)	110.93(18)
C(23)-C(22)-H(22A)	109.5
C(21)-C(22)-H(22A)	109.5
C(23)-C(22)-H(22B)	109.5
C(21)-C(22)-H(22B)	109.5
H(22A)-C(22)-H(22B)	108
C(24)-C(23)-C(22)	110.82(18)
C(24)-C(23)-H(23A)	109.5
C(22)-C(23)-H(23A)	109.5
C(24)-C(23)-H(23B)	109.5
C(22)-C(23)-H(23B)	109.5
H(23A)-C(23)-H(23B)	108.1

C(25)-C(24)-C(23)	110.67(18)
C(25)-C(24)-H(24A)	109.5
C(23)-C(24)-H(24A)	109.5
C(25)-C(24)-H(24B)	109.5
C(23)-C(24)-H(24B)	109.5
H(24A)-C(24)-H(24B)	108.1
C(24)-C(25)-C(26)	111.22(18)
C(24)-C(25)-H(25A)	109.4
C(26)-C(25)-H(25A)	109.4
C(24)-C(25)-H(25B)	109.4
C(26)-C(25)-H(25B)	109.4
H(25A)-C(25)-H(25B)	108
C(25)-C(26)-C(21)	111.28(17)
C(25)-C(26)-H(26A)	109.4
C(21)-C(26)-H(26A)	109.4
C(25)-C(26)-H(26B)	109.4
C(21)-C(26)-H(26B)	109.4
H(26A)-C(26)-H(26B)	108
C(33)-O(1)-C(36)	105.4(2)
O(1)-C(33)-C(34)	107.3(3)
O(1)-C(33)-H(33A)	110.3
C(34)-C(33)-H(33A)	110.3
O(1)-C(33)-H(33B)	110.3
C(34)-C(33)-H(33B)	110.3
H(33A)-C(33)-H(33B)	108.5
C(33)-C(34)-C(35)	101.4(2)
C(33)-C(34)-H(34A)	111.5
C(35)-C(34)-H(34A)	111.5
C(33)-C(34)-H(34B)	111.5
C(35)-C(34)-H(34B)	111.5
H(34A)-C(34)-H(34B)	109.3
C(36)-C(35)-C(34)	104.2(2)
C(36)-C(35)-H(35A)	110.9
C(34)-C(35)-H(35A)	110.9
C(36)-C(35)-H(35B)	110.9
C(34)-C(35)-H(35B)	110.9
H(35A)-C(35)-H(35B)	108.9
C(35)-C(36)-O(1)	108.3(2)
C(35)-C(36)-H(36A)	110
O(1)-C(36)-H(36A)	110
C(35)-C(36)-H(36B)	110
O(1)-C(36)-H(36B)	110
H(36A)-C(36)-H(36B)	108.4

## **A2.10 XYZ coordinates**

XYZ files of all compounds are available by request via e-mail to [mdhannig@umich.edu](mailto:mdhannig@umich.edu)

## A2.11 References

---

- <sup>1</sup> Love, B. E.; Jones, E. G. The Use of Salicylaldehyde Phenylhydrazone as an Indicator for the Titration of Organometallic Reagents. *J. Org. Chem.* **1999**, *64*, 3755–3756.
- <sup>2</sup> Fulmer, G. R.; Miller, A. J. M.; Sherden, N. H.; Gottlieb, H. E.; Nudelman, A.; Stoltz, B. M.; Bercaw, J. E.; Goldberg, K. I. NMR Chemical Shifts of Trace Impurities: Common Laboratory Solvents, Organics, and Gases in Deuterated Solvents Relevant to the Organometallic Chemist. *Organometallics* **2010**, *29*, 2176–2179.
- <sup>3</sup> Vicic, D. A.; Jones, W. D. Room-Temperature Desulfurization of Dibenzothiophene Mediated by [(*i*-Pr<sub>2</sub>PCH<sub>2</sub>)<sub>2</sub>NiH]<sub>2</sub>. *J. Am. Chem. Soc.* **1997**, *119*, 10855–10856.
- <sup>4</sup> Vicic, D. A.; Jones, W. D. Deep Hydrodesulfurization in Homogeneous Solution: Access to a Transition-Metal Insertion Complex of 4,6-Dimethyldibenzothiophene *Organometallics* **1998**, *17*, 3411–3413.
- <sup>5</sup> Vicic, D. A.; Jones, W. D. Modeling the Hydrodesulfurization Reaction at Nickel. Unusual Reactivity of Dibenzothiophenes Relative to Thiophene and Benzothiophene. *J. Am. Chem. Soc.* **1999**, *121*, 7606–7617.
- <sup>6</sup> Willot, P.; Koeckelberghs, G. Evidence for Catalyst Association in the Catalyst Transfer Polymerization of Thieno[3,2-*b*]thiophene *Macromolecules* **2014**, *47*, 8548–8555.
- <sup>7</sup> Willot, P.; Koeckelberghs, G. Evidence for Catalyst Association in the Catalyst Transfer Polymerization of Thieno[3,2-*b*]thiophene *Macromolecules* **2014**, *47*, 8548–8555.
- <sup>8</sup> Provasi, P. F.; Sauer, S. P. A. Optimized Basis Sets for the Calculation of Indirect Nuclear Spin-Spin Coupling Constants Involving the Atoms B, Al, Si, P, and Cl. *J. Chem. Phys.* **2010**, *133*, 054308.
- <sup>9</sup> a) Balabanov, N. B.; Peterson, K. A. Systematically Convergent Basis Sets for Transition Metals. I. All-Electron Correlation Consistent Basis Sets for the 3d Elements Sc–Zn. *J. Chem. Phys.* **2005**, *123*, 064107.
- b) Balabanov, N. B.; Peterson, K. A. Basis Set Limit Electronic Excitation Energies, Ionization Potentials, and Electron Affinities for the 3d Transition Metal Atoms: Coupled Cluster and Multireference Methods. *J. Chem. Phys.* **2006**, *125*, 074110.
- c) Dunning, T. H. Gaussian Basis Sets for Use in Correlated Molecular Calculations. I. The Atoms Boron Through Neon and Hydrogen. *J. Chem. Phys.* **1989**, *90*, 1007–1023.
- d) Prascher, B. P.; Woon, D. E.; Peterson, K. A.; Dunning, T. H.; Wilson, A. K. Gaussian Basis Sets for Use in Correlated Molecular Calculations. VII. Valence, Core-Valence, and Scalar Relativistic Basis Sets for Li, Be, Na, and Mg. *Theor. Chem. Acc.* **2011**, *128*, 69–82.
- e) Wilson, A. K.; Woon, D. E.; Peterson, K. A.; Dunning, T. H. Gaussian Basis Sets for Use in Correlated Molecular Calculations. IX. The Atoms Gallium through Krypton. *J. Chem. Phys.* **1999**, *110*, 7667–7676.
- f) Woon, D. E.; Dunning, T. H. Gaussian Basis Sets for Use in Correlated Molecular Calculations. III. The Atoms Aluminum Through Argon. *J. Chem. Phys.* **1993**, *98*, 1358–1371.
- <sup>10</sup> CrystalClear Expert 2.0 r16, Rigaku Americas and Rigaku Corporation (2014), Rigaku Americas, 9009, TX, USA 77381-5209, Rigaku Tokyo, 196-8666, Japan.
- <sup>11</sup> Sheldrick, G. M. Crystal structure refinement with SHELXL. *Acta Cryst.* **2015**, *C71*, 3–8.



## Appendix 3 Supporting Information for Elucidating Ring-Walking in Catalyst-Transfer Polymerization

### A3.1 Computational Details

All computations were performed in Q-chem 5.3.<sup>1</sup> Initial geometries were construed using Avogadro and optimized at the B3LYP level of theory with the LANL2DZ basis set for Ni and Pd with added f-polarization functions,<sup>2</sup> and the 6-31G\* basis set for all other atoms. Ring-walking reaction paths were found using the sing-ended growing-string method described by Zimmerman, using driving coordinates that correspond to ring-walking. Transition state structures from the growing-string runs were optimized at the same level of theory. Stationary points were confirmed by the number of negative vibrational modes from frequency calculations at the B3LYP level of theory with the basis set described above; all reactants and products had 0 negative frequencies; all transition states had 1 negative frequency. Final energies were evaluated at the  $\omega$ B97X level of theory, with the def2-TZVP basis set, and SMD solvation in THF, with thermodynamic corrections applied at 298 K with the entropy and enthalpy values obtained from frequency calculations. Charge transfer values were obtained with the second-generation energy decomposition analysis scheme with absolutely localized molecular orbitals (ALMO-EDA2) with at the  $\omega$ B97M-V level of theory and def2-TZVPD basis set. For the ALMO-EDA2, molecules were fragmented along the bonds that connect ancillary ligand and metal, or the bonds that connect the metal and arene. The resulting fragments were assumed singlets.

### A3.2 Trends with Buried Volume

% Buried volume was calculated using SambVca2.1, a web application that takes a XYZ structure of an organometallic complex provides the buried volume of the ligand(s) on the complex.<sup>3</sup> The buried volume of each complex was evaluated and plotted against the  $\Delta G_{RW}^\ddagger$ , shown in Figure A3.1. The low  $R^2$  between %buried volume and ring-walking barrier indicated that buried volume was a bad predictor of ring-walking barrier.

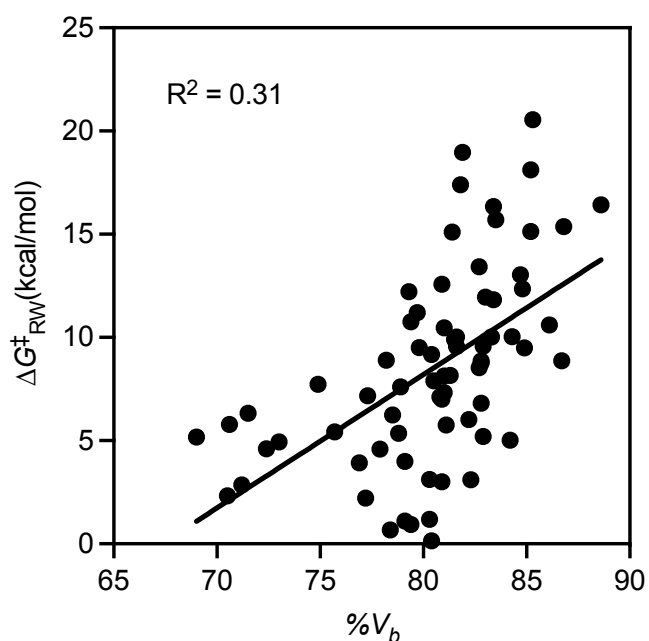


**Figure A3.1.** Plot of  $\Delta G_{RW}^\ddagger$  vs % buried volume.

### A3.3 XYZ Coordinates

XYZ files of all compounds are available by request via e-mail to [mdhannig@umich.edu](mailto:mdhannig@umich.edu)

### A3.4 References

- <sup>1</sup> Epifanovsky, E.; Gilbert, A. T.; Feng, X.; Lee, J.; Mao, Y.; Mardirossian, N.; Pokhilko, P.; White, A. F.; Coons, M. P.; Dempwolff, A. L.; Gan, Z.; Hait, D.; Horn, P. R.; Jacobson, L. D.; Kaliman, I.; Kussmann, J.; Lange, A. W.; Lao, K. U.; Levine, D. S.; Liu, J.; McKenzie, S. C.; Morrison, A. F.; Nanda, K. D.; Plasser, F.; Rehn, D. R.; Vidal, M. L.; You, Z.-Q.; Zhu, Y.; Alam, B.; Albrecht, B. J.; Aldossary, A.; Alguire, E.; Andersen, J. H.; Athavale, V.; Barton, D.; Begam, K.; Behn, A.; Bellonzi, N.; Bernard, Y. A.; Berquist, E. J.; Burton, H. G.; Carreras, A.; Carter-Fenk, K.; Chakraborty, R.; Chien, A. D.; Closser, K. D.; Cofer-Shabica, V.; Dasgupta, S.; de Wergifosse, M.; Deng, J.; Diedenhofen, M.; Do, H.; Ehlert, S.; Fang, P.-T.; Fatehi, S.; Feng, Q.; Friedhoff, T.; Gayvert, J.; Ge, Q.; Gidofalvi, G.; Goldey, M.; Gomes, J.; González-Espinoza, C. E.; Gulania, S.; Gunina, A. O.; Hanson-Heine, M. W.; Harbach, P. H.; Hauser, A.; Herbst, M. F.; Hernández Vera, M.; Hodecker, M.; Holden, Z. C.; Houck, S.; Huang, X.; Hui, K.; Huynh, B. C.; Ivanov, M.; Jász, Á.; Ji, H.; Jiang, H.; Kaduk, B.; Kähler, S.; Khistyayev, K.; Kim, J.; Kis, G.; Klunzinger, P.; Koczor-Benda, Z.; Koh, J. H.; Kosenkov, D.; Koulias, L.; Kowalczyk, T.; Krauter, C. M.; Kue, K.; Kunitsa, A.; Kus, T.; Ladjánszki, I.; Landau, A.; Lawler, K. V.; Lefrancois, D.; Lehtola, S.; Li, R. R.; Li, Y.-P.; Liang, J.; Liebenthal, M.; Lin, H.-H.; Lin, Y.-S.; Liu, F.; Liu, K.-Y.; Loipersberger, M.; Luenser, A.; Manjanath, A.; Manohar, P.; Mansoor, E.; Manzer, S. F.; Mao, S.-P.; Marenich, A. V.; Markovich, T.; Mason, S.; Maurer, S. A.; McLaughlin, P. F.; Menger, M. F.; Mewes, J.-M.; Mewes, S. A.; Morgante, P.; Mullinax, J. W.; Oosterbaan, K. J.; Paran, G.; Paul, A. C.; Paul, S. K.; Pavošević, F.; Pei, Z.; Prager, S.; Proynov, E. I.; Rák, Á.; Ramos-Cordoba, E.; Rana, B.; Rask, A. E.; Rettig, A.; Richard, R. M.; Rob, F.; Rossomme, E.; Scheele, T.; Scheurer, M.; Schneider, M.; Sergueev, N.; Sharada, S. M.; Skomorowski, W.; Small, D. W.; Stein, C. J.; Su, Y.-C.; Sundstrom, E. J.; Tao, Z.; Thirman, J.; Tornai, G. J.; Tsuchimochi, T.; Tubman, N. M.; Veccham, S. P.; Vydrov, O.; Wenzel, J.; Witte, J.; Yamada, A.; Yao, K.; Yeganeh, S.; Yost, S. R.; Zech, A.; Zhang, I. Y.; Zhang, X.; Zhang, Y.; Zuev, D.; Aspuru-Guzik, A.; Bell, A. T.; Besley, N. A.; Bravaya, K. B.; Brooks, B. R.; Casanova, D.; Chai, J.-D.; Coriani, S.; Cramer, C. J.; Cserey, G.; DePrince, A. E.; DiStasio, R. A.; Dreuw, A.; Dunietz, B. D.; Furlani, T. R.; Goddard, W. A.; Hammes-Schiffer, S.; Head-Gordon, T.; Hehre, W. J.; Hsu, C.-P.; Jagau, T.-C.; Jung, Y.; Klamt, A.; Kong, J.; Lambrecht, D. S.; Liang, W. Z.; Mayhall, N. J.; McCurdy, C. W.; Neaton, J. B.; Ochsenfeld, C.; Parkhill, J. A.; Peverati, R.; Rassolov, V. A.; Shao, Y.; Slipchenko, L. V.; Stauch, T.; Steele, R. P.; Subotnik, J. E.; Thom, A. J.; Tkatchenko, A.; Truhlar, D. G.; Van Voorhis, T.; Wesolowski, T. A.; Whaley, K. B.; Woodcock, H. L.; Zimmerman, P. M.; Faraji, S.; Gill, P. M.; Head-Gordon, M.; Herbert, J. M.; Krylov, A. I. Software for the Frontiers of Quantum Chemistry: An Overview of Developments in the Q-Chem 5 Package. *J. Chem. Phys.* **2021**, *155*, 084801.
- <sup>2</sup> Ehlers, A. W.; Böhme, M.; Dapprich, S.; Gobbi, A.; Höllwarth, A.; Jonas, V.; Köhler, K. D.; Stegmann, R.; Veldkamp, A.; Frenking, G. A Set Of F-Polarization Functions For Pseudo-Potential Basis Sets Of The Transition Metals Sc-Cu, Y-Ag and La-Au. *Chem. Phys. Lett.* **1993**, *208*, 111–114.
- <sup>3</sup> Falivene, L.; Cao, Z.; Petta, A.; Serra, L.; Poater, A.; Oliva, R.; Scarano, V.; Cavallo, L. Towards the Online Computer-Aided Design of Catalytic Pockets. *Nat. Chem.* **2019**, *11*, 872–879.